# Quantification of Coarse TiN-rich Precipitates in High Ti Microalloyed Steels Using EMPA Mapping and SEM/EDX

by

Tamara Kazoun

A thesis submitted in partial fulfillment of the requirements for the degree of

Master of Science
in
Materials Engineering

Department of Chemical and Materials Engineering
University of Alberta

# Abstract

Microalloyed steels are high strength steels with low alloying additions of Ti, Nb, and V. These microalloying elements form carbonitride precipitates during thermomechanical controlled processing (TMCP), which enhance the mechanical properties of steel. TiN is one of the first precipitates to form during steel production. It forms in the liquid during solidification and is coarse. It can also precipitate with other elements and form TiN-rich precipitate complexes.

A precipitate analysis was performed to quantify and characterize two types of coarse titanium precipitates in seven titanium rich microalloyed steels. The steels varied in titanium (Ti) and niobium (Nb) contents, ranging from 0.047 – 0.122 wt% Ti and 0.015 – 0.088 wt% Nb. The Ti precipitates studied were titanium nitride (TiN) precipitating on calcium sulfide (CaS) inclusions and TiN-rich precipitates that have Nb precipitating on them, forming (Ti,Nb)N.

Electron microprobe analysis (EMPA) mapping of the steel samples was undertaken to quantify the prevalence of TiN nucleation on CaS inclusions and Nb on TiN to form (Ti,Nb)N. Elemental maps for Ti, Nb, Mn, Ca, and S were generated through the thickness of the microalloyed steels. Each elemental map consisted of approximately 300,000 – 900,000 pixels. The greyscale intensity and location of each element through the thickness of the strips were obtained using a custom developed code. The greyscale elemental maps were correlated with EMPA line scan data to quantify the greyscale intensities into an approximate wt% value. For a given Ti pixel concentration, co-precipitates of TiN and CaS, including spatial locations, were counted. It was found that the total amount of TiN-CaS precipitates was relatively low compared to the total amount of Ti precipitates in the sample. For the amount of CaS inclusions in the samples, approximately 85-90% were nucleation sites for TiN and formed TiN-CaS precipitates. Steels with higher Ti contents (4372, 4175, and 4280) exhibited the largest amounts of TiN precipitating on

CaS inclusions. Most TiN-CaS precipitates were found at the steel quarter thickness or near the surface.

Similarly, for a given Ti and Nb pixel concentrations, co-precipitates of Ti and Nb, including spatial locations, were counted. For (Ti,Nb)N, steels 4372 and 4280, which had the highest Ti and Nb concentrations exhibited the largest counts. The number of (Ti,Nb)N throughout the thickness of the steels was almost constant in all samples.

Scanning electron microscopy (SEM) and energy dispersive x-ray (EDX) spectroscopy were used to verify the presence and composition of TiN-CaS assemblages and (Ti,Nb)N at a number of specific locations in the steels. SEM was also used to capture micrographs of Ti precipitates to develop size distributions. A size analysis was done on sample 4280 to explore the difference in size between TiN/(Ti,Nb)N and TiN-CaS. The analysis showed that TiN that nucleated on CaS inclusions was approximately 4 μm larger than TiN or (Ti,Nb)N that nucleated on its own. Another size analysis was performed on samples 4280, 4175, 4052, and 4093 to study the size difference between TiN and (Ti,Nb)N. Results showed that (Ti,Nb)N particles were approximately 1.6 μm in size, and TiN particles were approximately 2.7-3.8 μm in size. The size of TiN was constant across the different samples.

*"The people you love become ghosts inside of you and like this you keep them alive"*

- *Robert Montgomery*

To my dad,

Although I've always dreamt of sharing this moment with you, I'll settle for sharing it with the ghost of you. I know if you were here, you would have been the proudest and to me knowing that is enough.

May your soul continue to rest in peace. Allah yerhamak baba habibi.

# Acknowledgements

First and foremost, I would like to thank my family, especially my parents and brothers, for their endless support and for believing in me. I am forever grateful for all that you do for me, and I am forever indebted to you. No words will ever be enough to express my gratitude and love for you.

I also want to express my absolute appreciation to Dr. Wiskel, Dr. Henein, and Dr. Ivey for their guidance throughout this project. I am grateful for everything you taught me. Thanks to you I was able to develop skills that I can carry on with me for the rest of my life.

To my girls Yasmine, Rawan, Donia, Bailey, and Ayan: thank you for the support and all the caffeine. I wouldn't have been able to finish this without all the coffee and energy drinks, so I appreciate you.

To the friends I made along the way Dylan, Ry, and the ECERF crew, thank you for listening to me and always helping me out. I always had something to look forward to in my days at university knowing it's a fun time during breaks with you. Also, a special thanks to Sohaib and Nazzal for all their help.

I would also like to thank Nadim for being supportive, keeping me entertained and accompanied with great music throughout the all-nighters I had to pull, and for making this whole process a lot better and easier.

To my steel group colleagues, Tailin, Vanda, and Rishav, thank you for all your help, training, and advice.

Thanks to Fayad Rahaman for his help developing the codes used in this project.

# Table of Contents

# List of Tables

# List of Figures

# Nomenclature

| | |
|---|---|
| *EMPA* | Electron microprobe analysis |
| *SEM* | Scanning electron microscope |
| *EDX* | Energy dispersive x-rays |
| *WDS* | Wavelength dispersive spectroscopy |
| *TMCP* | Thermomechanical controlled processing |
| *HSLA* | High strength low alloy |
| $\delta$ | Delta phase |
| $\gamma$ | Austenite |
| *Y.S* | Yield strength |
| *CL* | Center line |
| *QL* | Quarter line |
| *LN* | Lognormal |
| *L* | Liquid |
| *BCC* | Body centered cubic |
| *FCC* | Face centered cubic |

# Chapter 1: Introduction

Microalloyed steels are a widely used type of high strength low alloy steels (HSLA) in engineering applications for their high strengths, toughness, fatigue strength, weldability, and relatively low cost [1]. They are used extensively in the pipeline industry due to their weldability and in the automotive industry for their good toughness and impact strength [1,2]. They contain additions of the alloying elements niobium (Nb), titanium (Ti), and vanadium (V) and are produced through thermomechanical controlled processing (TMCP) [1]. Processing parameters and alloying elements play a major role in defining the mechanical properties of microalloyed steels through grain refinement and precipitation hardening [1,2].

There are four steps to TMCP: homogenization/reheating, rough rolling, finish rolling, and laminar/accelerated cooling [3]. Homogenization is the first step in TMCP and is used to produce a uniform chemical composition and microstructure in the steel and helps reduce segregation [4]. After homogenization, rough rolling and finish rolling are used to produce finer grain sizes and enhance the steel's mechanical properties while reducing the thickness of the steel [5]. Lasty, accelerated cooling is utilized to cool the skelp at a given cooling rate, where fine austenite grains are transformed to ferrite and bainite [6].

Microalloying elements (Ti, Nb, and V) precipitate during all stages of TMCP and aid with enhancing the steel strength by grain refinement and precipitation strengthening [7]. In particular, TiN and (Ti,Nb)N will form during solidification and at higher temperatures [8,9]. For the former, relatively large (> 0.5 μm) TiN/(Ti,Nb)N precipitates can form.

The work presented in this thesis will focus on characterizing the relatively large TiN/(Ti,Nb)N that form during solidification. In particular, a methodology that quantifies Ti precipitates using electron microprobe analysis (EMPA) mapping will be presented. Scanning electron microscopy and energy dispersive x-ray spectroscopy (SEM/EDX) were also undertaken to validate the EMPA technique and provide size and composition data. In addition, the effect of both CaS inclusions and Nb content on TiN/(Ti,Nb)N morphology will be studied.

The objectives of this work are to answer the following questions:

1. What is the prevalence of TiN precipitates on preexisting CaS nonmetallic inclusions, and how abundant are these precipitates through the thickness of the steels?

2. How does TiN precipitating on CaS inclusions affect the size and morphology of the precipitate?
3. What is the effect of Nb composition on the amount of (Ti,Nb)N forming and its morphology?

Seven microalloyed steel samples that varied in Ti and Nb content were studied. Ti and Nb concentrations ranged from 0.047 to 0.122 wt% Ti and 0.015 to 0.088 wt% Nb. SEM/EDX analysis in conjunction with EMPA mapping coordinates were used to quantify the size and composition of TiN, (Ti,Nb)N, and TiN-CaS through the skelp thickness.

There are six chapters in this thesis. Chapter 2 is a literature review which covers relevant topics to this research, such as: microalloyed steels, TMCP, fundamentals of Ti precipitation, characterization techniques utilized, precipitation of TiN on CaS inclusions, and precipitation of (Ti,Nb)N. Chapter 3 introduces the steel samples being studied along with the methodology used for obtaining the results and analysis. Chapter 4 presents and discusses the TiN-CaS EMPA count, SEM/EDX characterization of TiN-CaS precipitates, and their size distributions. Chapter 5 presents and discusses the TiN-Nb EMPA count, SEM/EDX characterization of (Ti,Nb)N, and size distributions of TiN and (Ti,Nb)N in steels with varying Ti and Nb contents. Lastly, Chapter 6 concludes the research that was performed and discusses suggestions for future work.

# Chapter 2: Literature Review

This chapter includes a literature review on microalloyed steels, TMCP, fundamentals of Ti precipitates, characterization of precipitates, and precipitation of CaS and (Ti,Nb)N

## 2.1 Microalloyed Steels

Microalloyed steels are a type of high strength low alloy (HSLA) steels with low concentrations of carbon and the microalloying elements Nb, Ti, and V [10]. They exhibit high strength, good toughness, and good weldability. The typical range for yield strength in microalloyed steels is 350 – 550 MPa, which depends on the thermomechanical processing of the steel and its alloying elements [1]. Since this project studies Ti precipitates, which may contain Nb, the roles of these two microalloying additions will be reviewed.

### 2.1.1 Role of Ti and Nb in microalloyed steels

Titanium plays two roles in microalloyed steels depending on its composition: grain refinement and precipitate strengthening. Generally, it is a strong austenite grain size refiner. At concentrations greater than 0.05 wt%, it begins to exhibit strengthening effects [10]. Ti also improves the toughness of the steel by stabilizing dissolved nitrogen [10]. Typical Ti contents range between 0.01 – 0.02 wt% [10]. However, the Ti contents in the samples studied in this project are all greater than 0.02 wt%, which is why characterizing the precipitates to explore the effects of higher Ti contents is important.

Similar to the Ti, Nb can also play a role in grain refinement and precipitate strengthening. However, it mainly contributes to the refinement of austenite grain size by forming precipitates above transformation temperatures [10]. When it comes to precipitate strengthening, it is not as strong as Ti [10]. Typical Nb contents range between 0.02 – 0.1 wt% [10]. All the samples being studied in this project contain amounts of Nb that fall within this range, except for sample 4093.

### 2.1.2 Precipitation strengthening

Precipitation strengthening enhances the strength, weldability, and in some cases, toughness of microalloyed steels. Fine grained second phase precipitates can increase the strength of the steel by precipitation strengthening. It is the precipitation of Ti, Nb, and V carbonitrides at the austenite/ferrite interface upon reheating of the steel, which impedes dislocations, and pins the growth of the austenite grains producing finer ferrite grains [11]. Ti plays a major role in

precipitation strengthening as it precipitates early on in the liquid in the form of TiN and can prevent grain growth and pin dislocations at elevated temperatures [11]. Precipitation strengthening is an important concept to study as it contributes significantly to an increase in strength in the steel. However, precipitates contributing to precipitate strengthening are finer sized precipitates (<20 nm) [11]. To optimize precipitate strengthening, it is important to produce finer sized precipitates and increase their volume fraction [12].

Precipitation strengthening can be calculated using the Ashby-Orowan relationship in Equation 1 [13].

$$\sigma_{ppt} = \frac{K}{d} f^{1/2} \ln \frac{d}{b} \quad (1)$$

where $K$ is a constant, $d$ is the diameter, $f$ is the volume fraction, and $b$ is the burgers vector.

Using the Ashby-Orowan model, Figure 2.1 was developed, which illustrates the strengthening effects of precipitates in steel and how that can be affected by the precipitate particle size and volume fraction. From the figure, experimental data shows that finer Ti precipitates at higher volume fractions can increase precipitate strengthening to a value between approximately 150 – 400 MPa, which is greater than the experimental values observed in V and Nb [14]. Hence, it is important to quantify macro Ti precipitates to study the effect that they can have on the steel as they can become stress concentrators that negatively impact the strength [15].

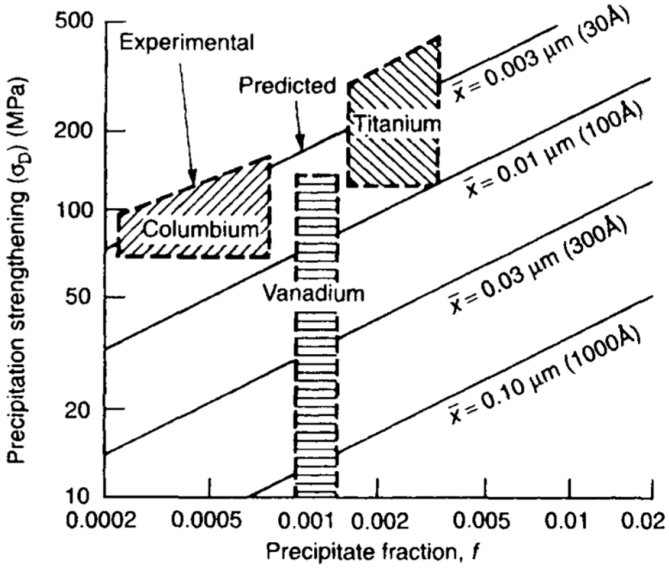


**Figure 2.1** The effect of precipitate volume fraction and size on the strengthening of the steel [14]

A study by Q. Yuan et. al. explored the effect of Ti content in microalloyed steels on the mechanical properties [16]. Three steels with different Ti compositions and similar Nb, C, and N contents were investigated. Their chemical compositions are presented in Table 2.1.

**Table 2.1** Chemical compositions of the steels used in the study by Q. Yuan et. al [16]

| No. | Ti | Nb | C | Si | Mn | Cr | N | S |
|---|---|---|---|---|---|---|---|---|
| 1 | 0.080 | 0.062 | 0.061 | 0.222 | 1.77 | 0.010 | <0.007 | <0.002 |
| 2 | 0.106 | 0.070 | 0.050 | 0.216 | 1.80 | 0.050 | <0.007 | <0.002 |
| 3 | 0.157 | 0.074 | 0.069 | 0.217 | 1.78 | 0.037 | <0.007 | <0.002 |

Tensile tests were conducted on all three steels and the data collected is presented in Table 2.2. The results obtained show an increase in yield strength (YS) and ultimate tensile strength (UTS) with increasing Ti content [16]. Steel 1, which had the least amount of Ti (0.080 wt%), yielded the lowest YS and UTS values of 533 MPa and 583 MPa, respectively [16]. On the other hand, steel 3, which had the highest amount of Ti (0.157 wt%), yielded the highest YS and UTS values of 658 MPa and 763 MPa, respectively [16].

**Table 2.2** Yield strength and tensile strength of the steels studied [16]

| No. | Yield Strength/MPa | Ultimate tensile strength /MPa |
|---|---|---|
| 1 | 533 | 583 |
| 2 | 558 | 653 |
| 3 | 658 | 763 |

## 2.2 Casting

The microalloyed steels being studied in this project were produced through continuous casting, which is utilized in modern day steel production. Continuous casting forms a continuous steel slab by pouring molten steel from a ladle at a controlled rate into a water cooled mold [17]. The molten metal then solidifies in the mold and is sent for further processing [17]. During solidification, the segregation of solutes and the precipitation of low solubility precipitates in the liquid, such as CaS and TiN, occur, which will all be discussed in further sections [18,19].

## 2.3 Segregation

Solutes are more soluble in liquid than in the solid phase [20]. Therefore, as steel solidifies, the temperature gradient from the steel surface to the center causes the formation of dendrites and

segregation of the solutes [18]. Segregation can occur as microsegregation, which happens on an interdentritic scale, or as macrosegregation, which happens at a larger scale from the movement of the interdendritic liquid towards the center of the slab during solidification [20].

Dendrites form in the steel during solidification. As secondary dendrite arms begin to form, solutes get rejected into the liquid regions between dendrites [21]. The concentration of solutes in the interdendritic regions begins to increase, and microsegregation occurs [21]. Hot working can be done on cast steels to reduce microsegregation significantly [22].

Macrosegregation changes the through-thickness composition of the steel and therefore changes the microstructure and properties throughout the thickness of the steel [18]. There are two reasons macrosegregation can occur: 1) density difference between the segregated interdendritic liquid and the nonsegregated liquid, and 2) other forces that can cause the interdendritic liquid to move [20].

Macrosegregation can be minimized using multiple techniques, with the most widely used one in the casting of steel being mechanical soft reduction. In mechanical soft reduction, the remaining liquid at the end of solidification is redistributed via mechanical forces applied by rolls [23].

## 2.4 Thermo-Mechanical Controlled Processing (TMCP)

Thermo-Mechanical Controlled Processing (TMCP) is utilized in the production of microalloyed steels following casting. It consists of homogenization (reheating), rough and finish rolling, laminar/accelerated cooling, and ends with coiling as shown in Figure 2.2. During TMCP, the alloying elements (Nb, Ti, and V) form precipitates with the carbon and nitrogen in the steel.

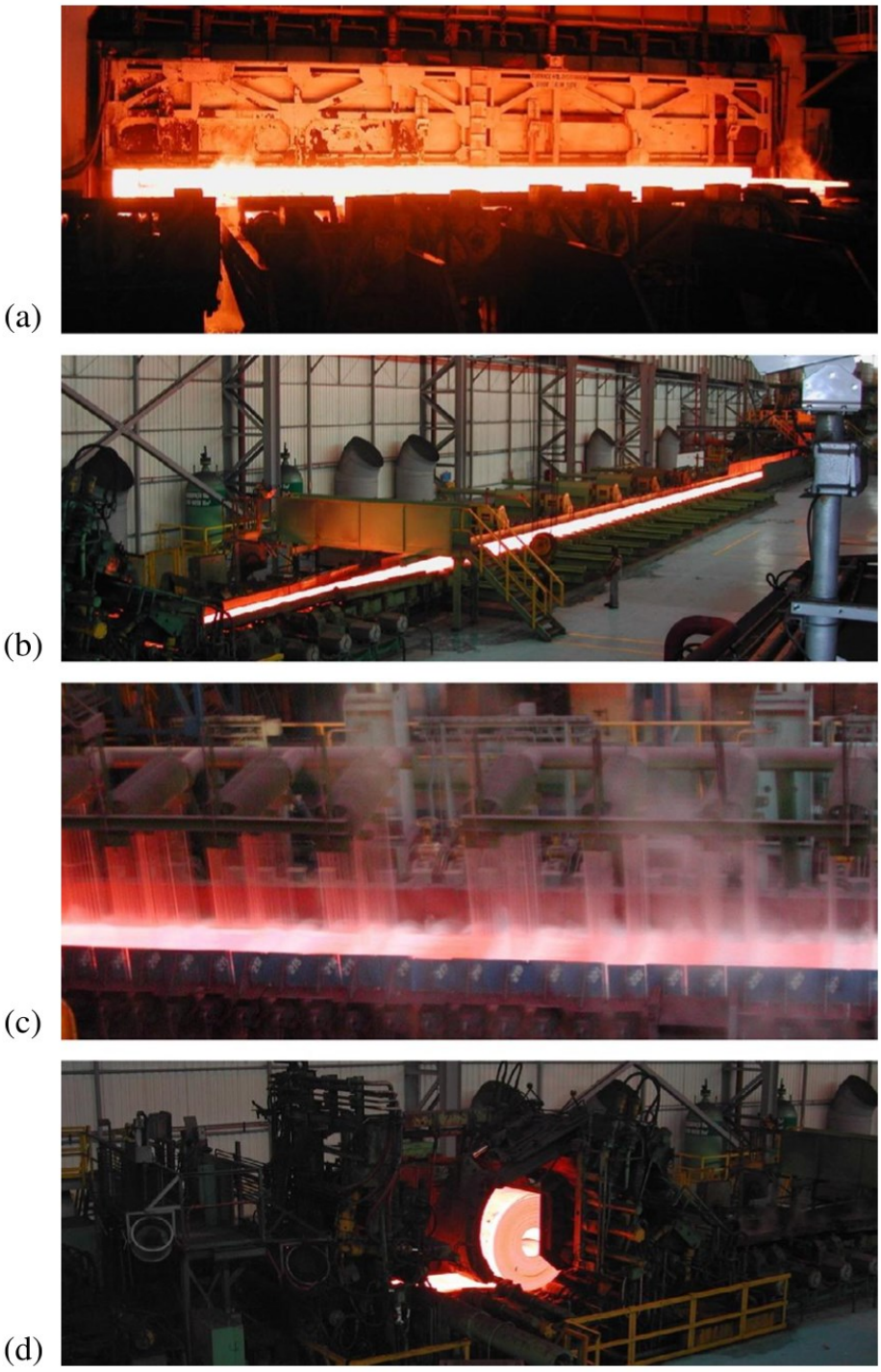


**Figure 2.2** TMCP steps (a) homogenization, (b) rolling, (c) cooling, (d) coiling [1]

Figure 2.3 shows the grain sizes forming during TMCP. During rough rolling, austenite recrystallization occurs. In finish rolling, the austenite grains get pancaked, and lastly, accelerated cooling determines the final microstructure [24].

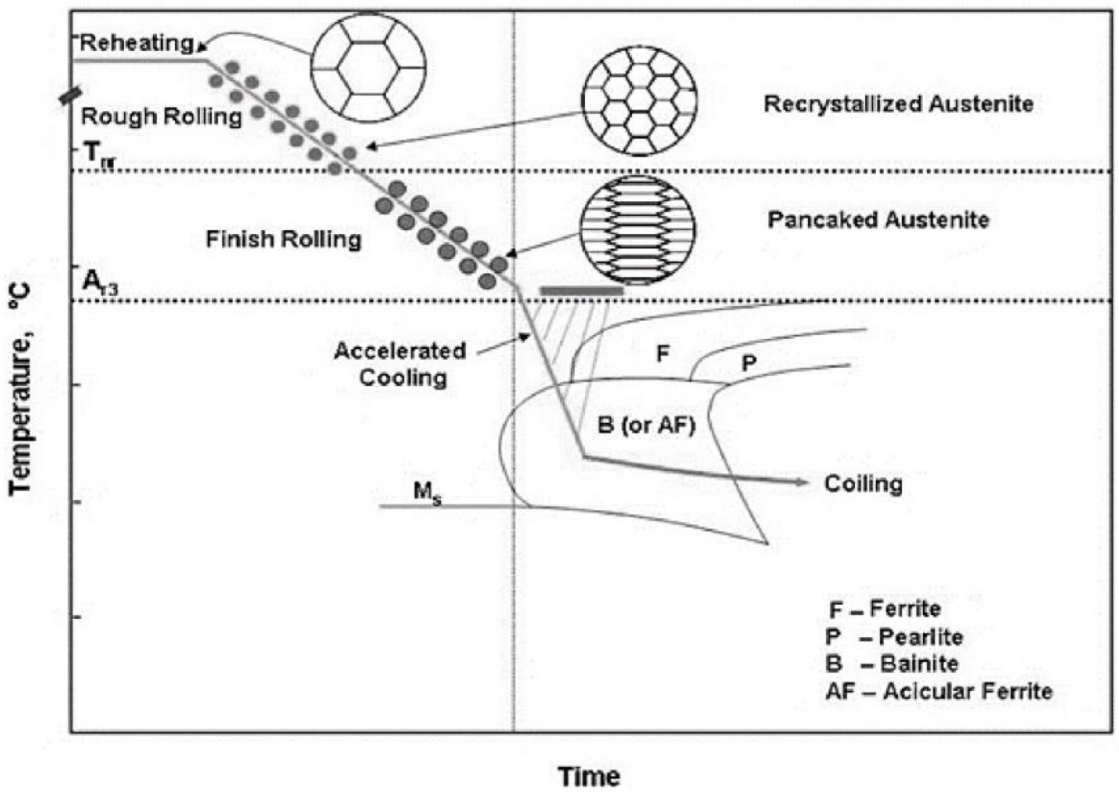


**Figure 2.3** Schematic diagram of TMCP steps [24]

2.4.1 Reheating/Homogenization

Reheating is the first stage in TMCP, which follows casting and helps reduce the microsegregation that occurs during solidification. Homogenization redistributes microsegregated alloying elements to achieve a more homogeneous profile in interdendritic regions throughout the sample thickness. It also controls the amount of microalloying elements dissolving back into solution and the starting grain size. Regarding Ti precipitates during homogenization, TiC requires reheat temperatures in the range of 1150 – 1300 ºC for complete dissolution [14]. On the other hand, TiN hardly dissolves back into the solution at normal reheat temperatures (~1300 ºC) [14]. Undissolved precipitates, such as TiN, help maintain a fine austenite grain size during reheating [14]. Precipitates that go back into solution during homogenization, such as TiC, are used in later stages for recrystallization control and precipitation strengthening [14]. Reheating affects the prior austenite grain size, which contributes to mechanical properties, such as toughness, yield and tensile strength, and fatigue, through the thickness of the steel [25]. Therefore, it is important to select a proper reheat temperature that is: high enough to dissolve a large amount of the alloying elements but low enough to prevent unwanted austenite grain growth [18]. For reheat temperatures used in practice

(~1250 ºC), small amounts of Ti(C,N) and Nb(C,N) remain undissolved [26]. Experimental results from this study show agreement with this, as larger macro Ti and Nb precipitates were characterized in the steels.

### 2.4.2 Rough and finish rolling

Rough rolling takes place at temperatures below reheating to reduce the rate of recrystallization. This happens with the help of solutes such as Ti and Nb, which slow down the recrystallization and growth of austenite grains through solute drag and strain-induced precipitation of fine carbonitrides [14]. Solutes continue to slow down recrystallization until it stops at the recrystallization stop temperature [14]. The effects of different solute contents on the recrystallization stop temperature is plotted in Figure 2.4, which indicates that Nb and Ti have the highest recrystallization stop temperatures of approximately 1025 ºC and 925 ºC, respectively. This makes Ti, preceded by Nb, the second most effective solute for slowing down recrystallization.

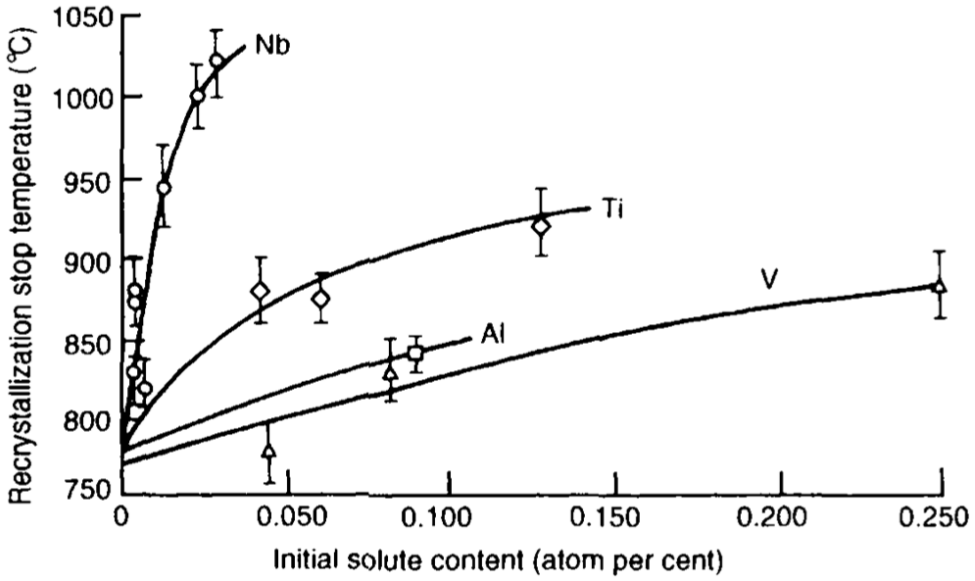


**Figure 2.4** Effect of solute content on the recrystallization stop temperature [14]

The effect of the solutes on the impediment of recrystallization depends on their solubility in the austenite. Solutes that are the least soluble in austenite, such as Nb and Ti in this case, have the greatest effect on recrystallization. That is because they have a greater driving force to precipitate at a given temperature and therefore increase the recrystallization stop temperature [14]. Rough

rolling occurs at temperatures above the recrystallization stop temperature to refine austenite grain size through complete recrystallization between passes [18].

Finish rolling takes place at lower temperatures (below 950 ºC) after some delay following rough rolling [14]. At such lower temperatures, precipitates that were dissolved, such as TiC and other carbonitrides, can now precipitate rapidly [14]. Subgrains in deformed austenite grains provide nucleation sites for the carbonitride precipitates to nucleate and grow [14]. The precipitates end up pinning the subgrains, therefore preventing further recrystallization [14]. The result is elongated austenite grains that are said to be "conditioned". The subgrains form intragranular nucleation sites for the formation of fine ferrite grains within the austenite grains as well as along the grain boundaries.

### 2.4.3 Laminar/accelerated cooling

The austenite to ferrite transformation occurs during laminar cooling [18]. A combination of finish rolling and accelerated cooling parameters are used to determine the final microstructure of the steel [14]. Alloying elements, such as Ti, play a role in determining that final microstructure as they are able to reduce the austenite to ferrite transformation temperature [14]. By doing so, alloying elements help produce a finer ferrite grain size during laminar cooling. A faster cooling rate can also retain solutes for further precipitation strengthening in the ferrite [6].

## 2.5 Fundamentals of Ti Precipitation

In order for Ti to precipitate, it needs to be thermodynamically stable and kinetically favourable. The thermodynamics and kinetics of Ti precipitation will be discussed in this section.

### 2.5.1 Thermodynamics of Ti precipitation

The precipitation of nitrides and carbides play a major role in grain refinement and precipitation strengthening of microalloyed steels. TiN is one of the highest contributing precipitates towards precipitate strengthening. TiN forms when Ti in the interdendritic liquid binds to N and precipitates on austenite grain boundaries [18]. Unlike other carbides and nitrides TiN does not dissolve completely during reheating, which can be attributed to its low solubility in austenite [26]. This is illustrated in Figure 2.5, which compares the solubility of different carbides and nitrides in austenite. The composition of the corresponding steels were not given, however, the thermodynamic trend is similar to that of the steels studied in this project. When comparing the

Nb, Ti, and V carbides, nitrides and carbonitrides, TiN has the lowest solubility. It is then followed by NbN. Their low solubilities, especially TiN, makes them a key factor in the refinement of austenite grains. Thus, this research quantifies and characterizes the TiN and (Ti,Nb)N in the steels being studied.

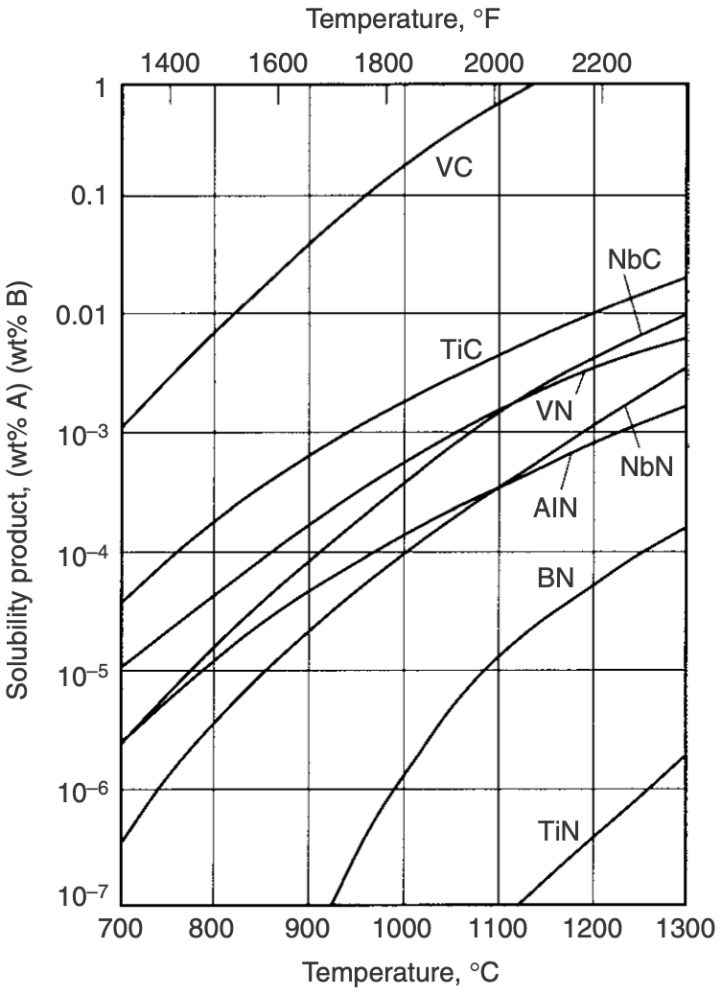


**Figure 2.5** Equilibrium solubility products of carbides and nitrides in austenite [27]

Ti precipitates that dissolve back into solution during reheating, such as TiC, slow down the recrystallization of austenite through solute drag and strain induced precipitation during rough rolling [14]. Ti precipitates on subgrains in the austenite grains, which pins the subgrains and stops the recrystallization of austenite at higher temperatures [14]. This occurs during finish rolling, where dissolved carbonitrides precipitate rapidly and impede the growth of austenite grains. Some other carbonitrides also precipitate during laminar cooling and help determine the final ferritic microstructure [14].

Because of Ti's affinity for nitrogen, most of the nitrogen found in the liquid precipitates with the Ti present during solidification [26]. This is illustrated in Figure 2.6, which shows the percent of N precipitating into TiN during solidification and the volume fraction of TiN. From the plots, approximately 60% of the nitrogen present in the interdendritic liquid precipitates into TiN, and the volume fraction of TiN gradually increases with the completion of solidification.

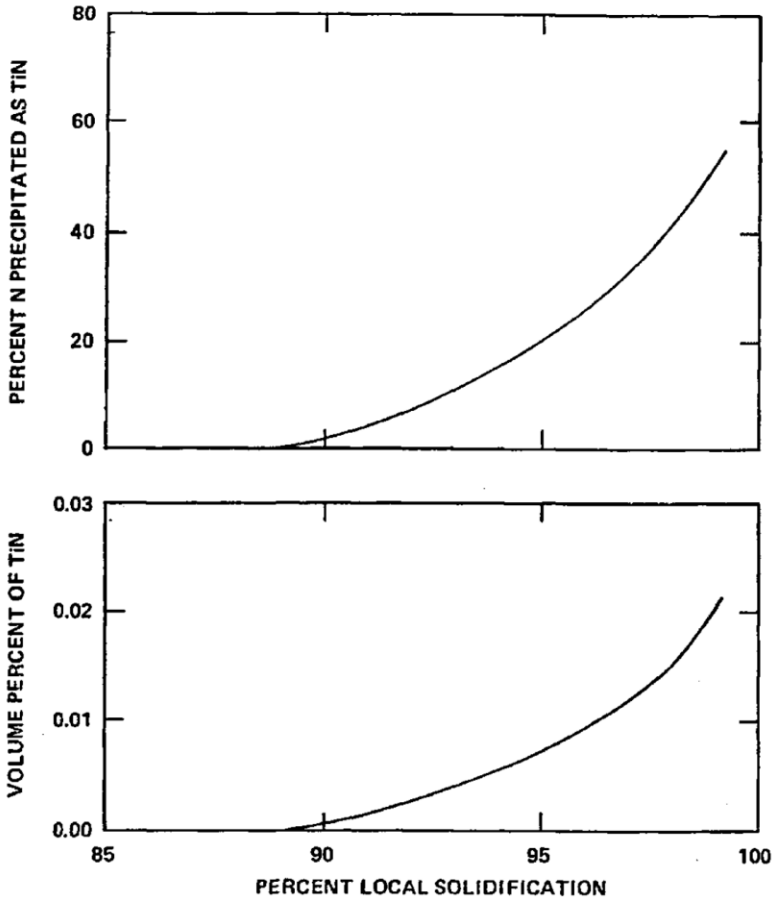


**Figure 2.6** Precipitation of N with Ti and the volume fraction of TiN formed during the solidification of a steel containing 0.02 wt% Ti and 60 ppm N [26]

TiN forms on austenite grain boundaries and serves as a precipitation site for NbC [26]. NbC is soluble in TiN, which allows it to precipitate epitaxially at higher temperatures [26]. At elevated temperatures, the NbC precipitates will grow coarser at the austenite grain boundary. The coarser precipitates will pin the austenite grain boundaries and limit the growth of the austenite grains, which therefore results in a finer grained steel [26]. Finer grains will enhance the properties of the steel by increasing its strength and hardness.

2.5.2 Precipitation kinetics

The nucleation of precipitates, such as TiN, is governed by Equation 2 [28]:

$$\Delta G = -V(\Delta G_v - \Delta G_s) + A\gamma + \Delta G_d \quad (2)$$

Where $\Delta G$ is the total free energy change for heterogeneous nucleation, $V$ is the precipitate volume, $\Delta G_v$ is the volume free energy, $\Delta G_s$ is the volume misfit strain energy, $A$ is the precipitate surface area, $\gamma$ is the surface energy, and $\Delta G_d$ is the defect free energy [28].

Nucleation rate can be predicted using Equation 3 [29]:

$$\frac{dN}{dt}\Big|_{nucleation} = N_o \cdot Z \cdot \beta \cdot e^{\left(-\frac{\Delta G_a}{kT}\right)} \quad (3)$$

Where $N_o$ is the number of nucleation sites, Z is the Zeldovich factor (≈1/20), β is the atomic impingement rate, and $\Delta G_a$ is the activation energy for precipitation [29].

Precipitate growth begins by the diffusion of atoms from the matrix into the nucleated site. Growth rate can be defined by Equation 4 [30]:

$$\frac{dR}{dt}\Big|_{growth} = \frac{D_{Ti}(T)}{R}\frac{X_{Ti} - X_{Ti}^{i}(T)}{X_p\frac{V_{Fe}}{V_{TiN}} - X_{Ti}^{i}(T)} \quad (4)$$

Where $D$ is the diffusion coefficient, $X$ is the atomic concentration of the solute in the matrix, $X^i$ is the concentration of the solute at the interface, and $X_p$ is the concentration in the precipitates [30].

Higher solute concentrations (such as Ti) in the matrix will cause precipitation to begin. At first, precipitates will have a size larger than the critical radius, and the solute concentration in the matrix will decrease due to precipitation growth [30]. This change in the matrix concentration then changes the critical radius until nucleation can no longer occur [30]. This causes smaller precipitates to go back into solution in order for larger precipitates to grow [30]. This is the last stage to precipitation and is known as coarsening. Once coarsening stops, precipitation is done.

The Lifshitz, Slyozov, and Wagner model (LSW model) is used to describe precipitate coarsening in Equation 5 [31]:

$$\bar{r}^3 - \bar{r}_o^3 = \frac{8 \cdot D \cdot \Omega_{MV} \cdot \sigma \cdot S \cdot t}{9 \cdot R_{gas} \cdot T} \quad (5)$$

Where $\bar{r}$ is the mean precipitate radius at time (t), $\bar{r_o}$ is the initial mean precipitate radius,σ is the surface energy, S is the soluble atom fraction, and $\Omega_{MV}$ is the molar volume [31].

## 2.6 Characterization Techniques

This study uses Electron Microprobe Analysis (EMPA) and Scanning Electron Microscopy/Energy Dispersive X-ray spectroscopy (SEM/EDX) to characterize Ti precipitates in the steel samples. EMPA and SEM are both electron beam instruments that generate x-ray maps in bulk specimens [32]. The x-rays produced are then measured with EDX and wavelength dispersive spectroscopy (WDS). By using EMPA and SEM on larger samples, more x-rays are able to be generated due to relatively large interaction volumes [32]. However, this results in a lower spatial resolution [32]. Figure 2.7 shows the interaction volume in a bulk sample within electron beam instruments such as EMPA and SEM. $L_S$, $L_B$, and $L_X$ are the depths of the secondary electrons (SE), backscattered electrons (BSE), and x-rays, respectively. $X_S$, $X_B$, and $X_X$ are the lateral probe sizes of the secondary electrons, backscattered electrons, and x-rays, respectively.

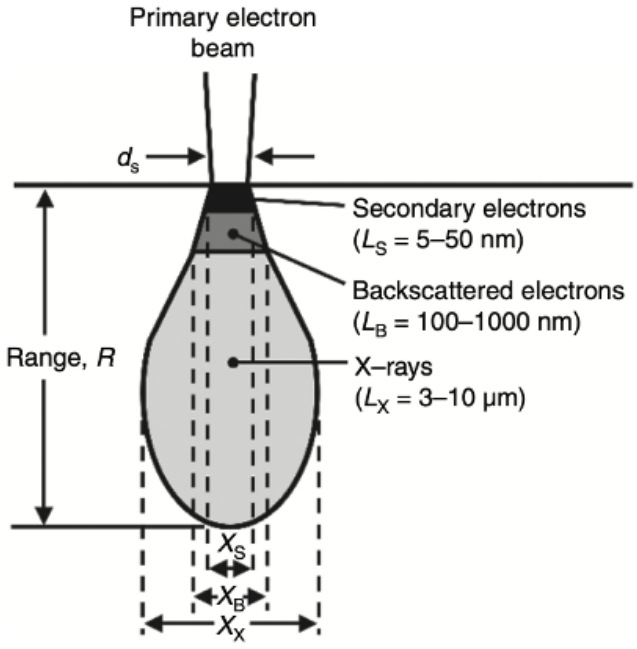


**Figure 2.7** X-ray interaction volume in a bulk sample [33]

2.6.1 EMPA and greyscale scaling

EMPA can provide images that show where a constituent is localized in a sample without undergoing a detailed quantitative analysis using WDS [34]. This is done via compositional mapping, where the greyscale at a pixel can be related to the elemental concentration [34]. EMPA samples need to be polished to a very fine degree of surface finish and should not be etched [35]. Specimen geometry can affect the quality of results obtained; therefore, samples need to be flat and free of any topography or geometric defects [35]. The advantages of using EMPA is its high photon count rate, its ability to map multiple constituents at the same time, and its resolution [34].

A schematic of the EMPA apparatus is shown in Figure 2.8. An electron beam is generated from an electron source and passes through the EMPA column onto the sample. Characteristic x-rays are then released and detected by WDS. Parameters such as dwell time, voltage, and current can be controlled for the EMPA.

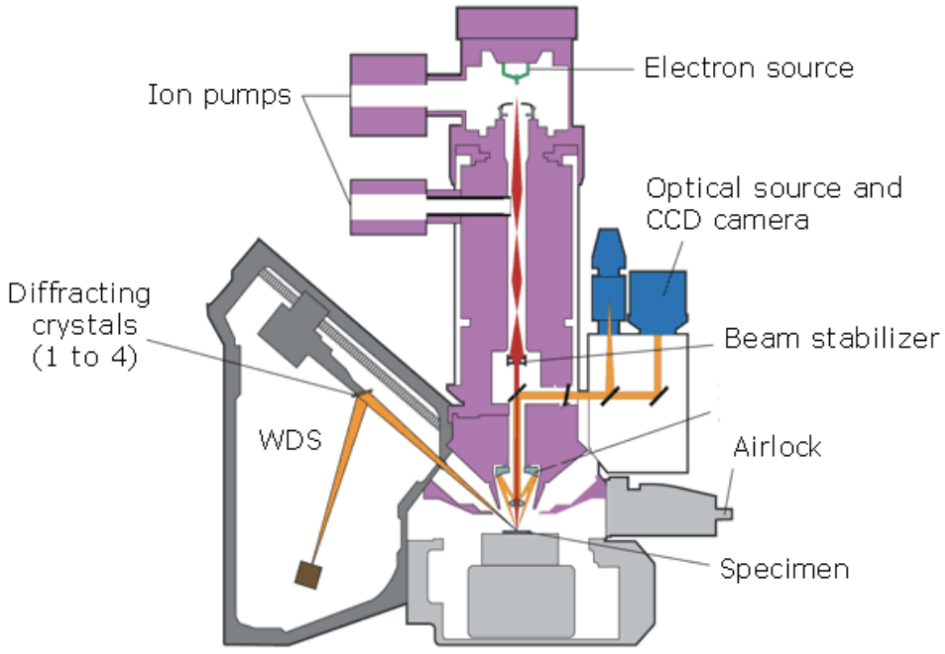


**Figure 2.8** Schematic of EMPA apparatus [36]

Greyscale mapping is the most commonly used form of x-ray mapping [34]. The intensity at every pixel is displayed as an equivalent greyscale number [34]. However, the relationship between pixel intensity and greyscale values is not a direct relationship as image scaling is automatically done

by the software system that produces the greyscale images [34]. Greyscale intensities range between 0 – 255, with 0 representing black pixels and 255 representing white pixels. Brighter pixels are representative of areas with higher elemental concentrations. When the pixel count exceeds 255, autoscaling is done where a scaling factor of "255/maximum count" is multiplied to all pixels so that the scaled data does not exceed a value of 255 [34].

In some cases, using the aforementioned scaling technique results in images with poor contrast. Thus, another scaling technique is done, where all greyscale values are subtracted by the lowest greyscale pixel value then multiplied by a factor of "255/highest greyscale value" [34]. This scaling technique is automatically performed by the software and is not subject to selection by the user [34].

Another scaling technique is "clipped scaling", which selects a small amount of greyscale pixels at both ends and assigns values of 0 and 255 to them, while assigning the rest of the pixels values between 0 – 255 [34].

Lastly, a method called "histogram equalization" can be used for scaling the images. This is a non-linear scaling technique that redistributes greyscale levels so that each greyscale value is assigned to an equal amount of pixels [34].

Although autoscaling improves the image for qualitative analysis, its drawback is that it is applied by the software without obtaining a record of the scaling that was done [34]. This makes it impossible to compare maps from different elements on the same sample, as each map could have undergone a different type of scaling. Therefore, greyscale intensities of one elemental map cannot be assumed to be equivalent to the greyscale intensities of another elemental map.

### 2.6.2 SEM/EDX

SEM and EMPA are similar instruments that differ mainly in the way they are used [37]. SEM allows for the characterization of heterogeneous materials and their topographies by utilizing a focused electron beam on the area of interest [37]. Some signals that can be produced include secondary electrons, backscattered electrons, and characteristic x-rays [37]. Some important SEM features include its high resolution and three-dimensional specimen view [37]. The electron scattering range in an SEM is approximately 1-5 μm in diameter [37]. Electron range, which can be used to estimate the interaction volume, can be calculated with Equation 6 [34].

$$R(\mu m) = \frac{0.0276A}{Z^{0.89}\rho} E_o^{1.67} \quad (6)$$

Where $A$ is the atomic weight (g/mol), $Z$ is the atomic number, $\rho$ is the density (g/cm$^3$), and $E_o$ is the electron beam energy (keV). For the steel samples being studied , the calculated electron range is 1.4 μm. It was calculated using the atomic weight, atomic number, and density of iron. As for $E_o$, a value of 20 kV was used since that was the voltage at which the SEM and EMPA were operated.

Compositional data can be obtained from SEM when used alongside an EDX, which captures the x-rays emitted from the sample when bombarded with electrons [38,39]. EDX is able to separate x-rays with different wavelengths to determine the elements present in the sample [39]. EDX was used in this study to distinguish between the compositions of different precipitates captured on SEM.

## 2.7 CaS Inclusions and TiN Precipitating on CaS

Sulfur in steel exists as MnS or as a sulfide-oxide complex with oxide inclusions in the core [40]. However, in calcium treated steels, the formation of CaS occurs [40]. Sulfur usually encapsulates brittle oxides like alumina [40].

Calcium is added to steels for calcium treatment, which is used to modify alumina to liquid calcium aluminate inclusions [41]. This can improve the mechanical properties of the steel and the manufacturing process [41]. Excess Ca in the steel produces solid CaS inclusions [41]. Alumina in the steel reacts with dissolved Ca to form an alumina-calcium oxide binary system [40]. Thus, a CaS ends up forming around the alumina as per the following chemical reaction: 3 CaO + 2 [Al] + 3 [S] = 3 CaS + $Al_2O_3$. Nonmetallic inclusions like CaS form in the liquid with the alumina, which acts as a deoxidizer in steel [19].

CaS inclusions typically exhibit an irregular/spherical morphology [41]. TiN precipitates on inclusions like CaS during solidification and forms a cuboidal precipitate surrounding the inclusion as shown in Figure 2.9. However, there is no direct relationship between sulfur content and TiN precipitation [40].

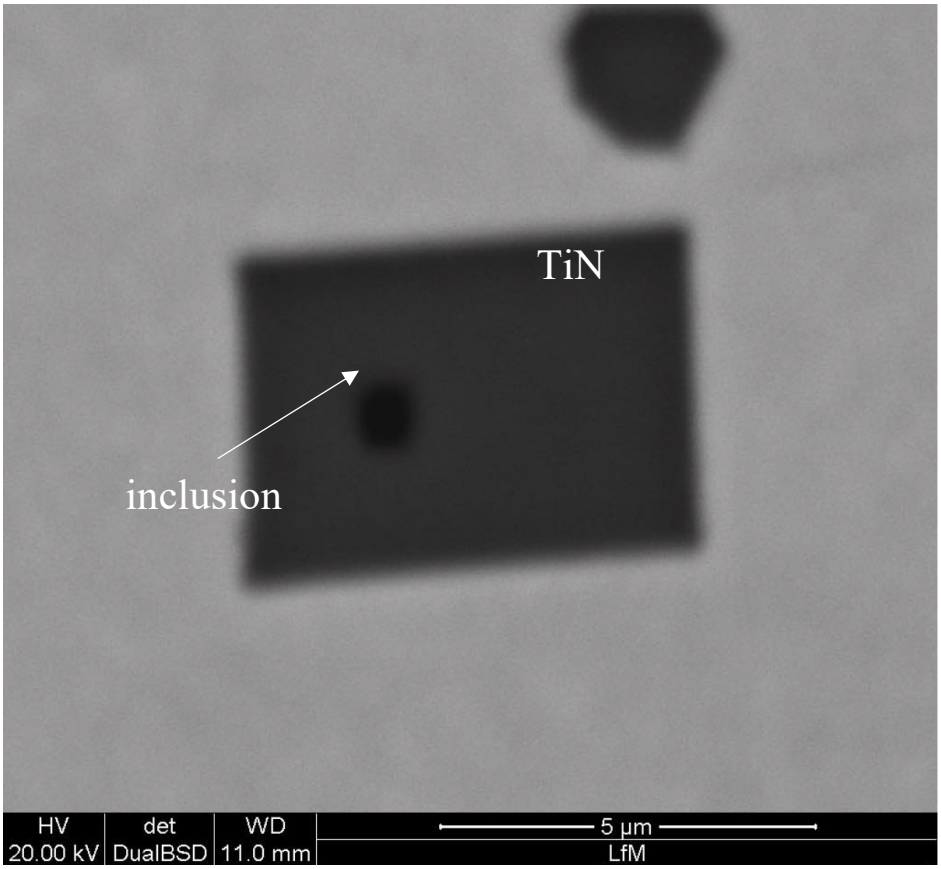


**Figure 2.9** SEM SE image of TiN precipitating on an inclusion [42]

Figure 2.10 shows another TiN precipitating on an inclusion (CaS) with an EDX spectrum from the center of the precipitate.

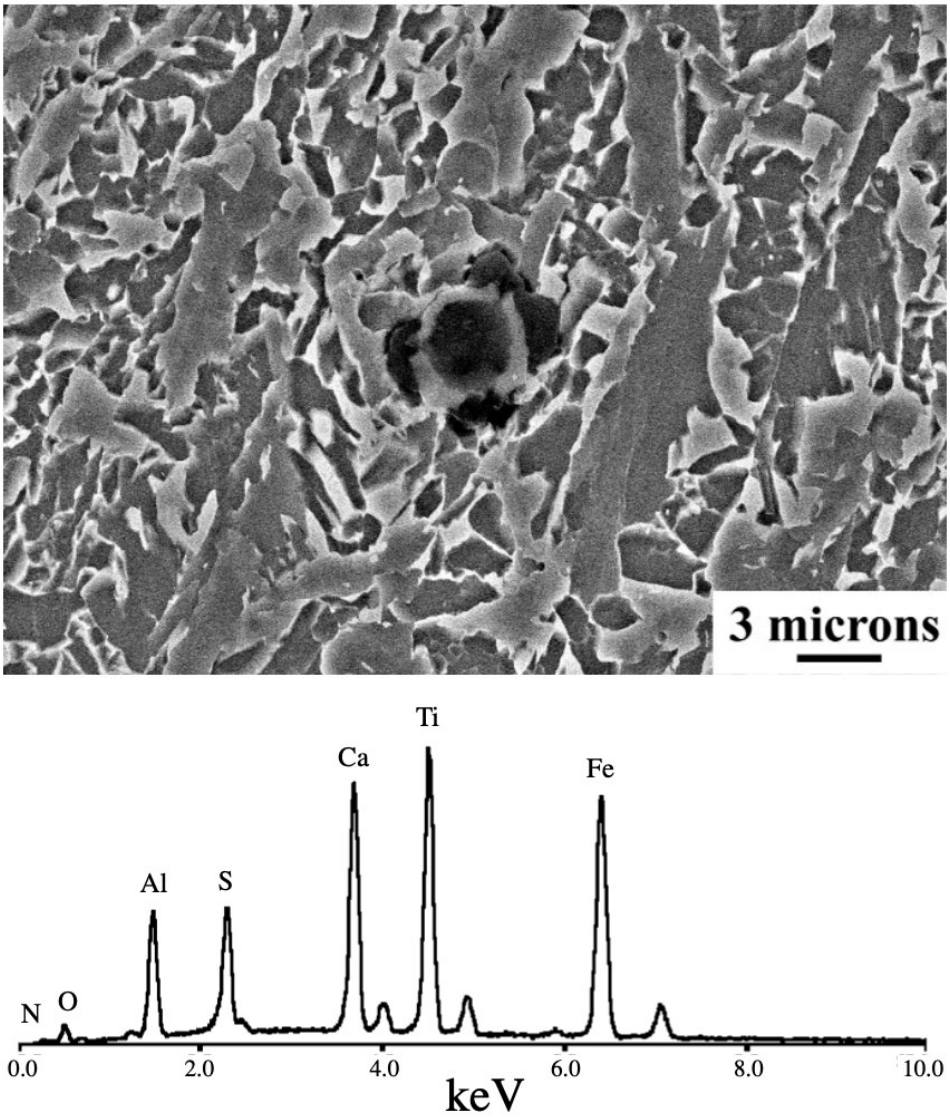


**Figure 2.10** TiN precipitating on a CaS inclusion with EDX spectrum of precipitate [11]

## 2.8 TiN and Ti,Nb Precipitates

TiN is one of the first nitrides that form in steels during solidification and tend to exhibit a cuboidal or pyramidal morphology [43]. Figures 2.11 and 2.12 present SEM images of cuboidal and pyramidal TiN with EDX mapping, respectively. As Ti content increases (>0.053 wt%), it begins forming earlier on during solidification and can be larger in size than TiN in steels with lower Ti

contents [43]. TiN possesses a cuboidal morphology most of the time as it minimizes the interface energy and lattice misfit with the austenite in the matrix [43].

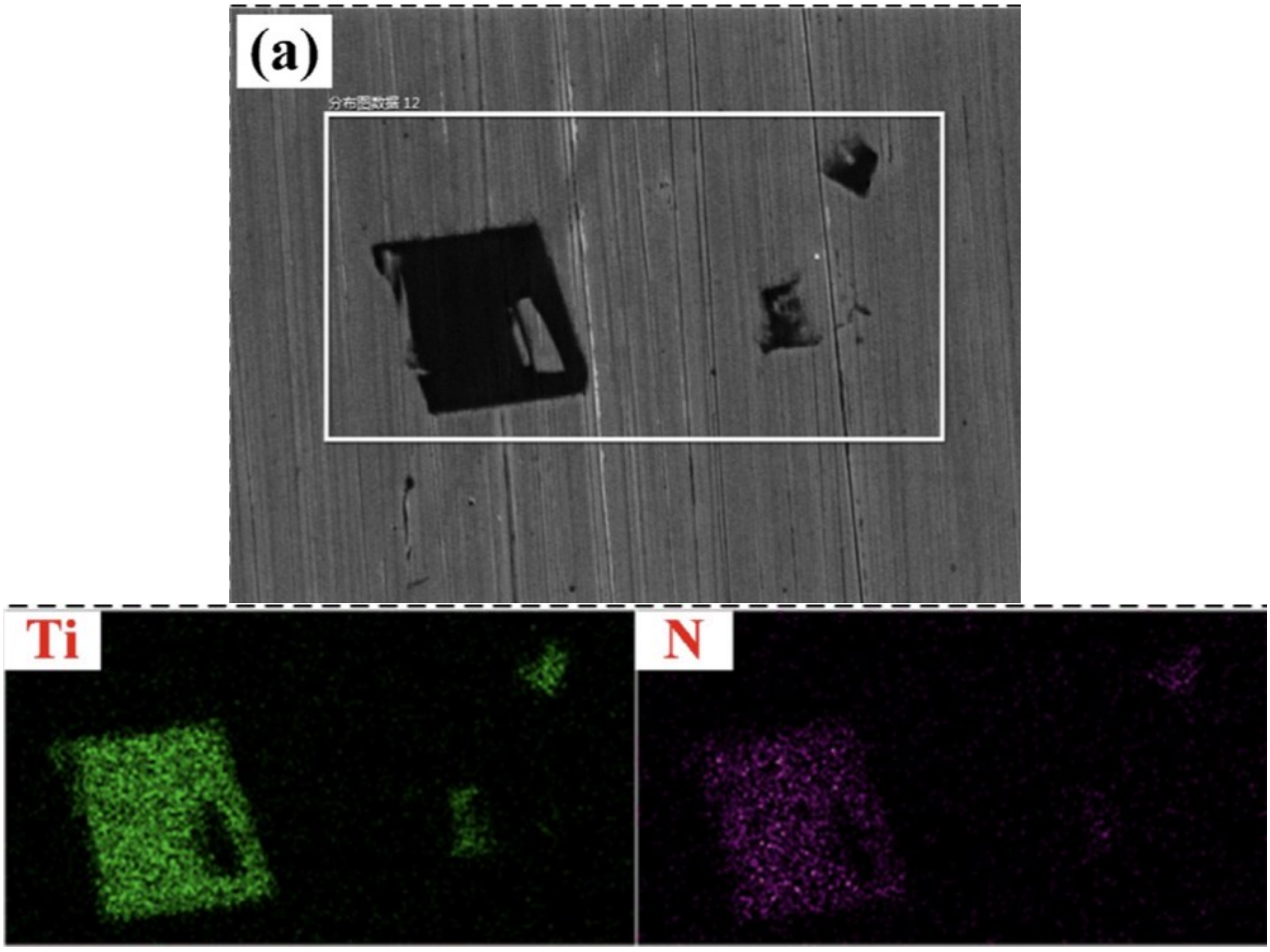


**Figure 2.11** SE SEM image of cuboidal TiN and EDX maps showing Ti and N [43]

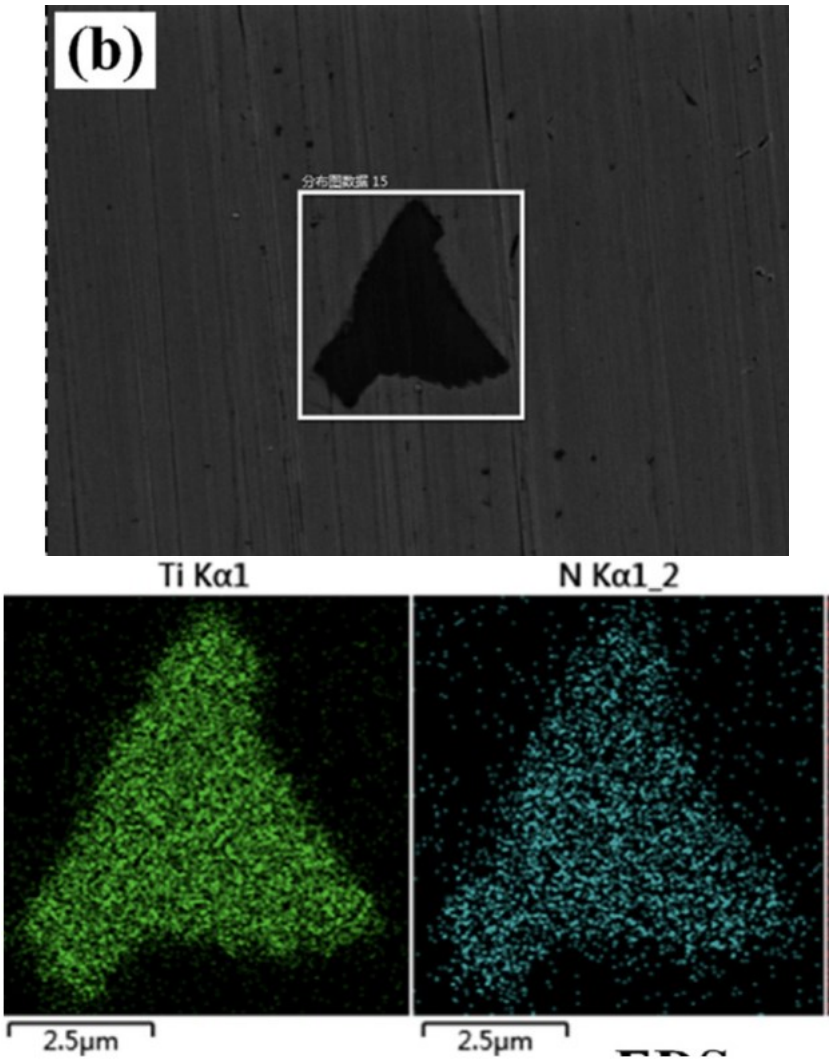


**Figure 2.12** SE SEM image of pyramidal TiN and EDX maps showing Ti and N [43]

TiN exhibits an NaCl-type face-centered cubic structure [44-46]. $\delta$-NbN precipitates with a NaCl-type crystal structure as well [47]. This causes the TiN and NbN to grow epitaxially with each other and form (Ti,Nb)N [48]. Primary nitrides like TiN act as nucleation sites for subsequent precipitation of NbN [49]. Depending on steel composition and precipitation temperatures, sometimes (Ti,Nb)N are the primary precipitates that form in the austenite [49]. For steels with high Nb contents, a fraction of the Nb remains undissolved at higher reheat temperatures [48]. Figure 2.13 shows a Fe-Nb phase diagram obtained through Thermocalc for a high Nb steel in a study by S. A. Yamini. The composition of the steel is given in Table 2.3. From the phase diagram, TiN begins precipitating at around 1450°C while Ti,Nb precipitates begin forming around 1100°C [50].

**Table 2.3** Chemical composition (wt%) of high Nb steel in study by S. A. Yamini [50]

| C | Mo | Ti | Nb | V | N | Mn | Si |
|---|---|---|---|---|---|---|---|
| 0.05 | 0.002 | 0.012 | 0.11 | 0.003 | 0.0048 | 1.5 | 0.16 |

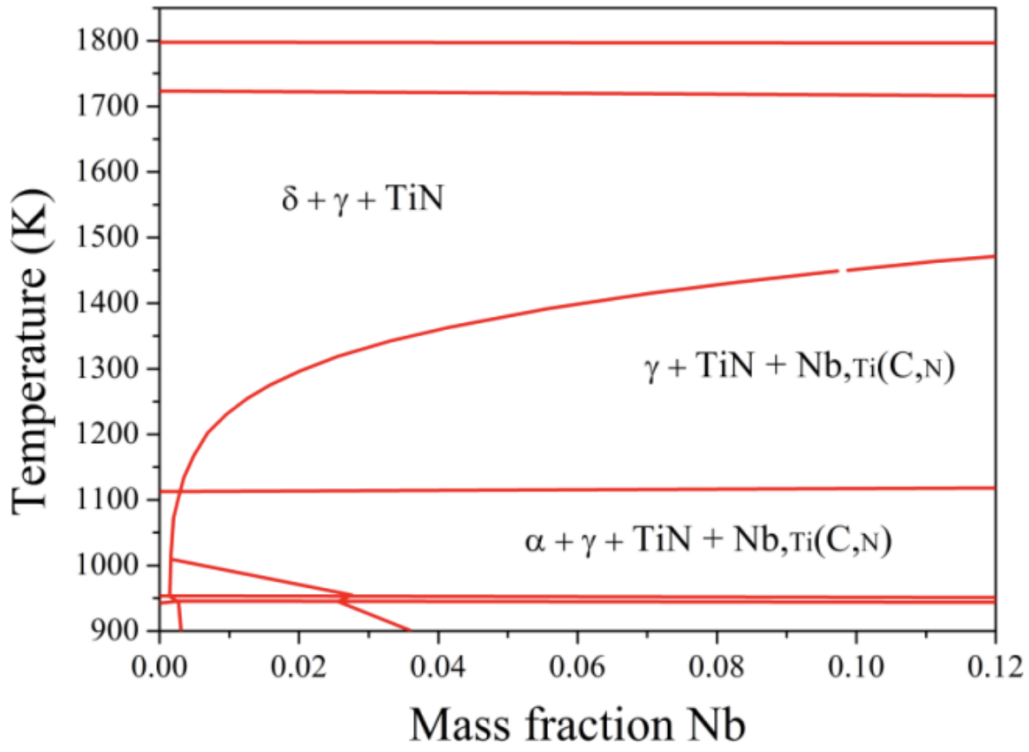


**Figure 2.13** Fe-Nb phase diagram calculated with Thermocalc for a high Nb steel [50]

The precipitates first form as TiN-rich precipitates at higher temperatures, and as the temperature is lowered, the Nb begins to come out and precipitates with the TiN to form (Ti,Nb)N [50]. $\delta$-NbN is stable at higher temperatures and can begin forming at around 1270°C [48]. Even at temperatures greater than 1200°C, traces of Nb can be found on TiN [48]. Other Nb carbonitrides can form on TiN, which acts as a preferential nucleation site [51,52].

Nb precipitating on TiN can affect its size and morphology. Precipitates in Ti,Nb rich steels are more likely to be smaller as their formation continues at lower temperatures under larger supersaturations [49]. Ti-rich precipitates containing Nb can be more irregularly shaped, as opposed to TiN, which is cuboidal [53].

## 2.9 Summary and objectives

As the steel solidifies during casting, the formation of TiN occurs since it is the most thermodynamically stable microalloying precipitate at higher temperatures. Nonmetallic inclusions, such as CaS, also precipitate during solidification and become favorable nucleation sites for TiN. TiN typically exhibits a cuboidal shape. CaS exhibits a spherical morphology and a cuboidal TiN precipitates around it.

For steels with high Nb contents, (Ti,Nb)N can precipitate near the end of solidification. When precipitating with Nb, the Ti precipitate is smaller and irregularly shaped. The formation of (Ti,Nb)N occurs at lower temperatures, which could be the reason behind its smaller size, as it forms at the final stages of solidification and has less growth time than TiN.

During TMCP, microalloying elements, such as Ti and Nb, precipitate out and aid with grain refinement and precipitation strengthening. This enhances steel properties. This includes precipitates such as TiN, NbN, (Ti,Nb)N, NbC, and many more.

To characterize and study the properties of TiN-rich precipitates, characterization techniques such as EMPA and SEM/EDX can be utilized. This work studies and characterizes coarse TiN-rich precipitates, like TiN-CaS and (Ti,Nb)N. The compositions of the steels being studied exhibit higher Ti and Nb concentrations than those observed in literature. Hence, a study investigating the effect of Ti and Nb contents on Ti precipitation was done. Not enough literature was found exploring the effects of CaS and Nb on the size of TiN-rich precipitates, therefore this thesis will fill this gap in research.

# Chapter 3: Materials and Methodology

This project studies seven steel samples ranging from grade 70 to grade 100. In Section 3.1, grades, thicknesses, and chemical compositions of the steels are presented and discussed. Section 3.2 presents the characterization techniques used in the project, which are EMPA, SEM, and EDX. Section 3.3 explains the program used to analyze EMPA data. Sections 3.4 and 3.5 cover the lognormal distributions used to determine greyscale boundaries for Ti and Nb, which are used in the program discussed in Section 3.3.

## 3.1 Steel Samples – Grades, Thicknesses, Chemical Compositions, and Processing Parameters

Seven microalloyed steel samples provided by Stelco Ltd. were studied in this project. In this section, the grade, thickness, chemical composition, and TMCP parameters of each of the seven samples are introduced.

### 3.1.1 Grades and thicknesses

The grades (Y.S – MPa) and thicknesses (mm) of the steels are presented in Table 3.1. All samples are approximately 3-4 mm thick, except for 4372 which is 9.7 mm thick.

**Table 3.1** Grade and thickness of studied steels produced at Stelco Ltd.

| Sample ID | 4280 | 4372 | 4175 | 4052 | 4081 | 4068 | 4093 |
|---|---|---|---|---|---|---|---|
| Grade (MPa) | 100 | 100 | 100 | 90 | 80 | 80 | 70 |
| Thickness (mm) | 3.2 | 9.7 | 3.1 | 4.8 | 4.0 | 4.0 | 4.0 |

### 3.1.2 Chemical compositions

The chemical compositions (wt%) of each steel is presented in Table 3.2. All samples exhibit conventional compositions for microalloyed steels and contain the microalloying elements Ti, Nb, and V. However, the Ti and Nb compositions vary across the samples, where Ti ranges between 0.047 wt% and 0.122 wt%, and Nb ranges between 0.015 wt% and 0.088 wt%. Samples 4280 and 4372 are highest in Ti and Nb, and sample 4093 is lowest in Ti and Nb.

**Table 3.2** Composition of studied steels produced at Stelco Ltd.

| Sample | C | Mn | Cr+Ni+Mo | Al+Cu+Si | Ti | Nb | N | V | Ca | S | P |
|---|---|---|---|---|---|---|---|---|---|---|---|
| 4280 | 0.07 | 1.88 | 0.16 | 0.35 | 0.109 | 0.086 | 0.005 | 0.009 | 0.0027 | 0.002 | 0.013 |
| 4372 | 0.08 | 1.95 | 0.15 | 0.36 | 0.122 | 0.088 | 0.003 | 0.011 | 0.0033 | 0.001 | 0.01 |
| 4175 | 0.04 | 1.55 | 0.16 | 0.36 | 0.118 | 0.025 | 0.006 | 0.009 | 0.0038 | 0.003 | 0.015 |
| 4052 | 0.04 | 1.39 | 0.06 | 0.24 | 0.096 | 0.021 | 0.005 | 0.008 | 0.0038 | 0.005 | 0.012 |
| 4081 | 0.05 | 1.04 | 0.07 | 0.25 | 0.077 | 0.021 | 0.004 | 0.005 | 0.003 | 0.004 | 0.012 |
| 4068 | 0.05 | 0.97 | 0.06 | 0.29 | 0.063 | 0.021 | 0.004 | 0.005 | 0.0034 | 0.003 | 0.008 |
| 4093 | 0.05 | 1.05 | 0.05 | 0.15 | 0.047 | 0.015 | 0.004 | 0.005 | 0.0033 | 0.003 | 0.009 |

### 3.1.3 Processing parameters

All samples were processed using TMCP at similar parameters. The steels were all homogenized at temperatures around 1200 – 1300℃ then cooled to around 1100℃, at which rough rolling and finish rolling took place. After rolling, each steel skelp was reduced to its corresponding final thickness. The finish temperatures of the steels were around 900 ℃, where they then proceeded to undergo laminar cooling.

## 3.2 Characterization Techniques

In this section, the EMPA and SEM procedures will be discussed. EMPA was undertaken to quantify localized compositions of Ti, Nb, Mn, Ca, and S via greyscale mapping and line scans. SEM and EDX analysis were done on select regions to confirm EMPA findings, verify compositions, and quantify sizes of Ti precipitates.

### 3.2.1 EMPA

A JEOL JXA-8900R EMPA was used to measure the elemental compositions of Ti, Nb, Mn, Ca, and S in the seven steels listed in Table 3.1 both qualitatively and quantitatively. Transverse cuts were made along the quarter point of the width on each steel sample and mounted in an epoxy resin solution. They were ground and polished down to 1 μm in a MetaDi oil based polishing solution to avoid the dissolution of any inclusions of interest. After polishing, a carbon coating was applied. The samples are shown in Figure 3.1.

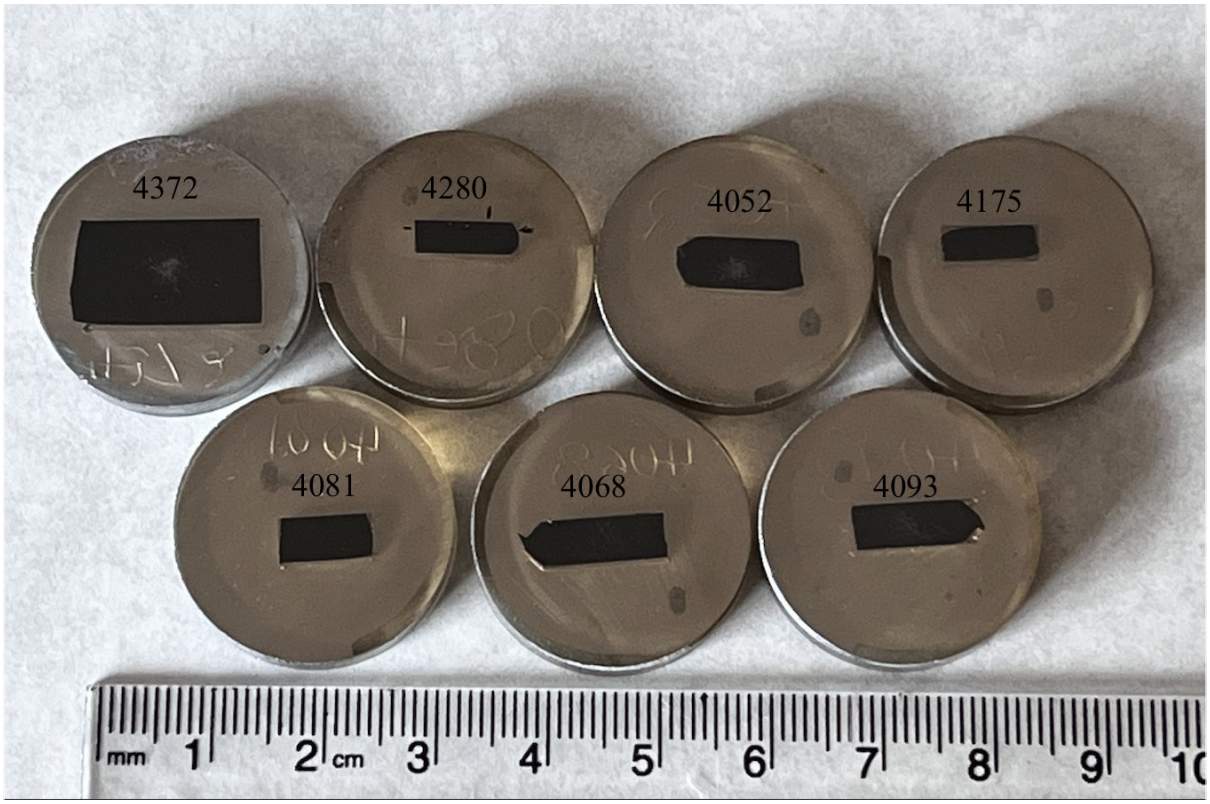


**Figure 3.1** Samples mounted, polished, and carbon coated for EMPA

3.2.1.1 EMPA mapping

Qualitative measurements were obtained through the mapping of each individual element on a tif. greyscale image. Pixel intensity is proportional to chemical wt%, where areas with high concentrations are white and areas with a concentration of zero are black. Grey pixels represent concentrations that fall in between, with the brighter ones exhibiting higher concentrations. Table 3.3 presents the parameters used for EMPA mapping. The electron beam size was 8 μm with a count time of 10 ms per pixel. Each pixel was 10x10 μm in size. The interaction volume was approximated to be 10.8 μm in diameter and 1.4 μm in depth, which covers the whole pixel size. The values were calculated by adding the electron range to the beam size and assuming a depth equivalent to the electron range. The electron range was calculated using Equation 6 in Chapter 2.

**Table 3.3** EMPA mapping parameters

| Beam Size (μm) | Pixel Count Time (ms) | Pixel Size (μm) | Current (nA) | Voltage (kV) |
|---|---|---|---|---|
| 8 | 10 | 10x10 | 200 | 20 |

The map region is divided into numerous single pixels and is scanned one pixel at a time across the surface, as shown in Figure 3.2. If a precipitate is within the pixel's 10x10 µm region, the electron beam will capture it, and it will appear as a brighter pixel on the map.

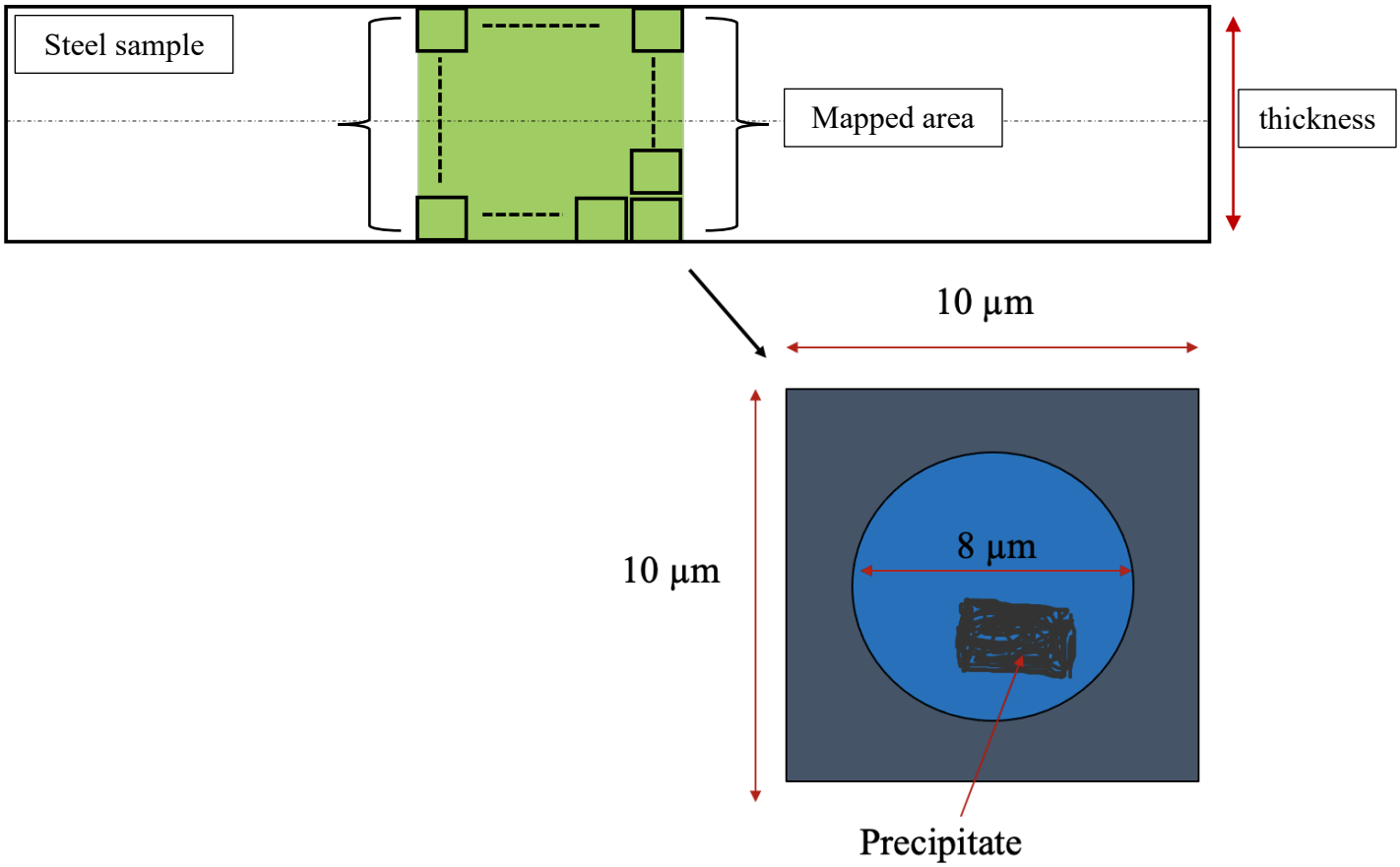


**Figure 3.2** Schematic of EMPA mapping region divided into single pixels

Mapping was performed for Ti, Nb, Mn, Ca, and S in all the steels, and the maps can be found in Appendix A. EMPA was calibrated for the elements analyzed using standards prior to the analysis. Figure 3.3 shows the greyscale map for Mn in sample 4280 (10x3 mm). From the Mn map, it is evident that there are no lines across the thickness of the sample that show a higher concentration, indicating limited macrosegregation. The same results were observed for the remaining elements in all the samples, found in Appendix A.

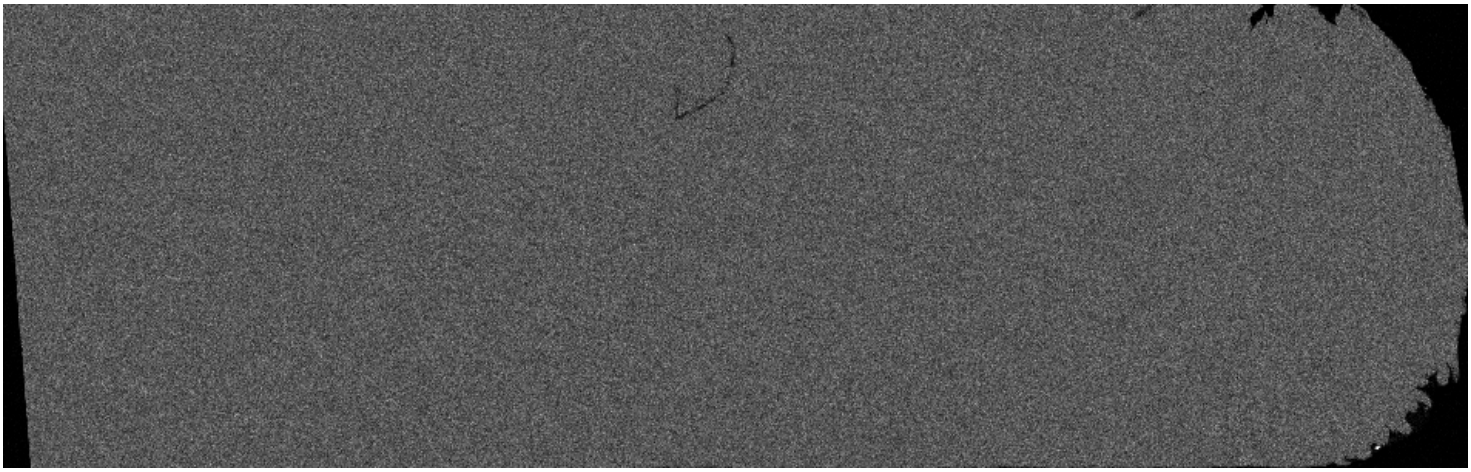

**Figure 3.3** Mn EMPA greyscale map for sample 4280

As discussed in Chapter 2, scaling of EMPA maps is done via multiple different scaling techniques. Thus, the intensities of the elements in the different elemental maps cannot be compared together. However, each map can be analyzed separately in terms of the number of precipitates present at certain locations. Although the brightness of most of the pixels in the Mn map in Figure 3.3 are high, that does not necessarily mean that the elemental concentrations in those pixels are higher than a pixel with a lower intensity on a different map. The presence of more bright pixels is an indication that most pixels are similar in elemental concentration for the same map, whereas a greater amount of contrast is an indication of a bigger difference in the elemental concentration for the same map.

To enhance post processing, the greyscale images were inverted such that the background is white, and the precipitates are black. The inverted images for Ti, Nb, Mn, Ca, and S in sample 4280 are presented in Figures 3.4 to 3.8 (10x3 mm), respectively. The rest of the inverted images for the remaining samples can be found in Appendix A. A magnified portion of the Ti map is presented in Figure 3.9 and is indicated by the dashed box in Figure 3.4.

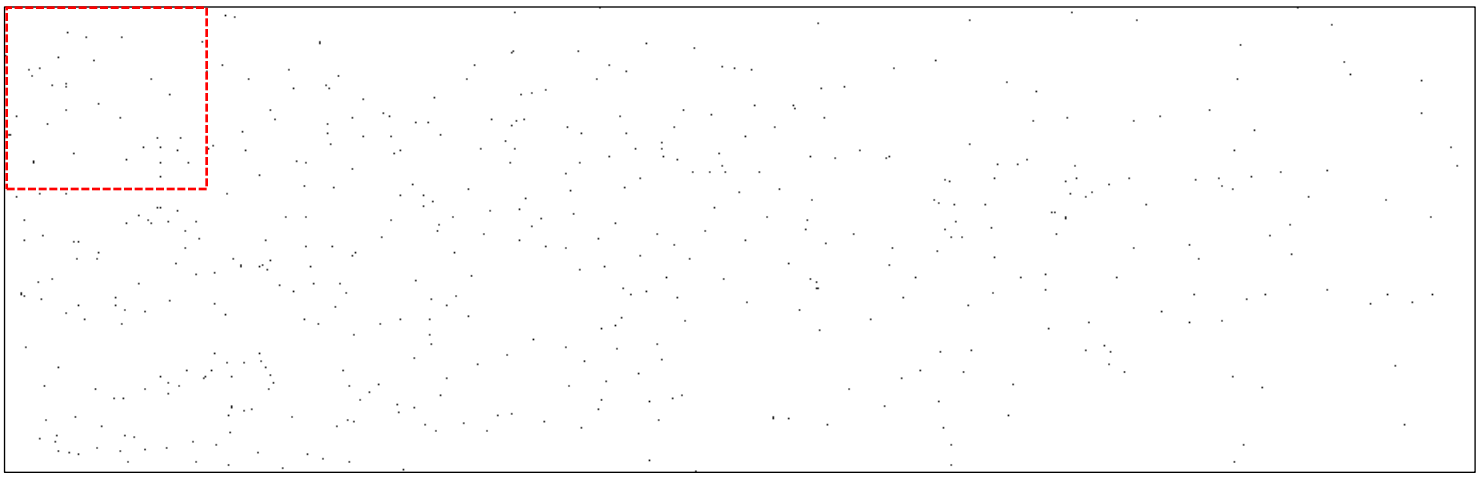

**Figure 3.4** Ti EMPA inverted greyscale map for sample 4280

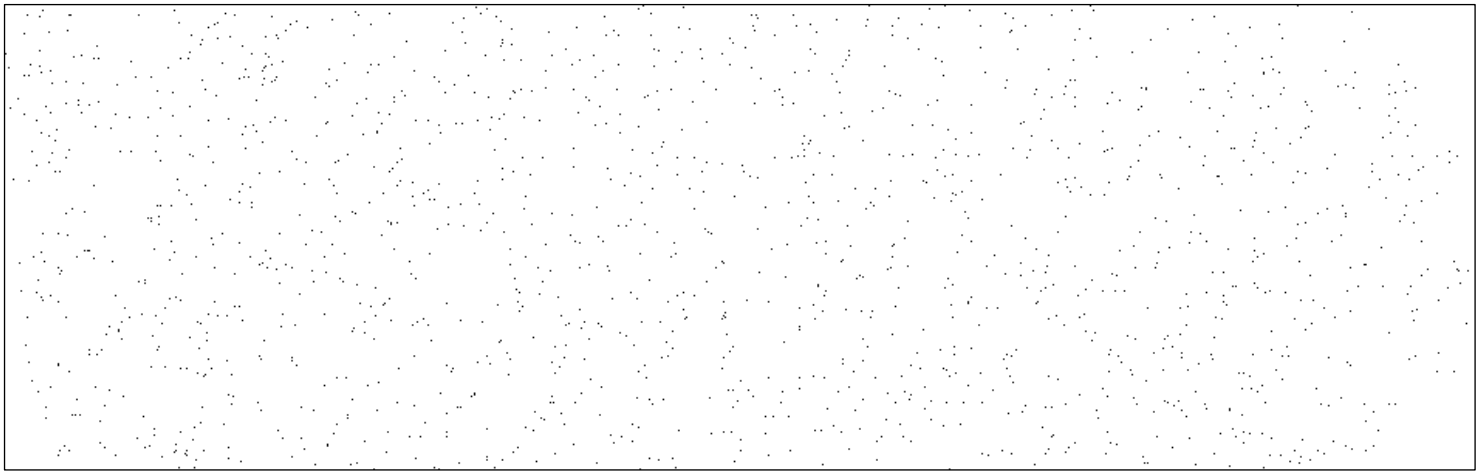

**Figure 3.5** Nb EMPA inverted greyscale map for sample 4280

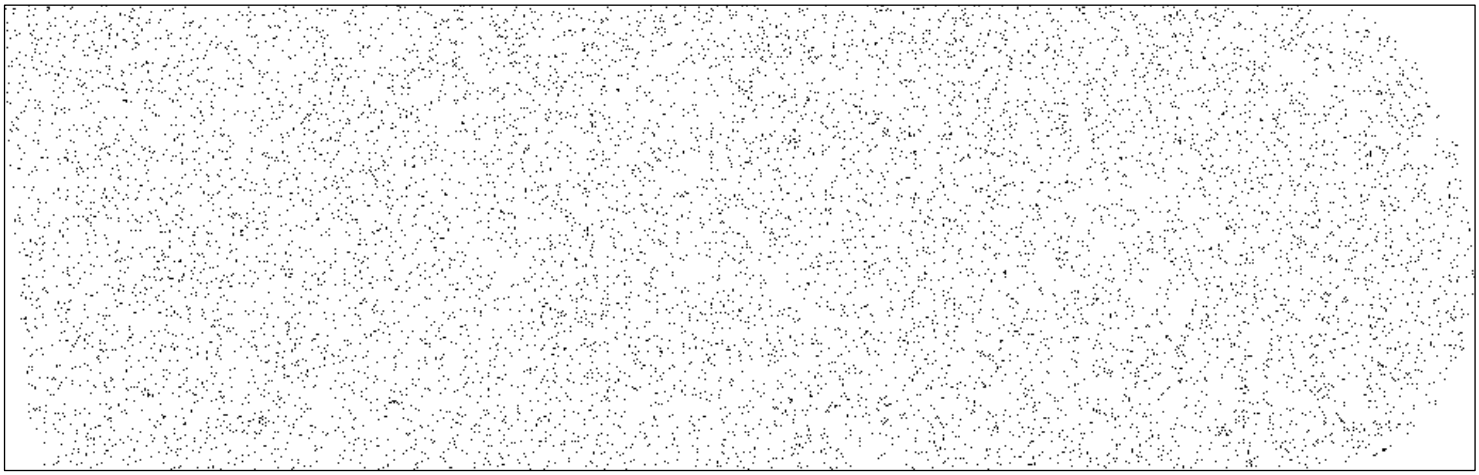

**Figure 3.6** Mn EMPA inverted greyscale map for sample 4280

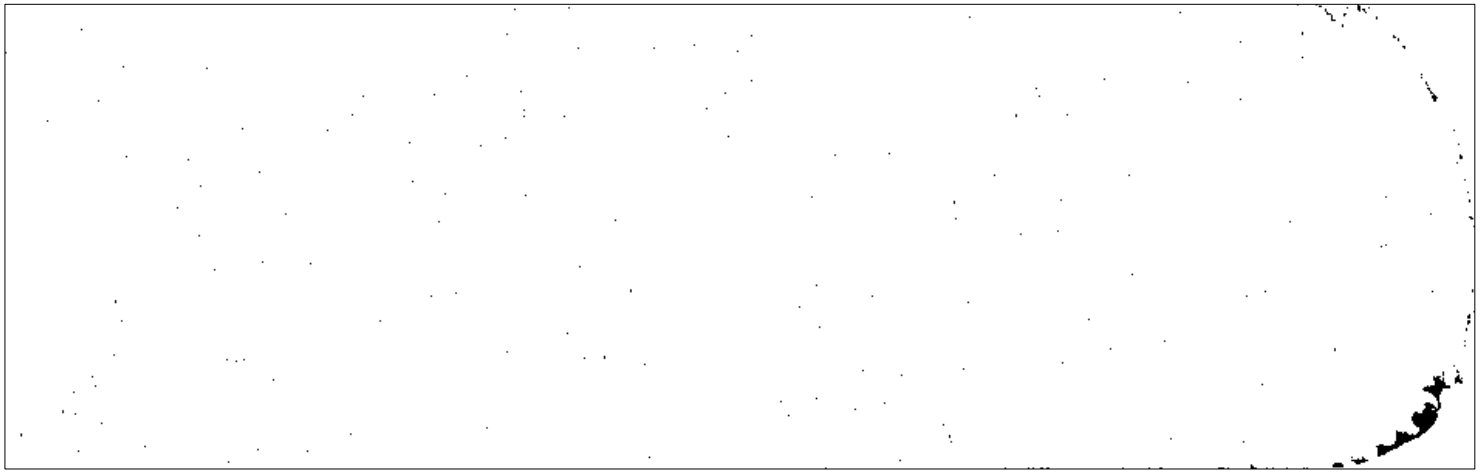

**Figure 3.7** Ca EMPA inverted greyscale map for sample 4280

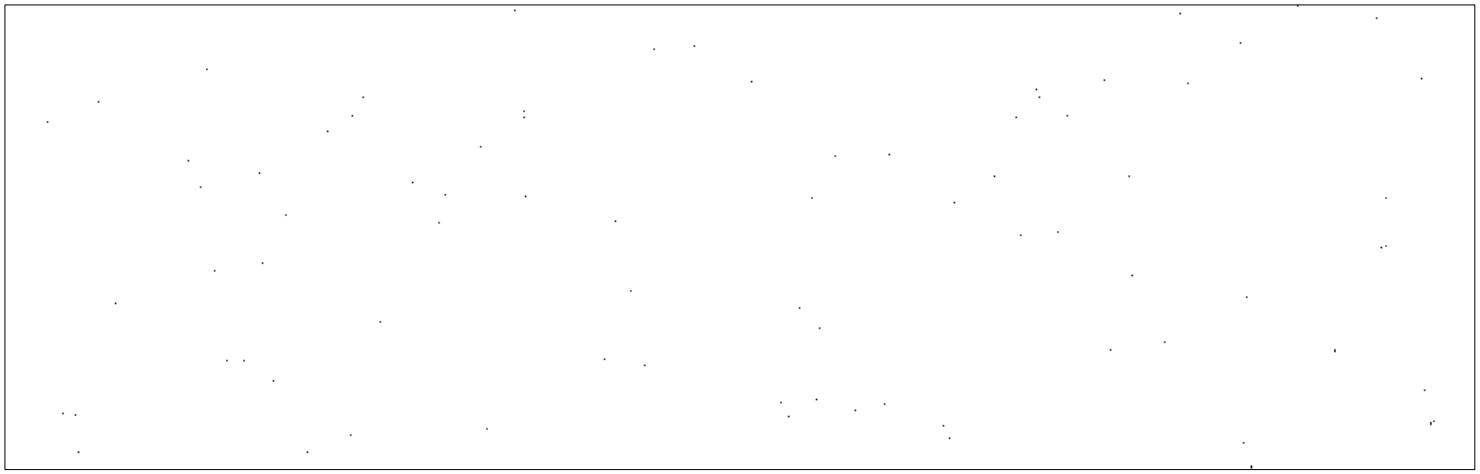

**Figure 3.8** S EMPA inverted greyscale map for sample 4280

A magnified view of the boxed area on the inverted Ti greyscale map, corresponding to an area of approximately 1x1 mm, is shown in Figure 3.9. Circled are areas where clustering of Ti is observed in this portion of the map. Clustering of Ti is found throughout the sample, which was defined as Ti precipitates present within an approximate 200 µm radius of a particular precipitate. Clustering is important to examine and identify as it could be detrimental to the mechanical properties, especially crack sensitivity, of the steel [54].

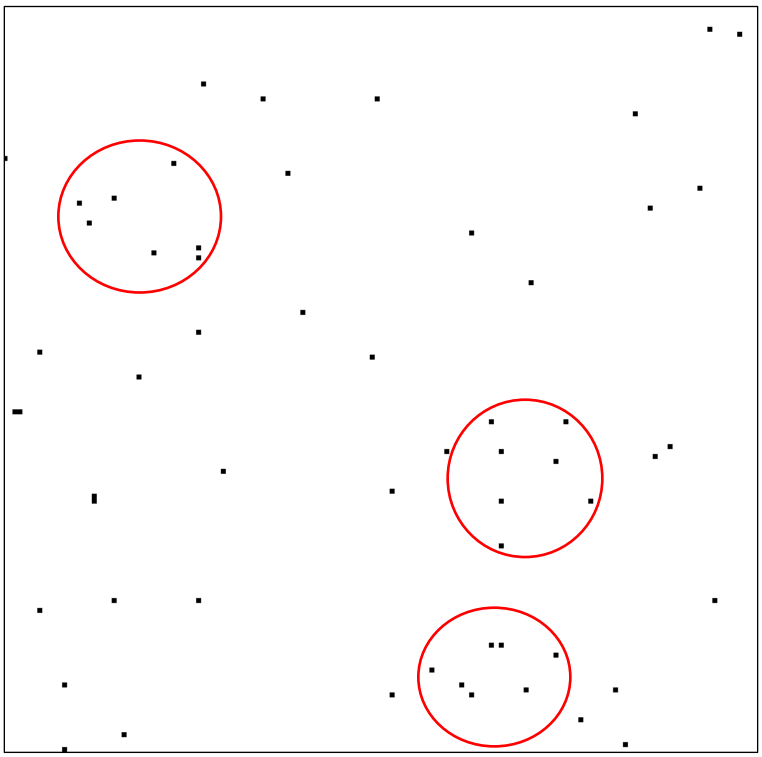

**Figure 3.9** Magnified area of the Ti EMPA greyscale map with clustering of Ti (circled)

3.2.1.2 EMPA line scans

Quantitative measurements were obtained from EMPA using line scans. For each sample, two lines that go through the thickness measured the weight percent of Ti, Nb, Mn, Ca, and S. EMPA was calibrated for Ti, Nb, Mn, Ca, and S prior to the line scans using standards. Each line had approximately 70 - 100 measurement points. Table 3.4 presents the parameters used for the line scans. An electron beam size of 10 µm was used with a count time of 21 s on each point. The step size between points was 50 µm.

**Table 3.4** EMPA line scan parameters

| Beam Size (μm) | Pixel Count Time (s) | Step Size (μm) | Current (nA) | Voltage (kV) |
|---|---|---|---|---|
| 10 | 21 | 50 | 200 | 20 |

Figure 3.10 shows the positions of the line scans taken for sample 4280. They are offset by 300 μm to the south. The images of the line scans for the other samples can be found in Appendix B.

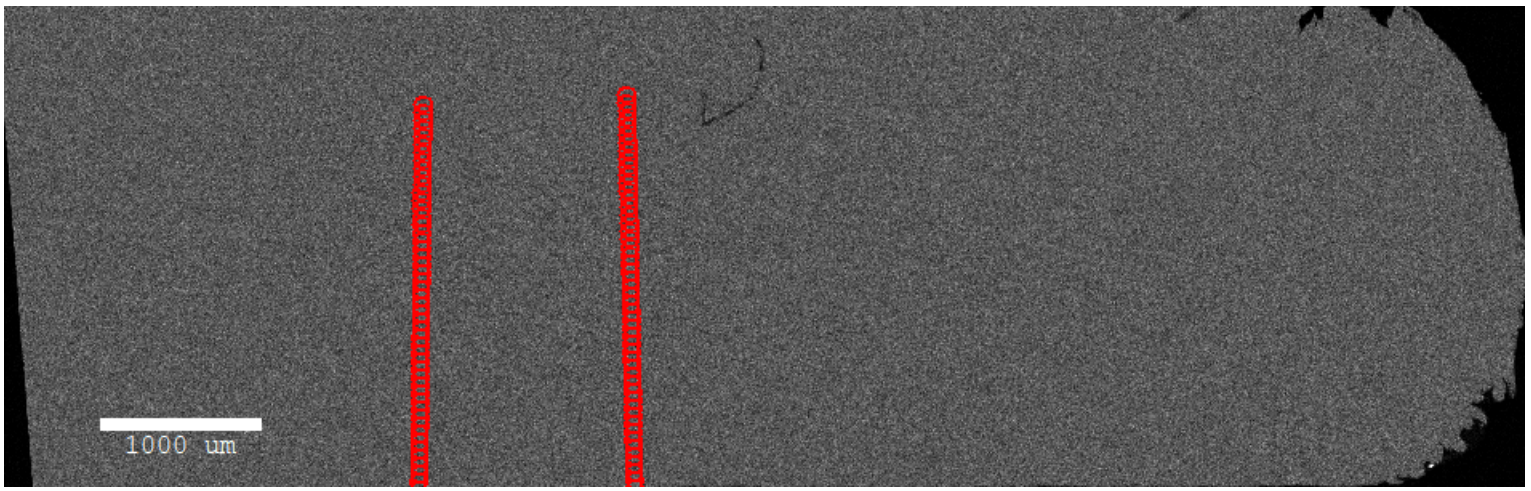


**Figure 3.10** Line scan location of points for sample 4280

Figures 3.11, 3.12, and 3.13 plot the wt% of Ti, Nb, and Ca vs. through thickness distance, respectively, in sample 4280. The line scan results for the remaining steels are presented in Appendix B. In Figures 3.11 and 3.12, the concentrations measured for Ti and Nb are consistent throughout the thickness around the nominal concentrations, with most concentrations falling below the nominal line. It is assumed that values above the nominal concentrations are macro-precipitates. These Ti, Nb macro-precipitates will be discussed further in following chapters. Since the precipitates detected are not packed around the centerline, macrosegregation is very minimal in these samples, as concluded prior from the Mn EMPA map. Altogether, no macrosegregation is observed from the maps or the line scans. However, some microsegregation of Ti and Nb can be seen from Figures 3.11 and 3.12.

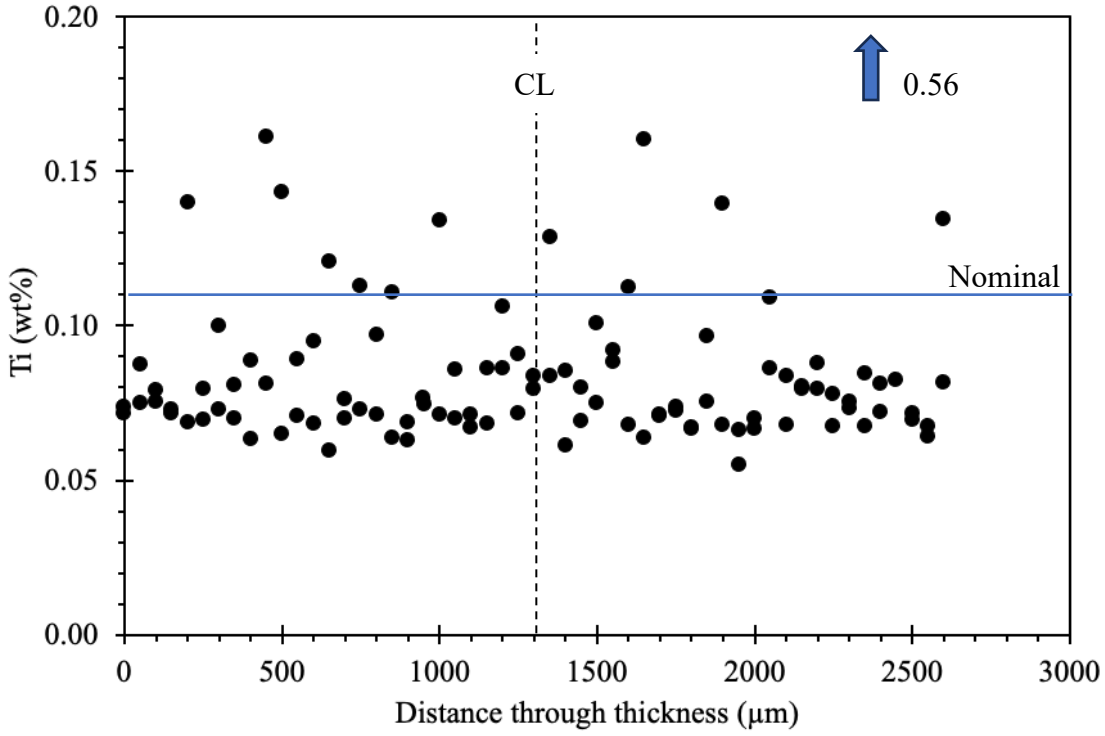


**Figure 3.11** Weight percent of Ti obtained from EMPA line scan in sample 4280

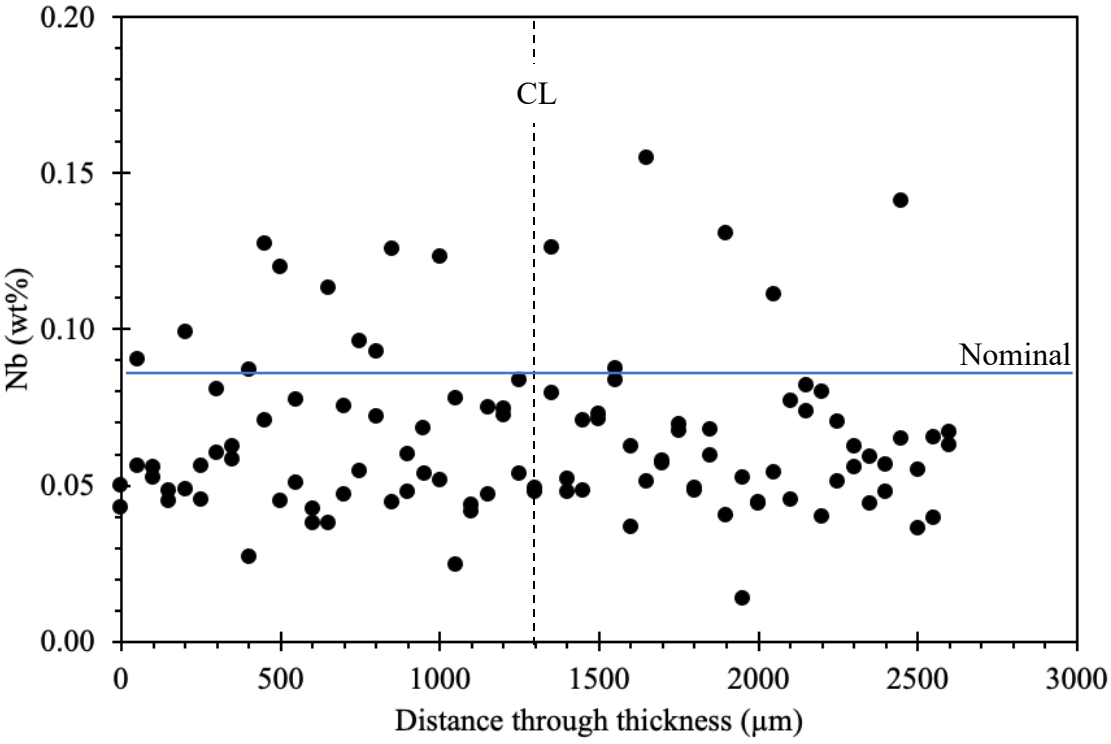


**Figure 3.12** Weight percent of Nb obtained from EMPA line scan in sample 4280

In Figure 3.13, the Ca concentrations are scattered all over the chart. That is due to the much lower concentrations of Ca in the samples. Because these concentrations all fall below the EMPA's detection limit of ~ 0.1 wt%, the data is considered inconsistent and unreliable when compared to the Ti and Nb data. This also resulted in a lot of the S not being detected. Due to the inaccuracy of the Ca and S line scans, their data will not be used for the analysis being described in Section 3.4.

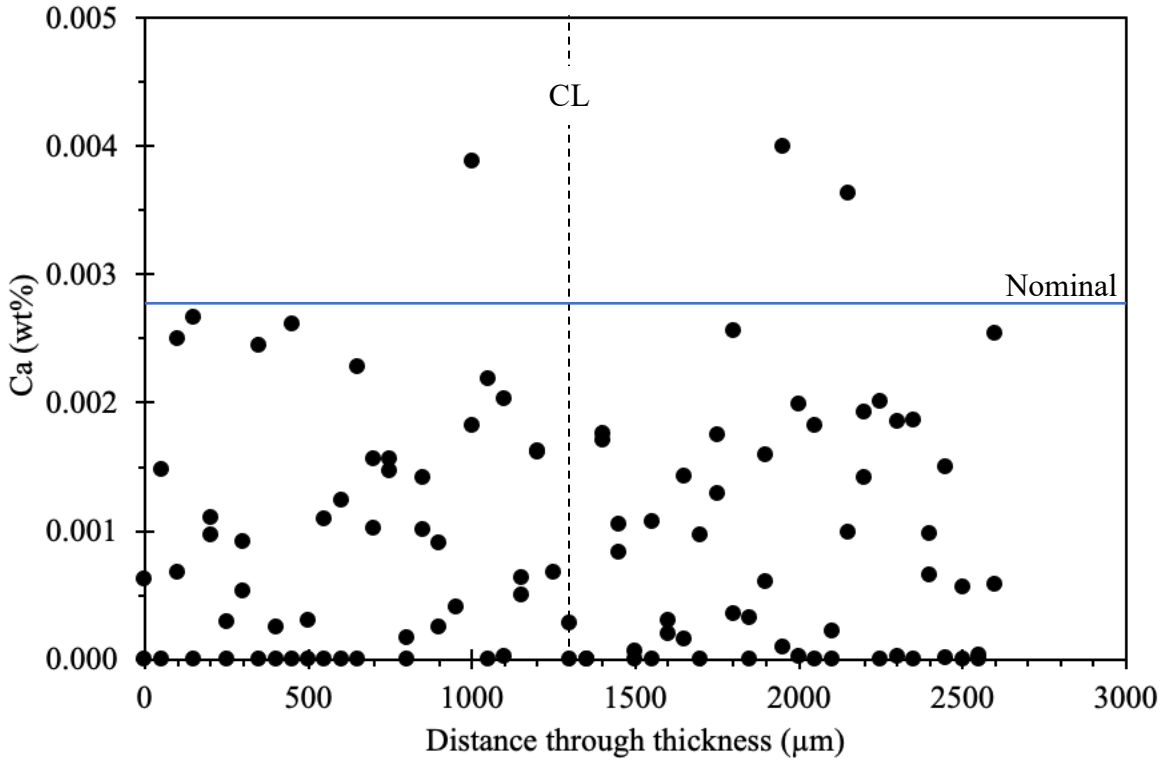


**Figure 3.13** Weight percent of Ca obtained from EMPA line scan in sample 4280

3.2.2 SEM/EDX

A Tuscan Vega3 equipped with an Oxford EDX detector was used for SEM/EDX. The accelerating voltage used for all SEM imaging was 20 kV, and all images, including EDX maps, were obtained using secondary electron mode.

SEM was used in two different ways to characterize Ti precipitates. Firstly, it was used to locate specific pixel coordinates given by the EMPA precipitate analysis program to confirm the presence of precipitates and validate the results obtained by EMPA. It was alternatively used to generate size distributions by locating random Ti precipitates at the quarter thicknesses in samples 4280,

4175, 4052, and 4093. Precipitate sizes were recorded by measuring the largest side of each precipitate.

EDX was used to confirm the composition of the precipitates observed and captured on the SEM via elemental mapping. The size of precipitates obtained on SEM images were measured to compare Ti associated with nonmetallic CaS inclusions to other Ti precipitates, such as TiN and (Ti,Nb)N, in sample 4280. For samples 4175, 4052, and 4093, size distributions of the Ti precipitates observed were generated to compare the difference in sizes to the difference in Ti and Nb content across the samples. SEM images, EDX maps, and size distributions are presented and discussed further in Chapters 4 and 5.

## 3.3 EMPA Analysis Procedure

Two codes were developed to aid with the data analysis: a greyscale image converting program and an EMPA precipitate analysis program. The full scripts for both codes can be found in Appendix C.

### 3.3.1 Greyscale Image Converting Program

This code works by converting greyscale images (has to be a tif. file) into a data array of greyscale values. The data array is outputted as a text file, which gets inputted into Excel for further use in analysis. Figure 3.14 shows the Excel file for the 4280 Ti greyscale image. Each cell has a greyscale value which corresponds to a single pixel on the image. The 4280 Ti image is 950 x 300 pixels in size, and therefore the excel file is also 950 x 300 cells with each cell corresponding to a single pixel. For example, cell A1 in Figure 3.14 is the pixel at the top left corner of the image, indicating that the pixel has a greyscale intensity of 15.


| | A | B | | | E | F | G | H | I | J | K | L | M | N | O | P |
|---|---|---|---|---|---|---|---|---|---|---|---|---|---|---|---|---|
| 1 | 15 | 17 | 14 | 13 | 15 | 16 | 25 | 18 | 9 | 13 | 14 | 14 | 18 | 18 | 11 | 16 |
| 2 | 14 | 13 | 8 | 16 | 18 | 12 | 25 | 12 | 15 | 18 | 15 | 11 | 16 | 37 | 15 | 13 |
| 3 | 10 | 15 | 12 | 10 | 9 | 9 | 15 | 13 | 27 | 12 | 12 | 11 | 24 | 13 | 22 | 15 |
| 4 | 15 | 12 | 12 | 16 | 15 | 28 | 14 | 13 | 13 | 20 | 18 | 15 | 18 | 11 | 14 | 8 |
| 5 | 10 | 12 | 15 | 17 | 9 | 11 | 18 | 9 | 9 | 12 | 15 | 16 | 13 | 17 | 12 | 12 |
| 6 | 9 | 15 | 25 | 10 | 13 | 14 | 12 | 17 | 15 | 16 | 11 | 26 | 12 | 16 | 12 | 28 |
| 7 | 9 | 15 | 11 | 13 | 15 | 13 | 12 | 16 | 15 | 14 | 15 | 18 | 11 | 12 | 7 | 12 |
| 8 | 14 | 14 | 14 | 14 | 28 | 12 | 20 | 15 | 10 | 16 | 22 | 37 | 12 | 18 | 12 | 14 |
| 9 | 15 | 18 | 12 | 9 | 20 | 10 | 12 | 12 | 19 | 26 | 10 | 14 | 13 | 13 | 13 | 11 |
| 10 | 13 | 9 | 10 | 19 | 11 | 17 | 12 | 18 | 15 | 13 | 16 | 13 | 15 | 13 | 25 | 17 |

**Figure 3.14** Portion of 4280 Ti greyscale image Excel file

Greyscale values range from 0 to 255, where 0 corresponds to the black pixels in the image and 255 are the whitest pixels in the image. All the remaining values in between form a grey gradient based on the elemental intensity measured by the EMPA at every pixel. Brighter pixels correspond to highly concentrated areas and would have a higher greyscale value associated with them, while darker pixels correspond to lower concentrated areas and would have a lower greyscale value assigned to them.

### 3.3.2 EMPA Precipitate Analysis Program

The EMPA precipitate analysis program takes up to five EMPA maps of a sample and analyzes them based on the greyscale values of interest. A flowchart of how the program works is presented in Figure 3.15. First, the number of elements that will be analyzed is chosen, and the elements of interest (out of Ti, Nb, Mn, Ca, and S) are selected. Greyscale value thresholds for each chosen element are then inputted. The program will output: a list of coordinates with a count for each element selected, a list of coordinates with a count of the pixels at which all the selected elements coexist, and a list of coordinates with a count of all the selected elements at quarter thicknesses of the samples. Pixels with elemental overlap can be linked to precipitates, such as TiN-CaS or (Ti,Nb)N.

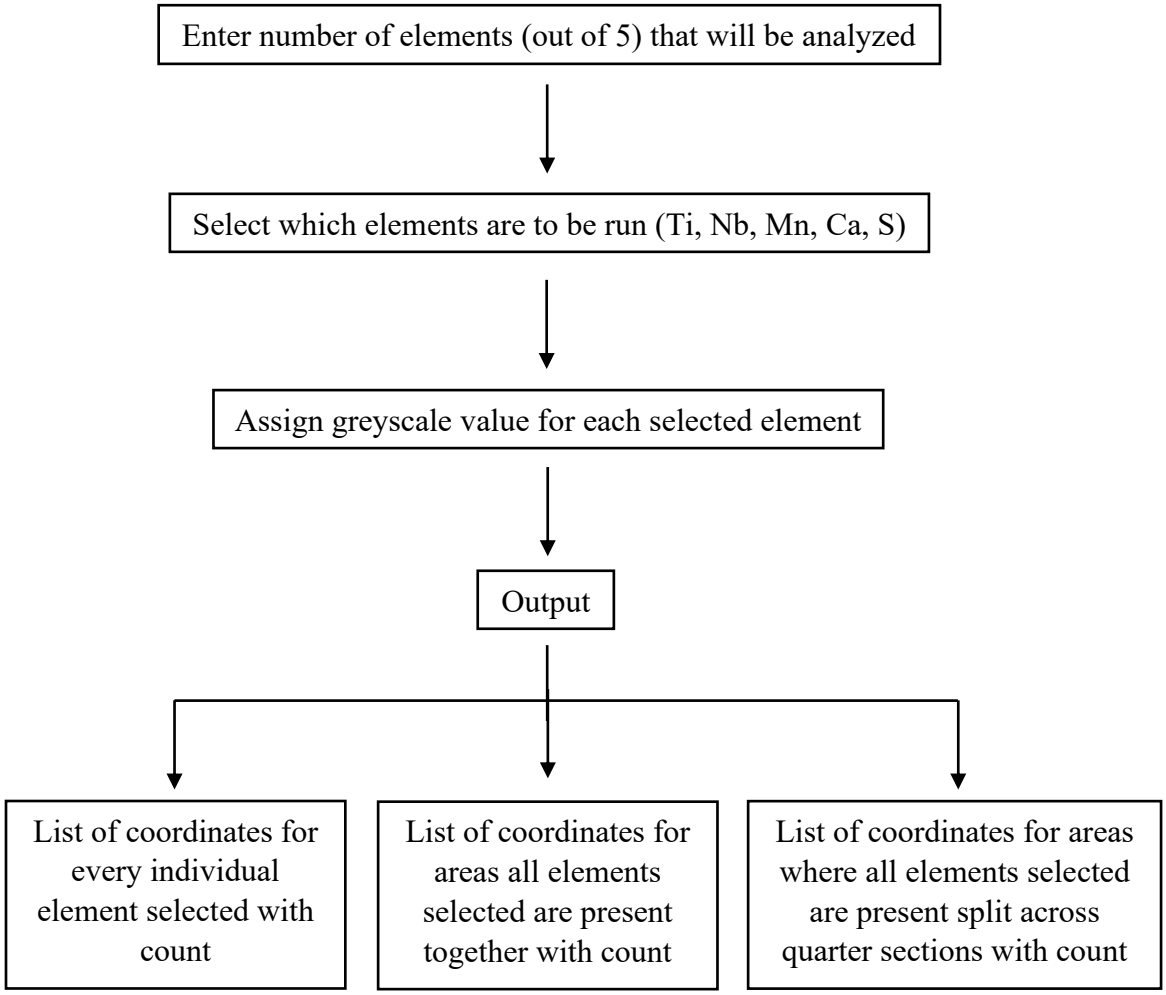


**Figure 3.15** EMPA precipitate analysis program interface

## 3.4 Ti Lognormal Distributions

This section covers the analysis of the results obtained from the Ti EMPA maps. EMPA maps were used alongside the data from the line scans to create an approximate relationship between greyscale values and weight percent. Using the greyscale image converting program discussed in Section 3.3.1, EMPA maps were converted into a matrix of their greyscale values using Excel for analysis. The relationship is created by fitting the map and line scan data by a lognormal distribution then superimposing the two distributions to create a correlation. It is assumed that the curves are representative of the microsegregation in the samples. The peak of the greyscale distribution represents the concentration at the dendrites while the end of the distribution represents the highly concentrated interdendritic regions, where the formation of Ti precipitates is most likely to occur. The points at the end of the distribution are those with the highest concentrations. They were confirmed to be precipitates on SEM, therefore validating the assumption.

### 3.4.1 Sample 4280

The first step to the analysis is to fit the Ti line scan and greyscale maps by a lognormal distribution. Figure 3.16 shows the lognormal fitting of: (a) Ti line scan data and (b) Ti greyscale data for sample 4280. The lognormal distribution for the line scans and greyscale maps of Ti in the remaining steels follow the same approach and can be found in Appendix D.

The line scan distribution peaks at 0.075 wt% Ti, which is the concentration detected for most of the line scan points. A number of points exceed a concentration of 0.100 wt% Ti and are most likely Ti macro-precipitates as they exhibit the highest concentrations. These points will be the focus of the study when completing the analysis and drawing conclusions. When fitting the data to the lognormal distribution, it can be seen that the distribution is a good fit compared to the raw data.

The greyscale distribution peaks at a greyscale value of 12, which is the number recorded at most of the pixels from the Ti EMPA map. There are points at the end of the distribution, beyond a value of approximately 20, that are considered to be Ti macro-precipitates. The distribution shows a good fit with the exception of two outlier points at greyscale values 13 and 14. These points were taken out of the lognormal fit. With the large amounts of data points being analyzed for EMPA maps, taking out two points did not show any significant effect on the distribution.

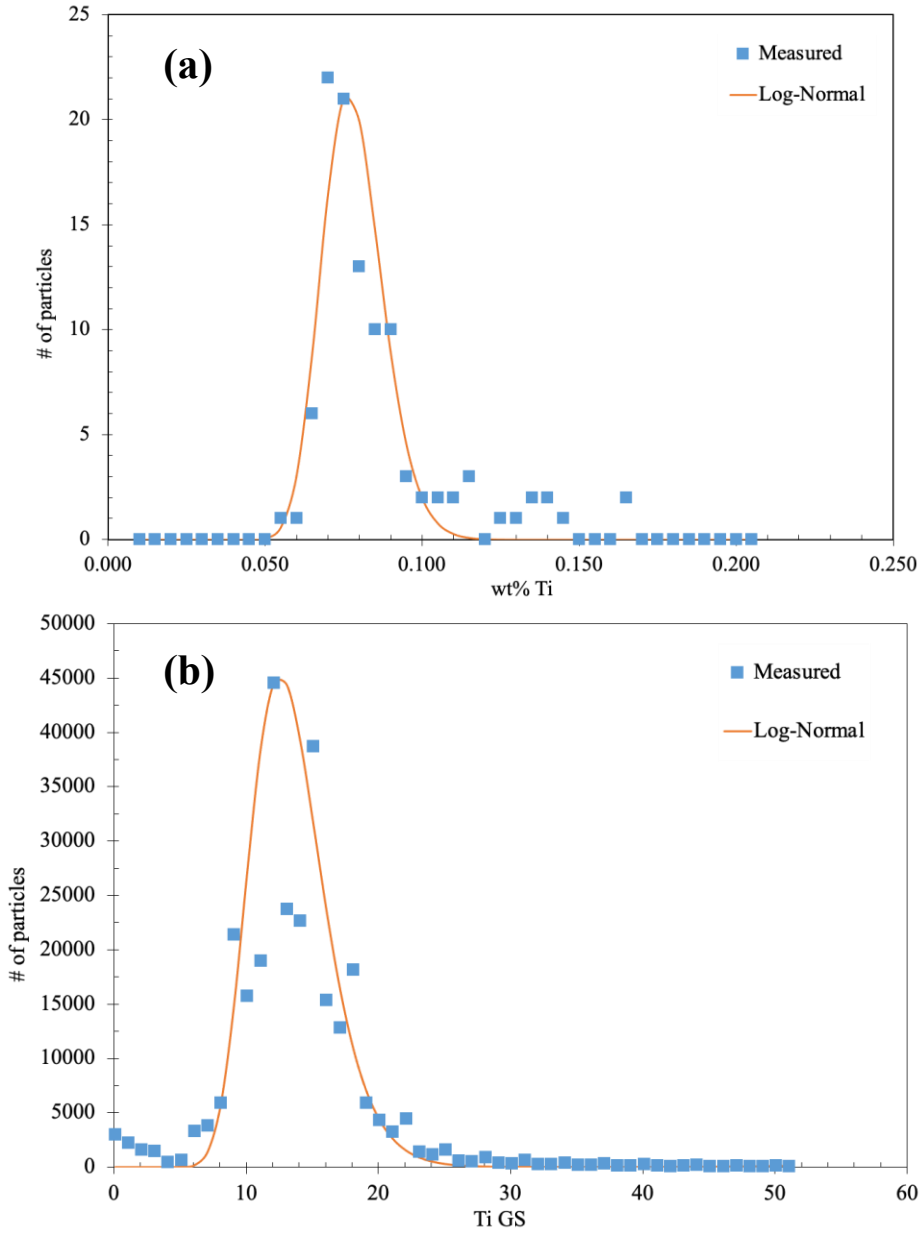


**Figure 3.16 (a)** Ti line scan data plotted against its lognormal distribution for sample 4280 **(b)** Ti greyscale data plotted against its lognormal distribution for sample 4280

Once the lognormal distributions for the line scan data and the greyscale data are generated, they are superimposed onto each other. Since the line scans and greyscale numbers are obtained from the same samples, both plots should exhibit a similar trend. Once overlapped, an approximation of the relationship between the line scans and the greyscale maps can be obtained.

Figure 3.17 (a) shows the superimposed line scan distribution and greyscale lognormal distribution of Ti in sample 4280, which show a proper fit. This plot will be used for setting the greyscale boundaries used in the precipitate analysis code in Chapters 4 and 5. An approximate linear relationship between the Ti greyscale values and concentrations can be developed, shown in Figure 3.17 (b). The relationship produces the conversion equation: wt% Ti = 0.0033 × GS + 0.033. The peak of the distributions is at a greyscale value of 12 (0.073 wt% Ti) in sample 4280.

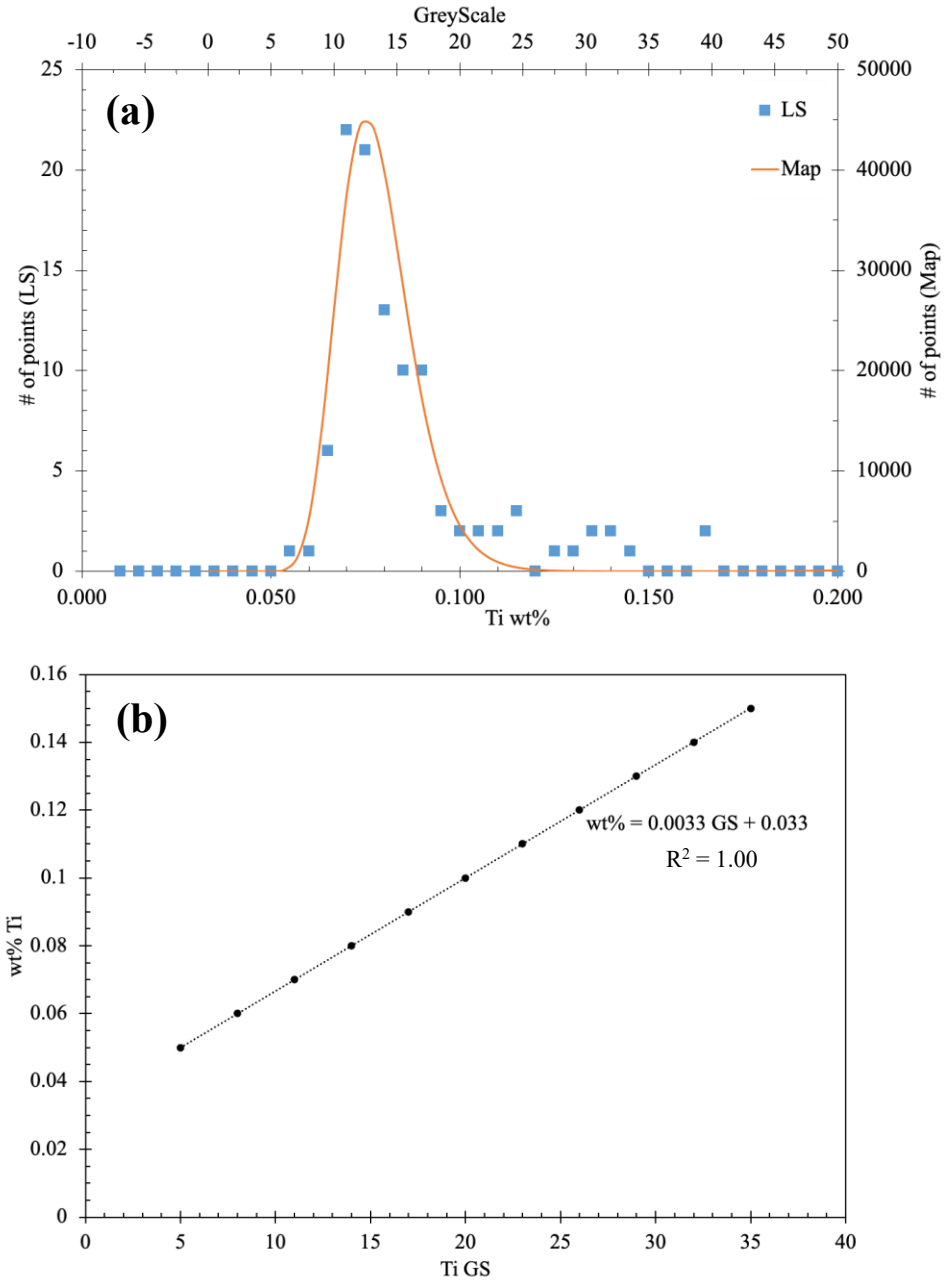


**Figure 3.17 (a)** Ti line scan distribution plotted against Ti greyscale distribution in sample 4280 **(b)** Linear relationship between wt% and greyscale Ti in sample 4280

3.4.2 Sample 4372

Figure 3.18 (a) shows the line scan distribution plotted on the lognormal greyscale distribution for Ti. The peaks of the distributions are at a greyscale value of 8 (0.087 wt% Ti) in sample 4372. Both distributions show a good fit with one another. Figure 3.18 (b) shows the linear conversion between Ti greyscale values and weight percent. The relationship yields the following equation: wt% Ti = 0.0056 × GS + 0.042.

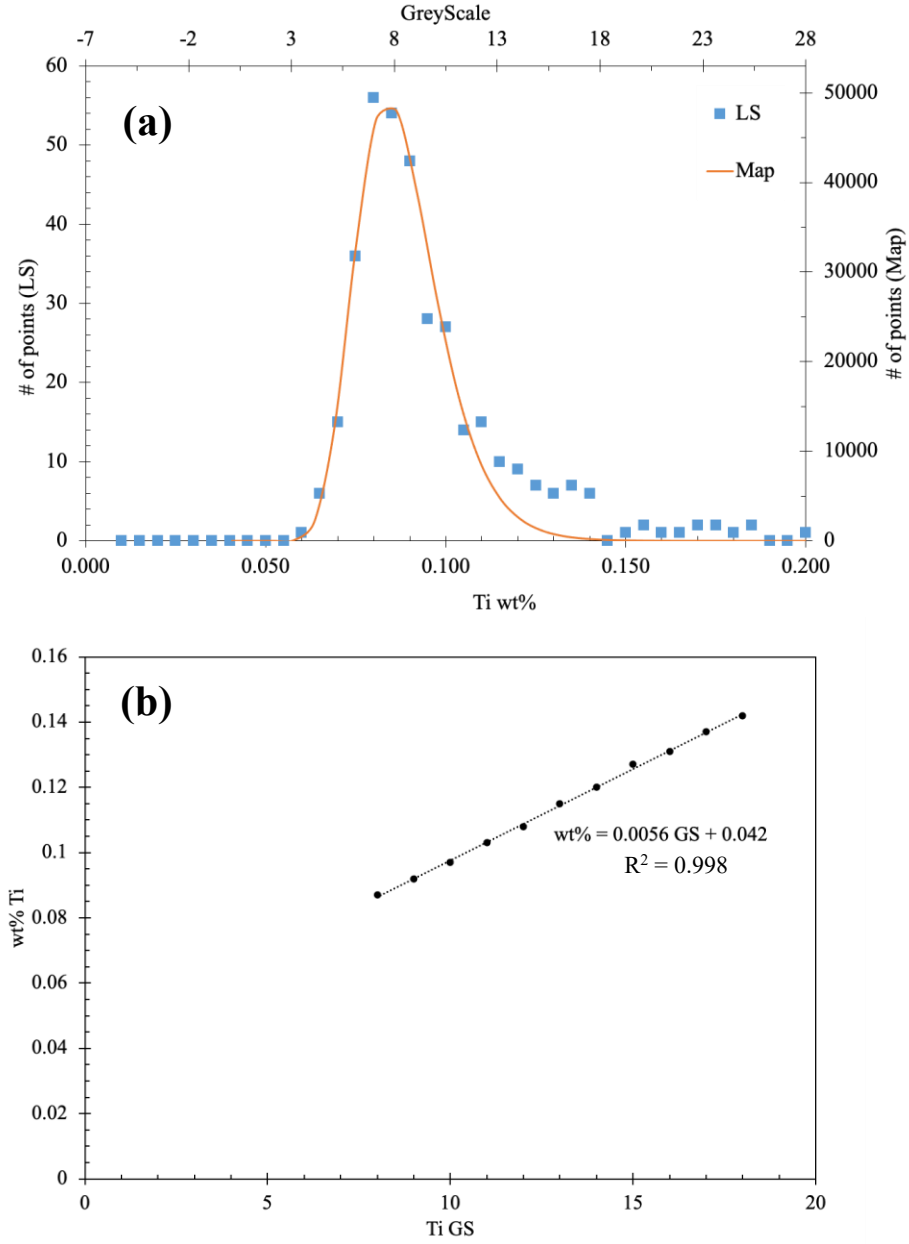


**Figure 3.18 (a)** Ti line scan distribution plotted against Ti greyscale distribution in sample 4372 **(b)** Linear relationship between wt% and greyscale Ti in sample 4372

3.4.3 Sample 4175

Figure 3.19 (a) shows the Ti line scan distribution plotted on the lognormal greyscale distribution. The peaks of the distributions are at a greyscale value of 8 (0.098 wt% Ti) in sample 4175, and the distributions show a good fit. Figure 3.19 (b) shows the linear conversion between Ti greyscale values and weight percent. The relationship yields the equation: wt% Ti = 0.0032 × GS + 0.072.

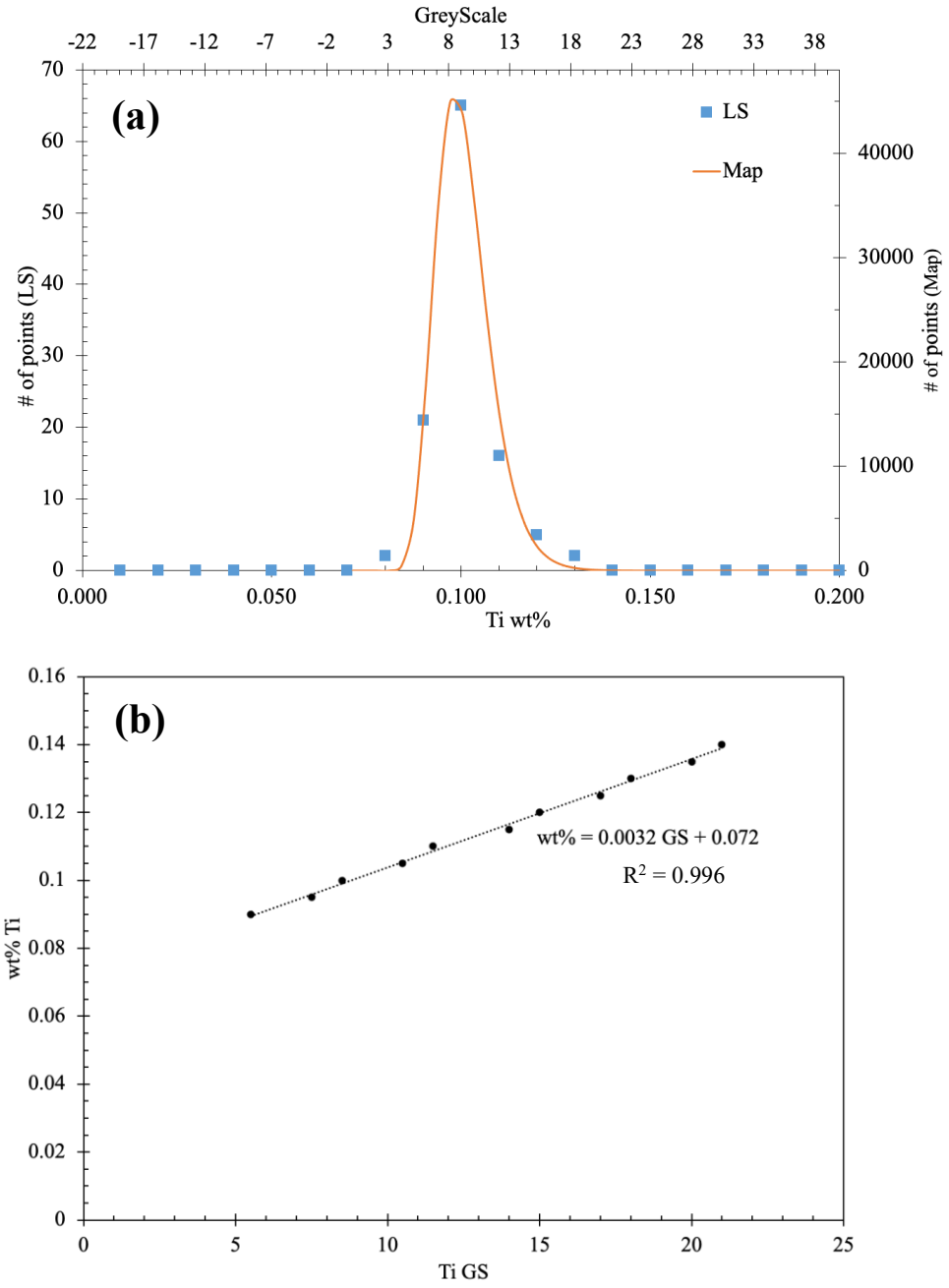


**Figure 3.19 (a)** Ti line scan distribution plotted against Ti greyscale distribution in sample 4175 **(b)** Linear relationship between wt% and greyscale Ti in sample 4175

3.4.4 Sample 4052

Figure 3.20 (a) shows the Ti line scan distribution plotted on the lognormal greyscale distribution in sample 4052. The peaks of the distributions are at a greyscale value of 7 (0.074 wt% Ti) and the distributions show a good fit. Figure 3.20 (b) shows the relationship between Ti greyscale values and weight percent. The relationship yields the following equation: wt% Ti = 0.0028 × GS + 0.054.

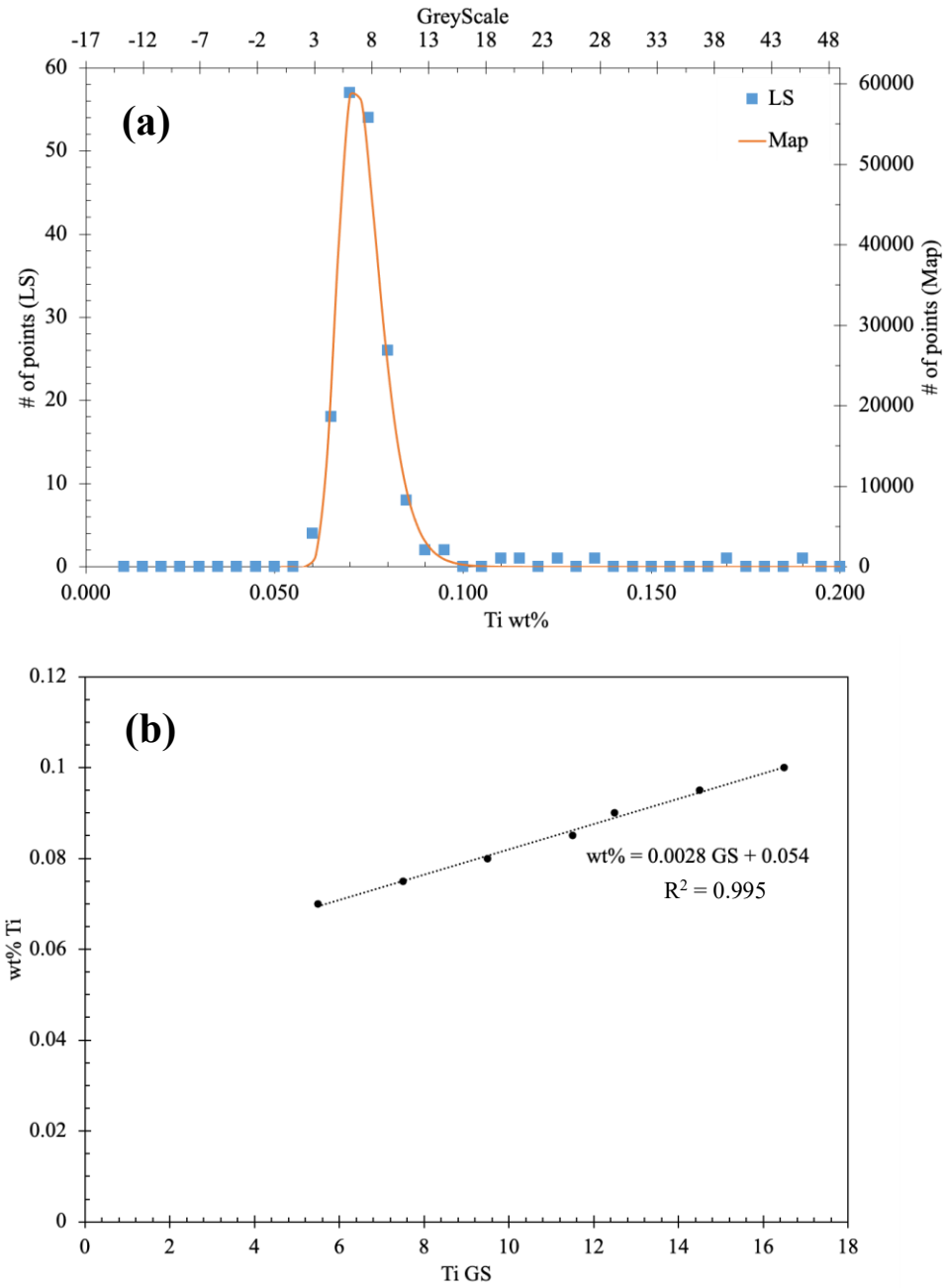


**Figure 3.20 (a)** Ti line scan distribution plotted against Ti greyscale distribution in sample 4052 **(b)** Linear relationship between wt% and greyscale Ti in sample 4052

3.4.5 Sample 4081

Figure 3.21 (a) shows the Ti line scan distribution plotted on the lognormal greyscale distribution in sample 4081. The peaks of the distributions are at a greyscale value of 7 (0.061 wt% Ti), and the distributions are a good fit. Figure 3.21 (b) shows the conversion between Ti greyscale values and weight percent. The relationship yields the following equation: wt% Ti = 0.0029 × GS + 0.041.

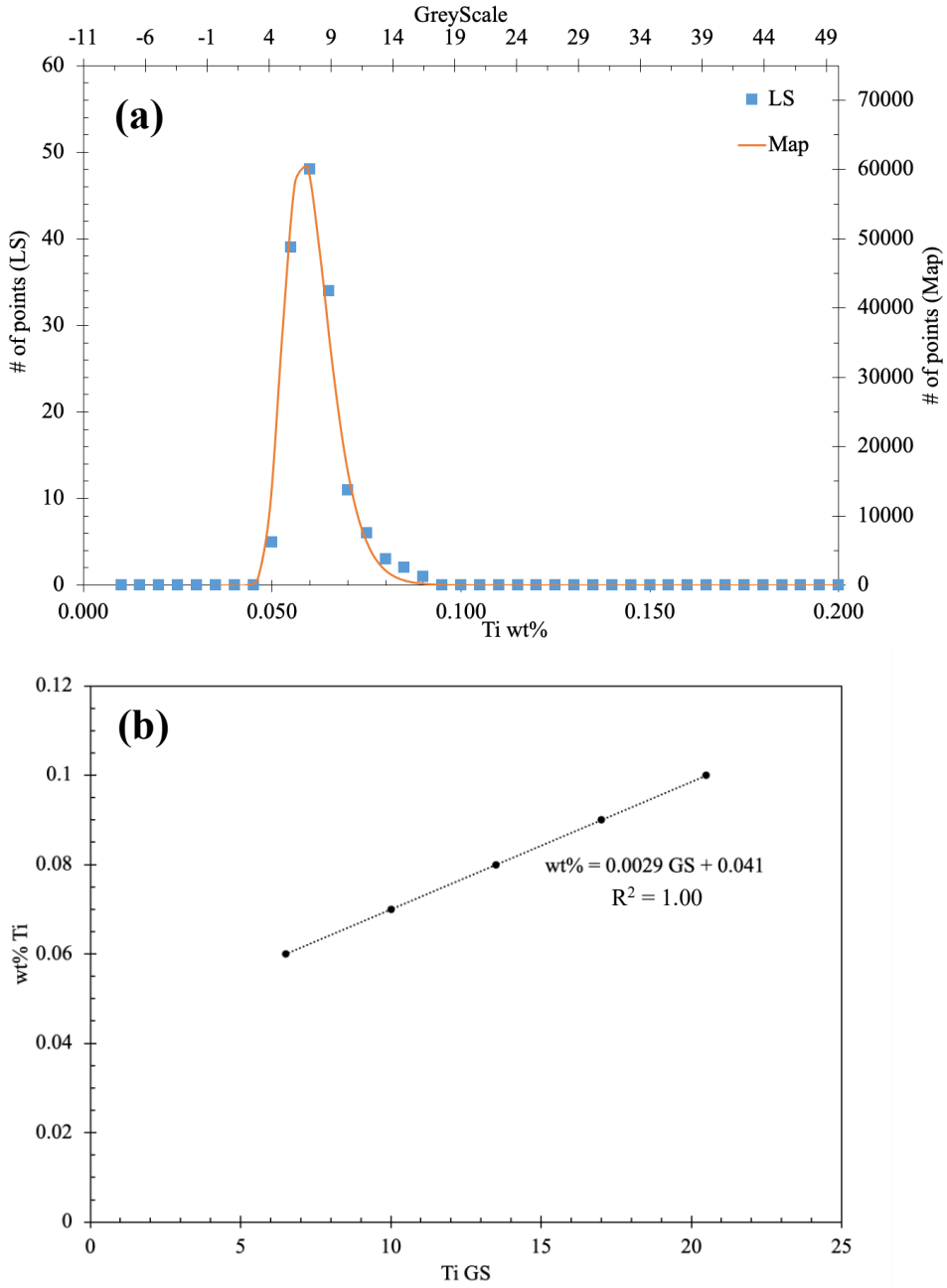


**Figure 3.21 (a)** Ti line scan distribution plotted against Ti greyscale distribution in sample 4081 **(b)** Linear relationship between wt% and greyscale Ti in sample 4081

3.4.6 Sample 4068

Figure 3.22 (a) shows the Ti line scan distribution plotted with the lognormal greyscale distribution in sample 4068. The peaks of the distributions are at a greyscale value of 8 (0.048 wt% Ti) and the distributions are a good fit. Figure 3.22 (b) shows the conversion relationship between Ti greyscale values and weight percent. It yields the following equation: wt% Ti = 0.0025 × GS + 0.028.

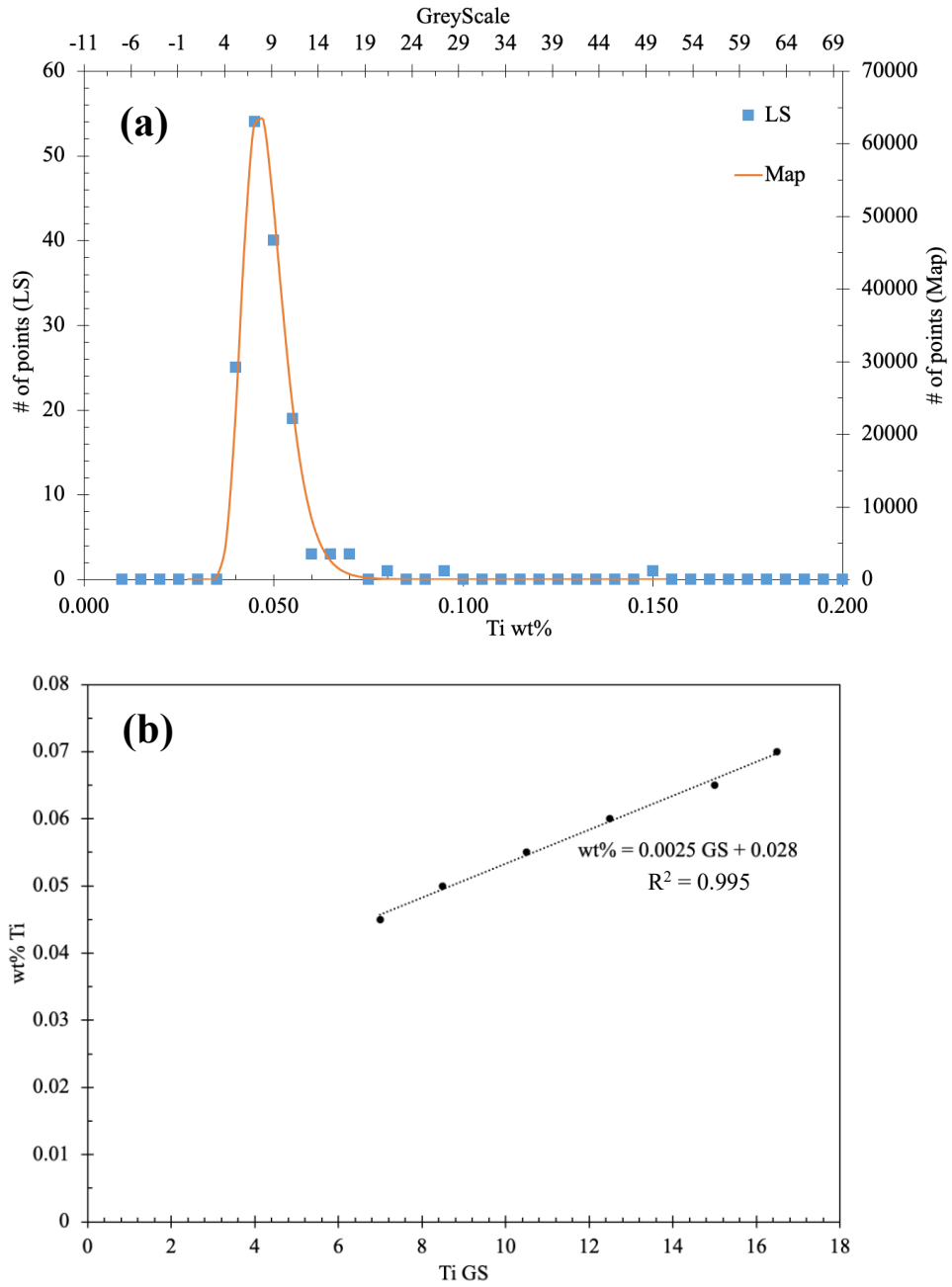


**Figure 3.22 (a)** Ti line scan distribution plotted against Ti greyscale distribution in sample 4068 **(b)** Linear relationship between wt% and greyscale Ti in sample 4068

3.4.7 Sample 4093

Figure 3.23 (a) shows the Ti line scan distribution plotted with the lognormal greyscale distribution in sample 4093. The peaks of the distributions land at a greyscale value of 6 (0.045 wt% Ti), and the distributions are a good fit. Figure 3.23 (b) shows the conversion between Ti greyscale values and weight percent. The relationship yields the following equation: wt% Ti = 0.0054 × GS + 0.012.

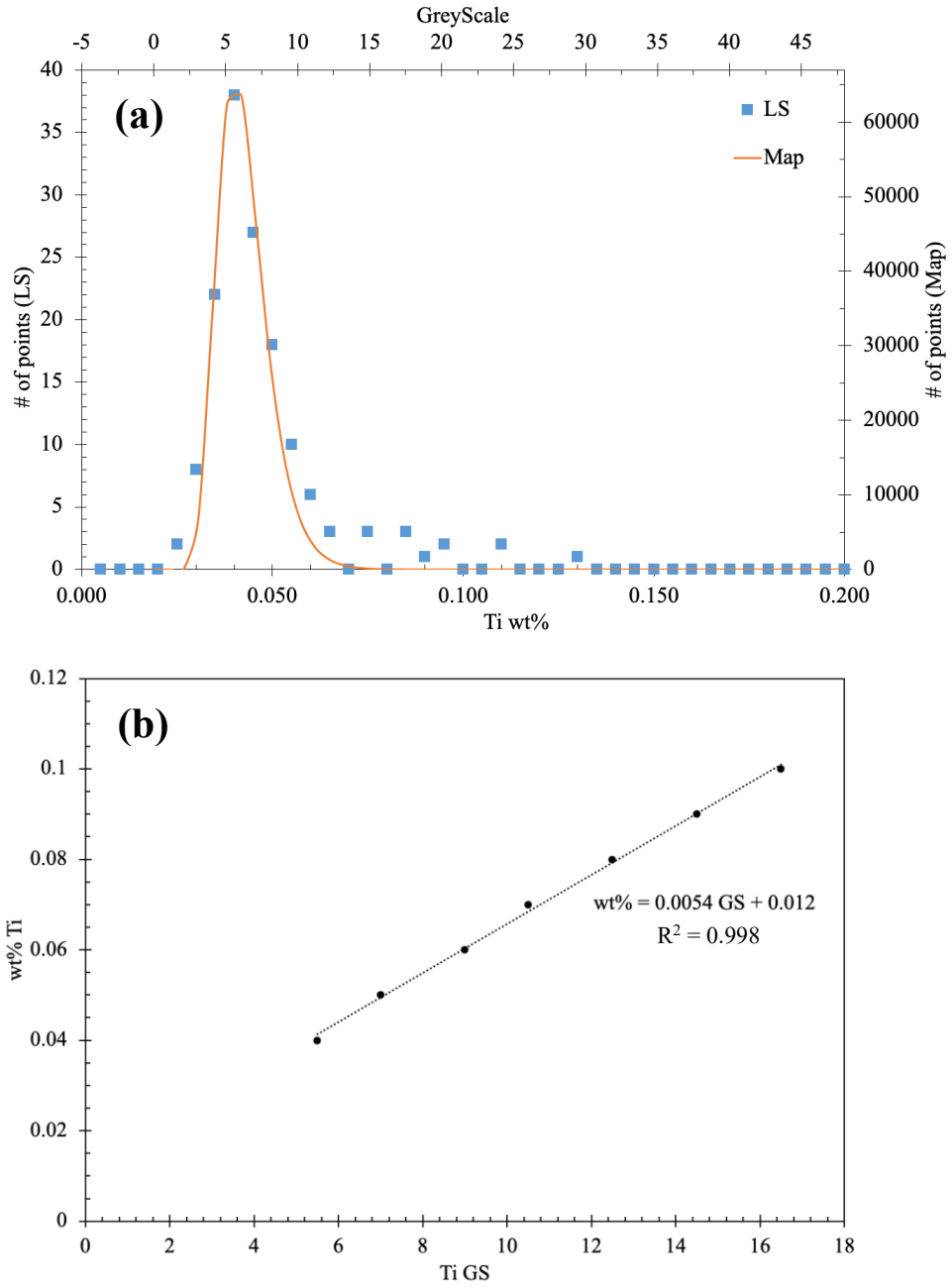


**Figure 3.23 (a)** Ti line scan distribution plotted against Ti greyscale distribution in sample 4093 **(b)** Linear relationship between wt% and greyscale Ti in sample 4093

## 3.5 Nb Lognormal Distributions

The Nb analysis was completed similarly to the Ti in Section 3.4, where line scan and greyscale data were fit to lognormal distributions and superimposed. This section outlines the superimposed distributions and their relationships for the Nb in all the steels.

### 3.5.1 Sample 4280

Figure 3.24 (a) shows the overlapped line scan and greyscale distributions for Nb in sample 4280. Unlike the Ti distributions, the Nb plots do not overlap as closely. Offset points were taken out of the analysis and were deemed outliers. The analysis was completed on data points at the end of the distribution, where overlapping becomes more evident. The peaks of the distributions are at a greyscale value of 25 (0.057 wt% Nb). Points following the peak were fit into a linear relationship to produce a conversion between wt% and greyscale Nb, shown in Figure 3.24 (b). The relationship generates the equation: wt% Nb = 0.0010 × GS + 0.032.

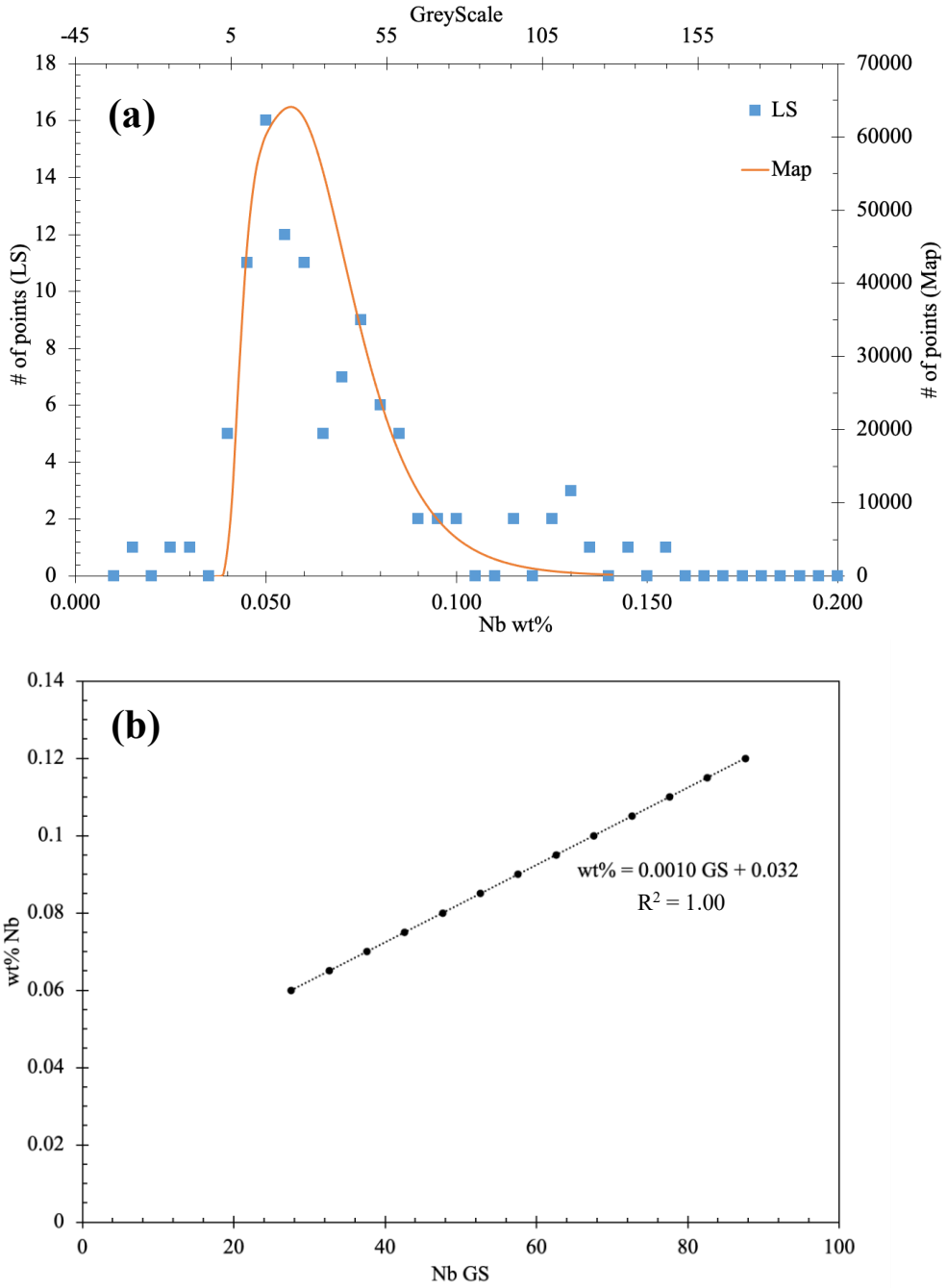


**Figure 3.24 (a)** Nb line scan distribution plotted against its greyscale distribution in sample 4280 **(b)** Linear relationship between wt% and greyscale Nb in sample 4280

3.5.2 Sample 4372

Figure 3.25 (a) shows the line scan distribution plotted on the lognormal greyscale distribution for Nb in sample 4372. The peaks of the distributions are at a greyscale value of 10 (0.053 wt% Nb). The distributions are a good fit with two outliers at greyscales 10 and 18. Figure 3.25 (b) shows the conversion between Nb greyscale values and wt%, yielding: wt% Nb = 0.0028 × GS + 0.025.

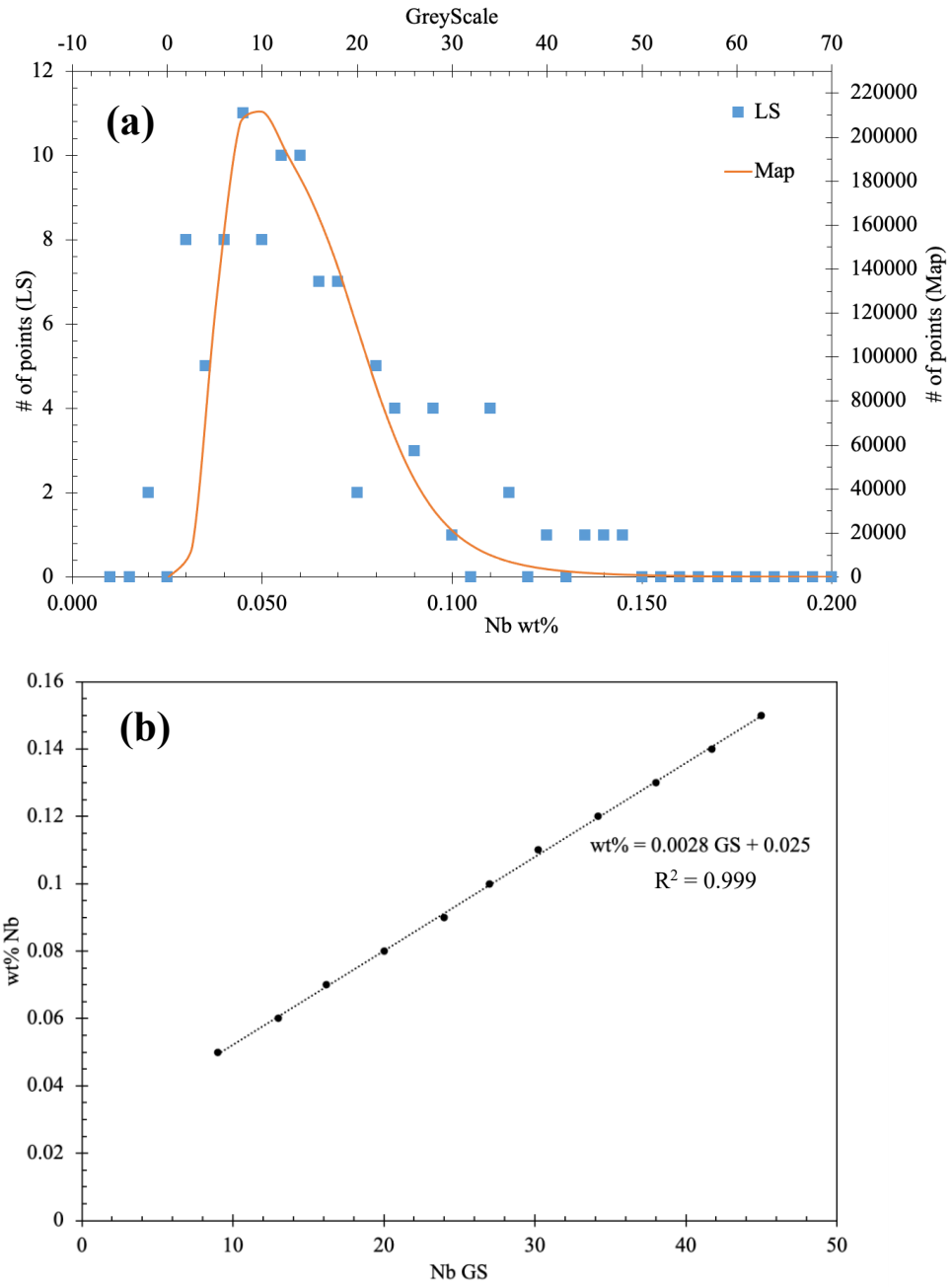


**Figure 3.25 (a)** Nb line scan distribution plotted against its greyscale distribution in sample 4372 **(b)** Linear relationship between wt% and greyscale Nb in sample 4372

3.5.3 Sample 4175

Figure 3.26 (a) shows the Nb line scan distribution with the lognormal greyscale distribution in sample 4175. The peaks are at a greyscale value of 35 (0.0087 wt% Nb), and the distributions are a good fit with the exception of three outliers at greyscales 40, 95, and 105. Figure 3.26 (b) presents the relationship between greyscale and wt% Nb, which yields: wt% Nb = 0.0003 × GS - 0.0018.

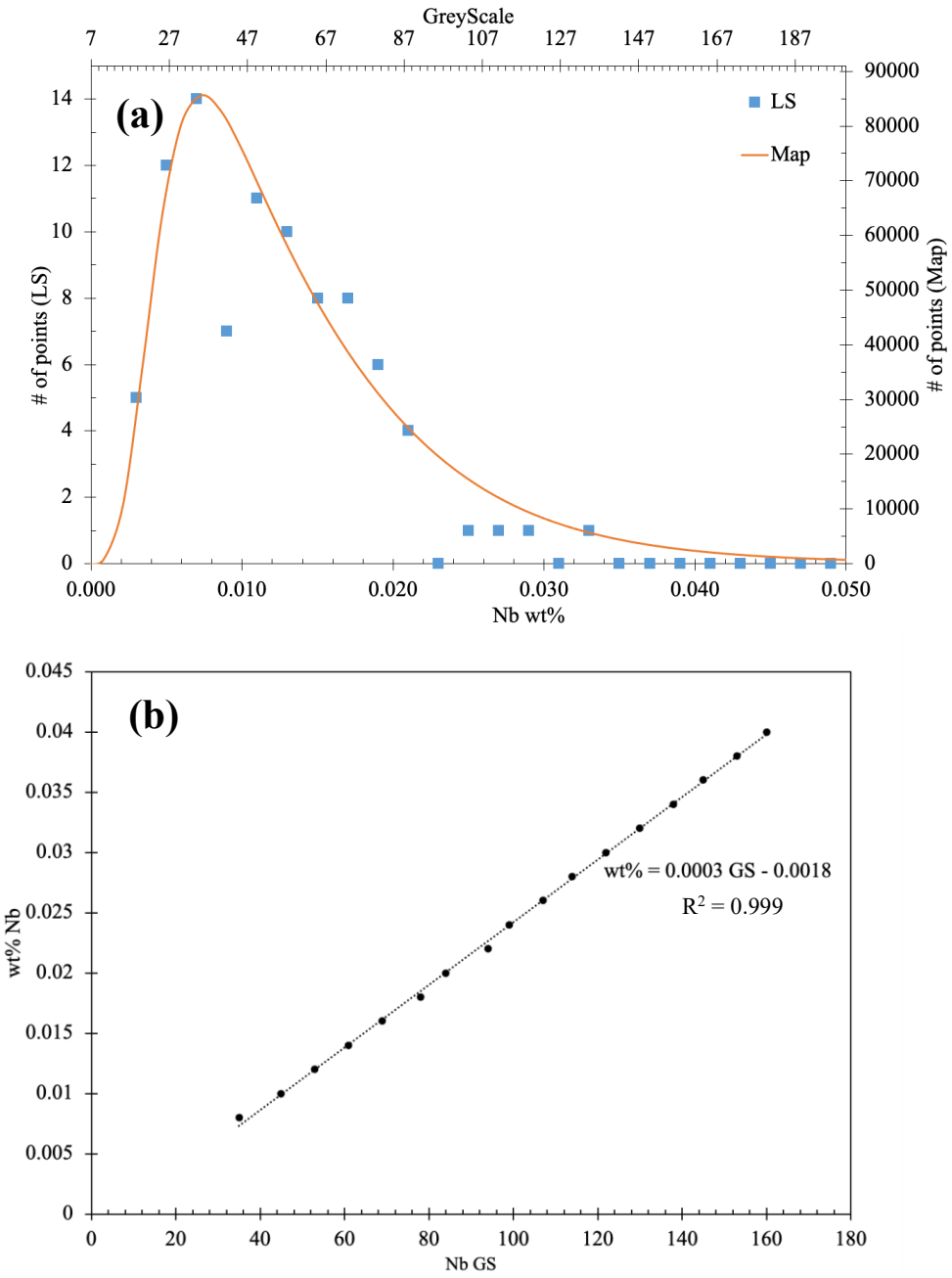


**Figure 3.26 (a)** Nb line scan distribution plotted against its greyscale distribution in sample 4175 **(b)** Linear relationship between wt% and greyscale Nb in sample 4175

3.5.4 Sample 4052

Figure 3.27 (a) shows the Nb line scan with the lognormal greyscale distributions in sample 4052. The peaks are at a greyscale value of 34 (0.005 wt% Nb), and the two distributions are a good fit with three outliers beyond the peak at greyscales 60, 80, and 100. Figure 3.27 (b) shows the relationship between greyscale and wt% Nb, yielding: wt% Nb = 0.0001 × GS + 0.0013.

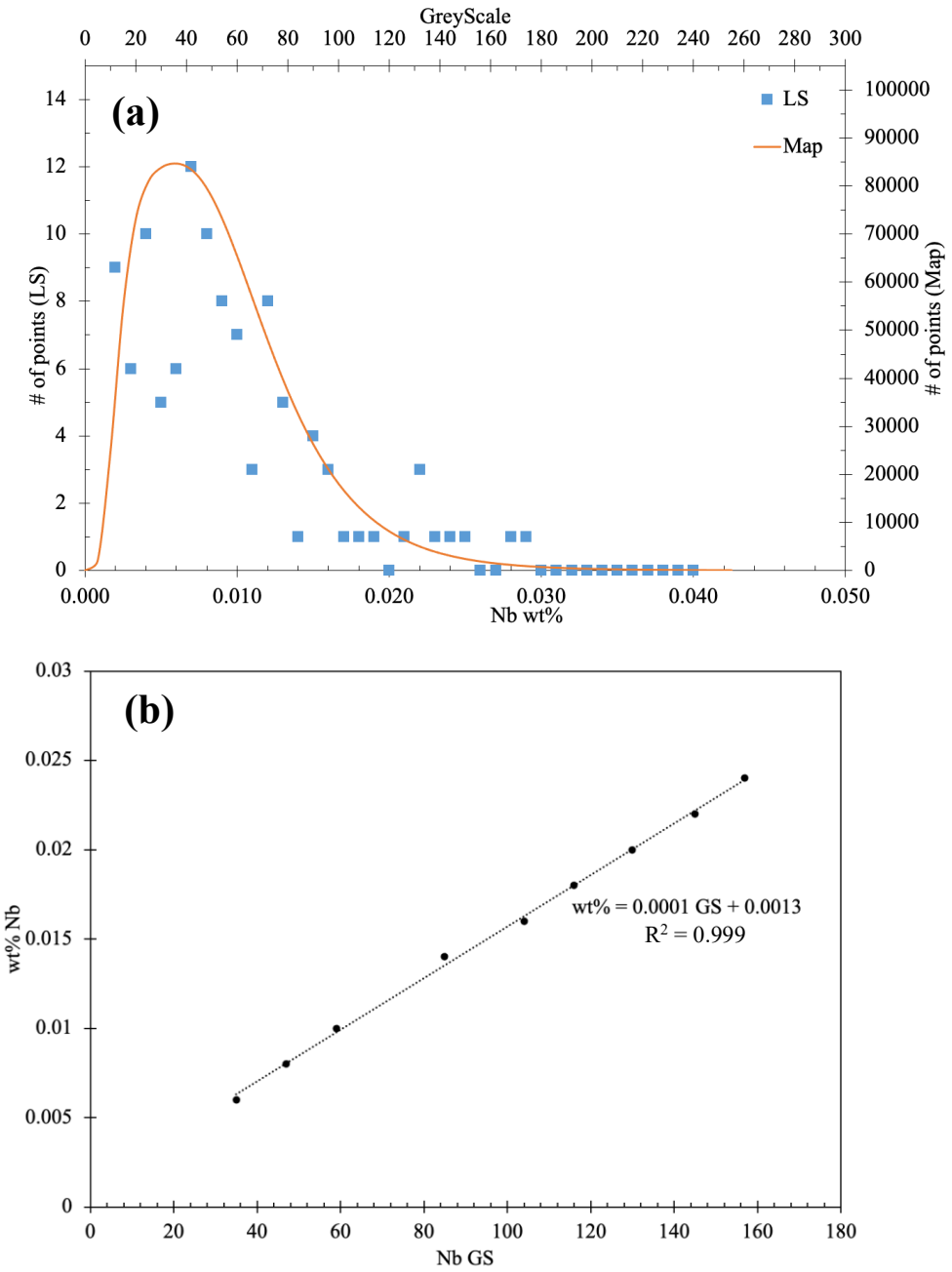


**Figure 3.27 (a)** Nb line scan distribution plotted against its greyscale distribution in sample 4052 **(b)** Linear relationship between wt% and greyscale Nb in sample 4052

3.5.5 Sample 4081

Figure 3.28 (a) shows the Nb line scan distribution plotted on the lognormal greyscale distribution in sample 4081. The peaks of the distributions are at a greyscale value of 28 (0.004 wt% Nb). The two distributions are a good fit with outliers at greyscales 45, 65, and 95. Figure 3.28 (b) presents the linear relationship between greyscale and wt% Nb, yielding: wt% Nb = 0.0001 × GS + 0.0005.

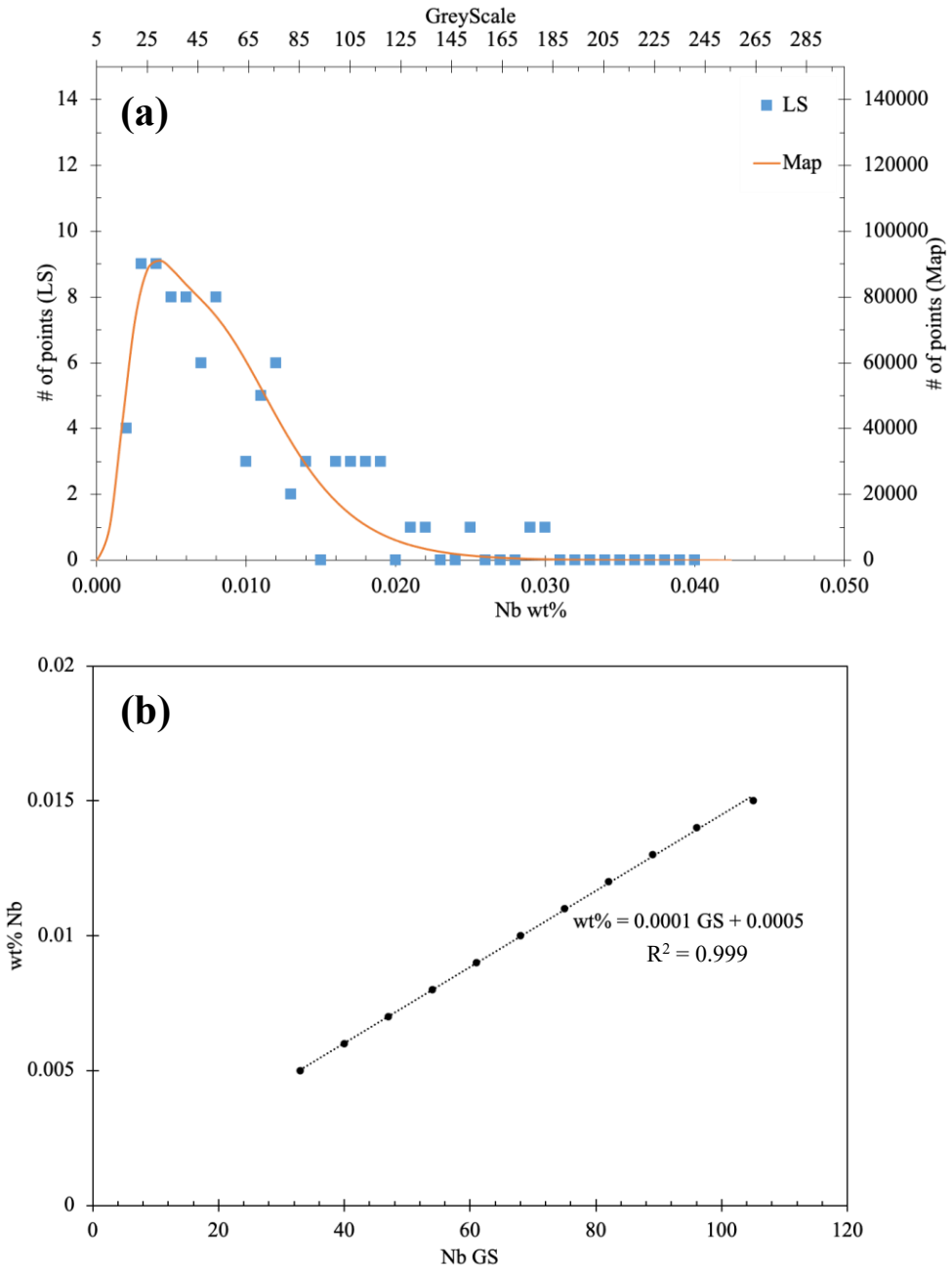


**Figure 3.28 (a)** Nb line scan distribution plotted against its greyscale distribution in sample 4081 **(b)** Linear relationship between wt% and greyscale Nb in sample 4081

3.5.6 Sample 4068

Figure 3.29 (a) shows the Nb line scan distribution with the lognormal greyscale distribution in sample 4068. The peaks of the distributions are at a greyscale value of 30 (0.006 wt% Nb), and the distributions are a good fit, with outliers at greyscales 35, 40, and 65. Figure 3.29 (b) presents the conversion between greyscale and wt% Nb, which yields: wt% Nb = 0.0002 × GS + 0.0004.

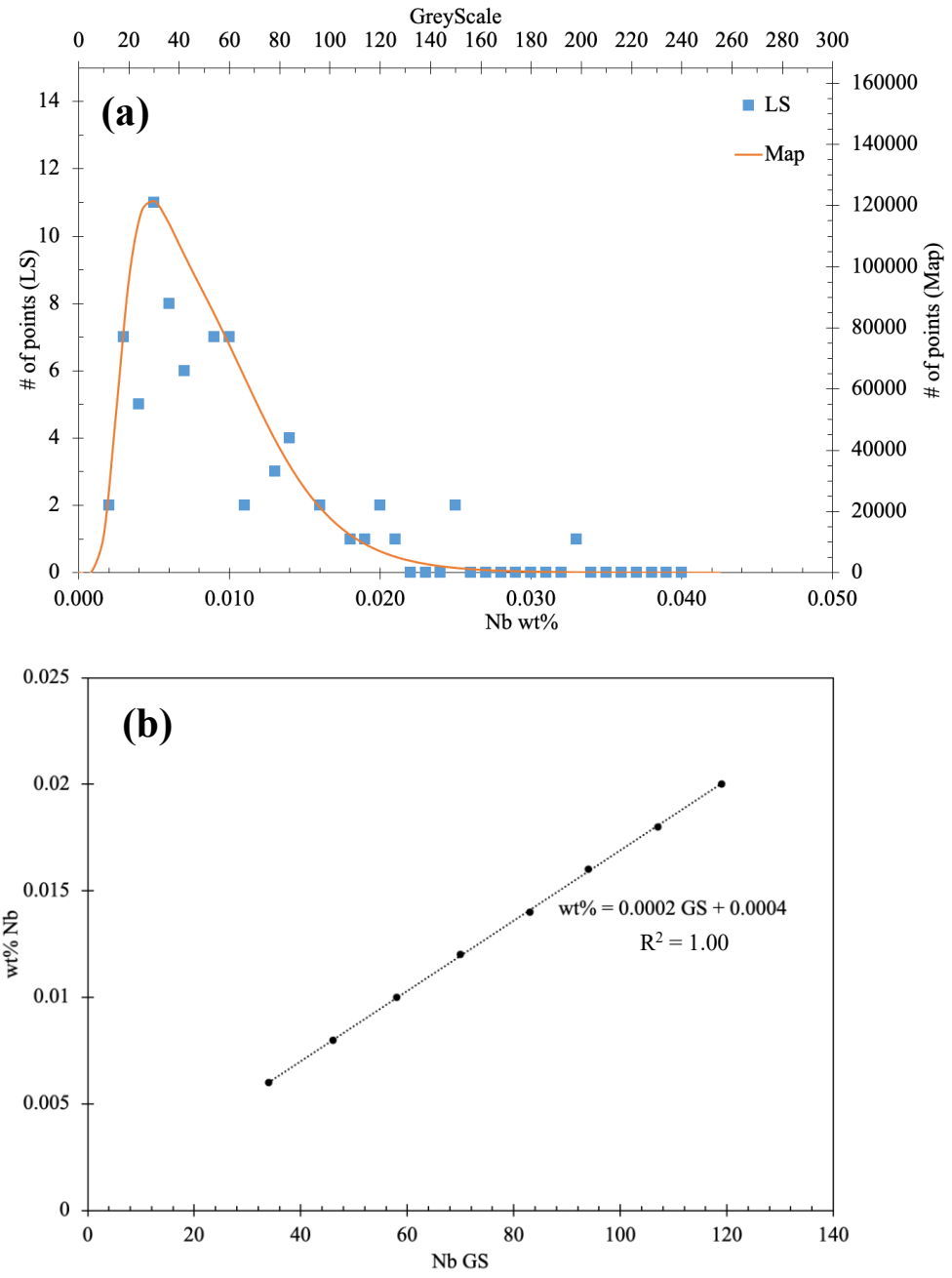


**Figure 3.29 (a)** Nb line scan distribution plotted against its greyscale distribution in sample 4068 **(b)** Linear relationship between wt% and greyscale Nb in sample 4068

### 3.5.7 Sample 4093

The Nb in sample 4093 undergoes problems similar to the Ca and S when it comes to the distribution. Since the Nb composition in sample 4093 is relatively lower compared to all the other samples, a distribution was not made. There were not enough points that spread across a wide range of concentrations to be able to form a distribution. Therefore, this sample's Nb values will be approximated based on sample 4068, since it is the closest to sample 4093 in chemical composition.

## 3.6 Lognormal Distributions Summary

Tables 3.5 and 3.6 present the mean values and standard deviations for the Ti and Nb lognormal distributions, respectively.

**Table 3.5** Mean and standard deviation of Ti lognormal distributions

| Steel | 4280 | 4372 | 4175 | 4052 | 4081 | 4063 | 4093 |
|---|---|---|---|---|---|---|---|
| Mean | 13.5 | 8.41 | 9.24 | 7.31 | 7.46 | 8.56 | 6.31 |
| Standard deviation | 2.96 | 2.13 | 2.25 | 2.03 | 2.03 | 2.38 | 1.79 |

**Table 3.6** Mean and standard deviation of Nb lognormal distributions

| Steel | 4280 | 4372 | 4175 | 4052 | 4081 | 4063 |
|---|---|---|---|---|---|---|
| Mean | 20.6 | 13.2 | 37.6 | 38.6 | 71.8 | 37.2 |
| Standard deviation | 11.7 | 7.37 | 14.4 | 24.0 | 26.3 | 18.2 |

# Chapter 4: Quantification and Characterization of Coarse TiN Precipitates Forming on CaS Inclusions

This chapter studies the effect of CaS on TiN precipitation. In Section 4.1, a precipitate count is performed to measure the number of these TiN-CaS precipitate complexes. Section 4.2 analyzes the spatial distribution of these precipitates. Section 4.3 presents SEM images along with EDX maps that show the morphology and confirm the chemical composition of these TiN-CaS conglomerates. The size of TiN precipitates was correlated with the presence or absence of CaS inclusions. Lastly, Section 4.4 discusses the formation of TiN-CaS.

## 4.1 Precipitate Count of Coarse TiN vs. TiN-CaS Precipitates

Using the Ti, Ca, and S EMPA maps alongside the EMPA precipitate analysis program discussed in Chapter 3, the number of TiN and TiN-CaS precipitates in all steels was obtained. The upper greyscale values for Ti were determined from the Ti lognormal distributions presented in Section 3.4. An example of the selected greyscale boundaries on the lognormal distribution of sample 4280 is shown in Figure 4.1.

The top 1% of precipitates were chosen for analysis in each steel. The 1% limit corresponds to a greyscale value of 33 in sample 4280. A list of coordinates was produced by the EMPA precipitate count program for Ti precipitates ranging in greyscale values from 30-250. Precipitates were then located in the SEM at the given coordinates. Precipitates were present at locations with greyscale values as low as 30. By considering the smallest precipitate found (0.5 μm), the concentration of Ti within that pixel was calculated to be 0.14 wt%. This corresponds to a greyscale value of 33 on the Ti distribution. Therefore, a 1% limit was used as a basis for analysis.

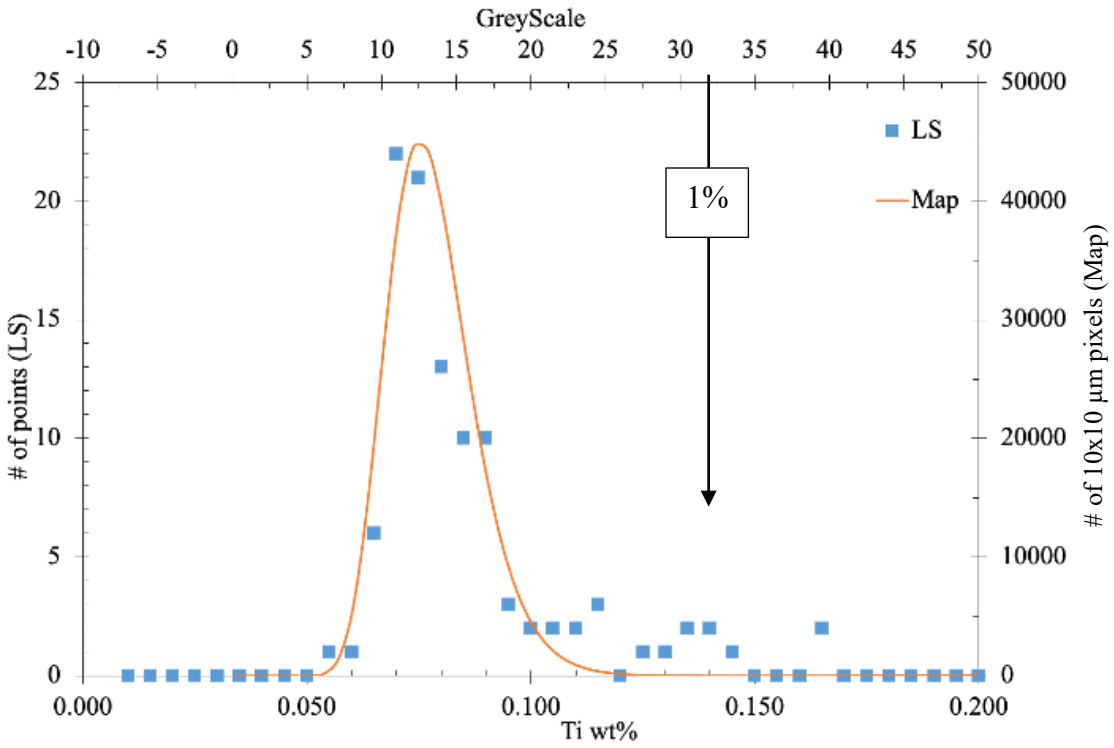


**Figure 4.1** Ti lognormal distributions for sample 4280 showing greyscale boundaries at 1%

Due to the very low concentrations of Ca and S, a greyscale value of 10 was assigned for both as it is the lowest number which can be entered into the program without incorporating areas that do not have any Ca and S.

Table 4.1 shows the precipitate counts for Ti and Ti-CaS at given greyscale values for all steels at the 1% cut off. With higher amounts of Ti present in the steels, more Ti is available to nucleate and grow on its own. Therefore, steels with higher Ti contents, such as 4280, 4372, and 4175, exhibit a larger amount of Ti precipitates that are not associated with CaS inclusions. Steels with lower Ti contents, such as 4081 and 4093, experience a smaller amount of Ti not associated to CaS inclusions. Thus, it is less likely for pure TiN to form in abundance as it does in steels with higher Ti contents.

The CaS count shows that most CaS inclusions in these steels tend to become nucleation sites for Ti precipitates to grow on. Regardless of the difference in Ti contents in the steels, the amount of Ti precipitating on CaS remains relatively similar (85-90%). Hence, the nucleation of TiN on CaS is unaffected by the Ti content. Sample 4068 is the only outlier in the data collected, having the

lowest amount of CaS associated to Ti relative to the total amount of CaS counted (69%). The steel's thickness and processing parameters are similar to those of the other low Ti samples (4081 and 4093). Other than the Ti content, the difference in chemical composition is a higher content of Mn and Al, which could be the reason behind the offset in the trend observed. Aluminum oxides and MnS are two inclusions that were not studied in this project but can also act as nucleation sites for Ti precipitates. One assumption made is that sample 4068 could have a higher amount of alumina and MnS than samples 4081 and 4093. Therefore, less Ti is being associated to the CaS inclusions as an increased amount is also nucleating on alumina and MnS inclusions. An SEM image of TiN precipitating on MnS in sample 4068 and its EDX maps are shown in Figures 4.2 and 4.3, respectively. For all the steels, most of the Ti precipitates growing on CaS inclusions exhibit the largest greyscale intensities and are the highest in concentration.

**Table 4.1** Ti precipitate count with and without CaS inclusions

| Sample | Nominal Ti wt% | Ti GS | Ti count | CaS count | Ti on CaS count | Ti on CaS/CaS |
|---|---|---|---|---|---|---|
| 4280 | 0.11 | 33 | 4744 | 130 | 118 | 91% |
| 4372 | 0.12 | 17 | 11585 | 967 | 875 | 90% |
| 4175 | 0.12 | 15 | 6195 | 404 | 362 | 90% |
| 4052 | 0.096 | 13 | 8310 | 1109 | 949 | 86% |
| 4081 | 0.077 | 13 | 4642 | 638 | 550 | 86% |
| 4068 | 0.063 | 14 | 7895 | 930 | 640 | 69% |
| 4093 | 0.047 | 11 | 5889 | 933 | 793 | 85% |

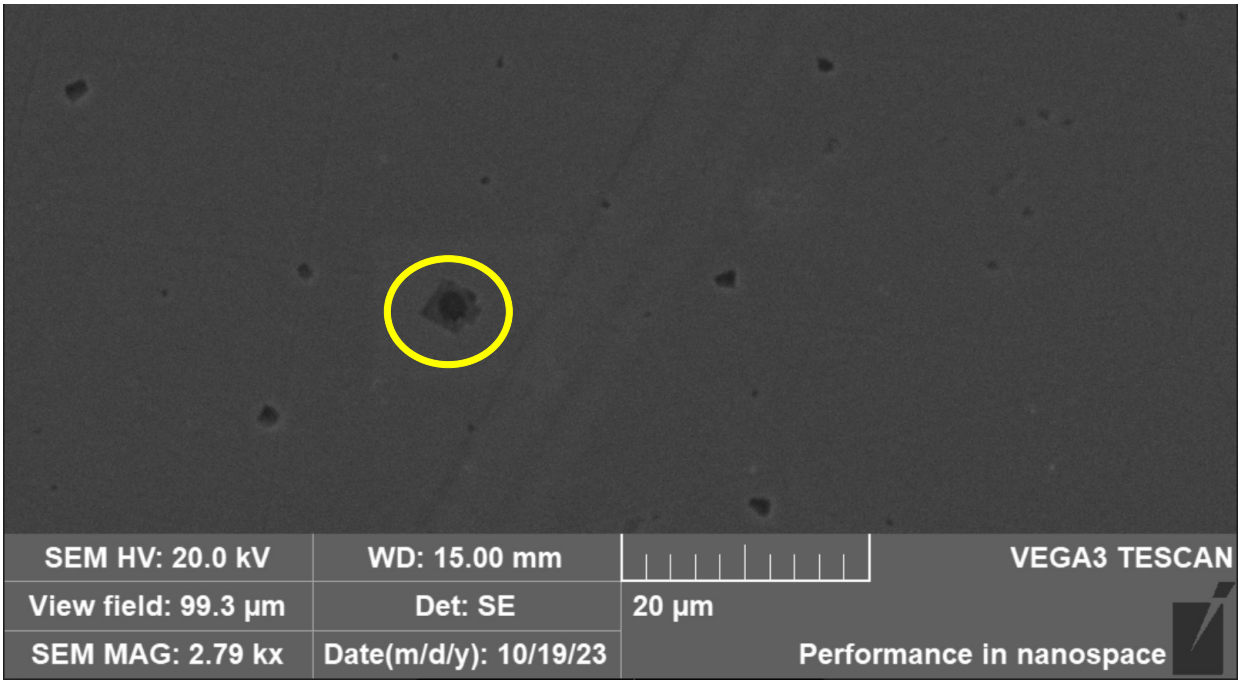


**Figure 4.2** SEM image of TiN on MnS in sample 4068

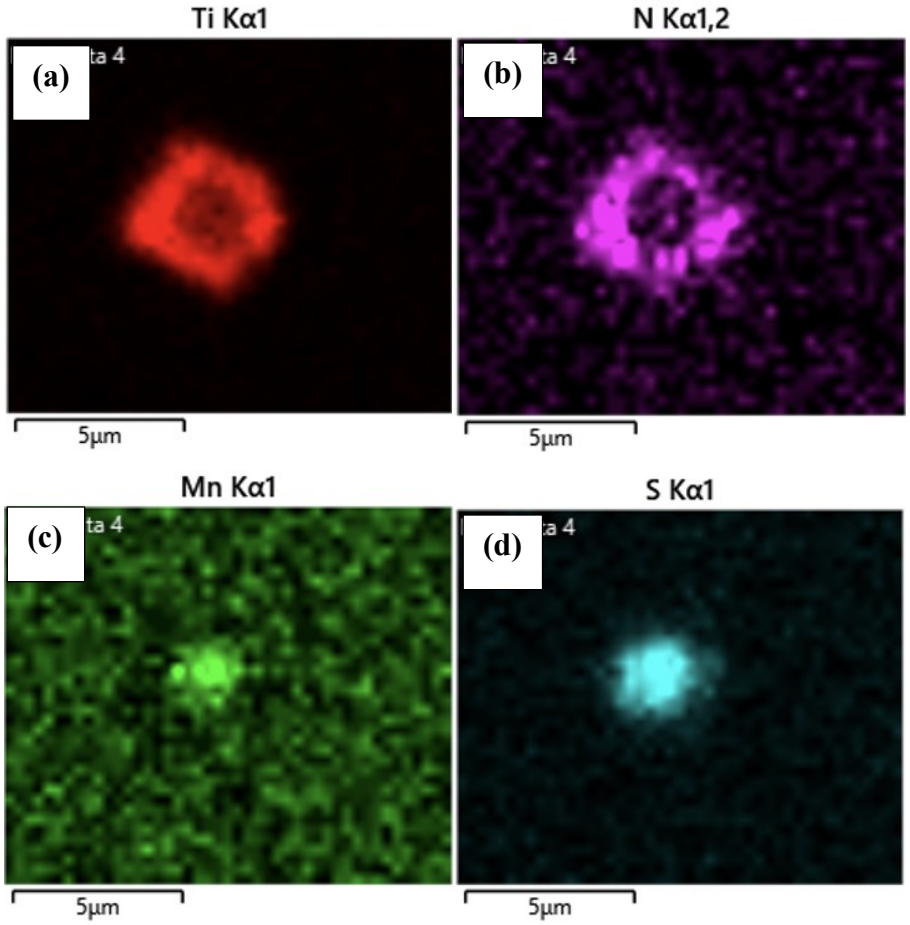


**Figure 4.3** EDX maps of TiN on MnS in sample 4068 showing **(a)** Ti, **(b)** N, **(c)** Mn, and **(d)** S

## 4.2 Through Thickness Precipitate Count of TiN-CaS Precipitates

The EMPA precipitate analysis program was used to analyze the abundance of TiN-CaS precipitates throughout the thickness of the steels, and a precipitate count at the four different quarter sections of each steel was produced. Figure 4.4 shows the locations at which the counts obtained for the 1% boundary exist. Most of the steels experience an increase in precipitate count at the area covering the centrerline (CL) and quarterline thicknesses (QL). This could be due to the movement of precipitates in the interdendritic liquid towards the center during solidification. However, the steels experience a larger presence of precipitates at one of the QL-CL areas than the other. This suggests the possibility of having the steels tilted towards one side during processing, causing the precipitates to move in the liquid towards one side. In some cases, like in samples 4052, 4068, and 4093, the surfaces of the steels contain more of these TiN-CaS precipitates. Since CaS usually encapsulates alumina, it is not unusual to find more of these nonmetallic inclusions around the surfaces. Aluminum acts as a deoxidizer in steel and forms alumina; therefore, most alumina is expected to be found at the top and bottom surfaces [19]. This results in the increased number of TiN-CaS precipitates at the sample surfaces and subsurfaces.

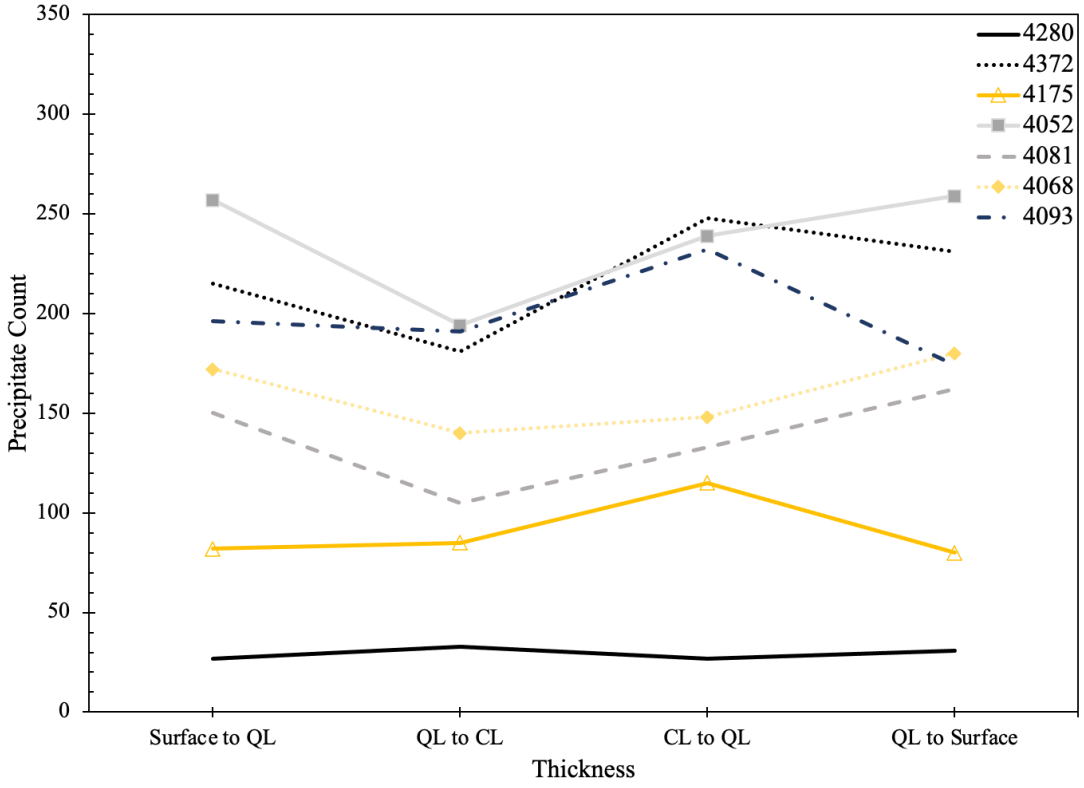


**Figure 4.4** Through thickness precipitate count of TiN-CaS at 1% boundary for all samples

## 4.3 SEM/EDX Characterization of Coarse TiN and TiN-CaS Precipitates

To confirm the findings from EMPA, SEM/EDX were used to locate some of the precipitates being counted. Coordinates produced by the EMPA precipitate analysis program were located physically on the samples through SEM. The composition of select precipitates was then validated by EDX elemental mapping. The sizes of the precipitates studied were also measured using the SEM.

### 4.3.1 SEM/EDX imaging of CaS, TiN, and TiN-CaS

Figure 4.5 shows a CaS and TiN in sample 4052. The boxed feature is a CaS inclusion. It is approximately 7 µm in size and has a spherical morphology. Similar properties were observed for CaS inclusions found in other samples. The circled rectangular feature is a TiN, approximately 4 µm in size. The lines going through the sample are scratches formed unrelated to any of the precipitates. The other smaller semi-round features are pits present on the sample surface and are assumed to not be linked to any precipitates since EDX performed on them showed no traces of Ti or Nb.

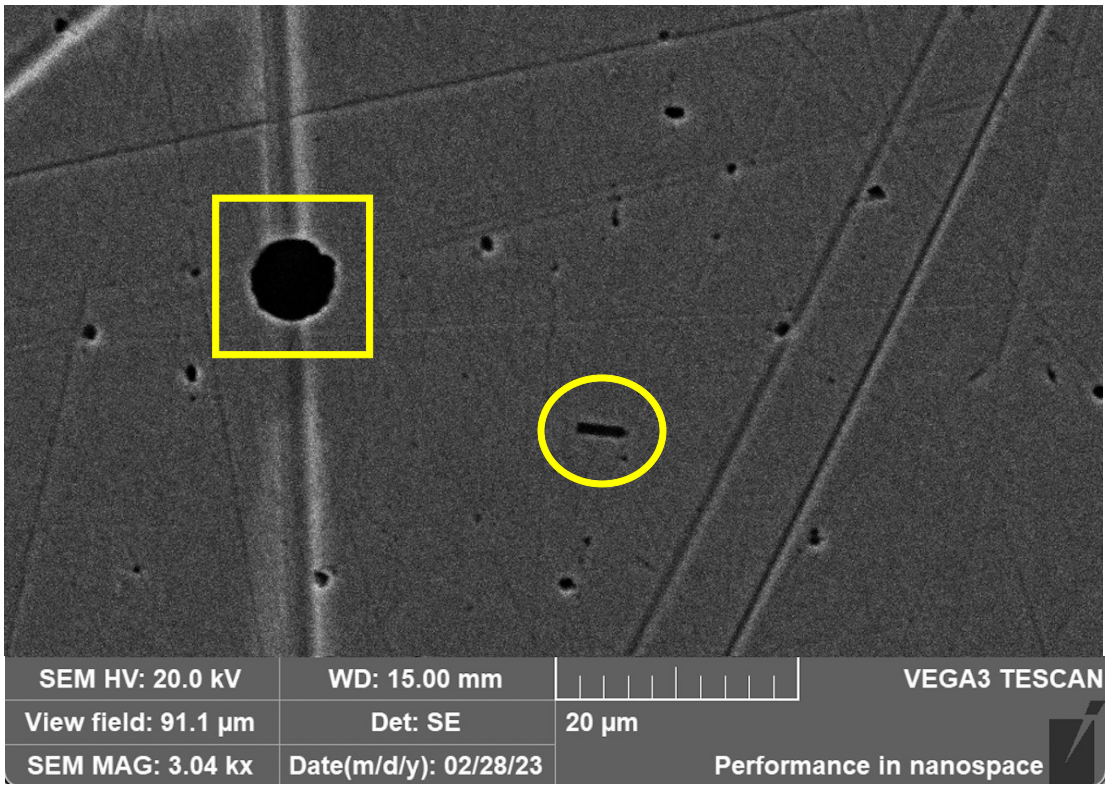


**Figure 4.5** SEM image of a CaS inclusion and TiN in sample 4052

For the precipitates captured in Figure 4.5, EDX maps were obtained. Figure 4.6 (a), (b), and (c) shows the EDX maps for the CaS inclusion observed, which detected Ca, S, and Al, respectively. Towards the center of the inclusion, Al is more abundant in comparison to the Ca and S. This is expected since CaS encapsulate alumina in the steel [41].

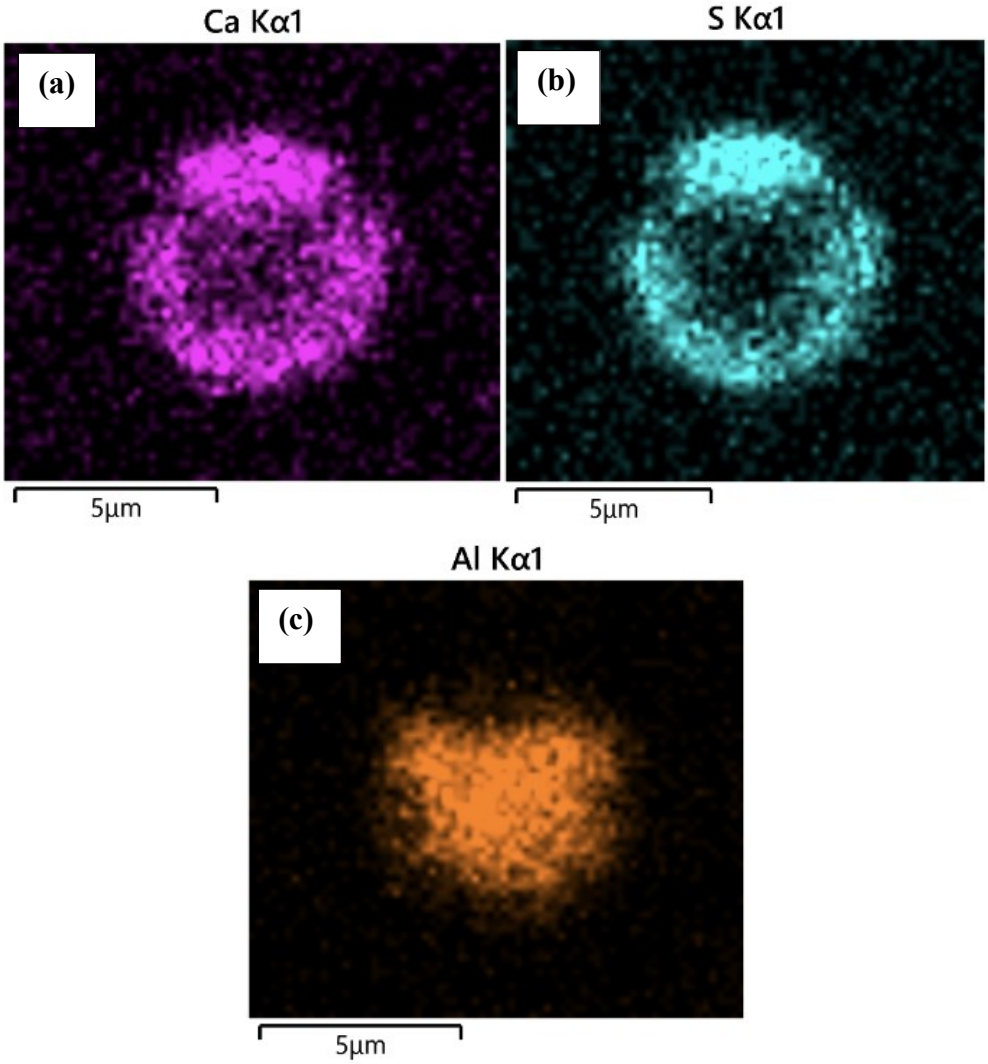


**Figure 4.6** EDX maps for CaS inclusion in sample 4052 showing **(a)** Ca, **(b)** S, and **(c)** Al

Figure 4.7 shows the EDX maps for the TiN observed in Figure 4.5. TiN tends to be cuboidal in shape, however this one appears to be more rectangular. In the EDX maps, a high concentration of (a) Ti and (b) N was found on the precipitate, which validates its identity.

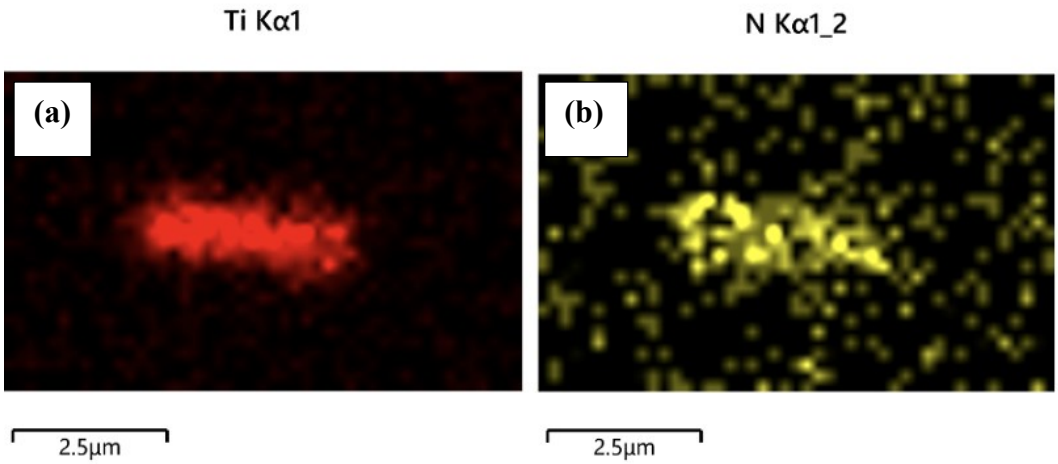


**Figure 4.7** EDX maps for TiN precipitate in sample 4052 showing **(a)** Ti and **(b)** N

Figure 4.8 is an SEM image of a CaS inclusion with TiN precipitating on it (circled) from sample 4280. It is approximately 4 µm in size, with a more irregular/semi-cuboidal shape. This TiN-CaS was one of the precipitates on the list of coordinates produced by the EMPA precipitate analysis program for Ti at a greyscale level greater than 240. This confirms that most of the Ti precipitates with the highest greyscale intensities tend to be linked to CaS inclusions.

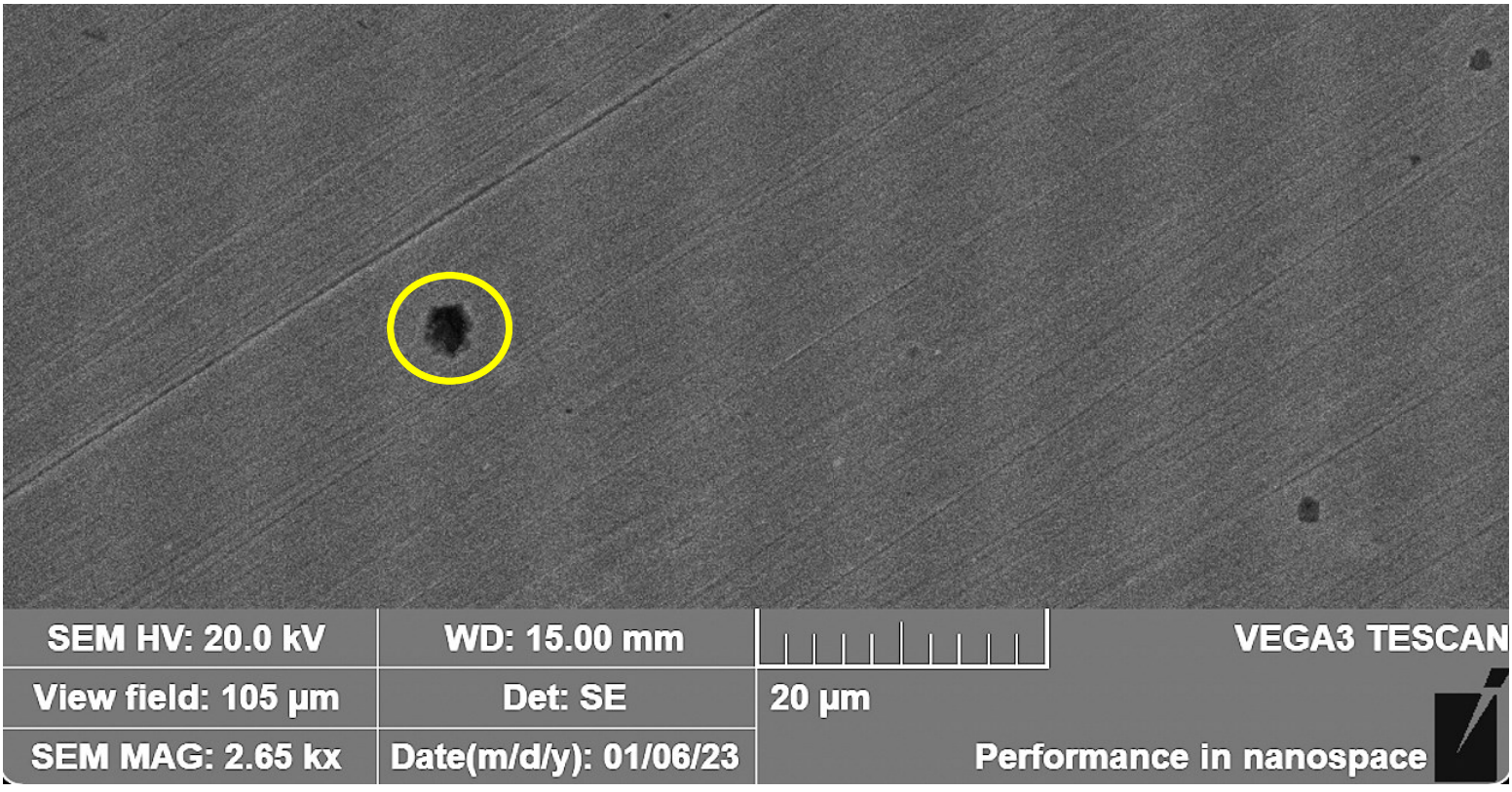


**Figure 4.8** SEM image of a TiN-CaS precipitate in sample 4280

The EDX maps in Figure 4.9 show (a) Ti, (b) Ca, (c) S, and (d) Al. In the center of the precipitate Ca, S, and Al are spherical and higher in concentration. Surrounding them, a cuboidal trace of Ti can be seen.

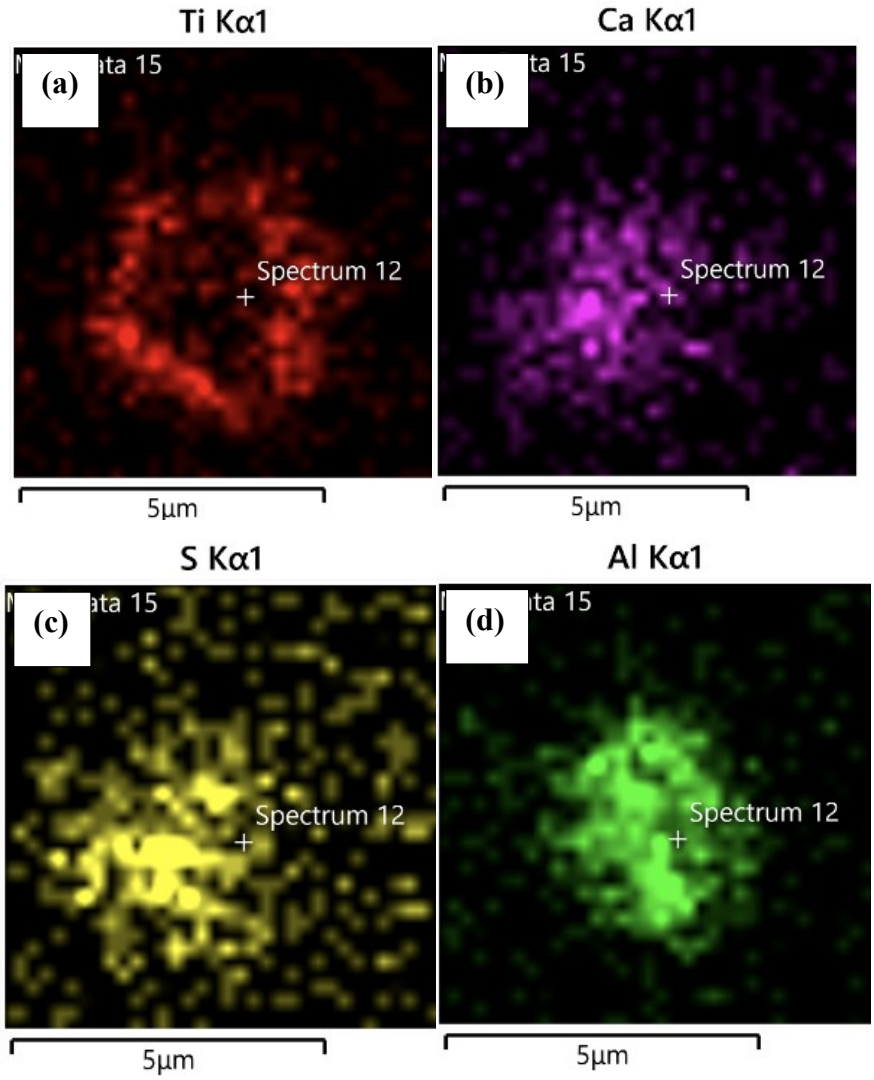


**Figure 4.9** EDX maps for TiN-CaS precipitate in sample 4280 showing **(a)** Ti, **(b)** Ca, **(c)** S, and **(d)** Al

4.3.2 SEM imaging of clustering TiN and TiN-CaS precipitates

In Chapter 3, clustering was observed on the Ti EMPA map. To validate what was seen on the map, SEM images were captured showing the clustering of TiN and TiN-CaS precipitates. Precipitate clustering can be detrimental to the steel as it causes clustered areas to have stress concentrations, therefore impacting the mechanical properties of the steel. Figure 4.10 presents an SEM image captured in secondary electron mode, with eight circled TiN precipitates at the quarter thickness of sample 4052 clustered in the vicinity of each other.

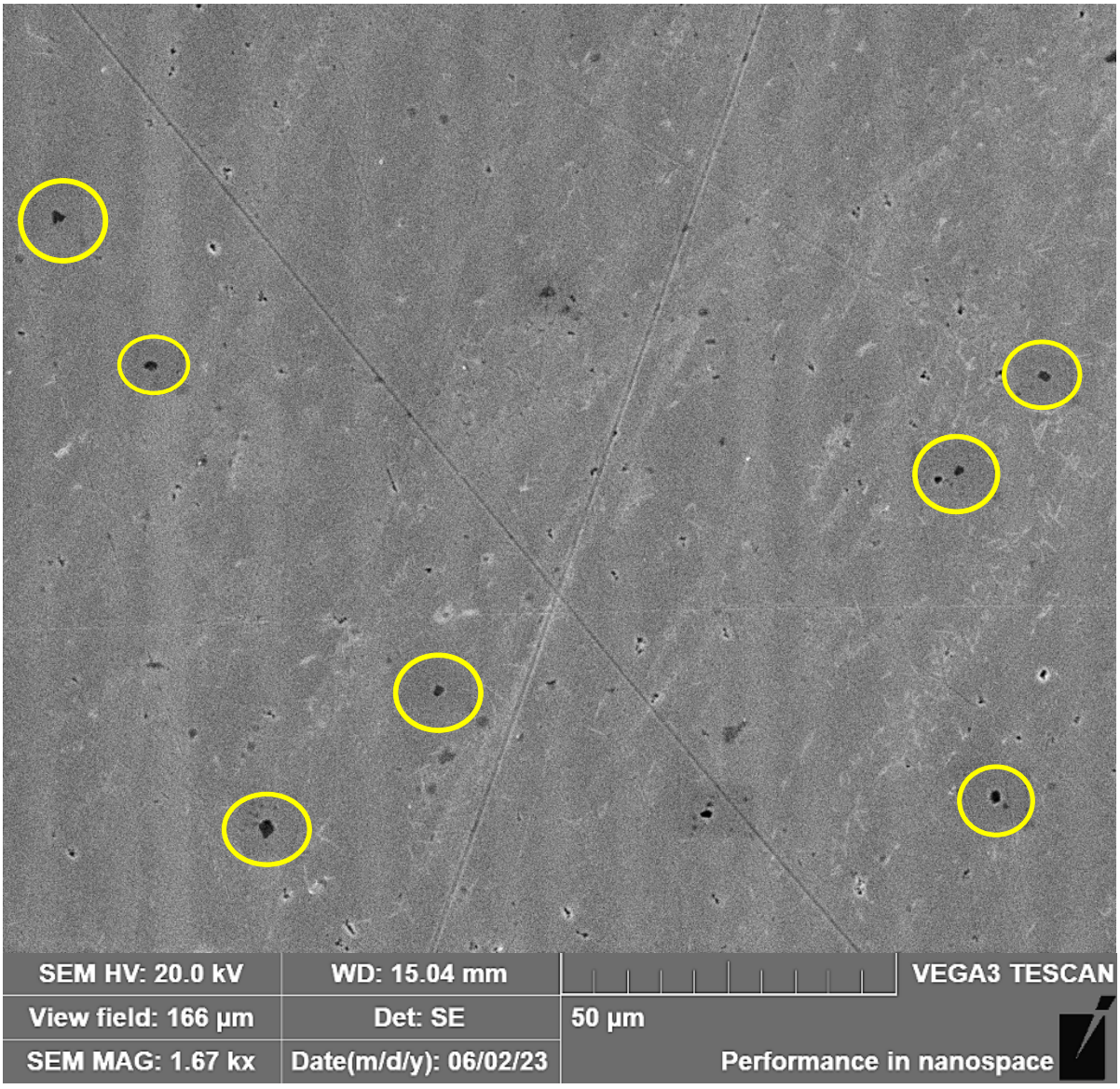


**Figure 4.10** SEM image showing clustering of eight TiN precipitates at the quarter thickness in sample 4052

Clustering was also observed for TiN-CaS. Figure 4.11 shows an SEM image of clustering of TiN-CaS precipitates in sample 4280. In the image, there are three circled TiN-CaS precipitates, and one boxed TiN, all precipitated around each other.

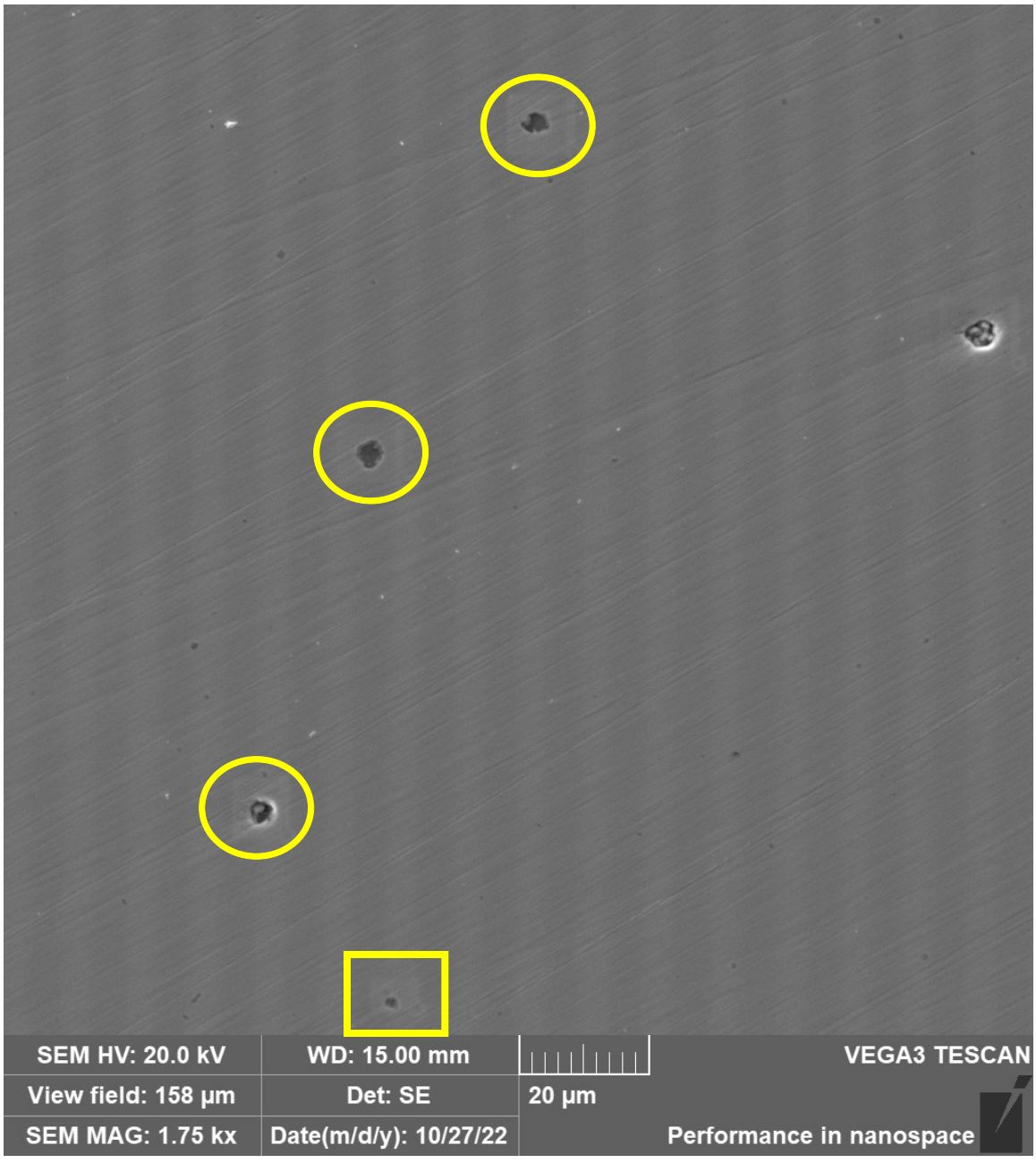


**Figure 4.11** SEM image showing clustering of three TiN-CaS and one TiN at the quarter thickness in sample 4280

4.3.3 Size analysis of TiN-CaS precipitates via SEM/EDX images

The sizes of Ti precipitates at random positions at the quarter thickness of the steels were measured for Ti precipitates that grow on CaS inclusions and for coarse TiN-rich precipitates not associated to any nonmetallic inclusions. Both size distributions were obtained for precipitates existing in the same area on the steel. Sample 4280 was used for the following size distributions.

Figure 4.12 presents the size distributions for Ti precipitates not linked to inclusions and Ti precipitates on inclusions. For the same area on the steel, 100 Ti precipitates not associated with any inclusions and 50 Ti precipitates associated with CaS were captured. All precipitates were captured and measured through SEM imaging. Their constituents were confirmed via EDX. Ti precipitates that did not grow on CaS are a mix of TiN and (Ti,Nb)N. Ti precipitates that did grow on CaS are a mix of TiN-CaS and (Ti,Nb)N-CaS conglomerates.

The majority of the Ti precipitates that are not on inclusions are between 1 and 2.5 μm in size, whereas the majority of the TiN-CaS precipitate complexes are between 4 and 6 μm in size. Similar sizes for Ti precipitates growing on CaS inclusions were observed for the other samples studied.

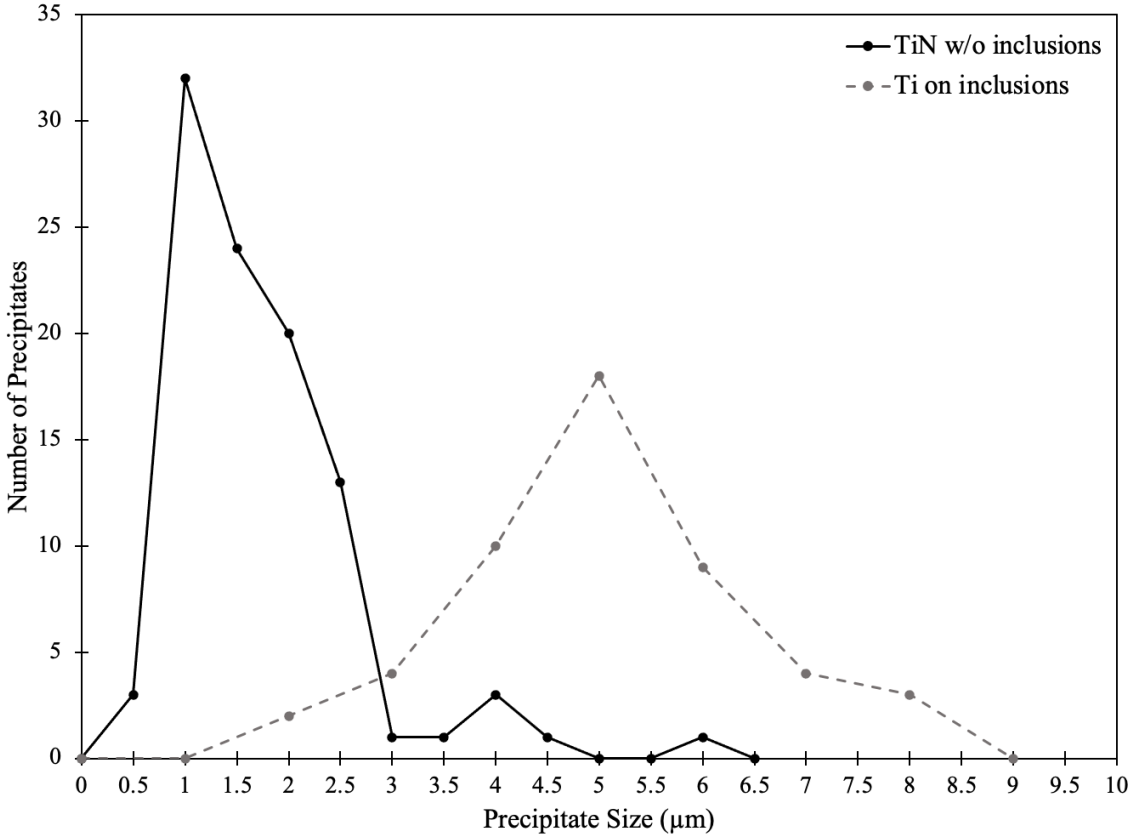


**Figure 4.12** Size distribution of coarse Ti precipitates not linked to inclusions in sample 4280

Comparing the two size distributions, approximately a 4 μm increase in size can be observed between the Ti precipitates not associated with inclusions and those growing on CaS inclusions. Therefore, it can be concluded that when TiN precipitates on nonmetallic inclusions, such as CaS, it can have an impact on the size of the TiN in the samples due to its formation at higher temperatures. Details behind why that happens are discussed further in the following section.

## 4.4 Discussion on the Formation of TiN-CaS Precipitates

From the EMPA counts of TiN and CaS, the relationship between the number of CaS inclusions and the number of TiN precipitating on CaS for all the steels was plotted in Figure 4.13. The relationship shows an increasing trend, where a higher number of CaS present in the steel results in a greater number of TiN nucleating on CaS inclusions. It also shows an almost 1:1 correlation between TiN-CaS and CaS, indicating that almost every CaS inclusion became a nucleation site for the TiN in the steels. However, EMPA counts are considered to be lower bound numbers as the sample surfaces have pits that could be Ti precipitates that were removed during the grinding steps of sample preparation.

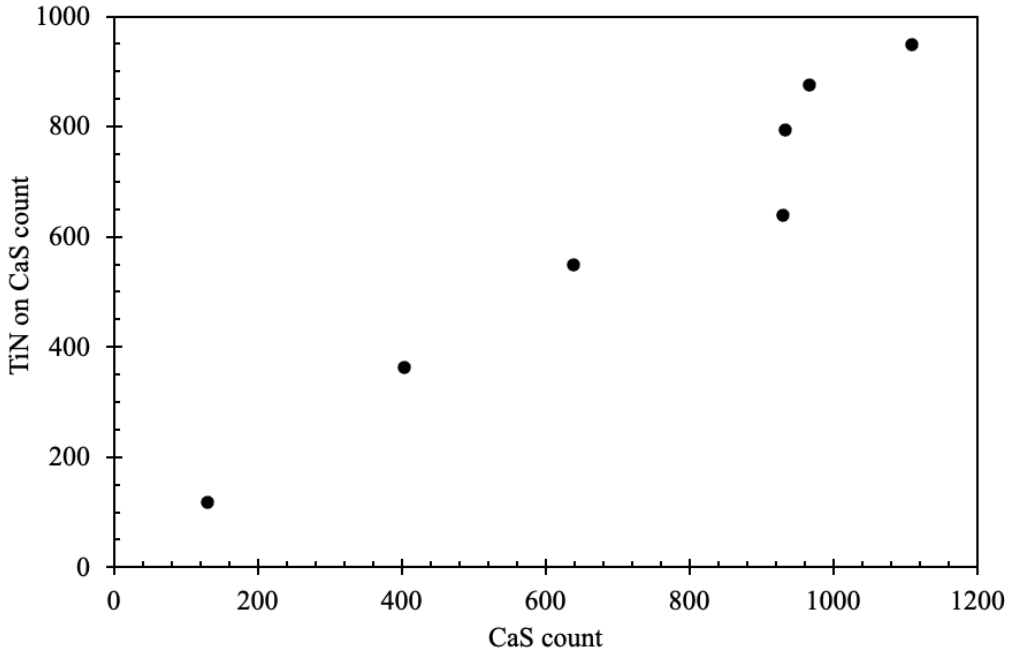


**Figure 4.13** Relationship between CaS inclusions and TiN-CaS precipitates

Nucleation and growth are driven by both thermodynamics and kinetics; however, in the case of TiN precipitating on CaS, the process appears to be more kinetically driven. From the EMPA counts, the precipitation of TiN on CaS had no dependence on the Ti, N, Ca, or S compositions. To further investigate this idea, the volume fractions of CaS in the steels were calculated using Thermocalc and compared to the different chemical compositions in the steels. There was no clear relationship between the Ti, N, Ca, or S chemical compositions in the steels and the calculated volume fractions. Plots of the comparisons made from Thermocalc can be found in Appendix E.

CaS is a nonmetallic inclusion that forms in the liquid of steels at higher temperatures during solidification [19]. Initially, alumina reacts with dissolved calcium to form a calcium oxide and alumina binary system [40]. Sulfur tends to encapsulate brittle oxides like alumina. Sulfur then reacts with the calcium to form a CaS on top of oxide inclusions [40]. This CaS is the first to form out of the precipitate conglomerates observed in this study, since the TiN is found precipitating around the CaS.

The homogeneous nucleation of TiN can be defined by Equation 7:

$$\Delta G = (a_{TiN})^3 \Delta G_v + 6(a_{TiN})^2 \gamma_{TiN/L} \quad (7)$$

However, TiN precipitates heterogeneously on CaS. Therefore, the heterogeneous nucleation of TiN on CaS in the liquid is defined by Equation 8:

$$\Delta G = [(a_{TiN})^3 - \frac{4}{3}\pi(r_{CaS})^3]\Delta G_v + 6(a_{TiN})^2 \gamma_{TiN/L} + 4\pi(r_{CaS})^2(\gamma_{TiN/CaS} - \gamma_{CaS/L}) \quad (8)$$

Where $a_{TiN}$ is the side measurement of a cuboidal TiN; $r_{CaS}$ is the radius of a spherical CaS; $\Delta G_v$ is the volume free energy; and $\gamma_{TiN/L}$, $\gamma_{CaS/L}$, and $\gamma_{TiN/CaS}$ are the interfacial surface energies of the TiN/liquid, CaS/liquid, and TiN/CaS interfaces, respectively. Comparing the homogeneous nucleation of TiN in Equation 7 to the heterogenous nucleation of TiN on CaS in Equation 8, $\Delta G$ is lowered due to the TiN/CaS interface. Thus, when TiN nucleates in the liquid, CaS becomes a favorable nucleation site as it minimizes the interfacial surface energy and lowers the volume free energy.

The difference in size between TiN and TiN that nucleated on CaS inclusions can be due to multiple reasons. Since CaS inclusions are relatively large, TiN that nucleate on CaS tend to be

larger in size than TiN that nucleate on their own. Also, TiN that does not nucleate on CaS tends to form at lower temperatures than the TiN forming on CaS, which causes it to be smaller in size than the TiN on CaS. Another reason is due to the mechanism behind precipitate coarsening. During coarsening, the concentration of Ti in the matrix will decrease until smaller precipitates can no longer nucleate, so the smallest precipitates will go back into solution to allow larger precipitates to grow [30]. This is known as Ostwald ripening, which is a mechanism based on the Gibbs-Thomson effect. The driving force for precipitate coarsening is the reduction in surface energy. Larger particles have a smaller surface area to volume ratio than smaller particles; therefore, they tend to be more stable and get bigger during coarsening while smaller particles shrink. Smaller precipitates have higher solute concentrations in the adjacent matrix phase than larger precipitates. This creates a concentration gradient, where the solute (Ti) travels from the smaller precipitate to the larger precipitate. Thus, during coarsening, Ti from smaller TiN diffuses to the larger TiN that nucleated on CaS, and larger precipitates are formed.

In samples with higher Nb contents, Nb precipitates with TiN as a (Ti,Nb)N precipitate near the end of solidification. In some cases, the (Ti,Nb)N forms on CaS inclusions as observed on SEM/EDX. (Ti,Nb)N will be studied and discussed further in Chapter 5.

## 4.5 Summary

The relationship between TiN and CaS was studied where precipitate counts, spatial distributions, and size distributions were performed. From the precipitate count, a relatively small amount of the total Ti precipitates was associated with CaS inclusions. As for the CaS, most of it became nucleation sites at which Ti precipitated and grew on. The trend shows an increased amount of Ti not associated with CaS as Ti contents increase, and that the nucleation of TiN on CaS is unaffected by the Ti contents. The Ti precipitates that grew on CaS inclusions exhibited the highest greyscale intensities.

The locations and spatial distributions of the TiN-CaS precipitates showed that the highest amounts were present at the quarter thickness and the surface. Precipitates formed in the interdendritic regions that travel towards the center of the steels during solidification are the cause for higher values observed at the quarter thickness. A tilt in the steels during processing could be the reason for some of the differences observed at the two quarter thicknesses. As for the TiN observed at the

surface, that is due to CaS that grows on the alumina from steel deoxidization. Therefore, some abundance is observed on the sample surfaces and subsurfaces. Clustering was observed for coarse TiN precipitates in the samples, and SEM was used to capture and show the clustering of TiN and TiN-CaS.

A size distribution was created for the TiN precipitates that are on CaS inclusions and the ones that are not on any inclusions. The majority of the ones that nucleated on CaS were 5 μm in size, whereas the majority of the ones nucleating on their own were 1 μm in size. An approximate 4 μm increase in size was observed for Ti precipitates linked to CaS. The increase in size is due to precipitation kinetics. To minimize surface energy, Ti favours nucleation on CaS, which are relatively large in size. During growth, smaller Ti precipitates will dissolve back into solution in order for larger precipitates, like TiN-CaS to grow and coarsen.

# Chapter 5: Quantification and Characterization of Coarse TiN and (Ti,Nb)N

This chapter will quantify the size and number of coarse (Ti,Nb)N precipitates present in the steels. In Section 5.1, SEM/EDX analysis of the morphology and chemical compositions of TiN and (Ti,Nb)N are summarized. In Section 5.2, the sizes of select TiN and (Ti,Nb)N were measured. Section 5.3 quantifies the number of Nb on Ti-rich precipitates using EMPA. Section 5.4 shows the spatial distribution of the quantified precipitates. Section 5.5 presents the Thermocalc analysis of (Ti,Nb)N formation.

## 5.1 SEM/EDX Characterization of Coarse TiN and (Ti,Nb)N

Select precipitates of either TiN or (Ti,Nb)N (located by the EMPA program) were examined by SEM/EDX to determine approximate sizes and chemical compositions.

### 5.1.1 SEM/EDX imaging of pure TiN precipitates

Figure 5.1 is an SEM image of a TiN precipitate (circled) at the quarter thickness of sample 4052. The precipitate is cuboidal in shape and is ≈ 4 μm in size. Figure 2.5 (a) and (b) are EDX maps of Ti and N for the precipitate observed in Figure 5.1. The presence of Nb was not detected in this precipitate. Similar TiN precipitates were observed in the other steel samples. The dark features around the precipitate are pits on the sample surface and are assumed to not be linked to any Ti precipitates since EDX did not detect any Ti in them. In most cases, this type of TiN precipitate occurs in relative isolation (i.e. absence of clustering).

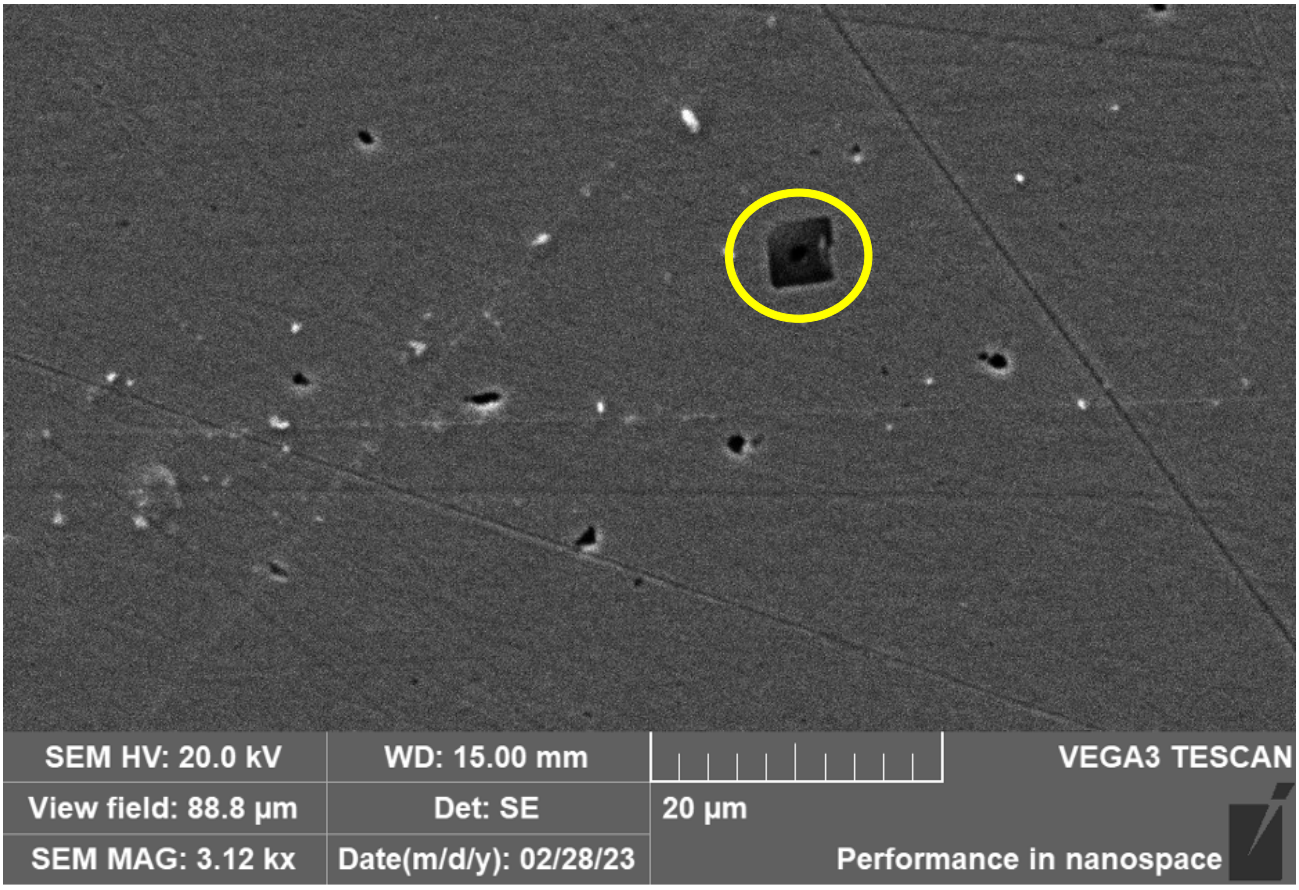


**Figure 5.1** SEM image of a cuboidal TiN at the quarter thickness in sample 4052

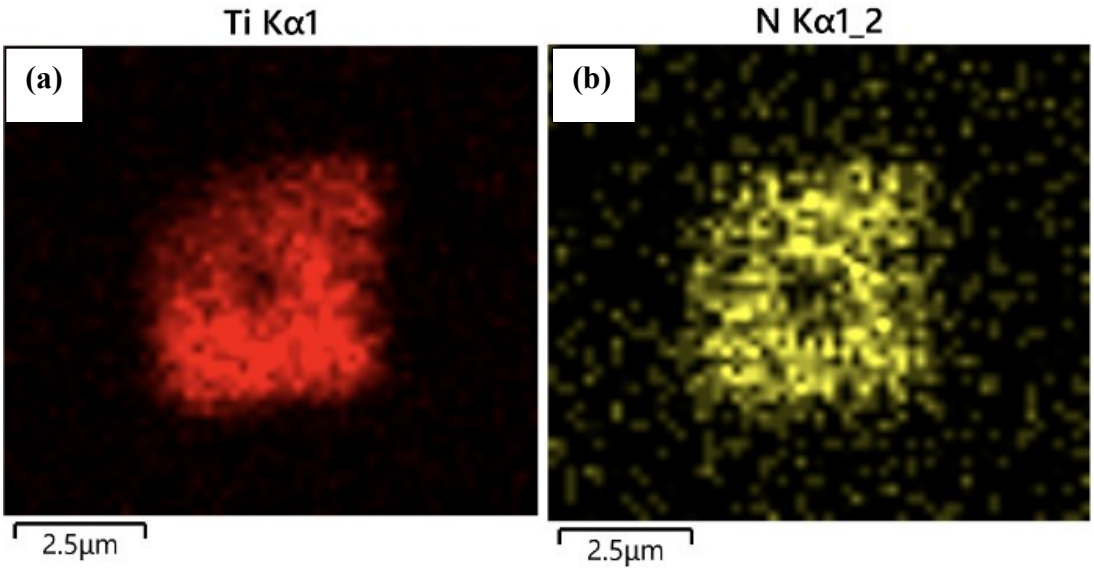


**Figure 5.2** EDX maps of TiN precipitate in sample 4052 showing **(a)** Ti and **(b)** N

### 5.1.2 SEM/EDX imaging of (Ti,Nb)N precipitates

In most instances, TiN is observed to be cuboidal in shape (Figure 5.1). However, when Nb precipitates on the TiN, smaller, irregularly shaped Ti/Nb-rich nitrides were observed. This change in the cuboidal morphology is due to the Nb precipitating on and around the TiN, which could happen during solidification and TMCP, as observed in high Nb content steels such as sample 4280. Figure 5.3 is an SEM image of a group of seven (Ti,Nb)N precipitates in sample 4280 at the quarter thickness. Unlike TiN, these precipitates are irregularly shaped, with most being semi-cuboidal and one triangular. They range in size from 1 – 2.5 μm. In general, the (Ti,Nb)N are typically observed in clusters. SEM analysis showed that (Ti,Nb)N precipitates are predominant in samples with higher Nb contents (4280 and 4372), which was confirmed by the EMPA precipitate count.

The EDX maps of Ti, N, and Nb for precipitate #1 (Figure 5.3) are shown in Figure 5.4 (a), (b), and (c). The Ti-rich region overlayed on the Nb map is smaller. This indicates that Nb is present in both, the precipitate and in the surrounding matrix. All the other circled precipitates (Figure 5.3) contained Ti, Nb, and N.

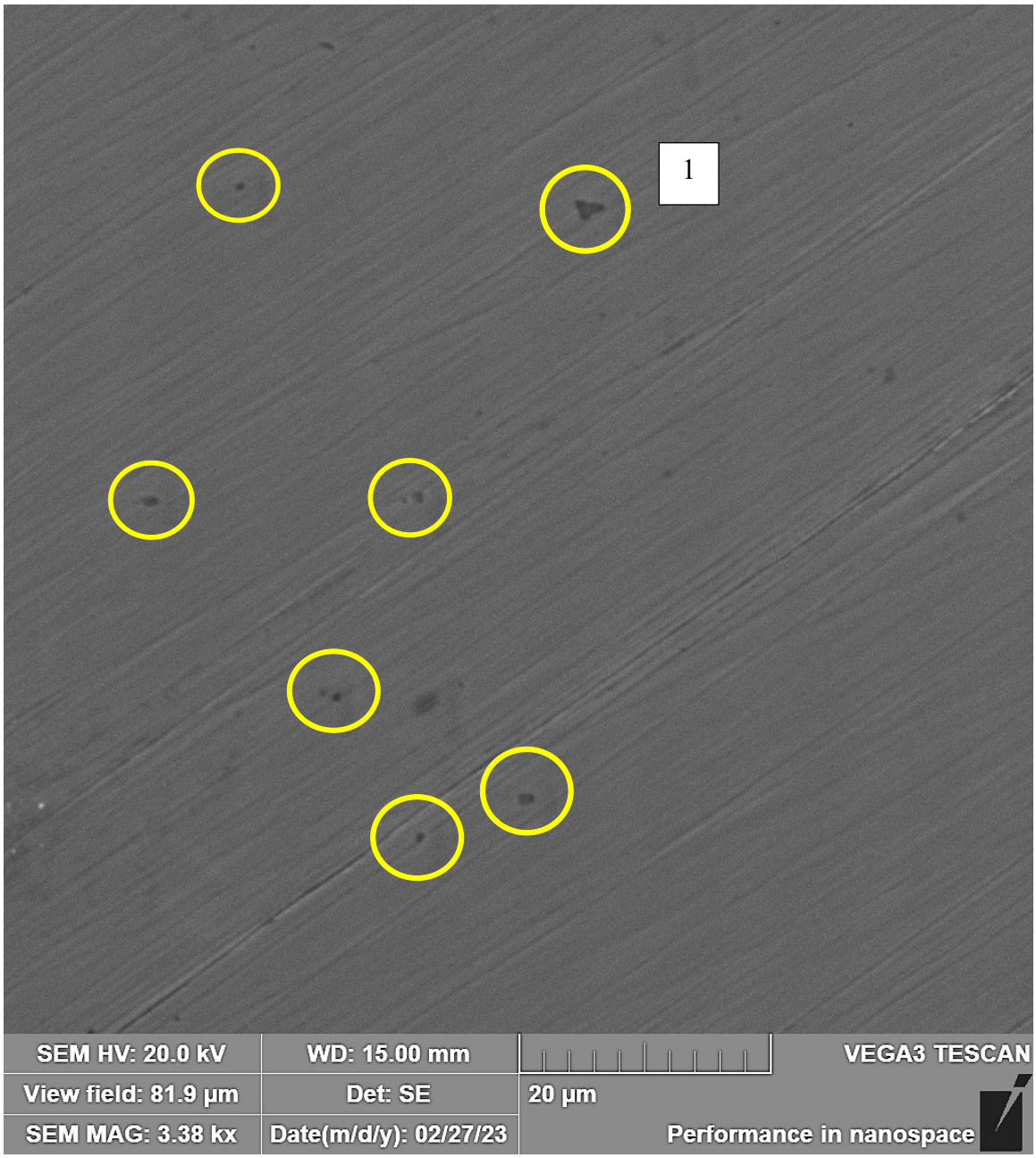


**Figure 5.3** SEM image of a seven clustered (Ti,Nb)N in sample 4280

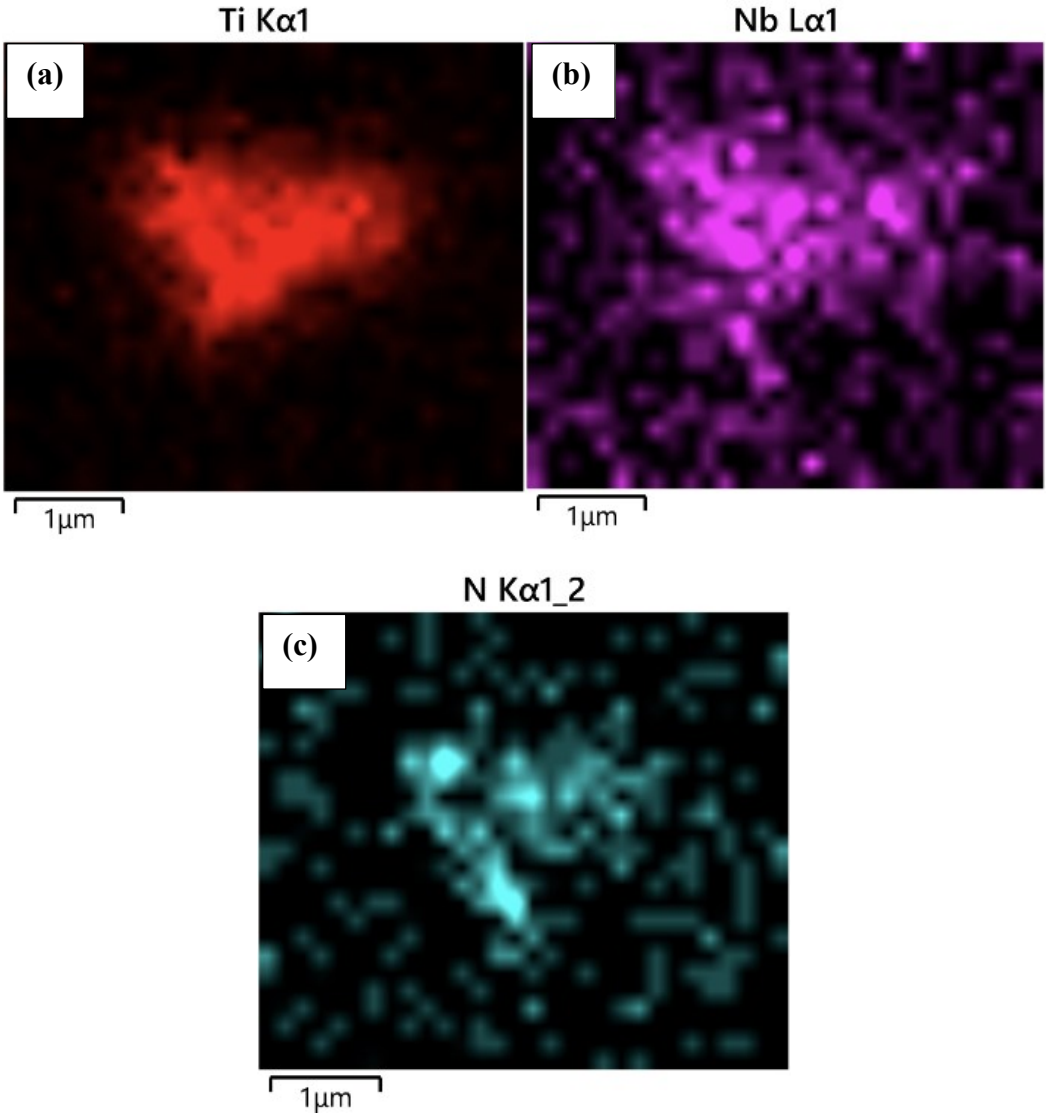


**Figure 5.4** EDX maps of (Ti,Nb)N precipitate in sample 4280 showing **(a)** Ti, **(b)** Nb, and **(c)** N

## 5.2 Size distributions of coarse Ti precipitates

The size of randomly selected Ti precipitates and the effect that Nb may have on them was studied. Ti precipitates from the quarter thicknesses of samples 4280, 4175, 4052, and 4093 were measured.

A frequency plot of the sizes measured via SEM was generated for every steel, and a lognormal or normal distribution was fitted. Figure 5.5 plots the measured and fitted size distribution data for sample 4280. Two lognormal distributions were fitted to the measured data. Lognormal distribution 1 (LN1) corresponds to the (Ti,Nb)N while lognormal distribution 2 (LN2)

corresponds to the TiN. The individual normal fits for the remaining samples can be found in Appendix F.

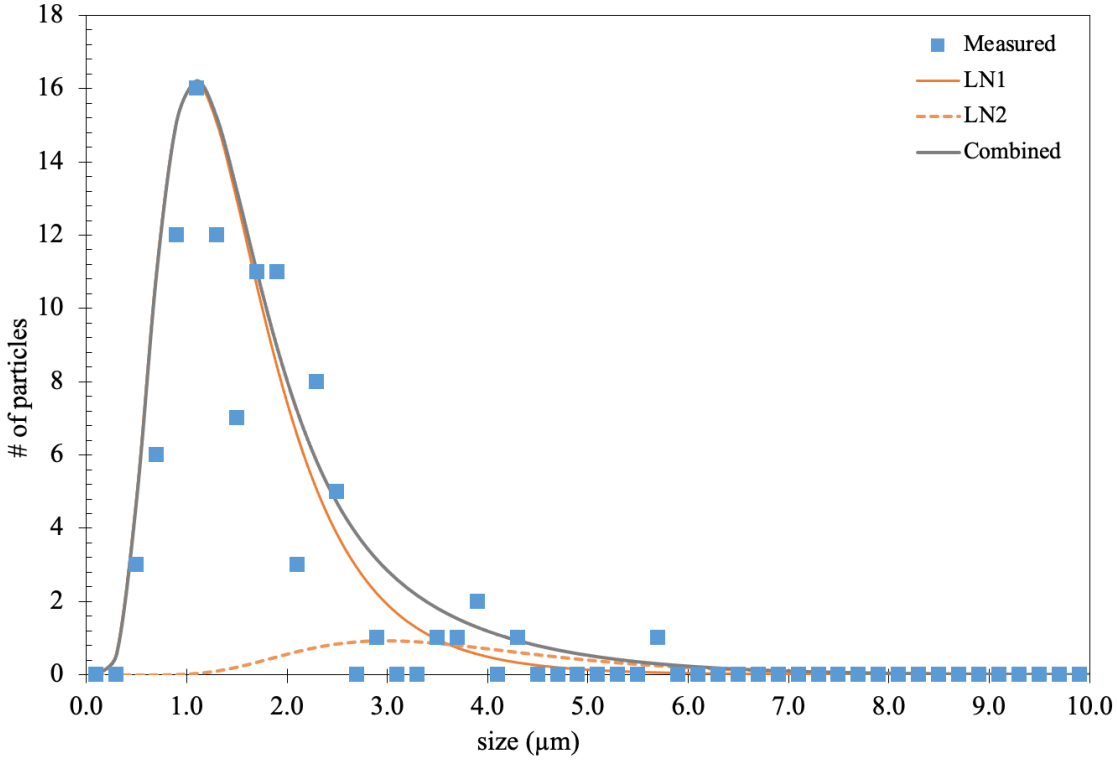


**Figure 5.5** Size distribution for Ti precipitates in sample 4280

Figure 5.6 compares the fitted size distributions of samples 4280, 4175, 4052, and 4093. All size distributions are based on precipitates captured from the same analysis area at the quarter thickness of each sample. The number of precipitates captured on each sample was 100, 91, 86, and 38, for samples 4280, 4175, 4052, and 4093, respectively.

The majority of the precipitates in sample 4280 exhibit the smallest Ti precipitate sizes amongst all samples (1.6 µm). The remaining samples, which have a lower Nb content, all exhibit similar size distributions with the majority of the precipitates being larger (2.7 – 3.8 µm). Ti precipitates captured from sample 4280 consist of both TiN and (Ti,Nb)N. Precipitates captured from samples 4175, 4052, and 4093 are all TiN. The distribution corresponding to the (Ti,Nb)N in sample 4280 exhibits smaller precipitate sizes. However, the distributions corresponding to the TiN in all the samples, including sample 4280, all fall within the same range of each other.

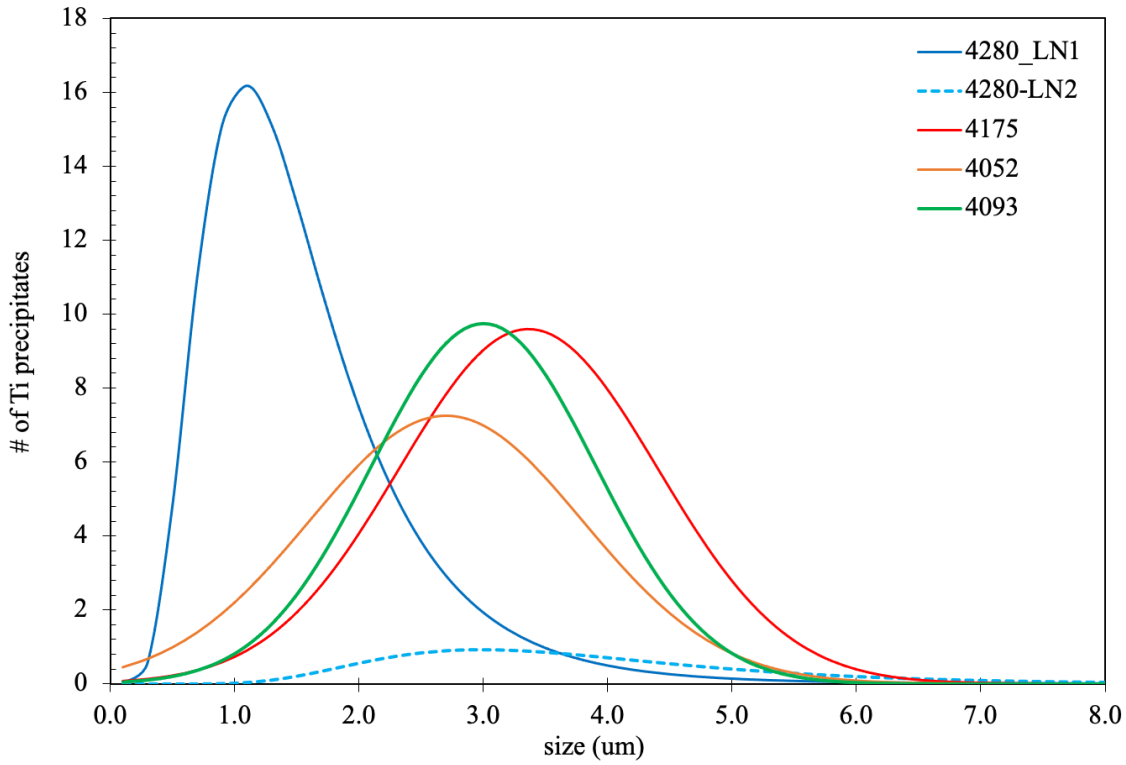


**Figure 5.6** Size distributions of coarse Ti precipitates in samples 4280, 4175, 4052, and 4093

Table 5.1 presents the distribution mean size and standard deviation from normal and lognormal analysis, along with the number of Ti precipitates measured in each sample. The mean sizes corresponding to TiN in all four steels (2.7 – 3.5 µm) are similar and indicate that the size of TiN is similar in all the steels. This shows a similar precipitation behaviour of the TiN during the production and processing stages of the steels for the Ti compositions being studied. The majority of the (Ti,Nb)N were smaller than TiN, with a mean size of 1.6 µm.

**Table 5.1** Summary of results for Ti size distributions of samples 4280, 4175, 4052, and 4093

| Sample | wt% Ti | wt% Nb | Mean size (µm) | Standard deviation | Total Ti precipitates | Ti precipitates with Nb |
|---|---|---|---|---|---|---|
| 4280 | 0.109 | 0.086 | 1.6, 3.5 | 0.6, 0.4 | 100 | 88 |
| 4175 | 0.118 | 0.025 | 3.4 | 1.0 | 91 | 0 |
| 4052 | 0.096 | 0.021 | 2.7 | 1.1 | 86 | 1 |
| 4093 | 0.047 | 0.015 | 3.0 | 0.9 | 38 | 0 |

A relationship can be made between the Nb composition and size of Ti precipitate. Samples with higher Nb contents (4280) are more likely to form (Ti,Nb)N, which tend to be smaller precipitates

as they form near the end of solidification (as will be shown with Thermocalc analysis in following sections). A study by Y. Tian et. al. showed that smaller (Ti,Nb)N precipitates are richer in Nb, which supports the findings in this section [53].

The formation of NbN, along with TMCP parameters, can affect the morphology of precipitates like TiN. TiN without NbN appeared to be more cuboidal in shape. NbN that forms on cuboidal TiN can make the precipitate shape more irregular and less cuboidal in most cases.

Figure 5.7 plots the number of (Ti,Nb)N and TiN precipitates per unit area (as counted from the SEM) as a function of [Ti][Nb]. The number of precipitates per unit area increases as the Ti and Nb contents increase. The biggest increase is observed between samples 4093 and 4052. This indicates that the composition of Ti is the dominant factor affecting the number of precipitates forming as the Ti content in sample 4093 (0.047 wt%) is half of that in sample 4052 (0.096 wt%). Samples 4280, 4175, and 4052 have relatively close Ti contents and therefore exhibit less of a difference.

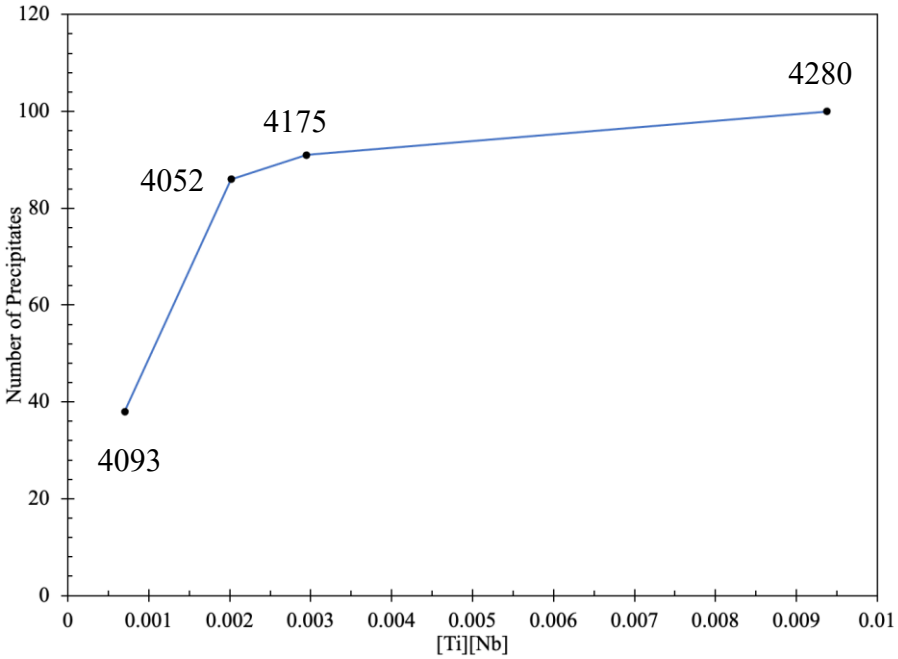


**Figure 5.7** Number of (Ti,Nb)N precipitates as a function of [Ti][Nb]

## 5.3 Quantification of (Ti,Nb)N Precipitates Using EMPA Precipitate Count

The number of (Ti,Nb)N precipitates present in the samples was quantified using EMPA mapping and analysis. The results were then validated with mass fractions obtained on Thermocalc.

5.3.1 EMPA precipitate counts

The EMPA precipitate evaluation methodology (described in Chapter 4) was utilized to quantify the number of either Ti or Nb rich pixels. Upper greyscale of 1% was used for both Ti and Nb distributions, as illustrated in Figure 5.8.

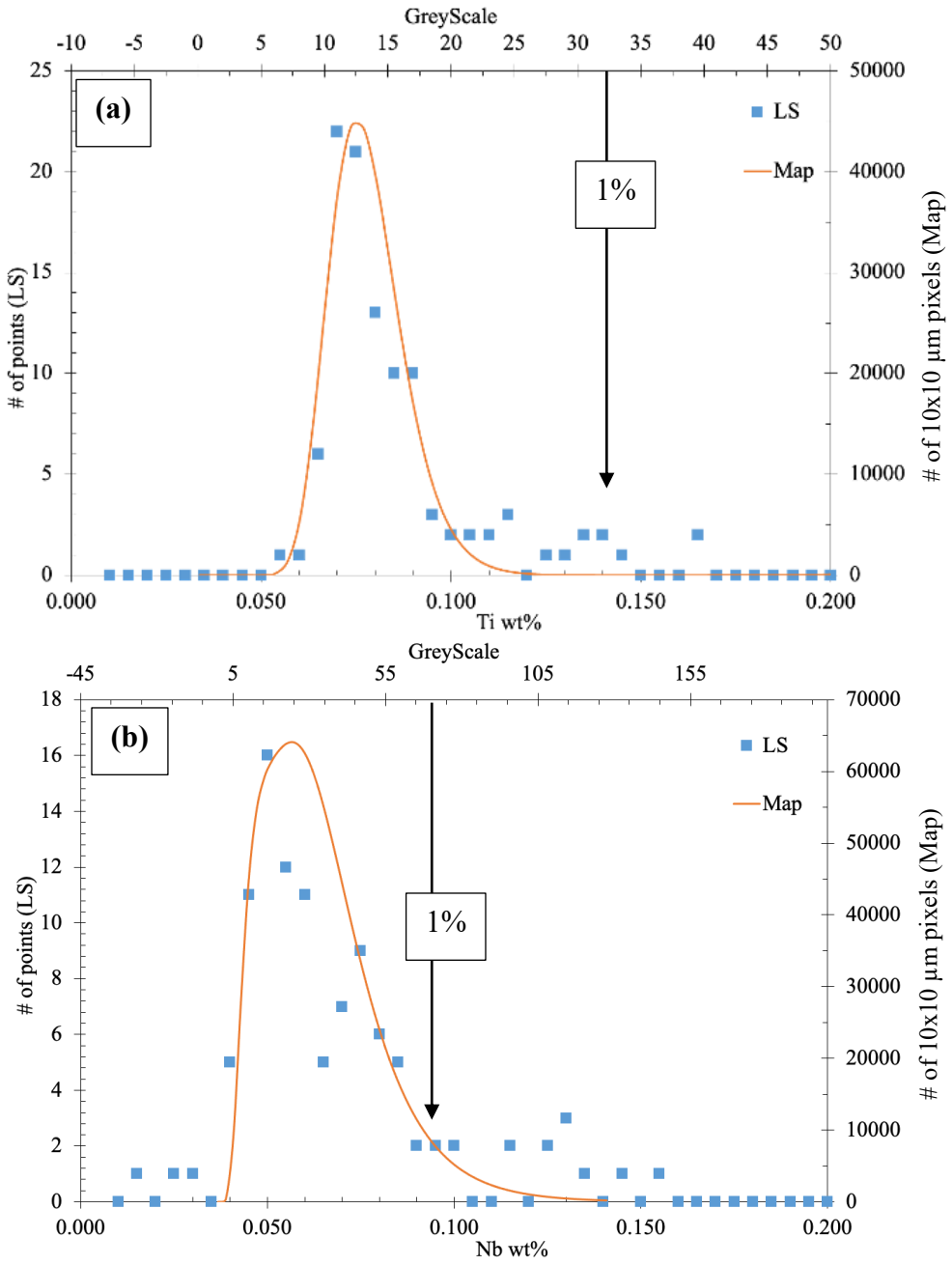


**Figure 5.8** 1% boundary on lognormal distributions for **(a)** Ti and **(b)** Nb in sample 4280

Table 5.2 tabulates the precipitate counts for TiN-rich precipitates that contain Nb at the given greyscale values. Since sample 4372 is larger in thickness than the other samples, sample data was normalized with respect to thickness to be able to compare the values between samples. For the non-normalized values of the total Ti counts in sample 4372, refer to the values in Table 4.1.

For samples 4280 and 4372, the fraction of Ti-rich pixels containing Nb is highest (>24%). Conversely, all the steels with low Nb contents exhibit < 2.4% of Nb at the Ti rich pixels. As the Nb content decreases, the amount of Nb forming on these Ti precipitates decreases.

**Table 5.2** Ti precipitate count with and without Nb for top 1% precipitates

| Sample | Nominal Ti wt% | Nominal Nb wt% | Ti GS | Nb GS | Total Ti count | Ti,Nb count | Ti,Nb fraction |
|---|---|---|---|---|---|---|---|
| 4280 | 0.109 | 0.086 | 33 | 70 | 4744 | 1155 | 24% |
| 4372 | 0.122 | 0.088 | 17 | 35 | 4456 | 1414 | 32% |
| 4175 | 0.118 | 0.025 | 15 | 140 | 6195 | 150 | 2.4% |
| 4052 | 0.096 | 0.021 | 13 | 140 | 8310 | 109 | 1.3% |
| 4081 | 0.077 | 0.021 | 13 | 140 | 4642 | 55 | 1.2% |
| 4068 | 0.063 | 0.021 | 14 | 150 | 7895 | 44 | 0.6% |
| 4093 | 0.047 | 0.015 | 11 | 150 | 5889 | 5 | 0.08% |

The precipitate count (Ti,Nb count from Table 5.2) was plotted against [Ti][Nb] for each sample in Figure 5.9. The trend shows that number of precipitates increases as the Ti and Nb content increases. This correlates with the trend observed from the precipitates counted for the SEM size distributions in the previous section.

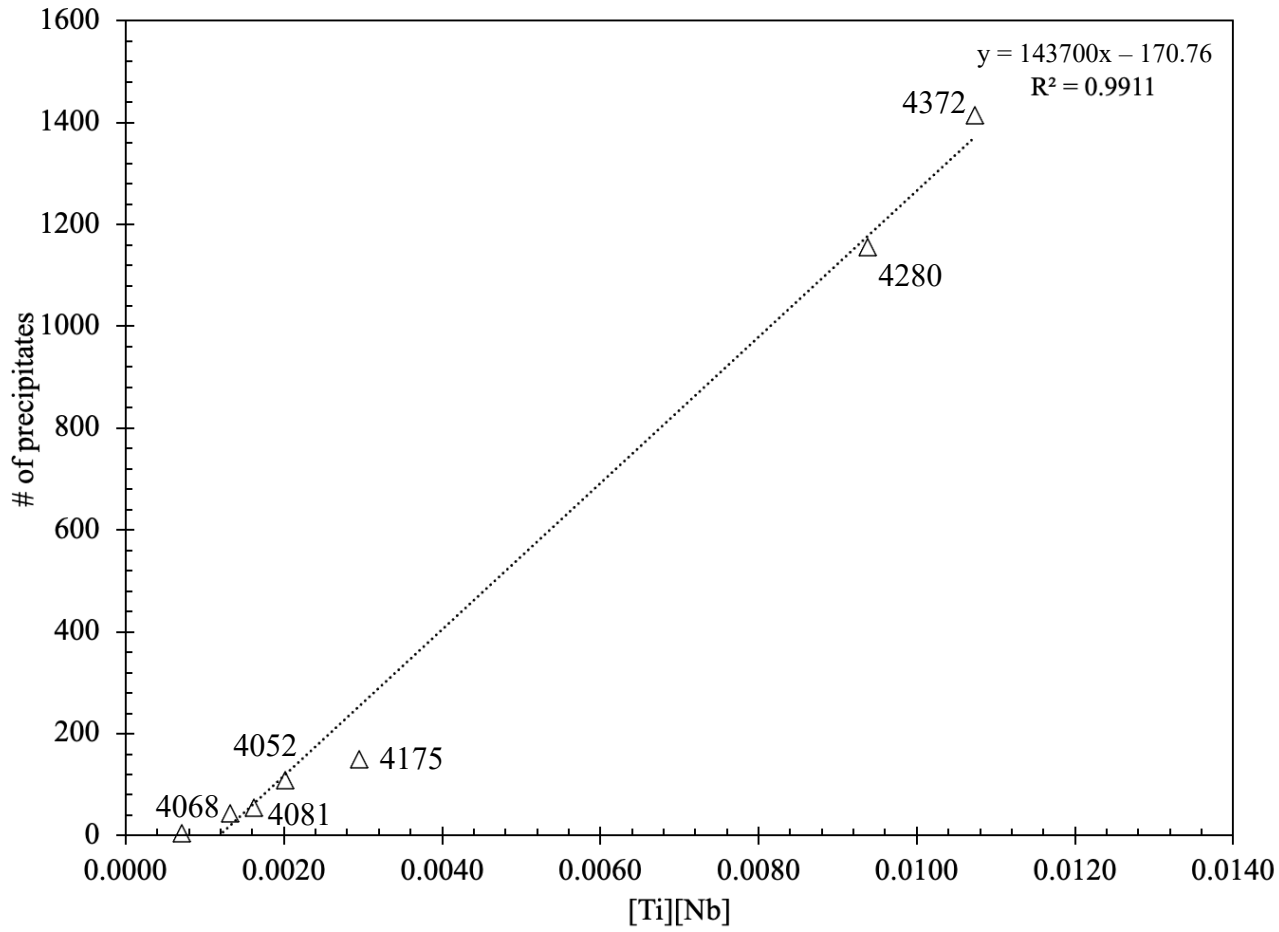


**Figure 5.9** Number of TiN precipitates containing Nb as a function of [Ti][Nb]

5.3.2 Thermocalc comparison

The mass fractions of the phase corresponding to the Ti/Nb precipitate at the end of solidification were determined using the database "TCFE10: Steels/Fe-Alloys v10.1" on Thermocalc v2022b. The full steel chemistries were used for this analysis, along with the same cooling rates and temperatures used during the production of the steels. Figure 5.10 shows (a) the mass fractions of (Ti,Nb)N calculated from the EMPA precipitate count and (b) the mass fractions of the Ti,Nb phase from Thermocalc, both plotted against the [Ti][Nb] compositions of the steels. The trend of the measured and calculated mass fractions corresponds well with the predicted values obtained from Thermocalc. In both cases, the highest amounts of Ti,Nb precipitates are recorded for samples 4372 and 4280, which are the highest in Ti and Nb content. Once the Nb content is largely decreased (starting at sample 4175), a gradual decrease in the amounts of Ti,Nb precipitates is observed.

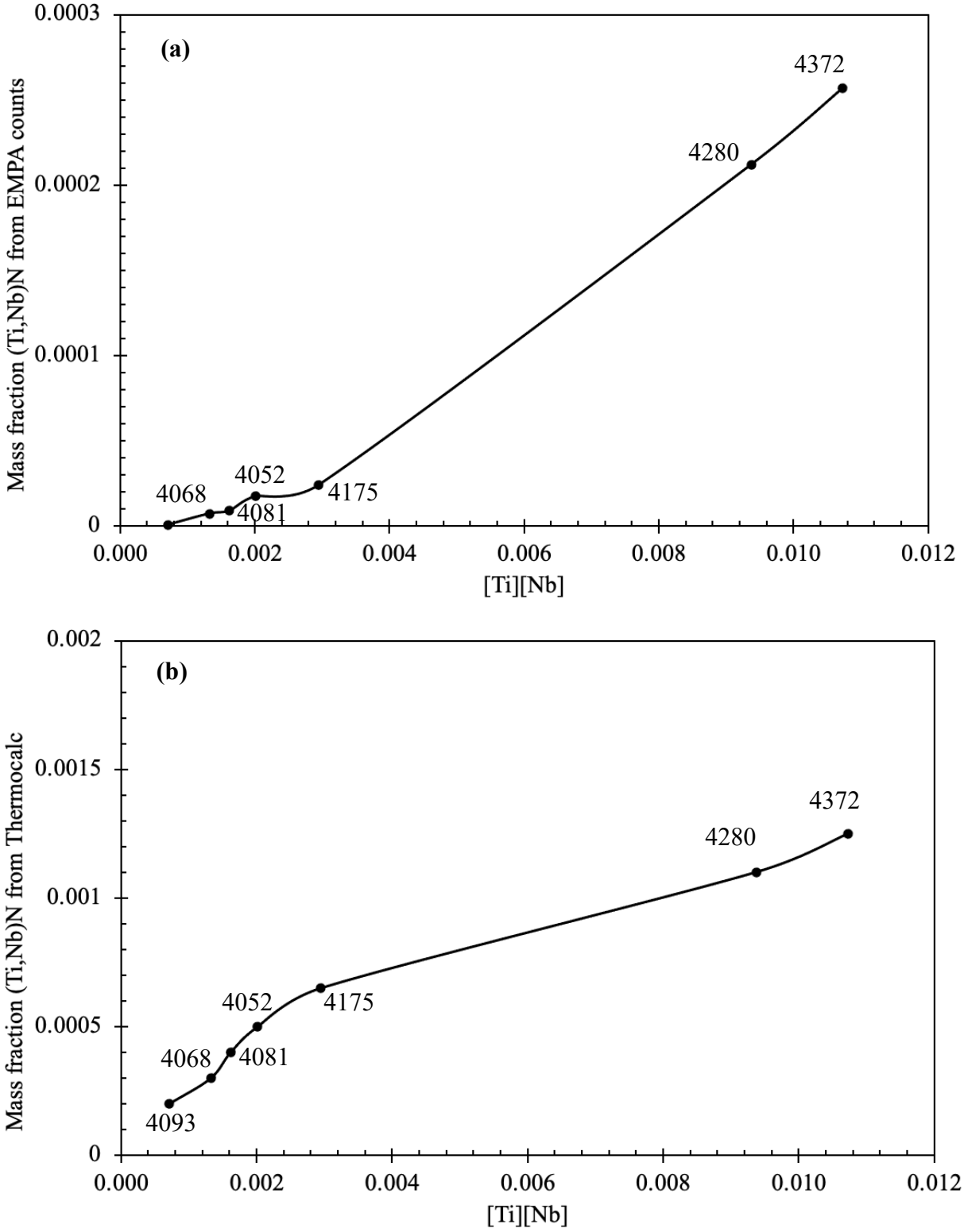


**Figure 5.10 (a)** Mass fractions of (Ti,Nb)N precipitates calculated from EMPA counts, **(b)** Thermocalc mass fractions of (Ti,Nb)N phase at 1300°C

## 5.4 Through Thickness Precipitate Count of Ti,Nb Precipitates

The EMPA precipitate analysis program was used to analyze the abundance of Ti,Nb precipitates throughout the thickness of the steels, and a precipitate count at the four different quarter sections of each steel was produced. Figure 5.11 shows the normalized precipitate counts across the thickness of the steels. The Ti,Nb counts were divided by the respective total Ti counts at every quarter for the normalization.

All steels exhibit the same trends, in that the number of precipitates is almost constant throughout the thickness. This is expected since the EMPA maps showed no signs of macrosegregation, and the line scans showed only limited Ti and Nb microsegregation.

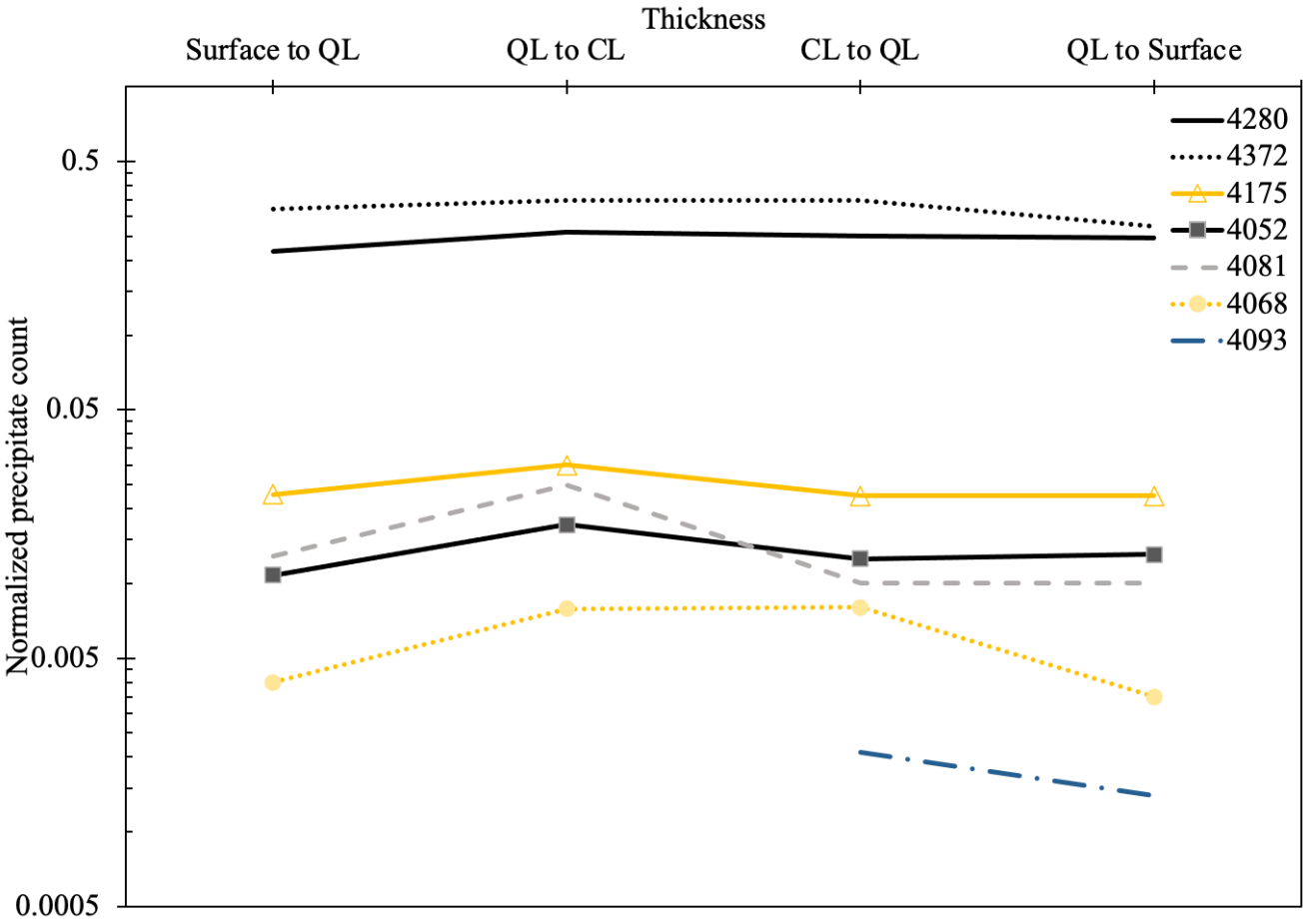


**Figure 5.11** Normalized through thickness precipitate count of (Ti,Nb)N for all steels

## 5.5 Discussion on TiN and (Ti,Nb)N formation

This section discusses the thermodynamics behind the formation of TiN and (Ti,Nb)N using Scheil solidification and single point equilibrium values obtained on Thermocalc. Scheil solidification is

a non-equilibrium simulation that estimates the solidification range of the steel by assuming infinitely fast diffusion rates in the liquid and no diffusion in the solid [55]. The TiN being studied forms in the liquid at the early stages of solidification, where diffusion would be relatively fast. Also, the cooling rates of the samples during solidification are similar to those used in Scheil. Therefore, for the extent of the analysis being done, Scheil solidification was deemed valid to use.

### 5.5.1 Thermocalc Scheil Solidification for TiN and (Ti,Nb)N

Figure 5.12 is a Scheil solidification plot for sample 4280. The phases BCC_A2 and FCC_A1#2 are delta ferrite and austenite, respectively. The phase FCC_A1 is a TiN-rich precipitate that forms around 1500°C and may precipitate with Nb depending on the composition of the steel. TiN begins forming at 1511ºC and 0.35 solid fraction. (Ti,Nb)N starts forming at 1465ºC near the end of solidification (0.88 solid fraction) due to enrichment of Nb during solidification. Solidification reaches its end at 1355ºC.

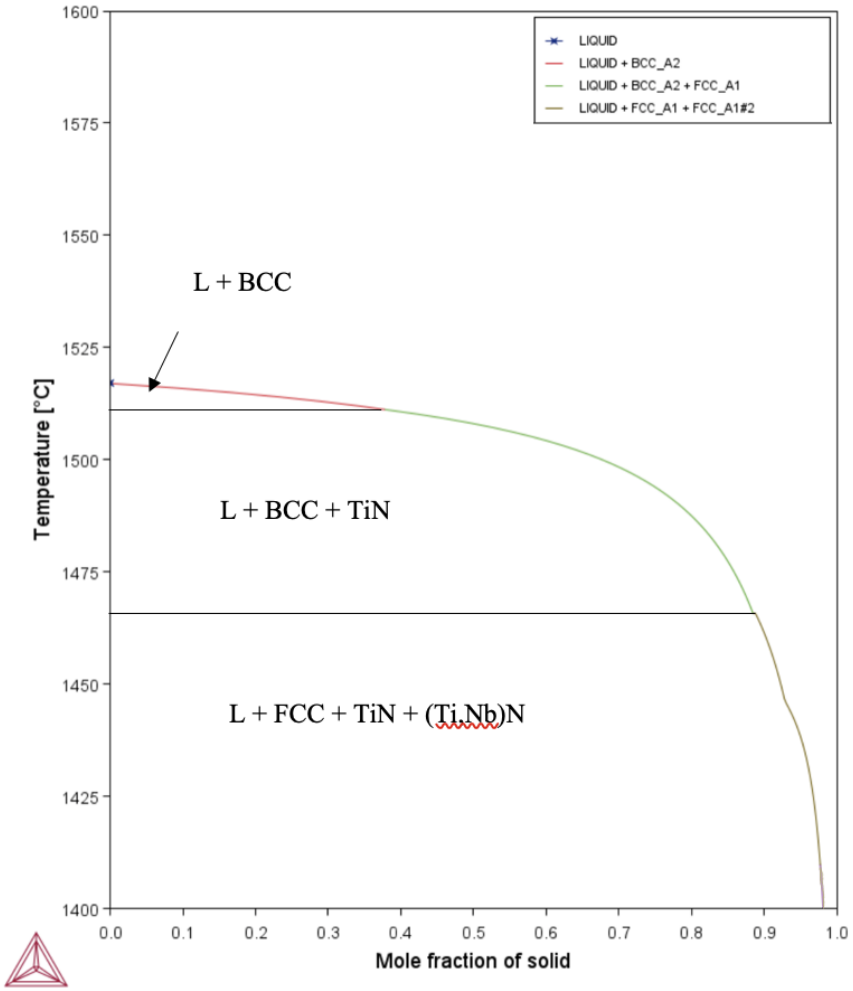


**Figure 5.12** Scheil solidification plot for sample 4280

Figure 5.13 shows the compositions of Ti and Nb in FCC_A1 ((Ti,Nb)N phase) during solidification in the temperature range 1400°C to 1511°C for sample 4280. At 1511ºC, TiN with a composition of 77% Ti and no Nb forms. The balance of the composition is N. At 1447°C, the mole fraction of the Ti,Nb phase begins to increase significantly due to the precipitation of (Ti,Nb)N. The amount of TiN is ≈ 0.0004 whereas the amount of (Ti,Nb)N forming is 0.0012. This confirms the large number of (Ti,Nb)N observed for sample 4280 (Table 5.1).

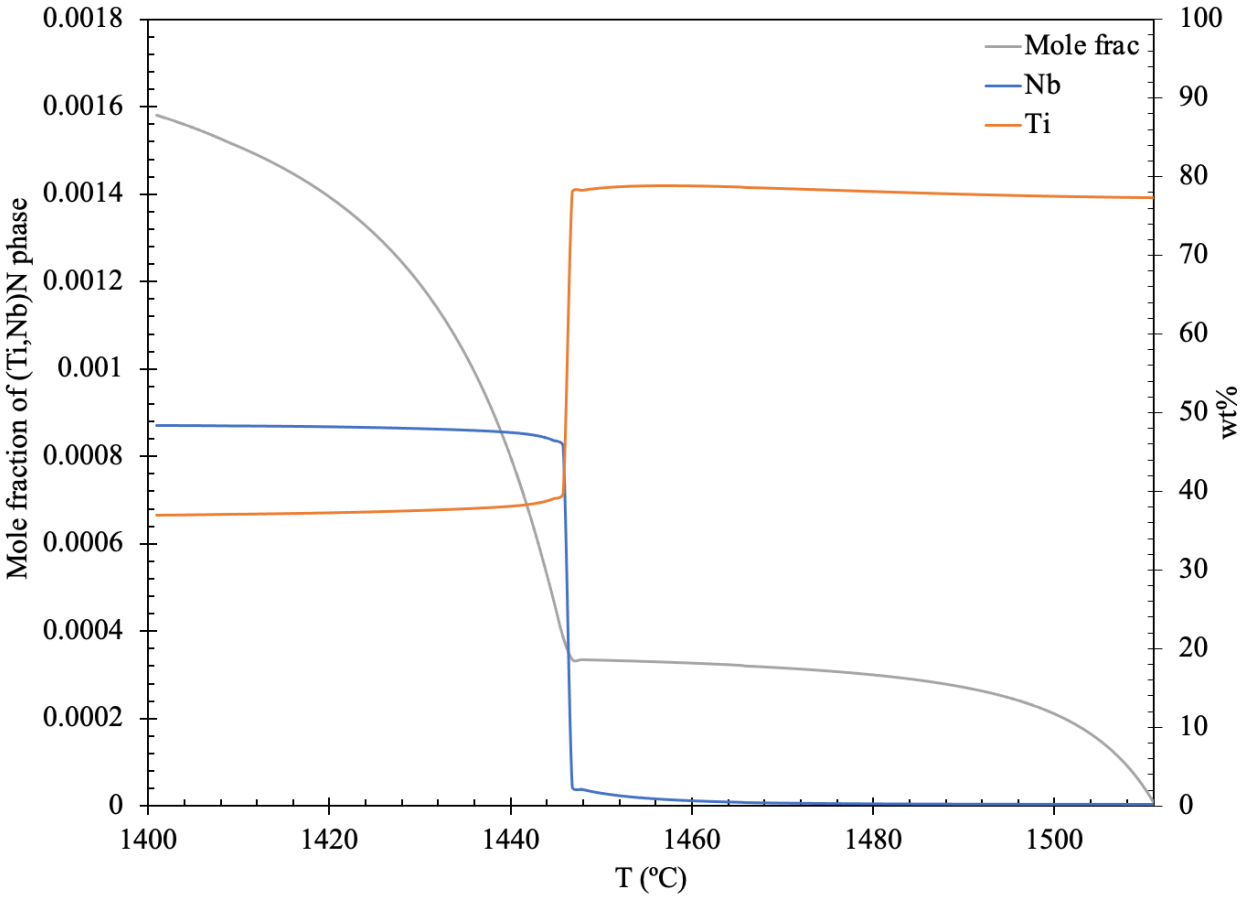


**Figure 5.13** Ti,Nb composition and mole fraction of FCC_A1 during solidification in sample 4280

Figure 5.14 presents the mole fractions of the Ti,Nb phase (FCC_A1) in samples 4280, 4052, and 4093. Samples 4280 and 4052 experience a significant increase in the mole fraction at around the same temperature (1447ºC). Both steels have similarly high Ti contents (0.109 wt% and 0.097 wt%, respectively) and therefore experience similar TiN thermodynamics up until the Nb begins to form at 1470ºC. Since sample 4280 has a much higher Nb content (0.086 wt%) than sample

4052 (0.021 wt%), its mole fraction for (Ti,Nb)N reaches higher values than sample 4052. Sample 4093 contains the lowest Ti and Nb contents (0.047 wt% and 0.015 wt%, respectively). Thus, it does not experience a significant increase in the mole fraction once the Nb begins to precipitate. It also has the lowest mole fraction of the (Ti,Nb)N phase, relative to the other steels.

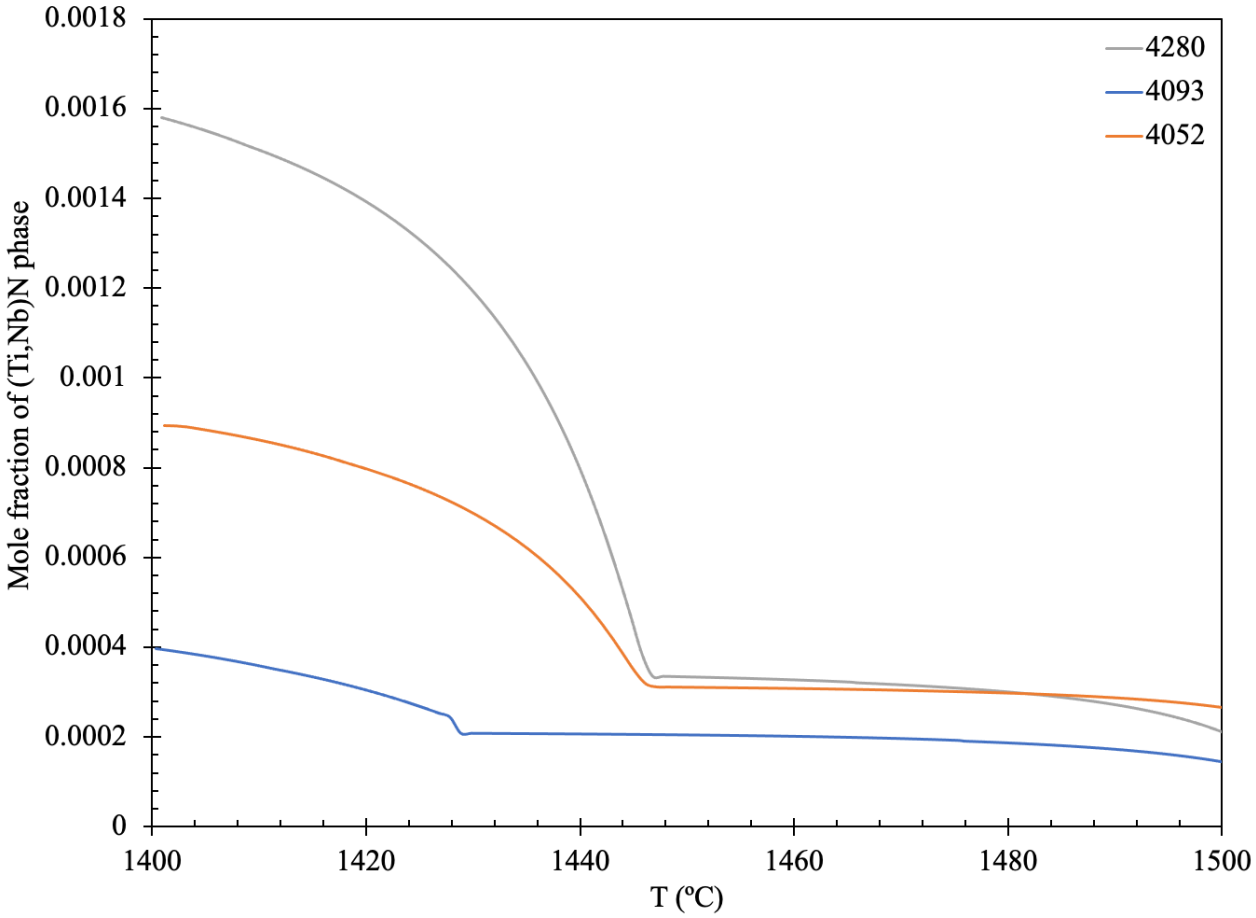


**Figure 5.14** Mole fraction of (Ti,Nb)N phase (FCC_A1) in samples 4280, 4052, and 4093 during solidification

Table 5.3 summarizes the compositions of Ti and Nb obtained from Scheil solidification using Thermocalc for samples 4280, 4052, and 4093 at 1511°C, 1447ºC, and 1400°C. Sample 4280, which has the highest Nb nominal composition (0.086 wt%), exhibits the largest amount of (Ti,Nb)N near the end of solidification. As for sample 4052, although it has a higher nominal Nb composition (0.021 wt%) than sample 4093 (0.015 wt%), less Nb is predicted to precipitate with the TiN. This is because the Ti content in sample 4093 (0.047 wt%) is lower than the Ti content in

sample 4052 (0.096 wt%). When TiN is done precipitating, (Ti,Nb)N begins to precipitate, and since sample 4093 has a lower amount of Ti it will begin Nb precipitation sooner than sample 4052. In all three steels, TiN begins forming at 1500°C with identical Ti contents. The excess composition is N. The similarity in TiN precipitation behaviour and processing parameters amongst all samples agrees with the size distributions from Section 5.2, which showed consistent TiN sizes across all three steels.

**Table 5.3** Ti and Nb compositions during solidification of samples 4280, 4052, and 4093

| Sample | Temperature (°C) | wt% Ti | wt% Nb | Mole frac. TiN | Mole frac. (Ti,Nb)N |
|---|---|---|---|---|---|
| 4280 | 1511 | 78 | 0.17 | 0.0001 | 0 |
| | 1447 | 78 | 2.4 | 0.0004 | 0 |
| | 1400 | 37 | 48 | 0.0004 | 0.0012 |
| 4052 | 1511 | 78 | 0.05 | 0.0002 | 0 |
| | 1447 | 76 | 5.5 | 0.0002 | 0 |
| | 1400 | 66 | 17 | 0.0002 | 0.0003 |
| 4093 | 1511 | 77 | 0.07 | 0.0001 | 0 |
| | 1447 | 79 | 0.5 | 0.0002 | 0 |
| | 1400 | 47 | 38 | 0.0002 | 0.0002 |

5.5.2 Equilibrium contents of TiN and (Ti,Nb)N at homogenization using Thermocalc

The precipitates being characterized are coarse Ti precipitates that are greater than 0.5 μm in size. Because of their sizes, it is assumed that these precipitates form during solidification, which was confirmed by running Scheil solidification simulations using the same chemistries and processing

parameters as the steels. Some of the large Ti precipitates contained large amounts of Nb, which in most cases is thermodynamically unstable at higher temperatures. However, with the size and amounts of Nb observed in steels with high Nb contents, some of the Nb is not going back into solution during homogenization.

Thermocalc was used to check for the presence of two phases in samples 4280, 4052, and 4093: TiN and (Ti,Nb)N. This was done for the homogenization temperatures ranging from 1300°C down to 1200°C. The amounts of TiN and (Ti,Nb)N formed can then be linked to experimental results. (Ti,Nb)N that forms during solidification would not dissolve back into solution completely during processing steps, which is the case seen in sample 4280. The results from Thermocalc are tabulated in Table 5.4. (Ti,Nb)N is present at 1300°C in sample 4280; however, that is not the case for samples 4052 and 4093. Since (Ti,Nb)N was not observed with the SEM or at homogenization temperatures with Thermocalc for samples 4052 and 4093, it can be concluded that (Ti,Nb)N forming during solidification is not thermodynamically stable at homogenization temperatures for these steels. Conversely, in sample 4280, (Ti,Nb)N does not dissolve completely. Hence, they are observed to be smaller precipitates than the TiN. Also, the (Ti,Nb)N formed at the very end of solidification. Therefore, they may initially be smaller (even without dissolution) than the TiN that forms in the initial stages of solidification.

The mass fraction of the (Ti,Nb)N in sample 4280 is slightly larger than the mass fraction of the TiN. This is expected since SEM analysis observed more (Ti,Nb)N than TiN in this steel. The mass fraction of TiN in sample 4052 is insignificantly lower than that in sample 4280, which agrees with the precipitate count obtained via SEM analysis. Sample 4093 has the smallest mass fraction of TiN, which is also in agreement with the SEM results. Thermocalc analysis shows no (Ti,Nb)N in samples 4052 and 4093, which is consistent with the experimental results obtained. Steels 4280 and 4052 have similar Ti compositions and significantly different Nb compositions, yet only steel 4280 has (Ti,Nb)N. Therefore, a threshold of the amount of Nb added to a microalloyed steel exists at which (Ti,Nb)N stops being stable at homogenization temperatures and dissolves back into the steel completely. Figure 5.15 plots the mass fractions of (Ti,Nb)N for steel 4280 at different Nb compositions while keeping the remaining chemistry the same. The threshold for Nb in high Ti steels (> 0.1 wt%), such as sample 4280, is determined to be approximately 0.035 wt%.

**Table 5.4** Thermocalc compositions of Ti, Nb, and mass fraction of TiN and (Ti,Nb)N phases over a range of homogenization temperatures

| Sample (Phase) | Composition (wt%) | Mass fraction of phase | 1300°C | 1250°C | 1200°C |
|---|---|---|---|---|---|
| 4280 (TiN) | Ti | 0.029 | 79 | 79 | 79 |
| | Nb | | 1.8 | 1.3 | 1.1 |
| 4280 (Ti,Nb)N | Ti | 0.032 | 40 | 36 | 36 |
| | Nb | | 46 | 50 | 50 |
| 4052 (TiN) | Ti | 0.025 | 79 | 79 | 79 |
| | Nb | | 0.1 | 0.2 | 0.4 |
| 4052 (Ti,Nb)N | Ti | 0 | - | - | - |
| | Nb | | - | - | - |
| 4093 (TiN) | Ti | 0.015 | 78 | 79 | 79 |
| | Nb | | 0.1 | 0.1 | 0.2 |
| 4093 (Ti,Nb)N | Ti | 0 | - | - | - |
| | Nb | | - | - | - |

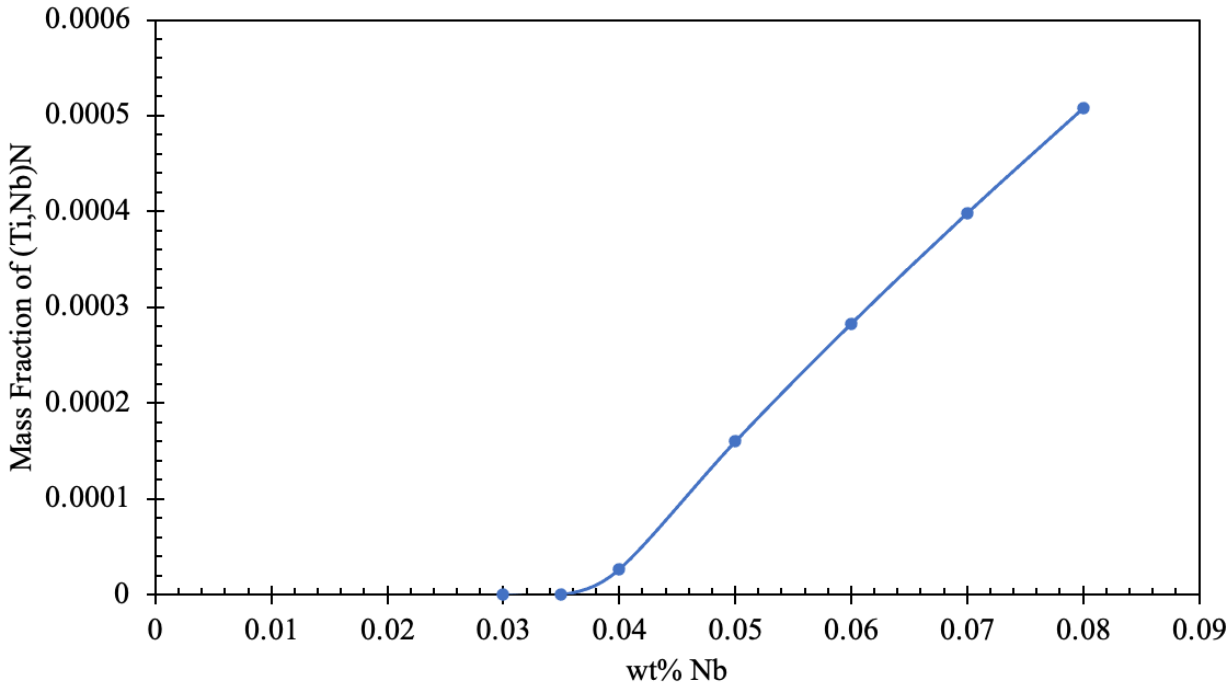


**Figure 5.15** Mass fraction of (Ti,Nb)N at various Nb compositions in steel 4280

## 5.6 Summary

The amounts of large (> 0.5 μm) TiN and (Ti,Nb)N were quantified with precipitate counts and EMPA analysis. From the precipitate count, it was established that samples with high Ti and Nb contents experience the largest amounts of (Ti,Nb)N precipitates. Predicted mass fractions obtained from Thermocalc of the phases containing (Ti,Nb)N exhibit a similar trend to the precipitate count obtained from experimental results.

The number of TiN and (Ti,Nb)N regions were relatively consistent through the thickness of the steels, confirming the absence of macrosegregation in the samples.

Size distributions for samples 4280, 4175, 4052, and 4093 were measured. Sample 4280's distribution had two mean sizes at 1.6 and 3.5 μm, for (Ti,Nb)N and TiN, respectively. Samples 4175, 4052, and 4093 had mean sizes of 3.4 μm, 2.7 μm, and 3.0 μm, respectively, for TiN. TiN in all the steels exhibited similar sizes. (Ti,Nb)N was smaller in size and was found only in sample 4280. It was concluded that samples with larger Nb contents were forming a larger amount of (Ti,Nb)N precipitates, which form near the end of solidification, and thus tend to be smaller in size. The effect of NbN on the morphology of TiN-rich precipitates was also investigated briefly, where TiN that did not contain large amounts of NbN were more defined and cuboidal, whereas TiN that contained NbN were more irregularly shaped and mostly semi-cuboidal. This difference may be attributed to the formation of NbN on and around TiN in the later stages of solidification and during TMCP, along with the effects that TMCP may have on the morphology of the precipitates.

Thermocalc was used to confirm the SEM findings. A Scheil solidification analysis showed that the TiN formed at the same temperature (1511°C) with similar compositions in all the steels. This explains the similar TiN sizes in all the steels. The amount of (Ti,Nb)N at temperatures below 1447ºC was largest for sample 4280 (relative to samples 4052 and 4093). (Ti,Nb)N that formed in samples 4052 and 4093 are thermodynamically unstable at the homogenization temperature (1300ºC) and will hence dissolve during homogenization. (Ti,Nb)N for sample 4280 do not completely dissolve. Thus, sample 4280 exhibits a greater amount of large (Ti,Nb)N compared to the other steels. To dissolve all (Ti,Nb)N in very high Ti steels (>0.1 wt%), such as 4280, the threshold for the amount of Nb that should be added is determined to be approximately 0.035 wt%.

# Chapter 6: Conclusions and Future Work

In this study, a quantification technique was developed for Ti precipitates analysis using EMPA. In addition, Ti precipitates were characterized using SEM/EDX. By combining the analysis developed using EMPA and SEM/EDX, the effects of CaS and Nb on TiN were explored on seven microalloyed steel samples with varying Ti and Nb contents of 0.047 – 0.122 wt% and 0.015 – 0.088 wt%, respectively. A precipitate count for Ti precipitates associated with CaS was performed via an EMPA code, then precipitate characterization and size analysis was done via SEM/EDX. The same procedure was also performed for a precipitate count, characterization, and size analysis of TiN and (Ti,Nb)N.

## 6.1 Conclusions

The conclusions can be made to answer the objective questions of this research:

1. What is the prevalence of TiN precipitates on preexisting CaS nonmetallic inclusions, and how abundant are these precipitates through the thickness of the steels?

Approximately 85-90% of the CaS inclusions present in the samples became nucleation sites for TiN. However, the overall number of TiN-CaS precipitates forming in the samples was minor when compared to the total amount of Ti counted in the samples. The amount of Ti precipitates not linked to CaS increased as the Ti content in the steels increased. This is expected since at higher Ti contents, more Ti is likely to precipitate. On the other hand, Ti precipitating on CaS exhibited similar behaviour in all the samples and was unaffected by their differences in Ti contents. Another observation made was that the TiN precipitating on CaS exhibited the highest greyscale intensities, which could be due to them being larger precipitates than TiN precipitates that are not associated to any nonmetallic inclusions.

The TiN-CaS precipitates were found in abundance at the quarter thickness and at the surface and subsurface of the steels. The precipitates found at the quarter thickness could be precipitates that existed in the interdendritic region during solidification and travelled towards the center of the steel. However, with mechanical soft reduction, they could have ended up at the quarter thicknesses of the steels. In some steels, it was observed that one quarter thickness had a higher TiN-CaS density, which could be attributed to a tilt in the steels towards one side during processing. As for the precipitates found on the surface and subsurface, that is due to the CaS

forming on alumina, which is a deoxidizer in steel and will therefore be more abundant at the surface and subsurface.

2. How does TiN precipitating on CaS inclusions effect the size and morphology of the precipitate?

From the size distributions developed, it was found that majority of TiN that precipitated on CaS were 5 μm in size, whereas majority of the TiN not precipitating on CaS were 1-3 μm in size. A 2-4 μm increase in size was observed, thus it was concluded that Ti precipitating on CaS results in a larger precipitate size. The increase in size is due to precipitation kinetics of Ti, which favors nucleation on CaS inclusions. CaS inclusions are usually large in size, so when the Ti nucleates on CaS, it forms a large precipitate that will grow and coarsen further. Also, TiN that nucleates on CaS tends to form at earlier stages of solidification. CaS inclusions always appeared as spherical precipitates whereas the TiN formed a cuboidal precipitate around the CaS.

3. What is the effect of Nb composition on the amount of (Ti,Nb)N forming and its morphology?

From EMPA precipitate counts, it was observed that for steels with higher Ti and Nb contents, a larger amount of (Ti,Nb)N precipitates were forming. The Ti,Nb precipitates counted at the greyscale values selected were all assumed to be (Ti,Nb)N. Mass fractions of the Ti,Nb containing phase in Thermocalc showed an identical trend to that obtained from the EMPA count. The same conclusion can be made from the precipitates characterized on SEM/EDX. Sample 4280, which contains 0.109 wt% Ti and 0.086 wt% Nb had a significantly larger amount of (Ti,Nb)N than the other samples, which contain a wide range of Ti content (0.047 – 0.118 wt%) but a much lower Nb content (0.015 – 0.025 wt%).

The number of (Ti,Nb)N precipitates throughout the thickness of the steels was almost constant. This confirms the absence of macrosegregation, as observed from the EMPA maps and line scans.

Steels with higher Nb concentrations had the smallest precipitate sizes, whereas steels containing a relatively lower amount of Nb, exhibited larger precipitate sizes. Samples with larger Nb contents were forming a larger amount of (Ti,Nb)N precipitates, which tend to be smaller in size than TiN because they form near the end of solidification and partially dissolve during homogenization. This shifted the size distribution of sample 4280, which has higher Nb contents, towards smaller sizes

since it included a larger amount of (Ti,Nb)N. TiN in sample 4280 that did not contain Nb exhibited sizes similar to the TiN in other samples. Majority of (Ti,Nb)N were 1.6 μm in size, whereas majority of TiN were 2.7-3.5 μm in size. The size of TiN not associated to Nb was uniform across all samples. TiN that did not contain large amounts of Nb were cuboidal in shape. However, TiN that contained Nb were more irregularly shaped and mostly semi-cuboidal. To prevent excessive (Ti,Nb)N that may remain after the processing of the steel, Nb contents can be reduced to a certain threshold. For example, in steels with similar chemistries to sample 4280, the limit of the Nb content at which (Ti,Nb)N dissolves completely at homogenization is 0.035 wt%. Scheil solidification along with equilibrium points at homogenization temperatures on Thermocalc confirmed the results through thermodynamic data.

## 6.2 Future Work

This work focuses on characterizing and quantifying Ti macroprecipitates. Therefore, some future work that can be done to complete the Ti precipitate analysis on these steel samples include:

- Quantifying and characterizing nanoprecipitates: since the analysis completed in this thesis is for macro Ti precipitates only, it does not encapsulate the full depth of a precipitate analysis on the steel samples. The data collected in this work is not enough to draw complete conclusions on the steel properties as nanoprecipitates are great contributors. Some additional characterization techniques that can be done on the samples include TEM/STEM and quantitative x-ray diffraction (XRD). Matrix dissolution can be performed on the steel samples, and TEM can be used to quantify nano Ti precipitates and calculate volume fractions. Size distributions can also be developed from TEM images.

- Mechanical testing of the steels: with the presence of a completed macroprecipitate analysis and characterization alongside the results from the nanoprecipitate analysis and characterization, testing for mechanical properties can link both studies on Ti precipitates to the steel properties. A relationship can then be developed between the different Ti precipitates and how they can impact the mechanical properties of steels with different Ti contents. Some mechanical tests to be considered include tensile tests, Charpy impact tests, and hardness tests. The Ti contents, amounts, and types of Ti precipitates can then be correlated to the steel strength, toughness, and hardness.

# References


[1] H. B. Tata, R. Honeycombe, Steels: Microstructure and Properties (Fourth Edition), *Thermomechanical Treatment of Steels*, 2017.

[2] C. I. Garcia, High strength low alloyed (HSLA) steels, *Automotive Steels*, 2017.

[3] J. R. Davis, Metals Handbook, Desk Edition (2nd Edition), *11.6.6.2 Conventional Controlled Rolling*, ASM International, p. 188-198, 1998.

[4] J. R. Davis, ASM Specialty Handbook, *Stainless Steels - 15.6.2.1 Solution Annealing*, ASM International, p. 303-313, 1994.

[5] Dieter, G. E. Kuhn, H. A. Semiatin, S. Lee, Handbook of Workability and Process Design, *17.1 Fundamentals of Controlled Rolling*, ASM International, p. 248-256, 2003.

[6] J. R. Davis, Metals Handbook, Desk Edition (2nd Edition), *11.6.7 Pickling*, ASM International, p. 198-202, 1998.

[7] Higgins, A. Raymond, Engineering Metallurgy - Applied Physical Metallurgy (6th Edition), *13.15 Bibliography*, Elsevier, p. 332, 1993.

[8] M. Kutz, Handbook of Materials Selection, *2.4 Role of Alloying Elements in Steel*, John Wiley & Sons, p. 44-50, 2002.

[9] G. Krauss, Steels - Processing, Structure, and Performance, *8.7 Austenite Grain Size Control in Microalloyed Steels*, ASM International, p. 153-159, 2005.

[10] P. H. Wright, High Strength Low-Alloy Steel Forgings, *Properties and Selection: Irons, Steels, and High-Performance Alloys,* ASM Handbook, vol. 1, p. 358-362, 1990.

[11] S. Akhlaghi, D.G. Ivey, Precipitation Behaviour of a Grade 100 Structural Steel, Canadian Metallurgical Quarterly, 41:1, p. 111-119, 2002.

[12] J. Lu, O. Omotoso, J. B. Wiskel, D. G. Ivey, H. Henein, Strengthening Mechanisms and Their Relative Contributions to the Yield Strength of Microalloyed Steels, *Metallurgical and Materials Transactions A,* The Minerals, Metals & Materials Society, ASM Internaational, vol. 43A, p. 3043-3061, 2012.

[13] M. P. Phaniraj et. al, Understanding dual precipitation strengthening in ultra-high strength low carbon steel containing nano-sized copper precipitates and carbides, *Nano Convergence,* Korea Nano Technology Research Society, 4:16, 2017.

[14] Llewellyn, D.T. Hudd, R.C., Steels - Metallurgy and Applications (3rd Edition)*, 2.3.3 Precipitation Strengthening,* Elsevier, p. 137-166, 1998.

[15] A. Mansoor et. al, *Effects of grain refinement and precipitate strengthening on mechanical properties of double-extruded Mg-12Gd-2Er-0.4Zr alloy, Journal of Alloys and Compounds*, vol. 898, 2022.

[16] Q. Yuan et al., *Effect of Ti on microstructure and properties of Ti-Nb microalloyed high strength steels*, 3rd International Conference on Material, Mechanical and Manufacturing Engineering, p. 1710-1715, 2015.

[17] American Water Works Association, *1.3.3 Casting,* Steel Pipe - A Guide for Design and Installation - Manual of Water Supply Practices, M11 (5th Edition), American Water Works Association (AWWA), p. 1-18, 2017.

[18] R. H. Petrov et. al., Oil and Gas Pipelines: Integrity and Safety Handbook (First Edition), *Microstructure and Texture Development in Pipeline Steels*, John Wiley & Sons, Inc., p. 159-183, 2015.

[19] A. L. Costa e Silva, *Non-metallic inclusions in steels – origin and control,* Journal of Materials Research and Technology, vol. 7, p. 283-299, 2018.

[20] H. Colpaert, "Chapter 8: Solidification, Segregation, and Nonmetallic Inclusions", Metallography of Steels – Interpretation of Structure and the Effect of Processing, ASM International, p. 129-188, 2018.

[21] J. Campbell, "Chapter 5: Solidification Structure", Complete Casting Handbook (Second Edition), *Metal Casting Processes, Metallurgy, Techniques and Design,* p. 163-222, 2015.

[22] A. Ghosh, "Segregation in cast products", *Sadhana,* vol. 26, p. 5-24, 2001.

[23] R. Thome, K. Harste, *Principles of Billet Soft-reduction and Consequences for Continuous Casting*, ISIJ International, vol. 26, p. 1839-1844, 2006.

[24] D. Bai et. al., "Process for making high strength micro-alloy steel", IPSCO Enterprise Inc., 2004.

[25] S. G. Jansto, *Reheat Furnace Thermodynamic, Kinetic and Combustion Considerations for TMCP Processing*, Materials Science Forum, vol. 941, p. 608-613, 2018.

[26] Turkdogan, E. T., *Fundamentals of Steelmaking - 10.6.4 Critical Microalloying Elements in HSLA Steel.* Maney Publishing for IOM3, the Institute of Materials, Minerals and Mining, p. 297-319, 1996.

[27] S. Yue, *26.5 Alloying in HSLA Steels* ,Thermomechanical processing of ferrous alloys, ASM Handbook, vol 14A, p. 286-296, 2005.

[28] G. E. Totten, Heat Treating of Nonferrous Alloys, *5.4.1 Nucleation and Growth*, ASM Handbook, vol. 4E, ASM International, p. 65-110, 2016.

[29] J. B. Wiskel, Lecture 17b NonREX Precipitation Rate, MAT E 689, University of Alberta, eClass, 2022.

[30] C. Chatelier, *Precipitation Analysis in Microalloyed X70 Steels and Heat Treated L80 and T95 Steels*, Department of Chemical and Materials Engineering, University of Alberta, 2017.

[31] J. B. Wiskel, Lecture 10C Model, MAT E 689, University of Alberta, eClass, 2022.

[32] J. J. Friel, C. E. Lyman, *X-ray Mapping in Electron-Beam Instruments,* Microscopy and Microanalysis, vol. 12, p. 2-25, 2006.

[33] R. Deacon, N. Maagdefrau, *Microscopy and Microanalysis,* ASM Handbook, ASM International, vol. 10, p. 543-574, 2019.

[34] J. Goldstein et. al., "Chapter 10: Special Topics in Electron Beam X-Ray Microanalysis", Scanning Electron Microscopy and X-Ray Microanalysis (Third Edition), Springer Science+Business Media, LLC, p. 485-499, 2003.

[35] D. E. Newbury, N. Ritchie, *Performing elemental microanalysis with high accuracy and high precision by scanning electron microscopy/silicon drift detector energy-dispersive X-ray spectrometry (SEM/SDD-EDS),* Journal of Materials Science, vol. 50, p. 493-518, 2015.

[36] "Introduction to EMPA", Cameca, www.cameca.com/products/epma/epma-introduce, Accessed Aug. 2023.

[37] J. Goldstein, H. Yakowitz, D. E. Newbury, "Introduction", Practical Scanning Electron Microscopy, Springer, Boston, MA., p. 1-17, 1975.

[38] W. F. Gale, T. C. Totemeier, "10.7 Applications in Failure Analysis", Smithells Metals Reference Book (8th Edition), Elsevier, p. 74-84, 2004.

[39] J. Heath, N. Taylor, Energy Dispersive Spectroscopy (Second Edition), Essential Knowledge Briefings, p. 4-27, 2015.

[40] P. Chen et. al., *Effect of Sulphur Concentration on Precipitation Behaviors of MnS-containing Inclusions in GCr15 Bearing Steels after LF Refining*, ISIJ International, vol. 57, p. 1019-1028, 2017.

[41] T. Zhang, C. Liu, H. Mu, Y. Li & M. Jiang, *Inclusion evolution after calcium addition in Al-killed steel with different sulphur content*, Ironmaking & Steelmaking, vol. 45, p. 447-456, 2018.

[42] J. H. Park, *Thermodynamic investigation on the formation of inclusions containing MgAl2O4 spinel during 16Cr–14Ni austenitic stainless steel manufacturing processes*, Materials Science and Engineering, p.43-51, 2008.

[43] L. Gui et. al., *Study on the precipitation and coarsening of TiN inclusions in Ti-microalloyed steel by a modified coupling model,* Journal of Materials Research and Technology, vol. 9, p. 5499-5514, 2020.

[44] Z. Wang et. al., *TiN/γ-Fe interface orientation relationship and formation mechanism of TiN precipitates in Mn18Cr2 steel,* Research & Development, vol. 18, p. 180-184, 2021.

[45] Z. Gao et. al., *Titanium microalloying of steel: A review of its effects on processing, microstructure and mechanical properties,* International Journal of Minerals Metallurgy and Materials, p. 645-658, 2022.

[46] W. F. Hosford, "Chapter 1: Chemistry Basics", Elementary Materials Science, ASM International, p. 1-10, 2013.

[47] N. Frenzel et. al., *Synthesis and Crystal Structure of $Nb_{0.84}N$,* vol. 66b, p. 1-6, 2010.

[48] M. Shinn, *Nucleation, structure, and mechanical properties of epitaxial titanium nitride/niobium nitride and vanadium(0.6) niobium(0.4) nitride/niobium nitride superlattice thin films*, Northwestern University, 1993.

[49] S. Zajac and B. Jansson, *Thermodynamics of the Fe-Nb-C-N System and the Solubility of Niobium Carbonitrides in Austenite,* Metallurgical and Materials Transactions B, vol. 29B, p. 163-175, 1998.

[50] S. Yamini, *Influence of Microalloying Elements (Ti,Nb) and Nitrogen Concentrations on Precipitation of Linepipe Steels – A Thermodynamic Approach,* p. 1-12, 2020.

[51] A. J. Craven et. al., *Complex Heterogeneous Precipitation in Titanium-Niobium Microalloyed Al-Killed HSLA Steels – I. (Ti,Nb)(C,N) Particles,* Acta Materialia, vol. 48, p. 3857-3868, 2000.

[52] A. J. Craven et. al., *Complex Heterogeneous Precipitation in Titanium-Niobium Microalloyed Al-Killed HSLA Steels – II. Non-Titanium Based Particles,* Acta Materialia, vol. 48, p. 3857-3868, 2000.

[53] Y. Tian, *Revealing Morphology Rules of MX Precipitates in Ti-V-Nb multi-microalloyed steels,* Materials Characterization, p. 1-10, 2022.

[54] L. Xing et. al., *Control of TiN precipitation behavior in titanium-containing micro-alloyed steel*, Materials Today Communications, vol. 25, 2020.

[55] "Scheil Solidification Simulations". Thermo-Calc, https://thermocalc.com/products/thermo-calc/scheil-solidification-simulations/ , Accessed Nov. 2023.

# Appendix A – Greyscale Maps

Appendix A contains the maps obtained from EMPA for Ti, Nb, Mn, Ca, and S in all the steels. Both greyscale and inverted maps will be presented.

## A.1 Raw Greyscale Images

### A.1.1 4280

**Figure A1** Ti greyscale map for sample 4280

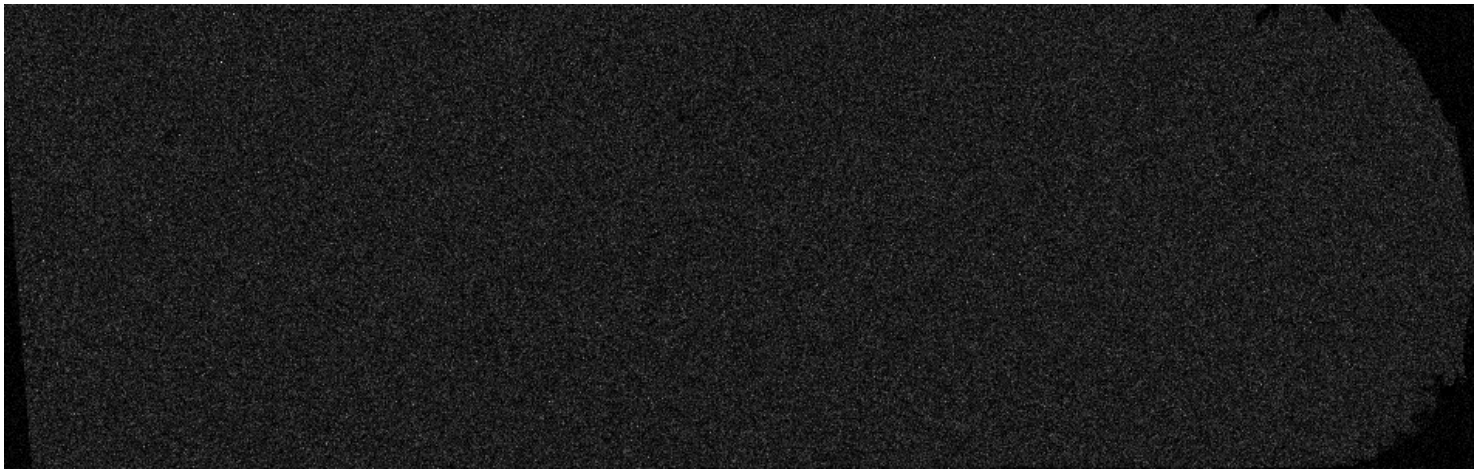

**Figure A2** Nb greyscale map for sample 4280

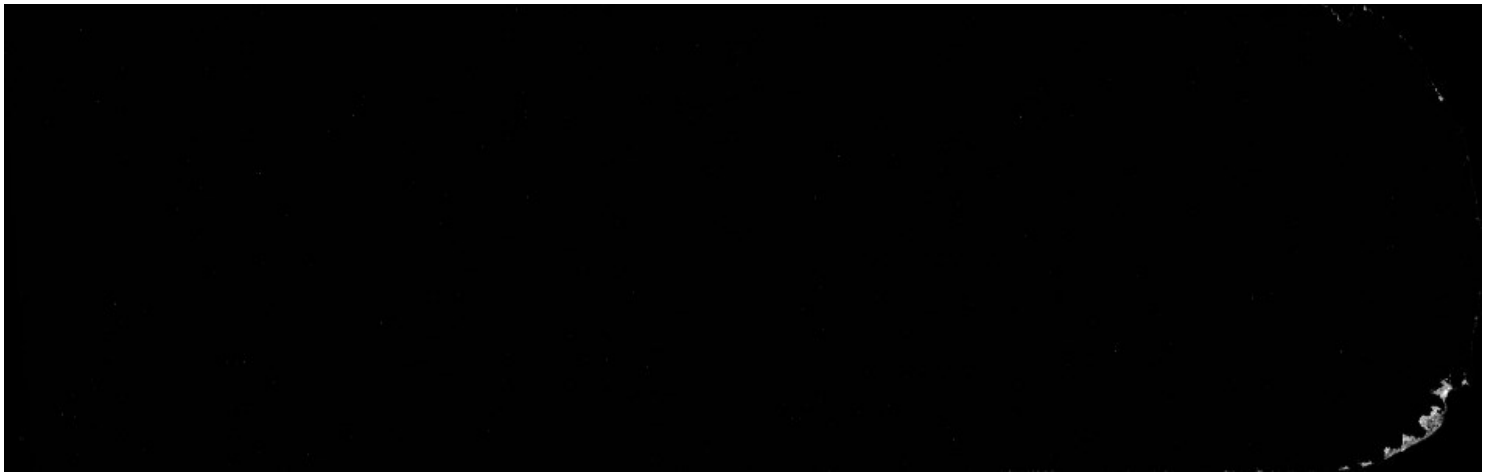

**Figure A3** Ca greyscale map for sample 4280

**Figure A4** S greyscale map for sample 4280

A.1.2 4175

**Figure A5** Ti greyscale map for sample 4175

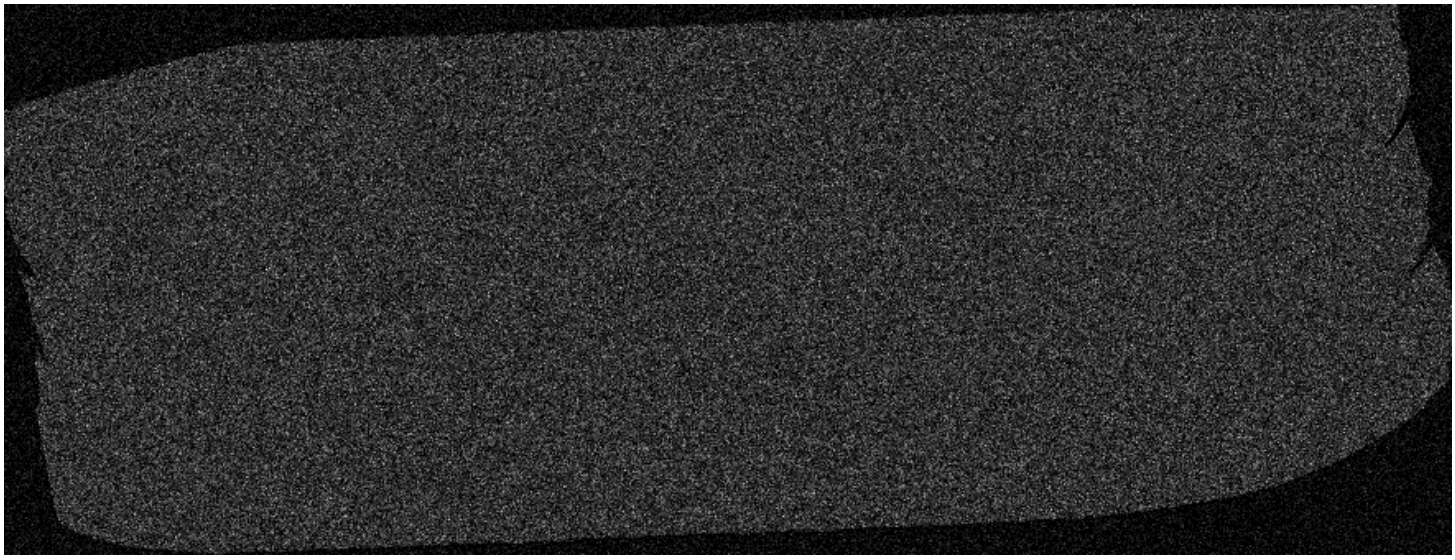

**Figure A6** Nb greyscale map for sample 4175

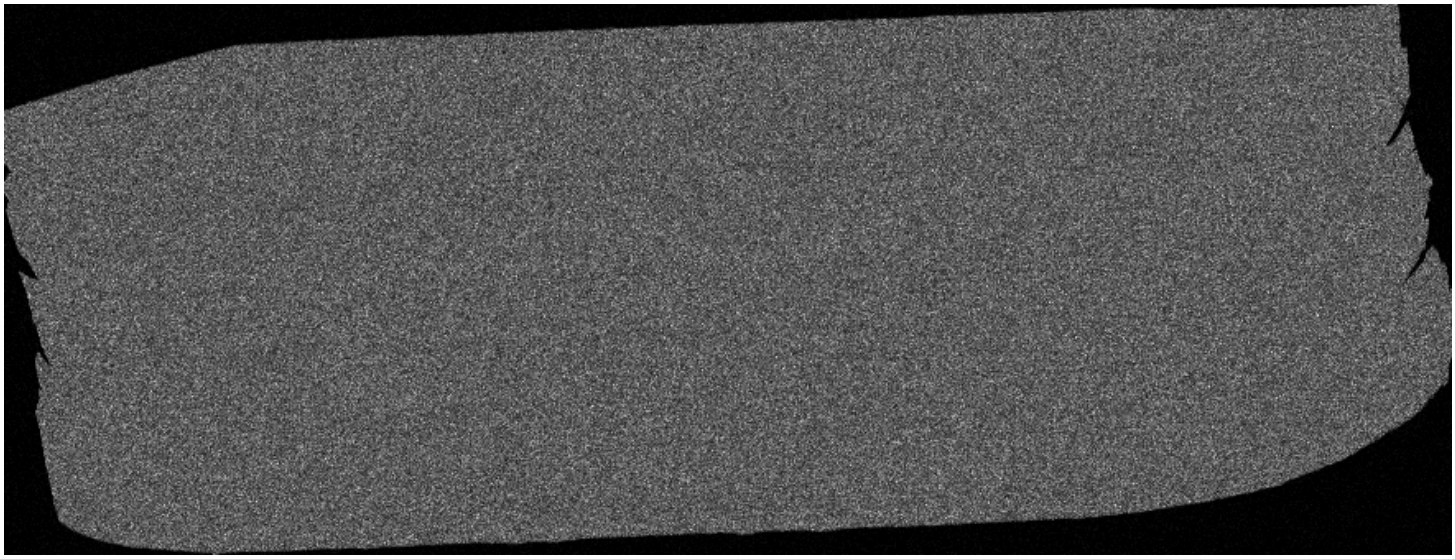

**Figure A7** Mn greyscale map for sample 4175

**Figure A8** Ca greyscale map for sample 4175

**Figure A9** S greyscale map for sample 4175

A.1.3 4372

**Figure A10** Ti greyscale map for sample 4372

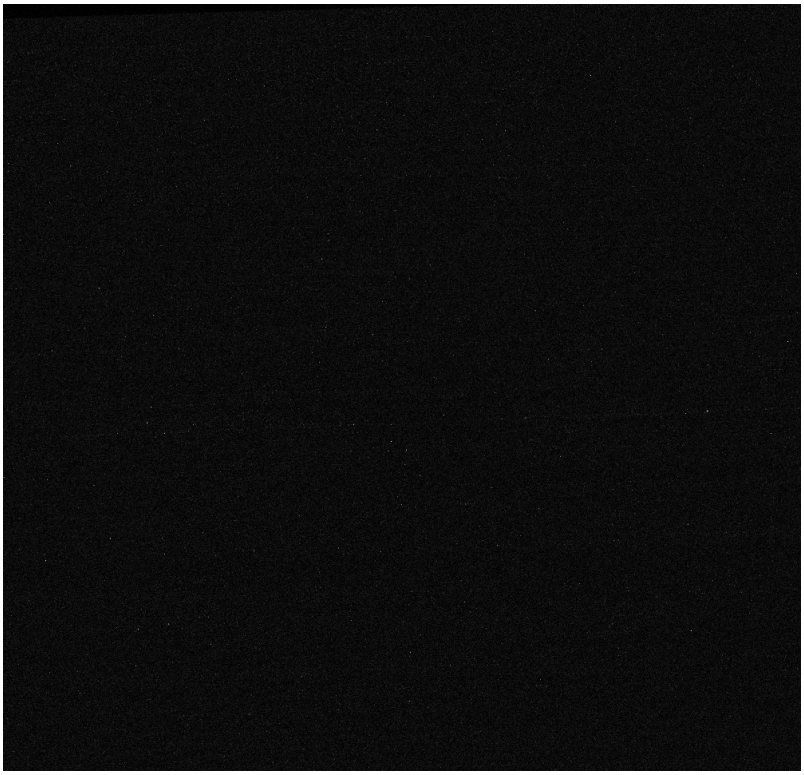

**Figure A11** Nb greyscale for sample 4372

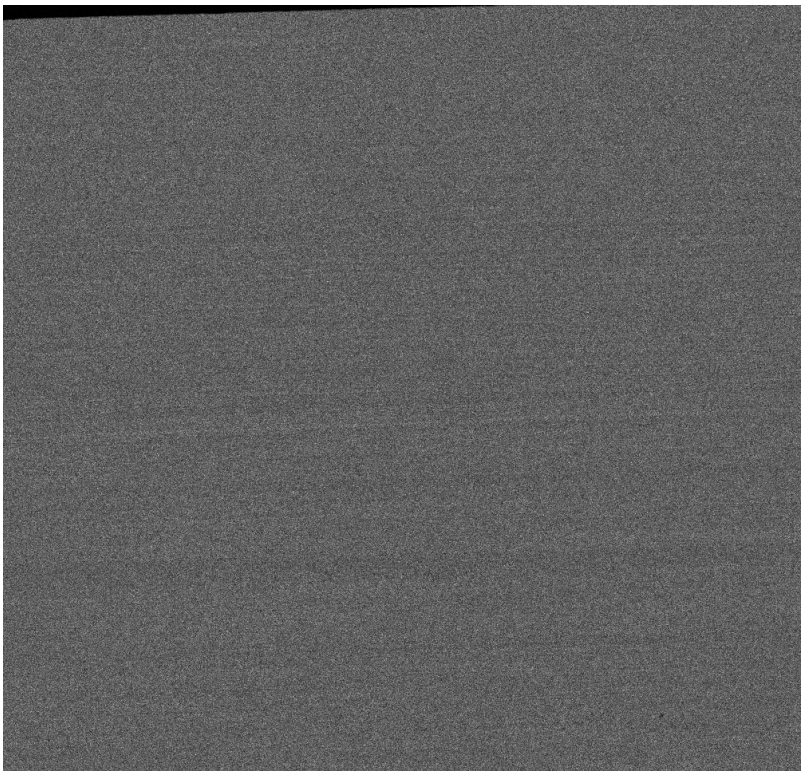

**Figure A12** Mn greyscale for sample 4372

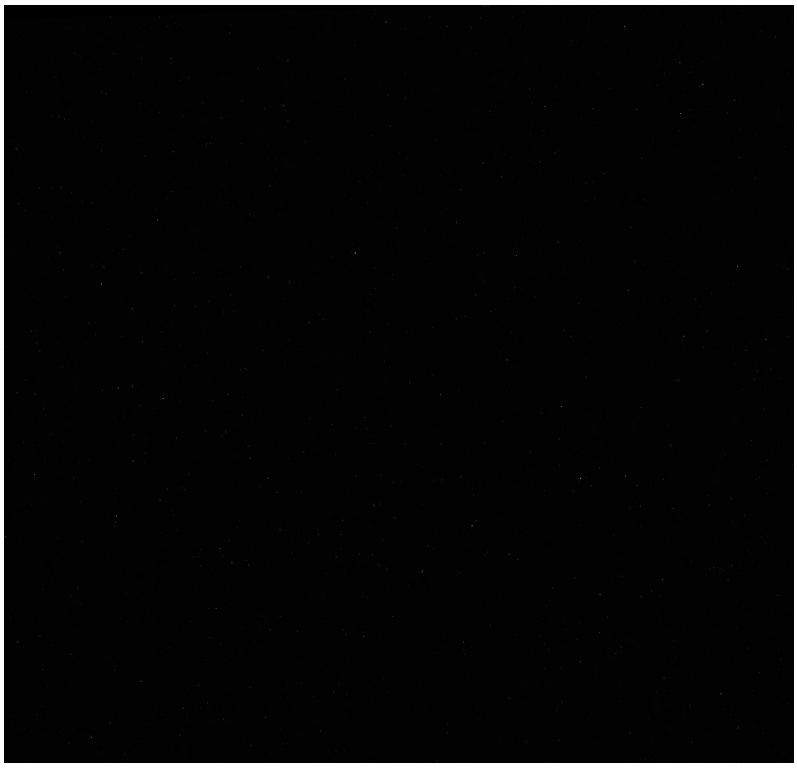

**Figure A13** Ca greyscale map for sample 4372

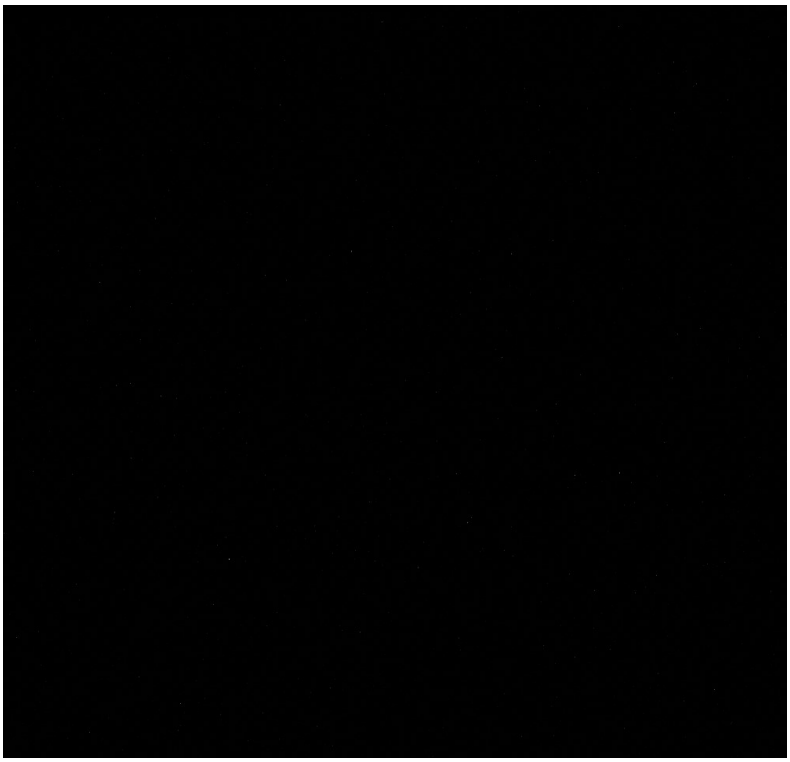

**Figure A14** S greyscale map for sample 4372

A.1.4 4052

**Figure A15** Ti greyscale map for sample 4052

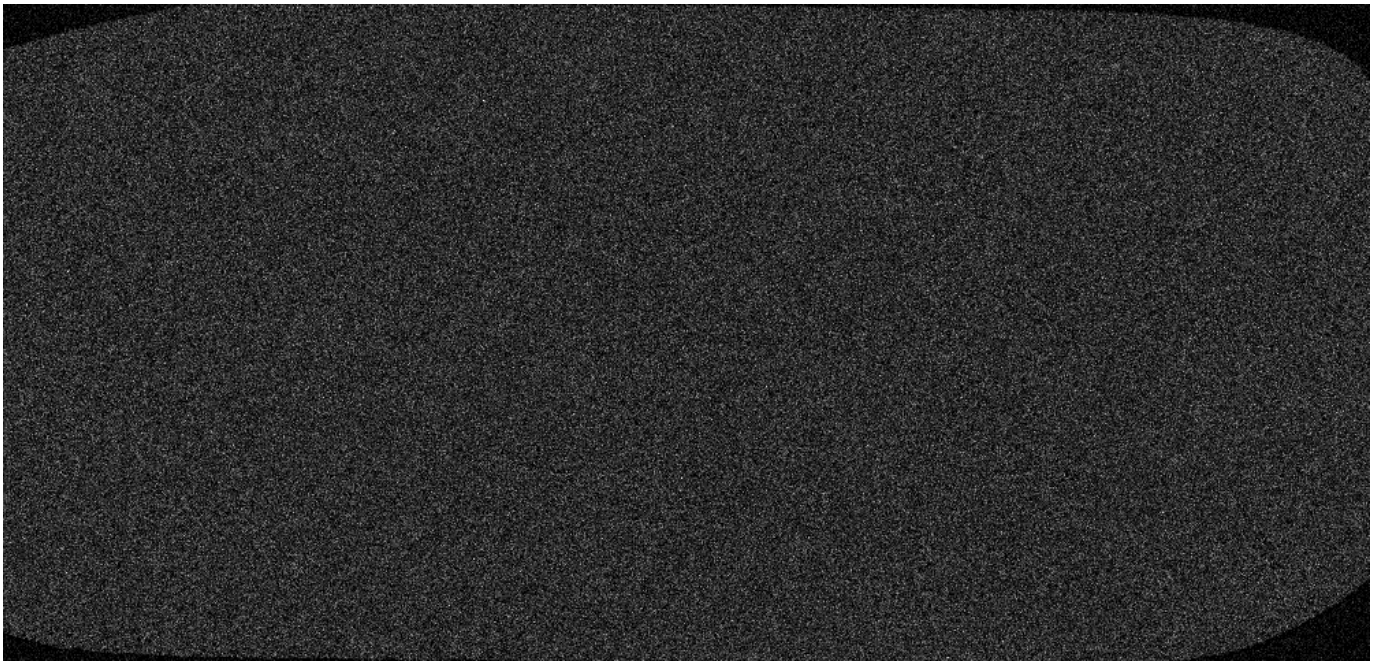

**Figure A16** Nb greyscale map for sample 4052

**Figure A17** Mn greyscale map for sample 4052

**Figure A18** Ca greyscale map for sample 4052

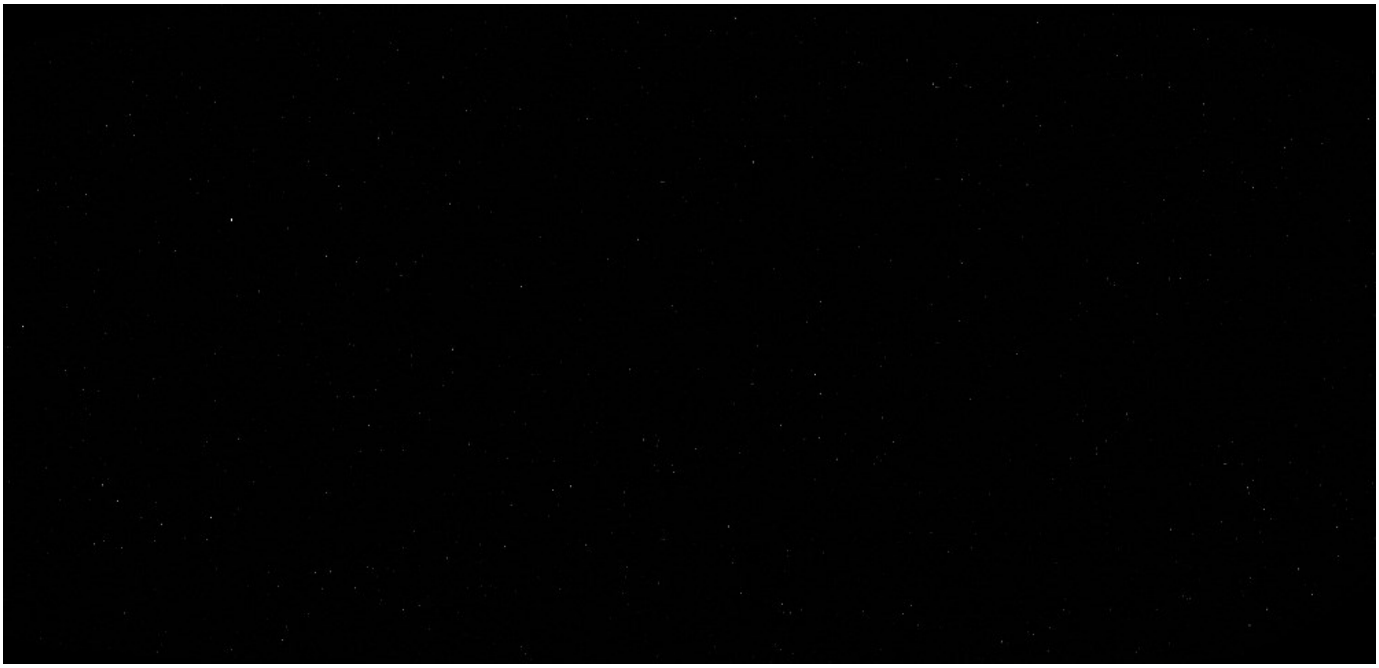

**Figure A19** S greyscale map for sample 4052

A.1.5 4081

**Figure A20** Ti greyscale map for sample 4081

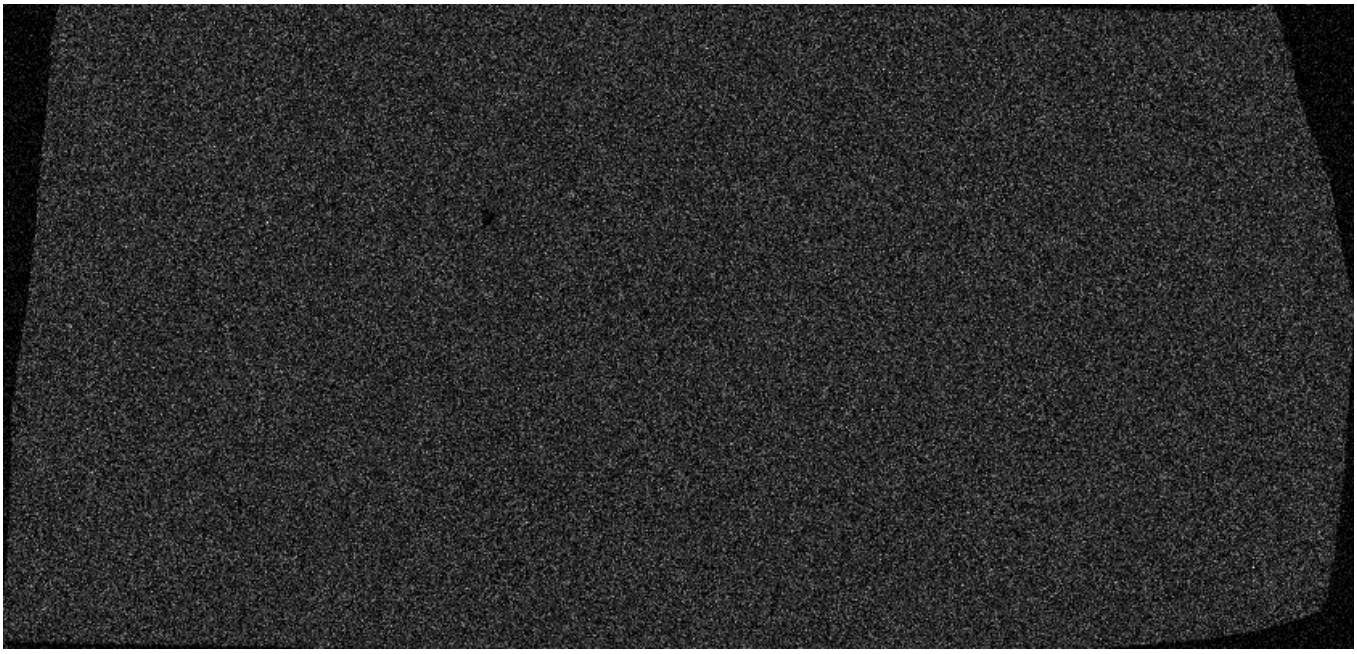

**Figure A21** Nb greyscale map for sample 4081

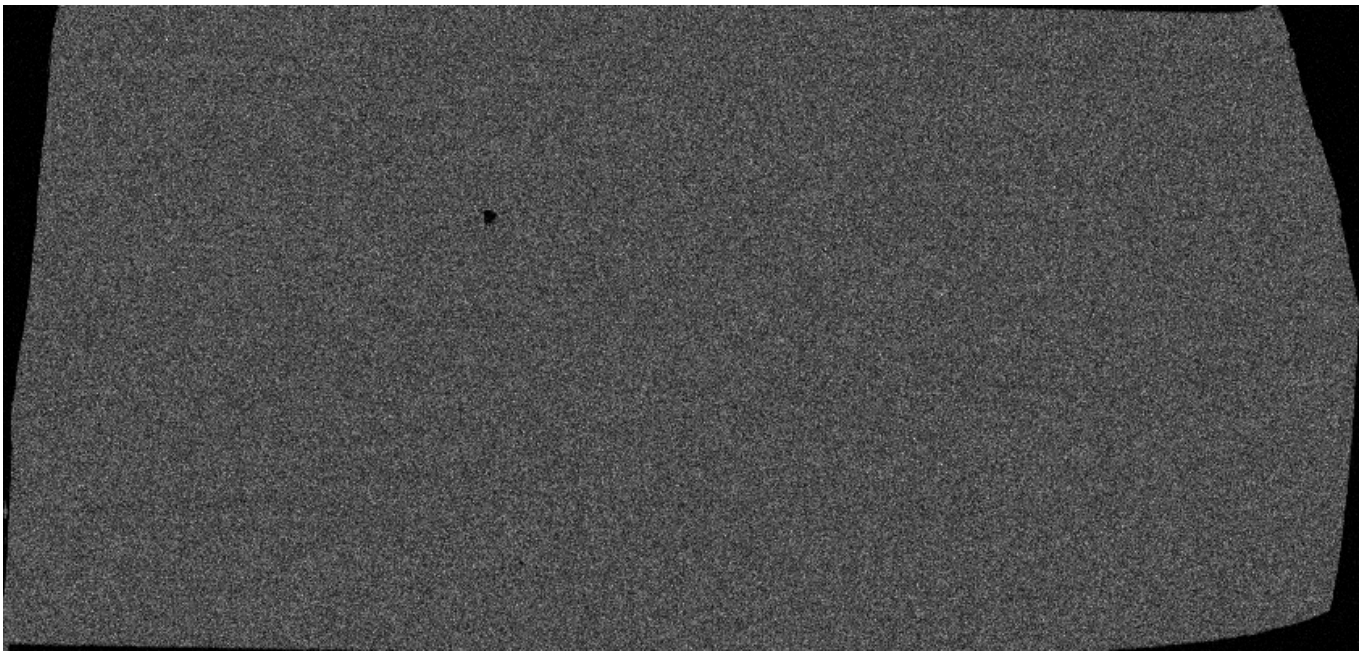

**Figure A22** Mn greyscale map for sample 4081

**Figure A23** Ca greyscale map for sample 4081

**Figure A24** S greyscale map for sample 4081

A.1.6 4068

**Figure A25** Ti greyscale map for sample 4068

**Figure A26** Nb greyscale map for sample 4068

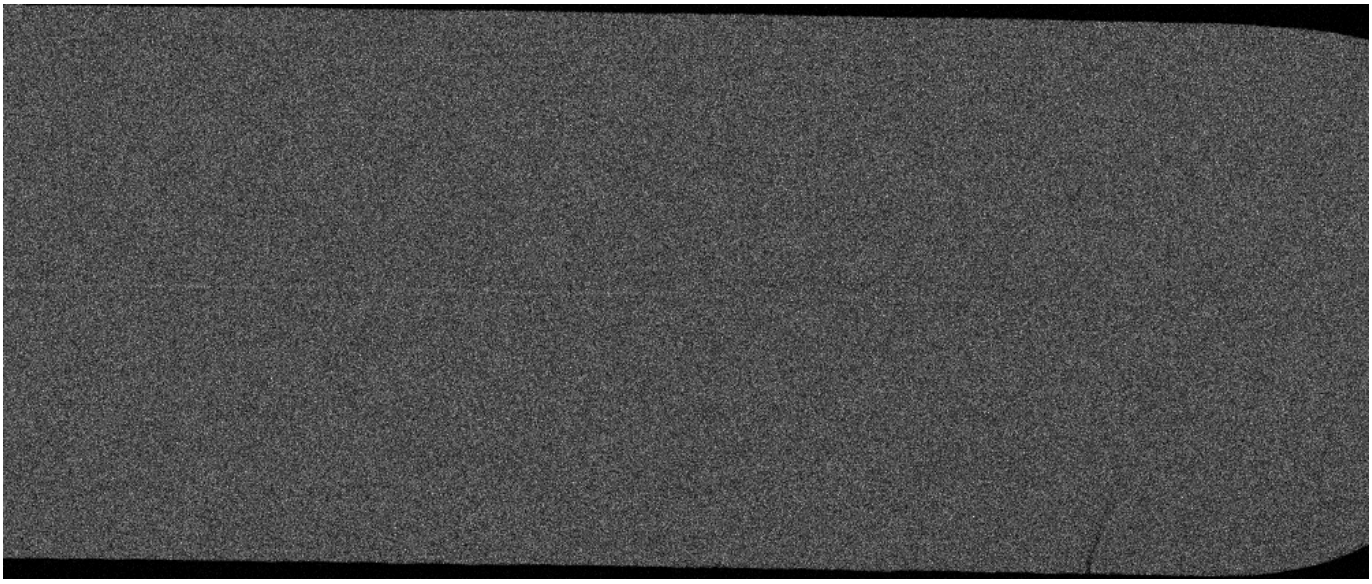

**Figure A27** Mn greyscale map for sample 4068

**Figure A28** Ca greyscale map for sample 4068

**Figure A29** S greyscale map for sample 4068

A.1.7 4093

**Figure A30** Ti greyscale map for sample 4093

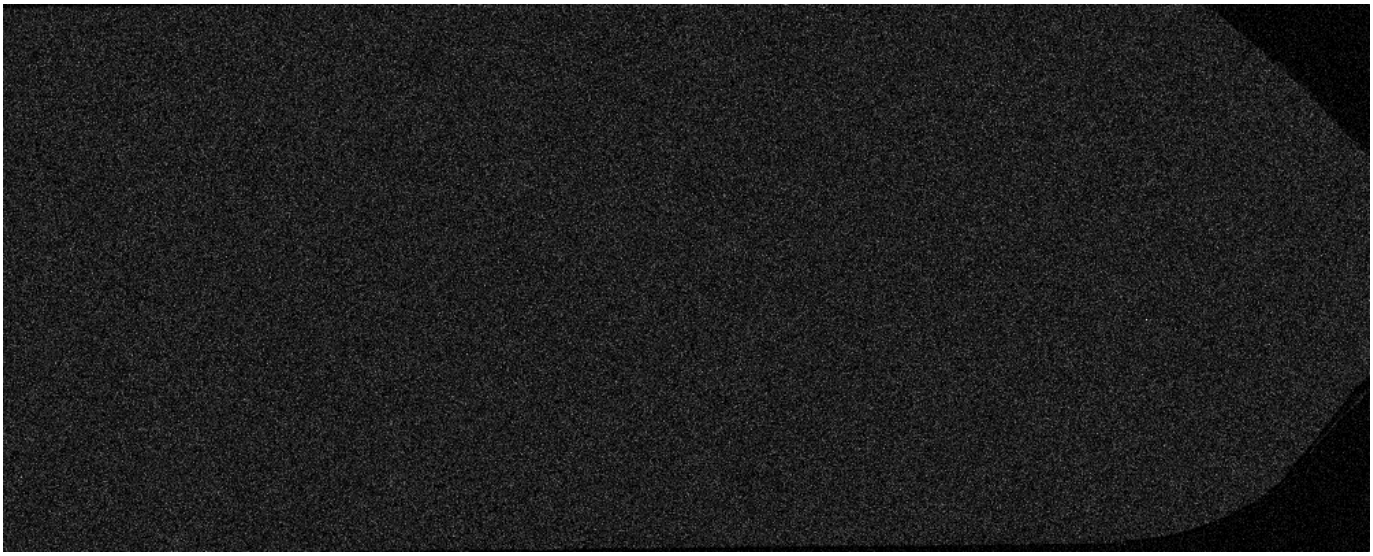

**Figure A31** Nb greyscale map for sample 4093

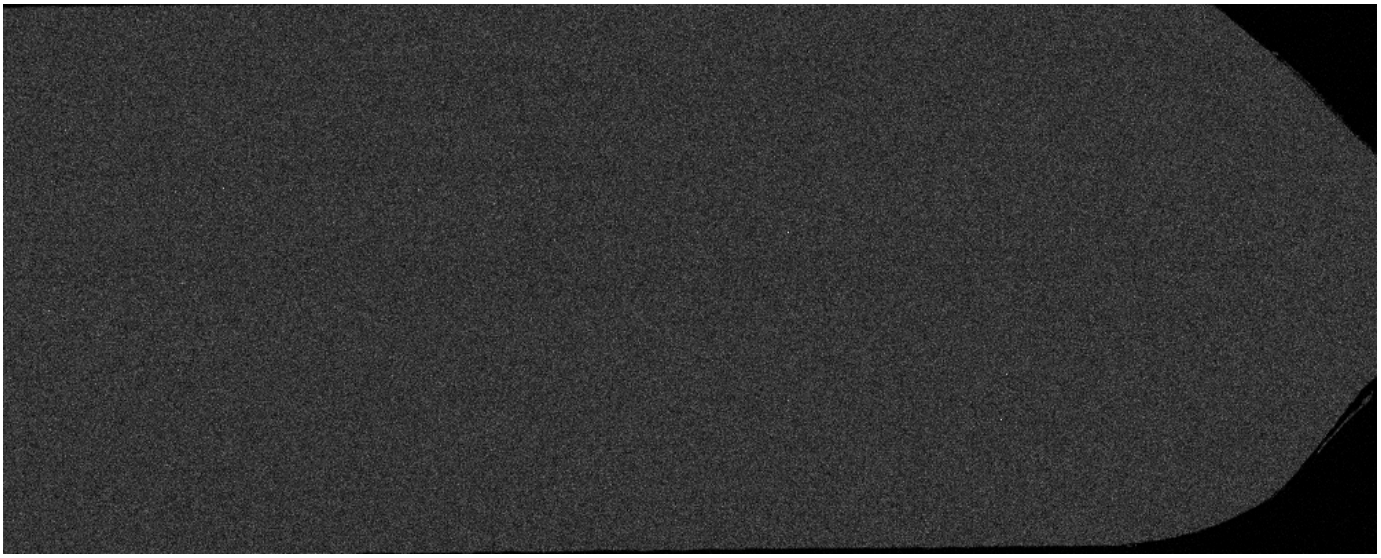

**Figure A32** Mn greyscale map for sample 4093

**Figure A33** Ca greyscale map for sample 4093

**Figure A34** S greyscale map for sample 4093

## A.2 Inverted Greyscale Images

### A.2.1 4175

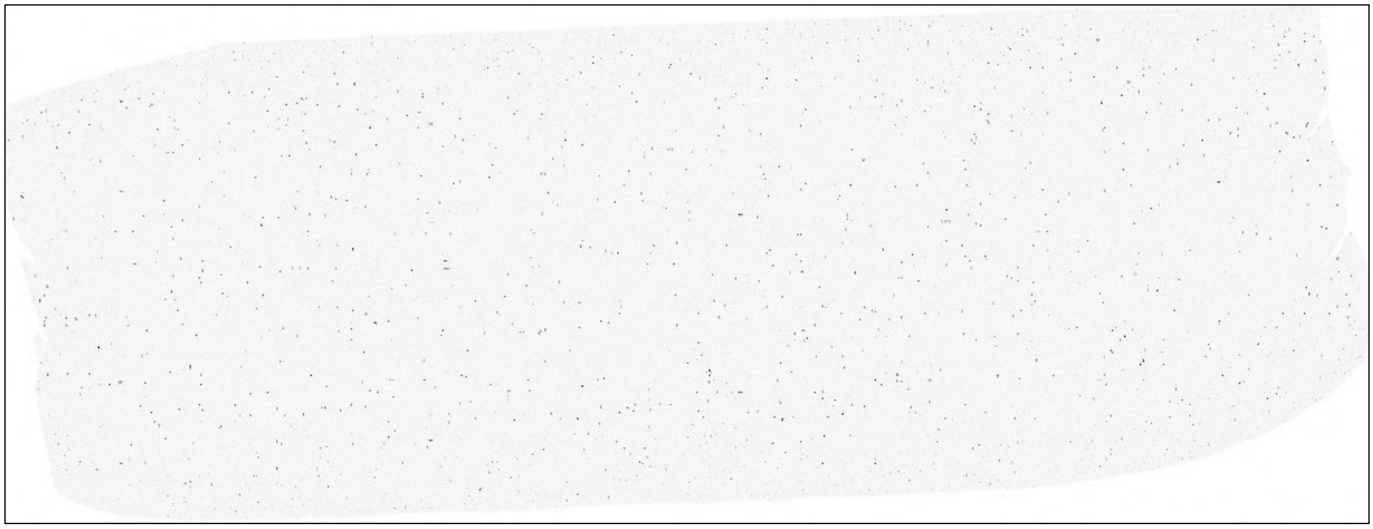

**Figure A35** Inverted Ti greyscale map for sample 4175

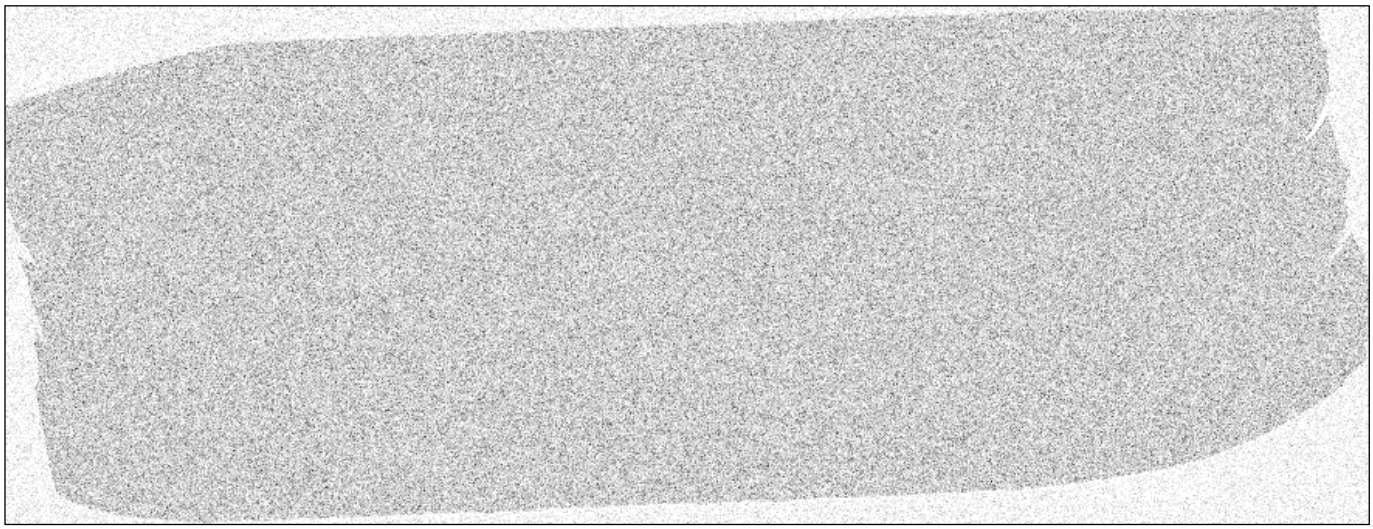

**Figure A36** Inverted Nb greyscale map for sample 4175

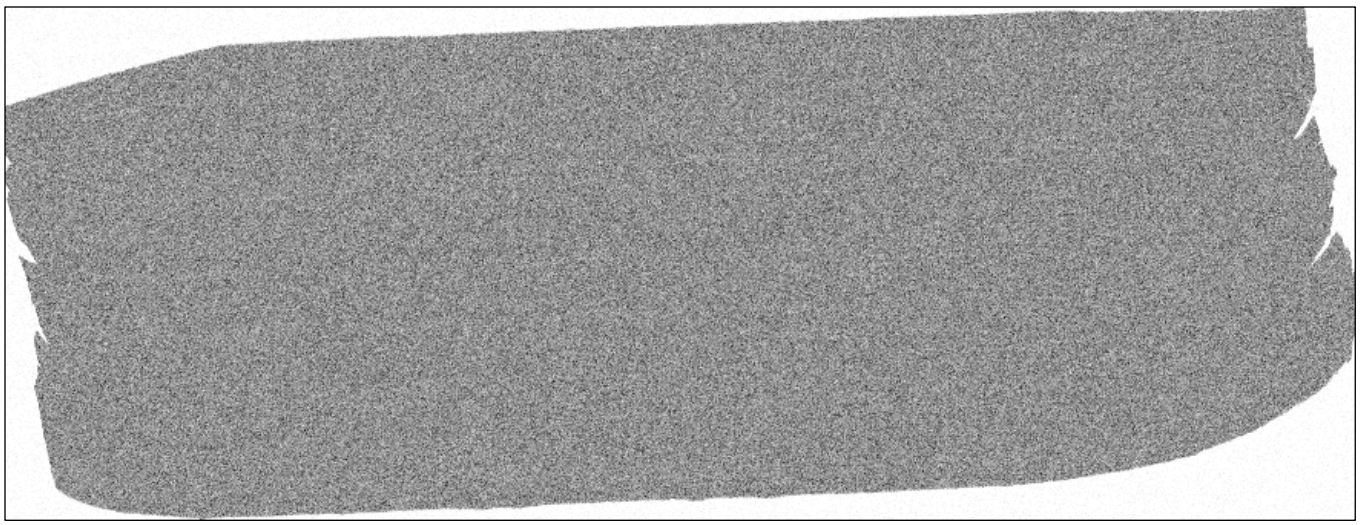

**Figure A37** Inverted Mn greyscale map for sample 4175

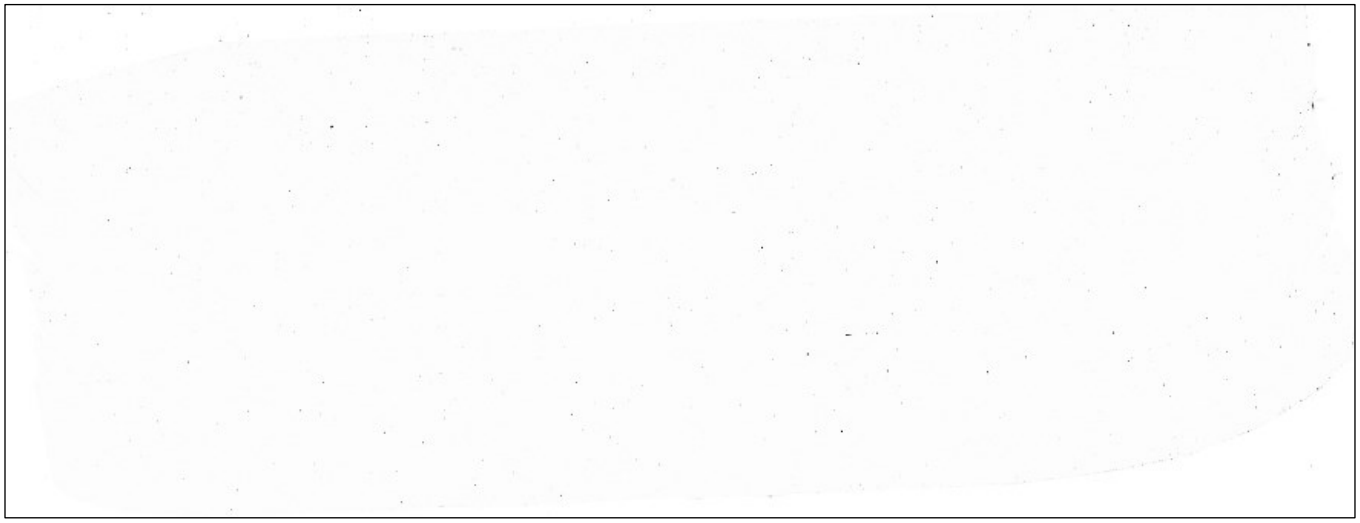

**Figure A38** Inverted Ca greyscale map for sample 4175

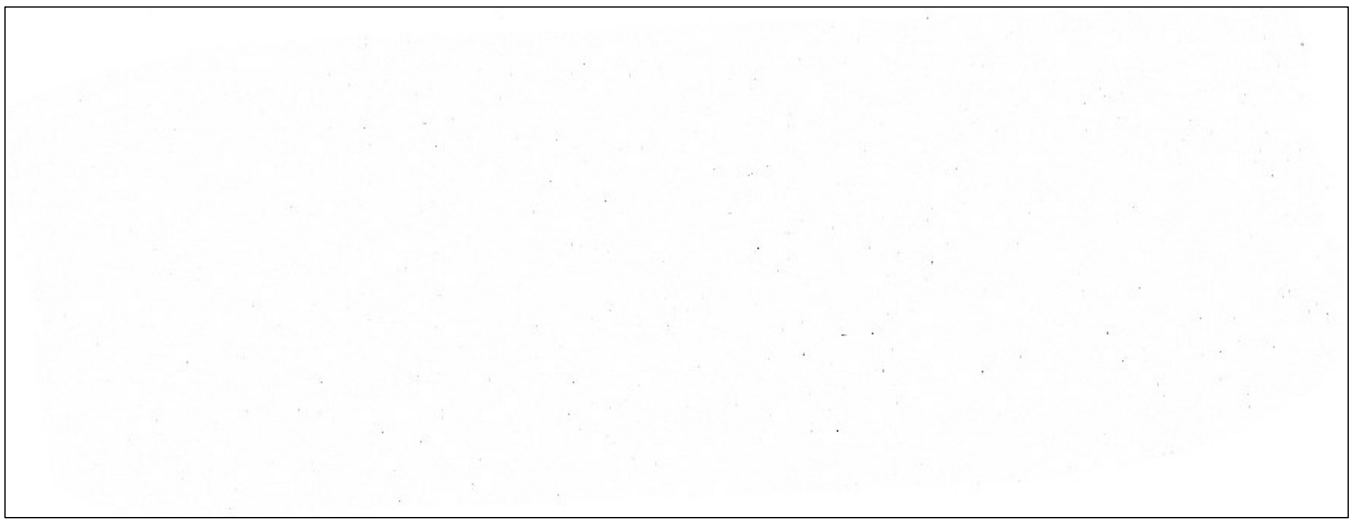

**Figure A39** Inverted S greyscale map for sample 4175

A.2.2 4372

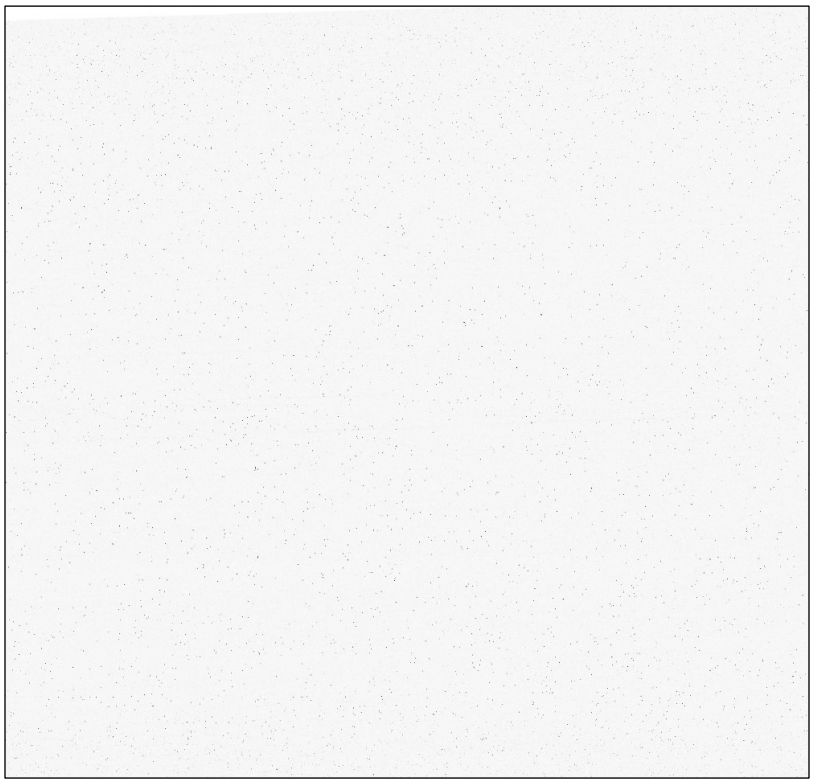

**Figure A40** Inverted Ti greyscale map for sample 4372

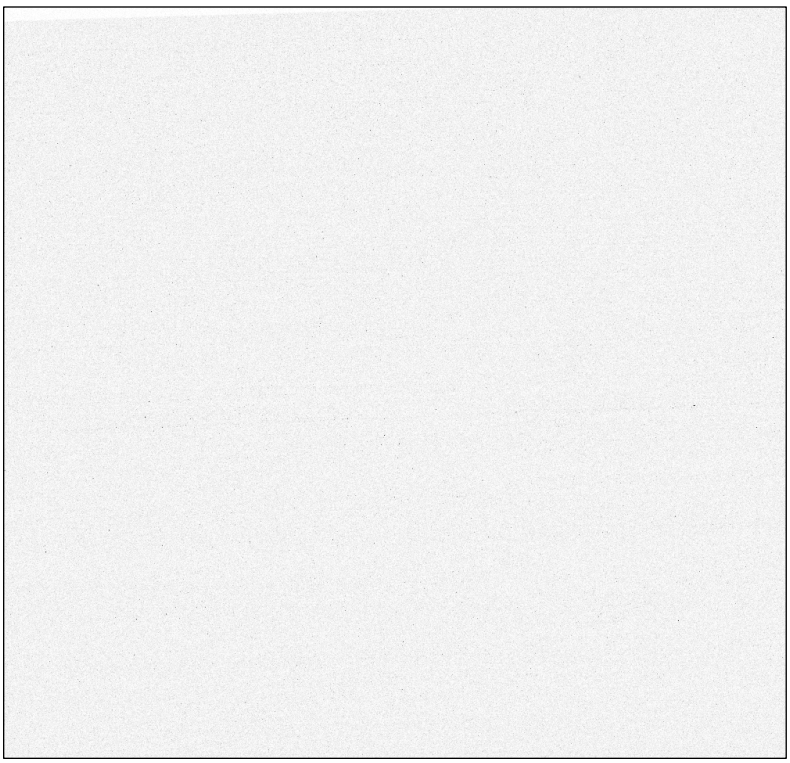

**Figure A41** Inverted Nb greyscale map for sample 4372

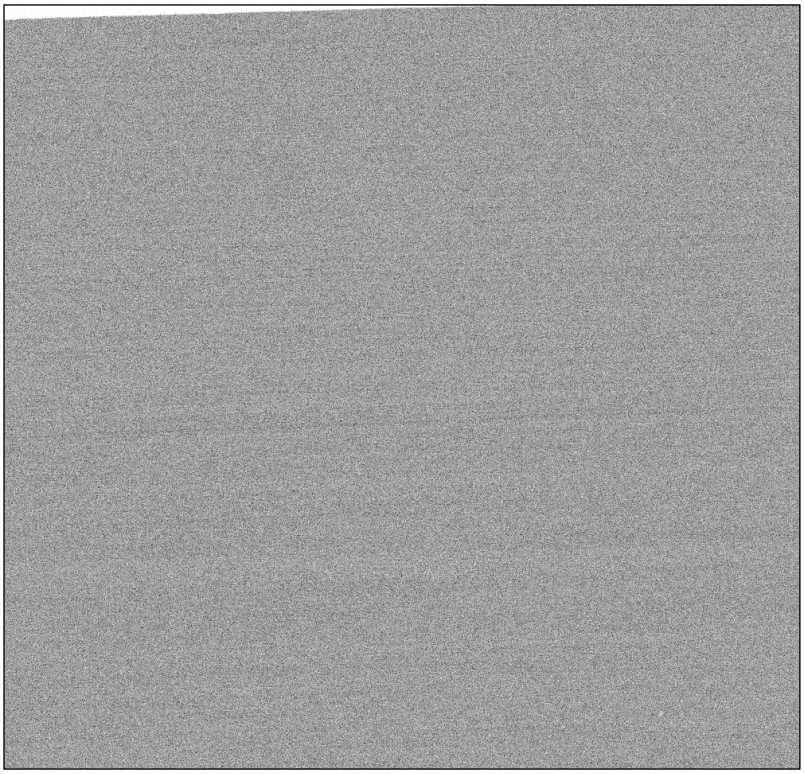

**Figure A42** Inverted Mn greyscale map for sample 4372

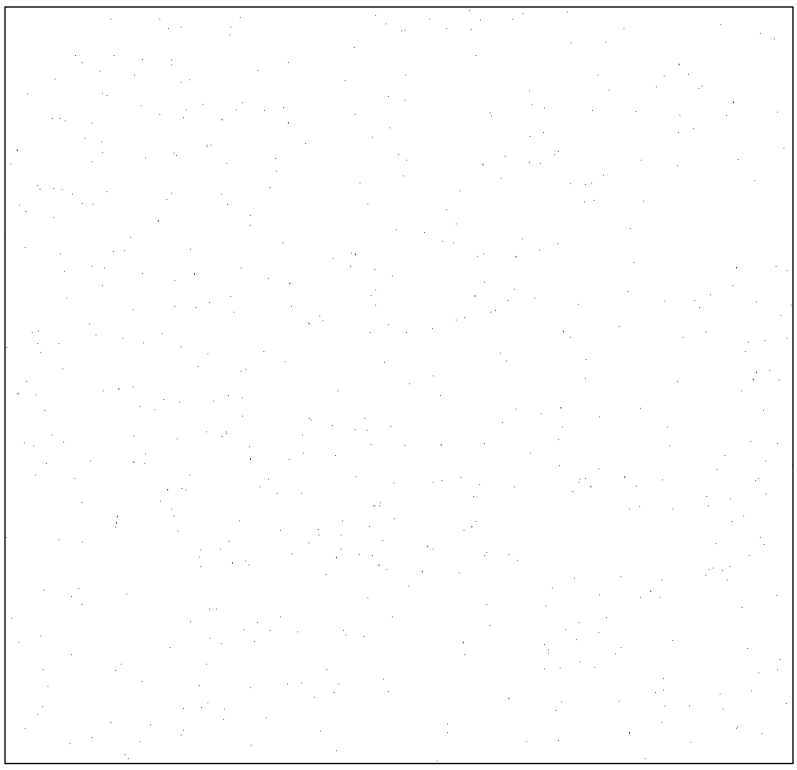

**Figure A43** Inverted Ca greyscale map for sample 4372

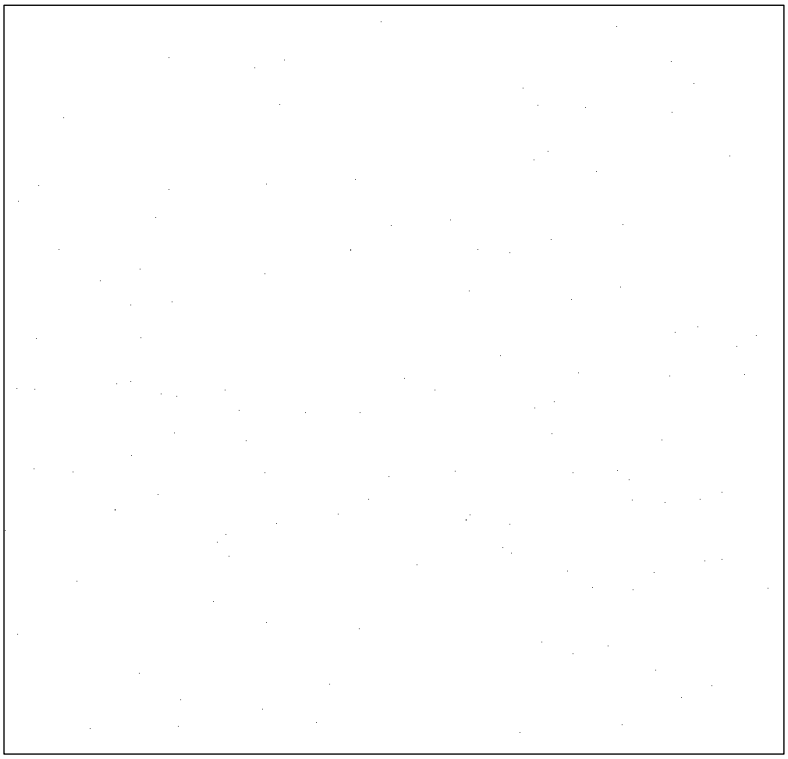

**Figure A44** Inverted S greyscale map for sample 4372

A.2.3 4052

**Figure A45** Inverted Ti greyscale map for sample 4052

**Figure A46** Inverted Nb greyscale map for sample 4052

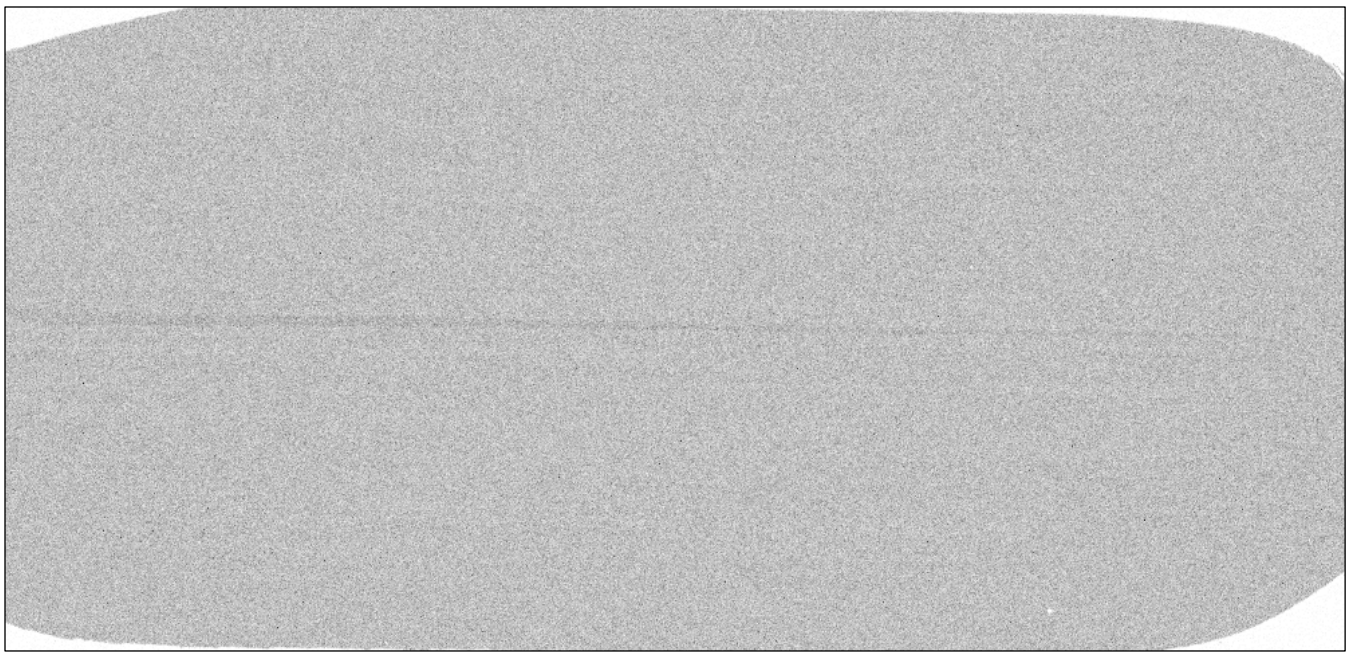

**Figure A47** Inverted Mn greyscale map for sample 4052

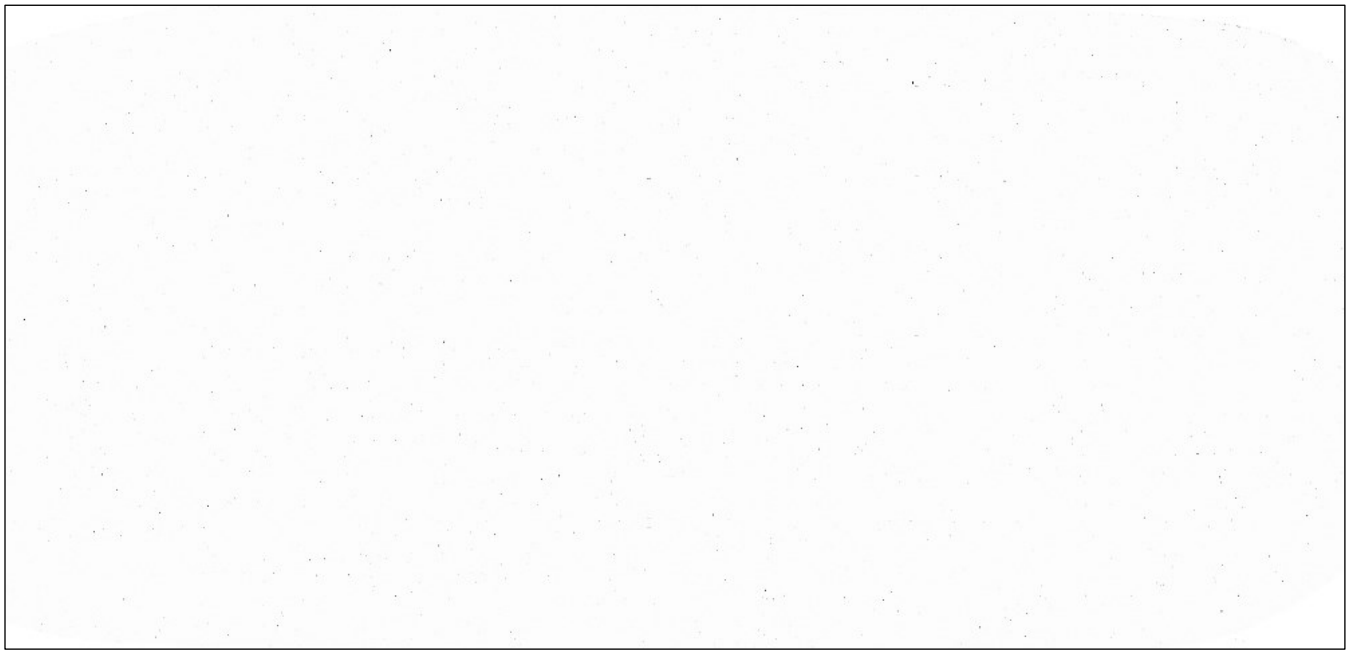

**Figure A48** Inverted Ca greyscale map for sample 4052

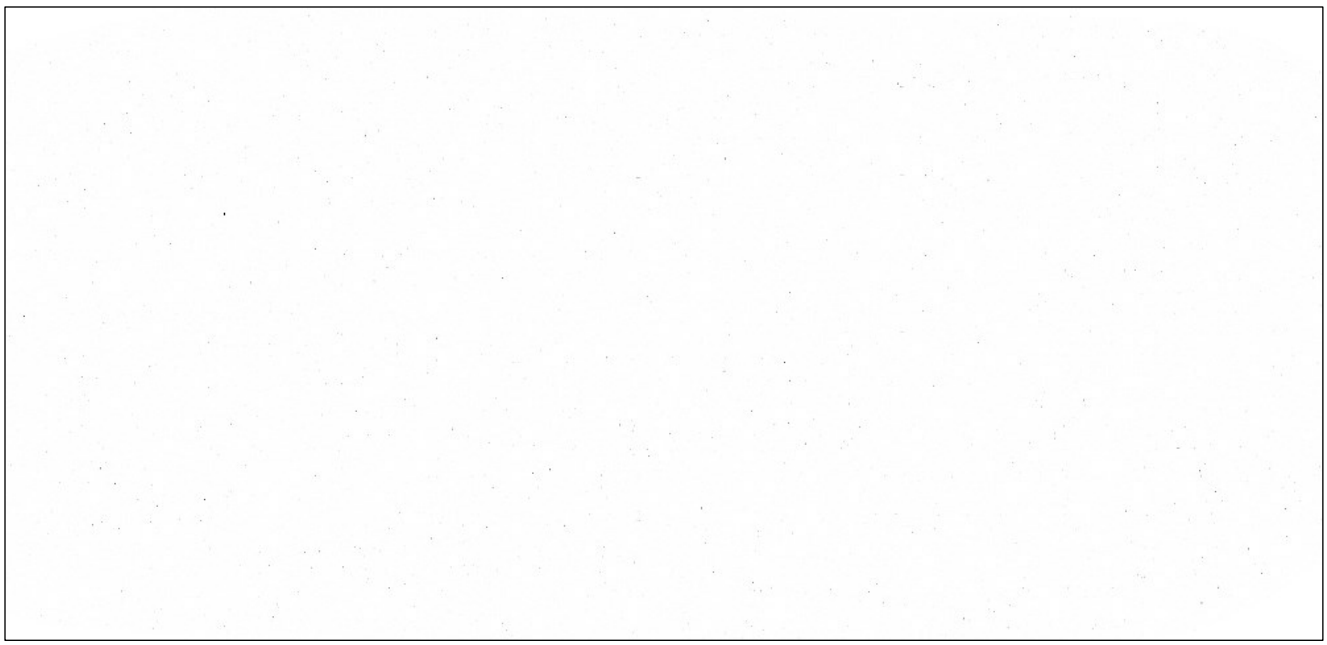

**Figure A49** Inverted S greyscale map for sample 4052

A.2.4 4081

**Figure A50** Inverted Ti greyscale map for sample 4081

**Figure A51** Inverted Nb greyscale map for sample 4081

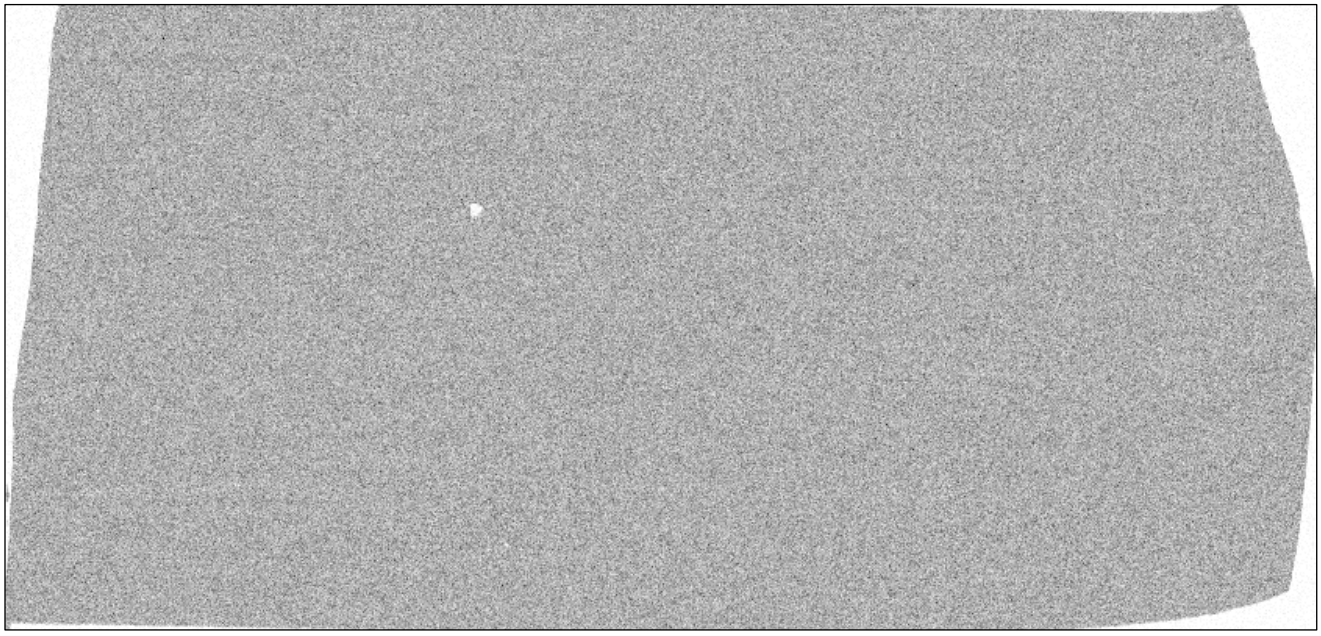

**Figure A52** Inverted Mn greyscale map for sample 4081

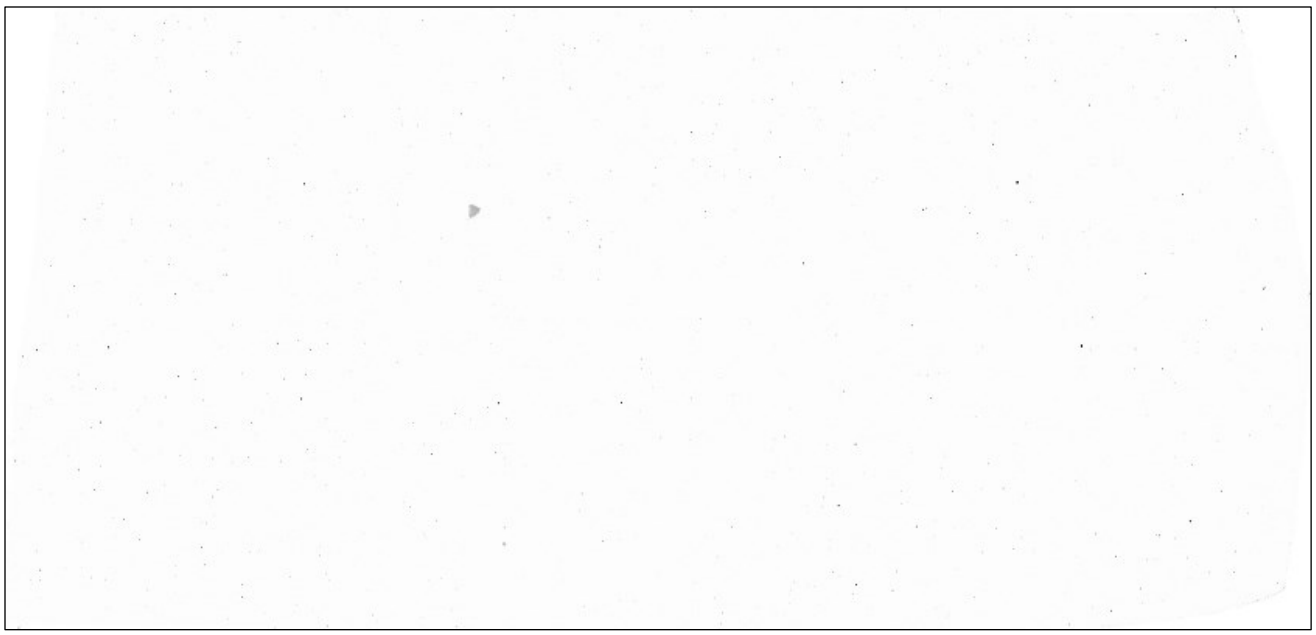

**Figure A53** Inverted Ca greyscale map for sample 4081

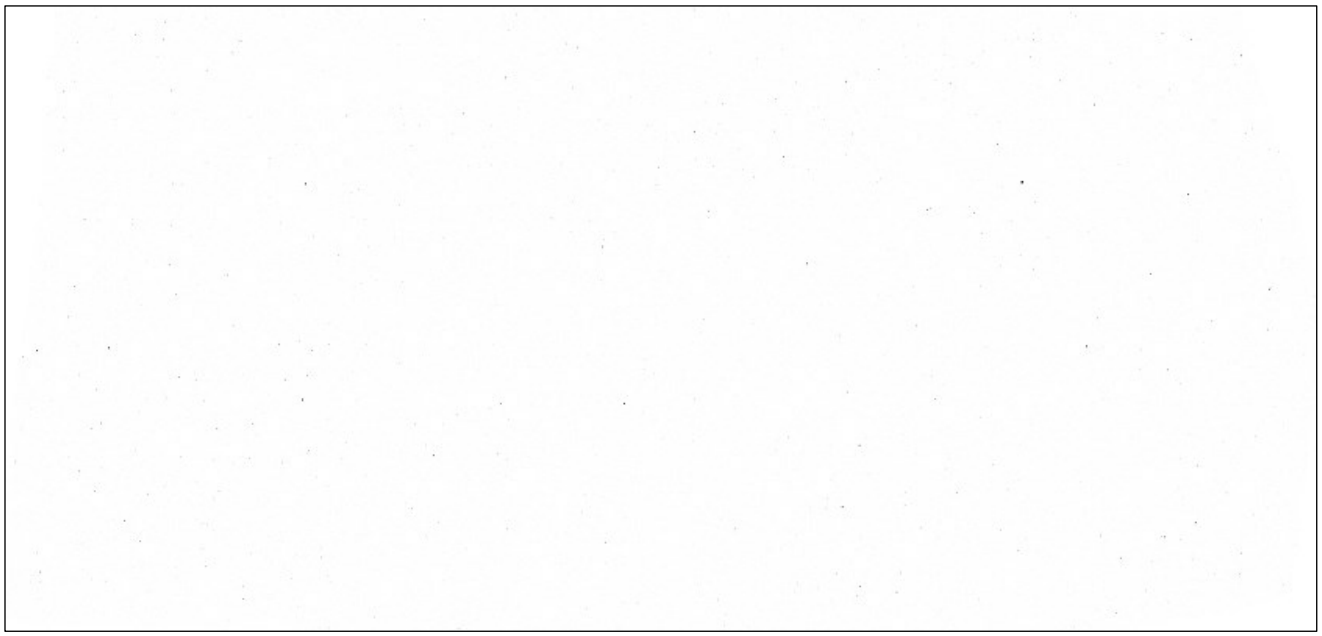

**Figure A54** Inverted S greyscale map for sample 4081

A.2.5 4068

**Figure A55** Inverted Ti greyscale map for sample 4068

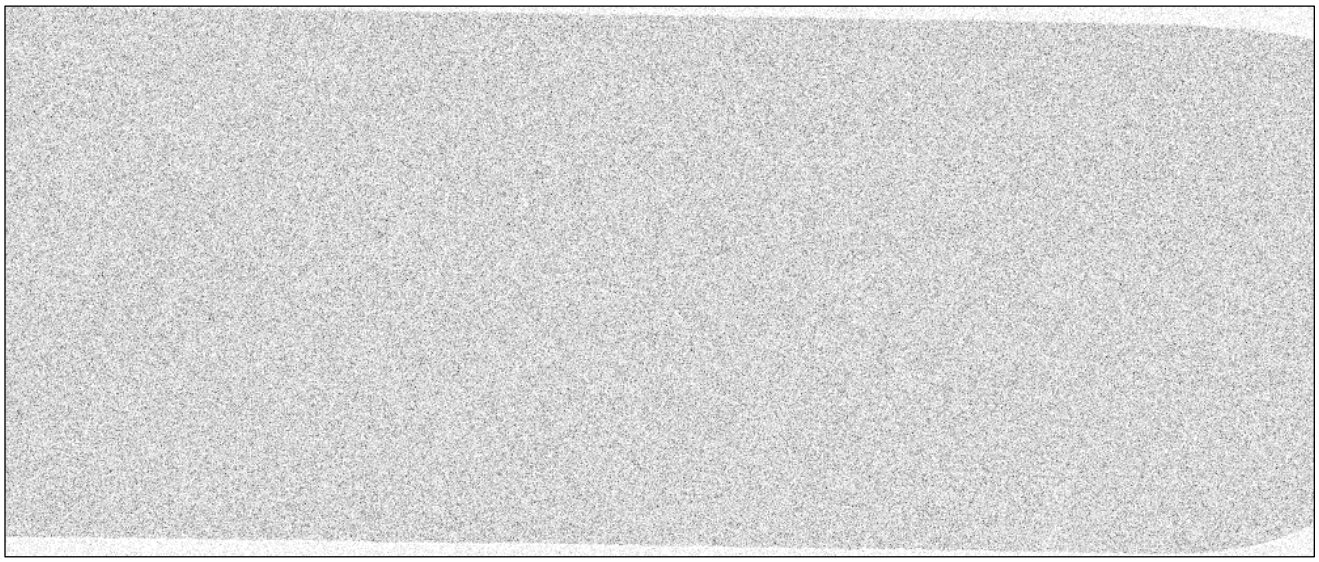

**Figure A56** Inverted Nb greyscale map for sample 4068

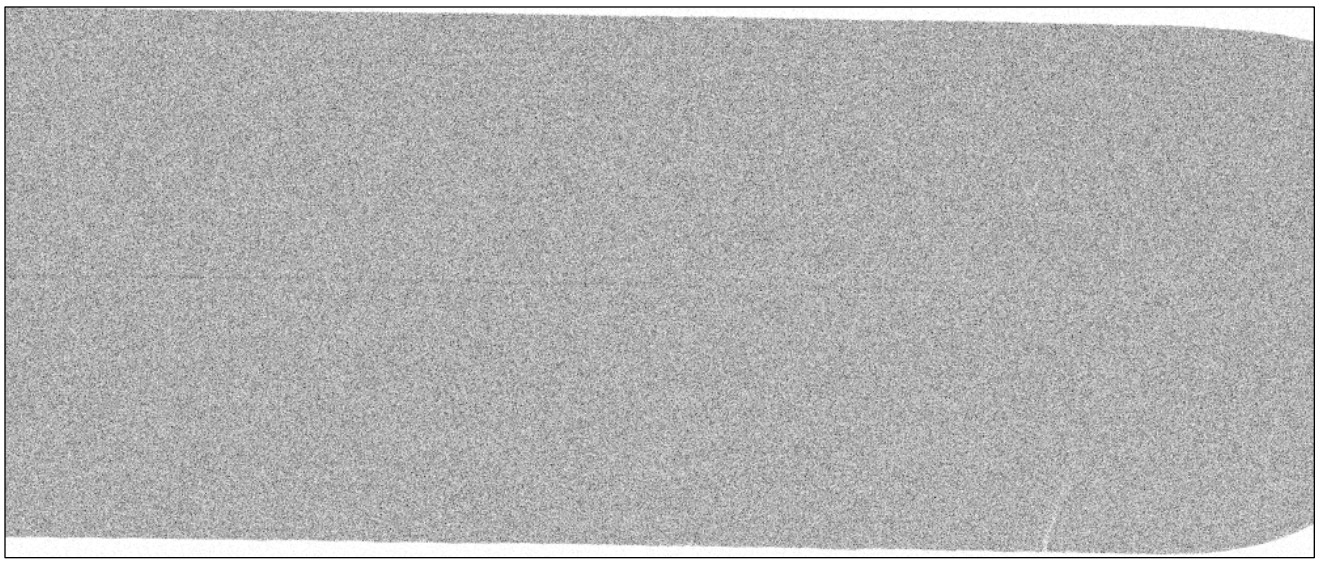

**Figure A57** Inverted Mn greyscale map for sample 4068

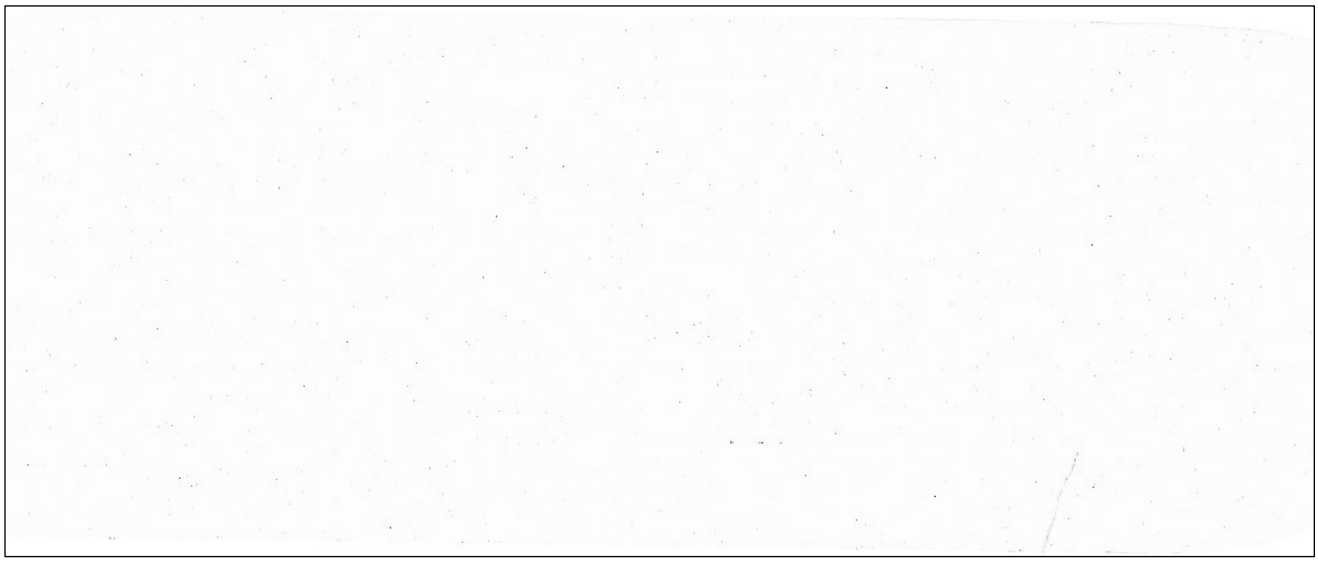

**Figure A58** Inverted Ca greyscale map for sample 4068

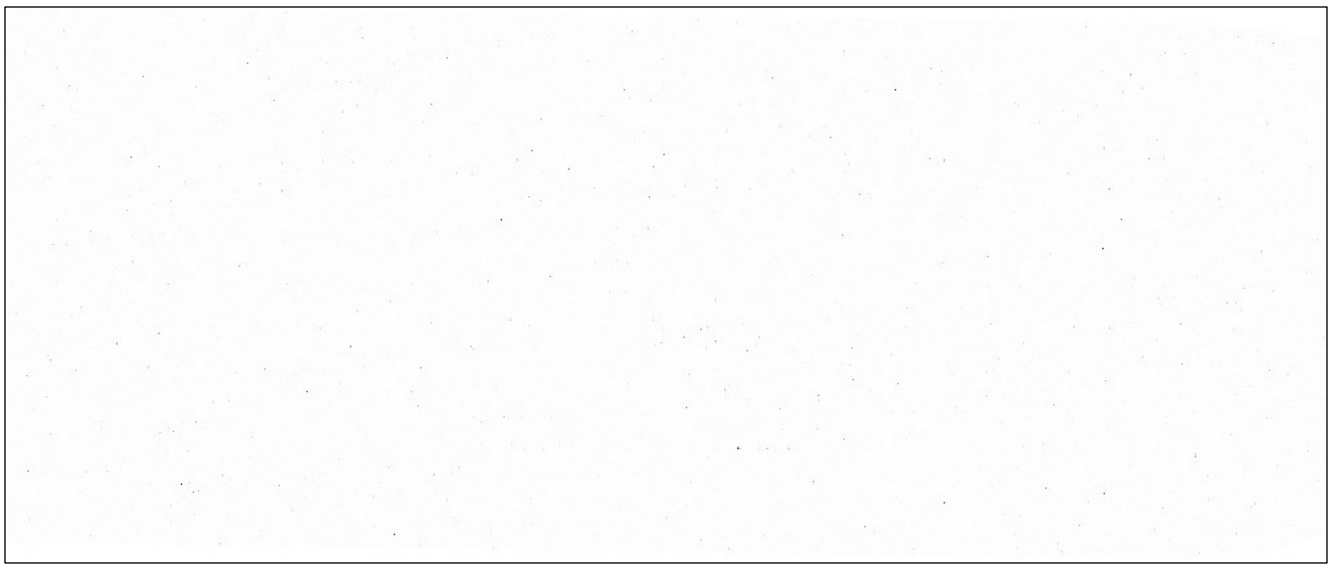

**Figure A59** Inverted S greyscale map for sample 4068

A.2.6 4093

**Figure A60** Inverted Ti greyscale map for sample 4093

**Figure A61** Inverted Nb greyscale map for sample 4093

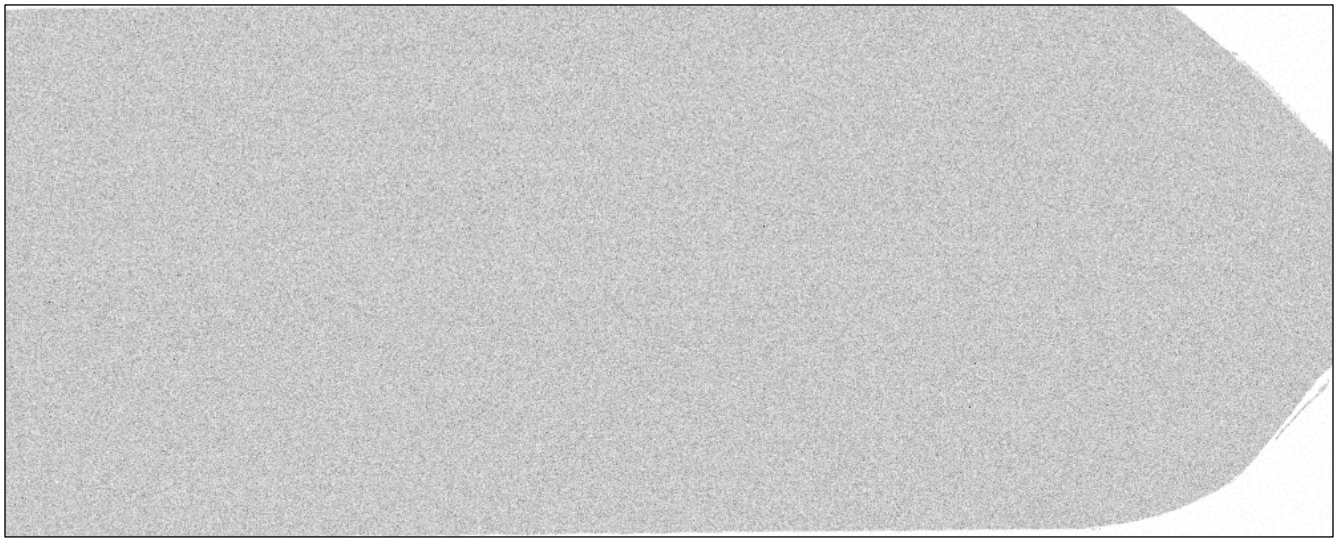

**Figure A62** Inverted Mn greyscale map for sample 4093

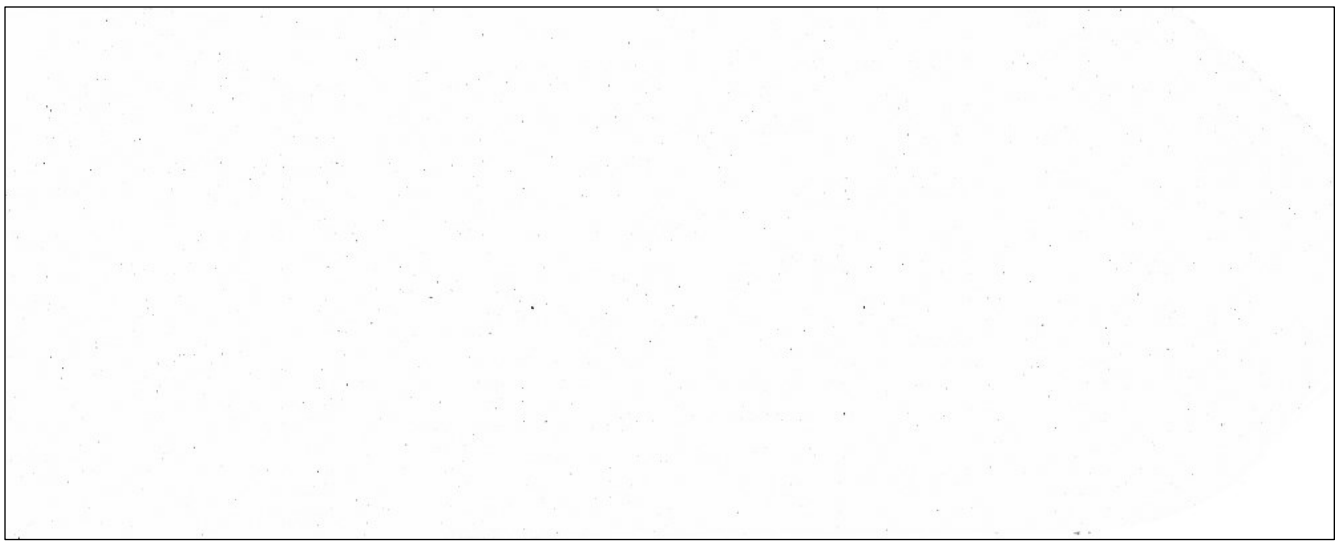

**Figure A63** Inverted Ca greyscale map for sample 4093

**Figure A64** Inverted S greyscale map for sample 4093

# Appendix B – Line Scans

Appendix B presents the line scans and the data collected for Ti, Nb, and Ca concentrations.

## B.1 4175

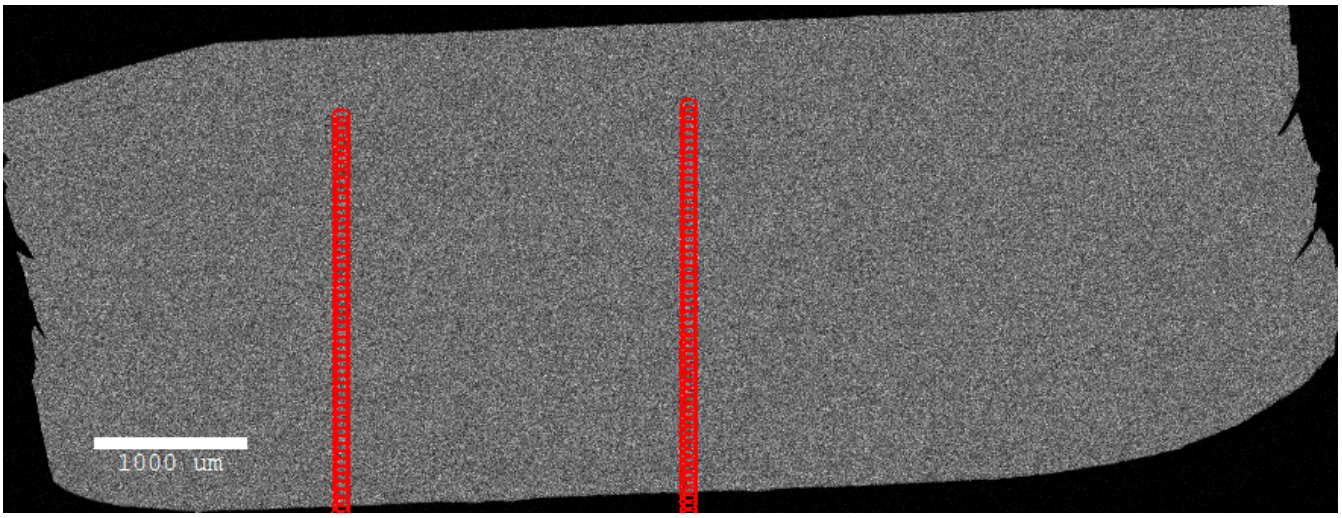


**Figure B1** Line scan location of points for sample 4175

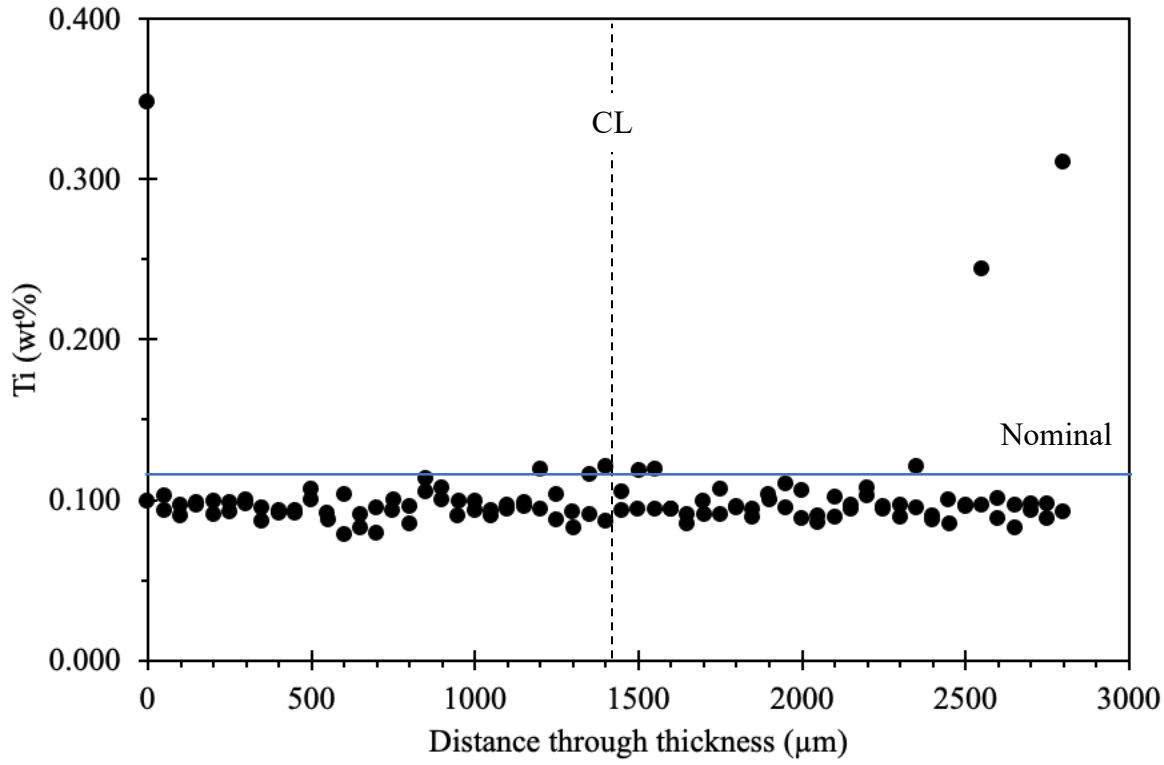


**Figure B2** Weight percent of Ti obtained from EMPA line scan in sample 4175

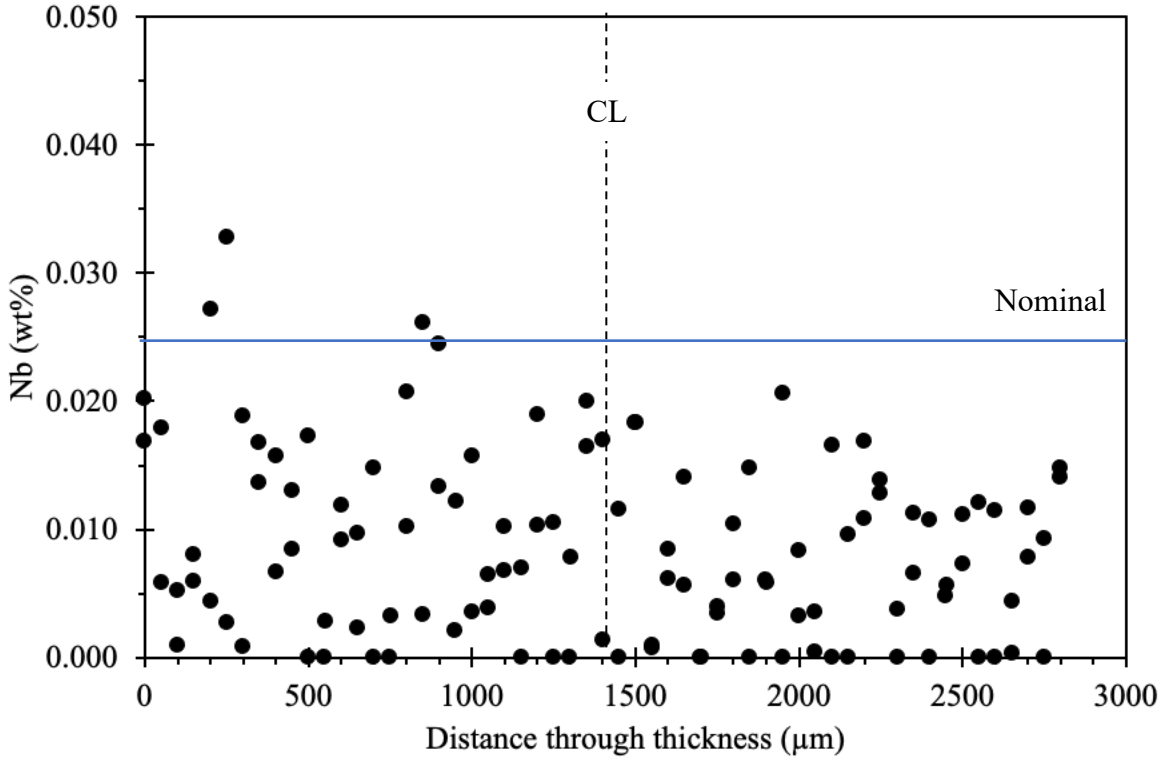


**Figure B3** Weight percent of Nb obtained from EMPA line scan in sample 4175

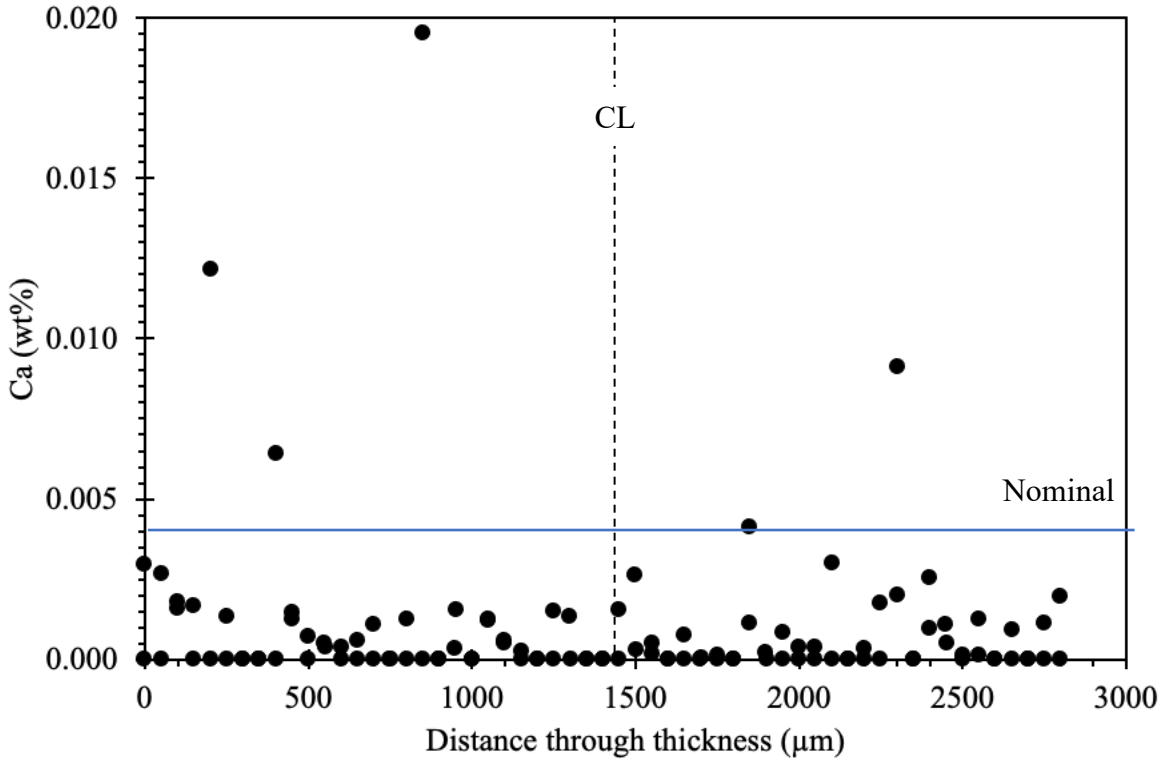


**Figure B4** Weight percent of Ca obtained from EMPA line scan in sample 4175

B.2 4372

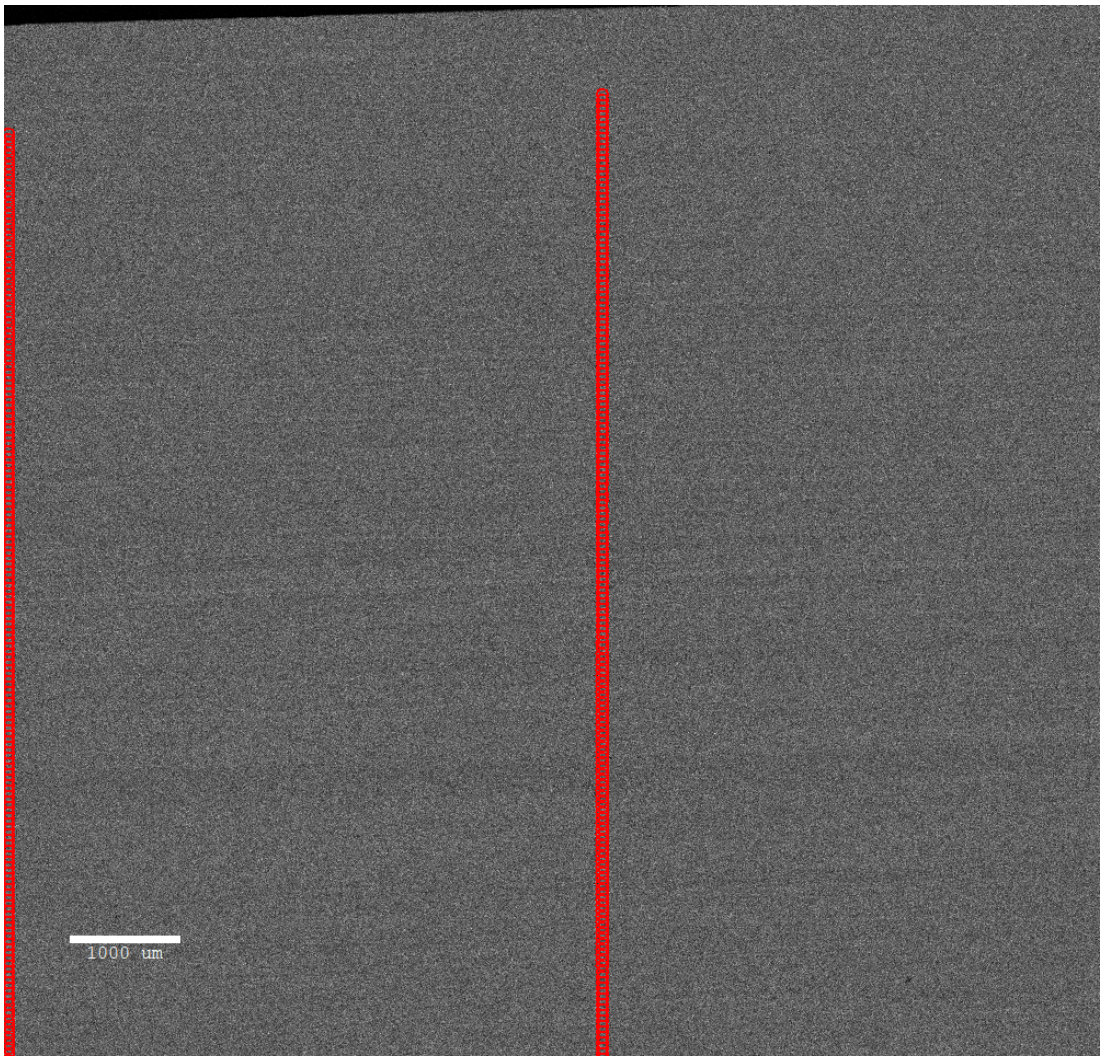


**Figure B5** Line scan location of points for sample 4372

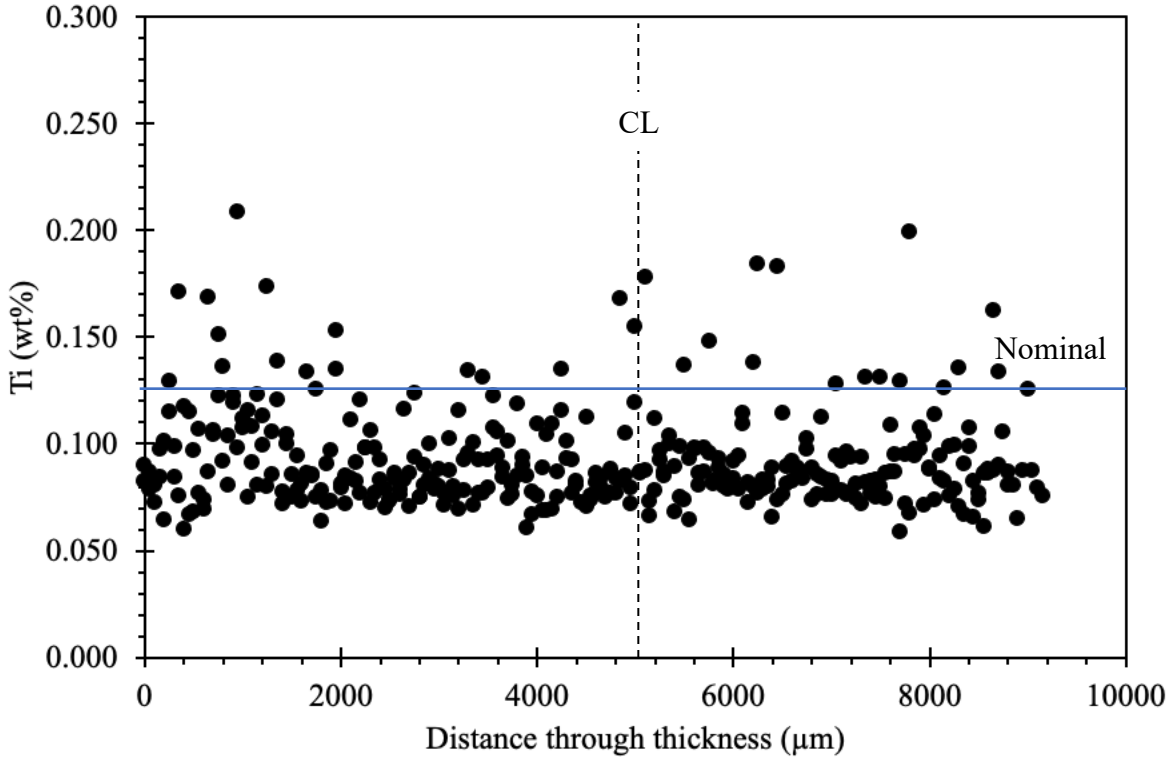


**Figure B6** Weight percent of Ti obtained from EMPA line scan in sample 4372

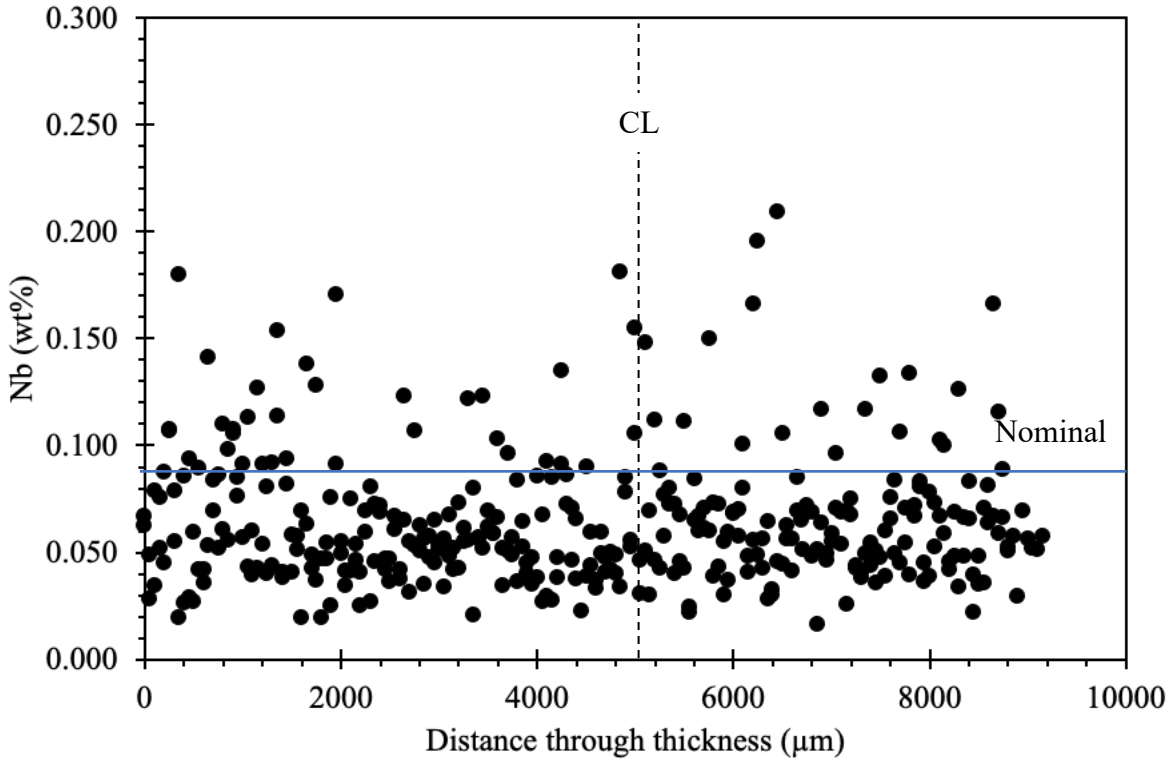


**Figure B7** Weight percent of Nb obtained from EMPA line scan in sample 4372

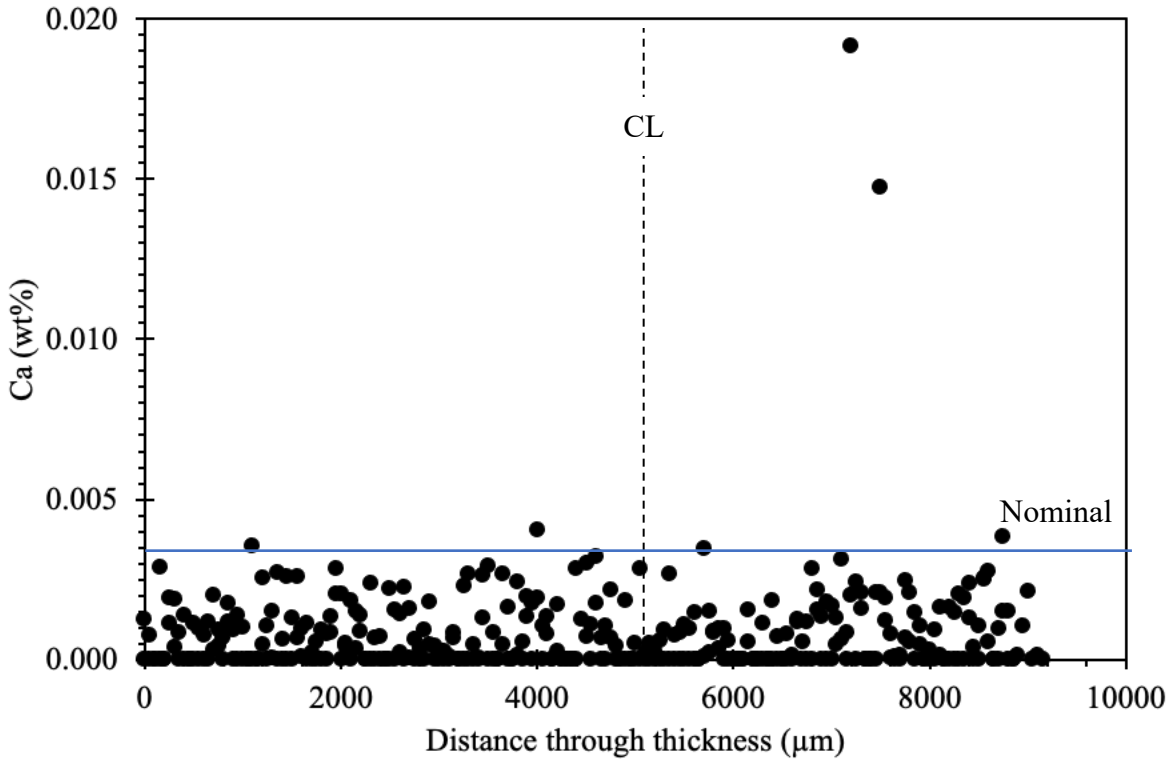


**Figure B8** Weight percent of Ca obtained from EMPA line scan in sample 4372

## B.3 4052

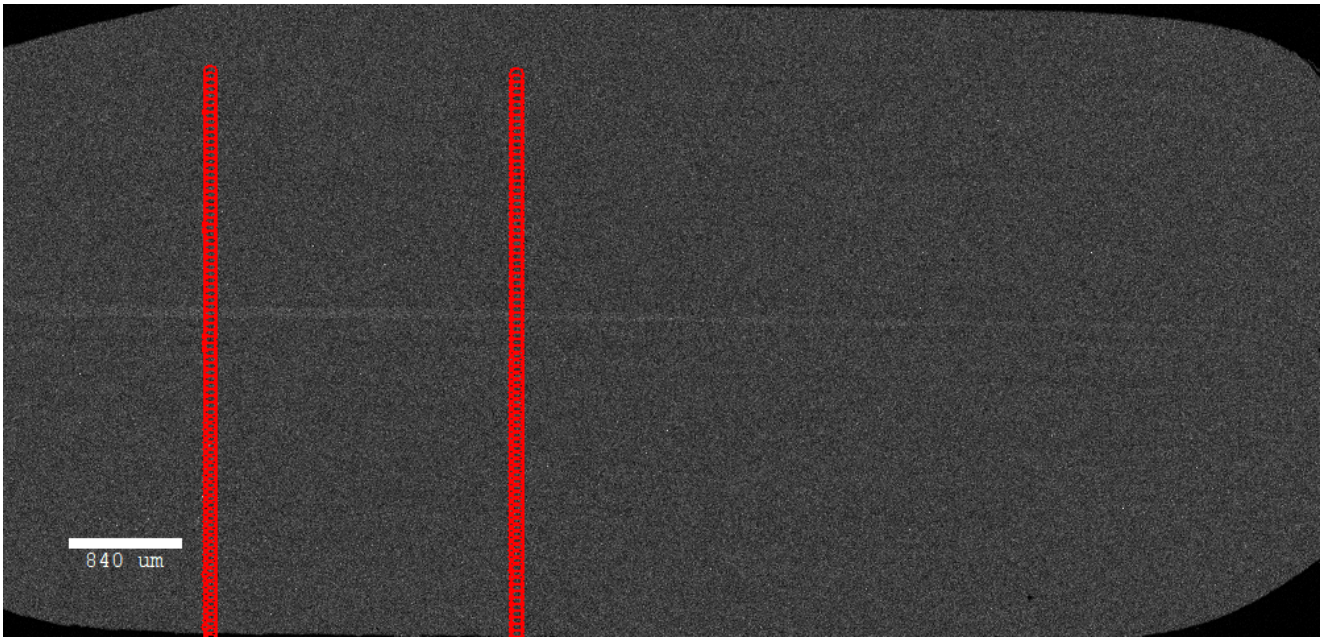


**Figure B9** Line scan location of points for sample 4052

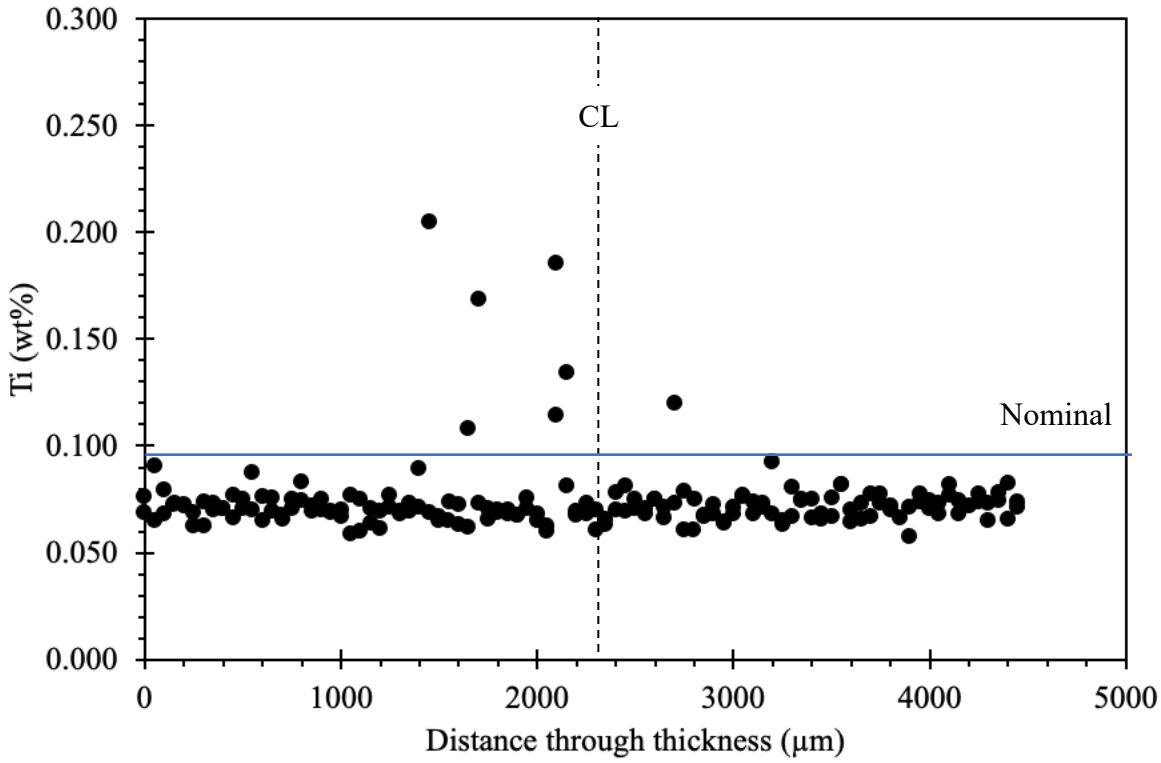


**Figure B10** Weight percent of Ti obtained from EMPA line scan in sample 4052

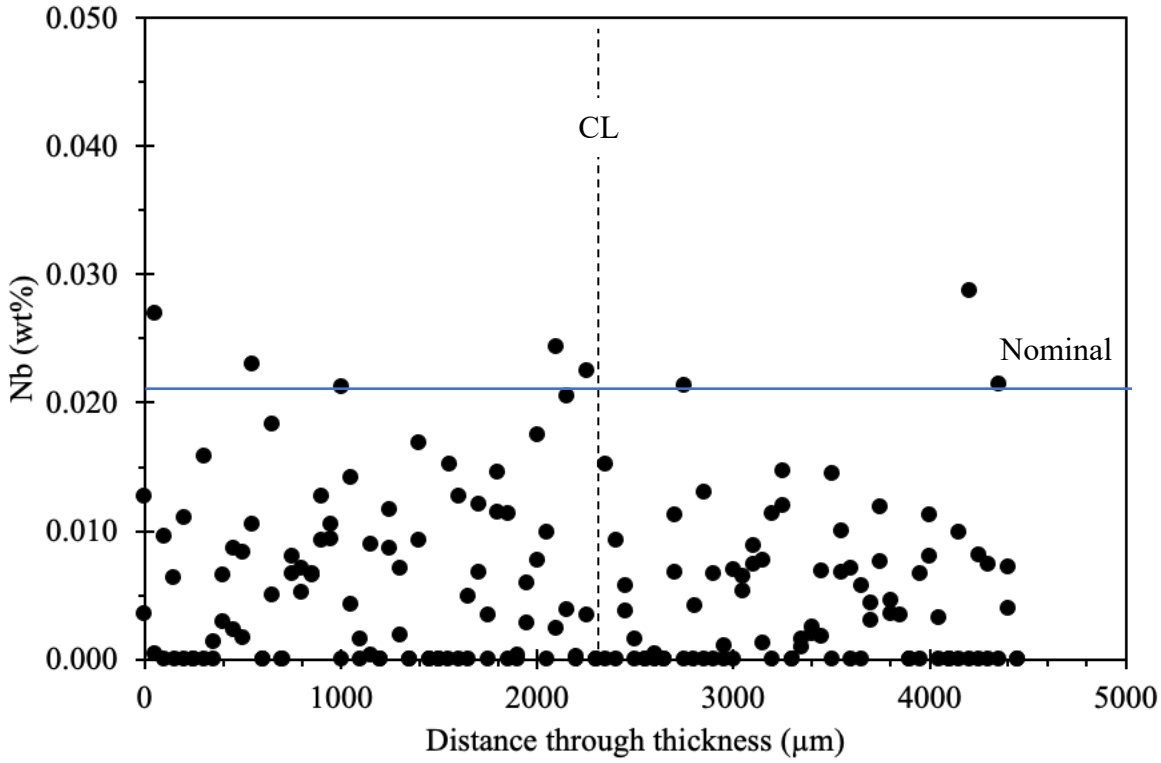


**Figure B11** Weight percent of Nb obtained from EMPA line scan in sample 4052

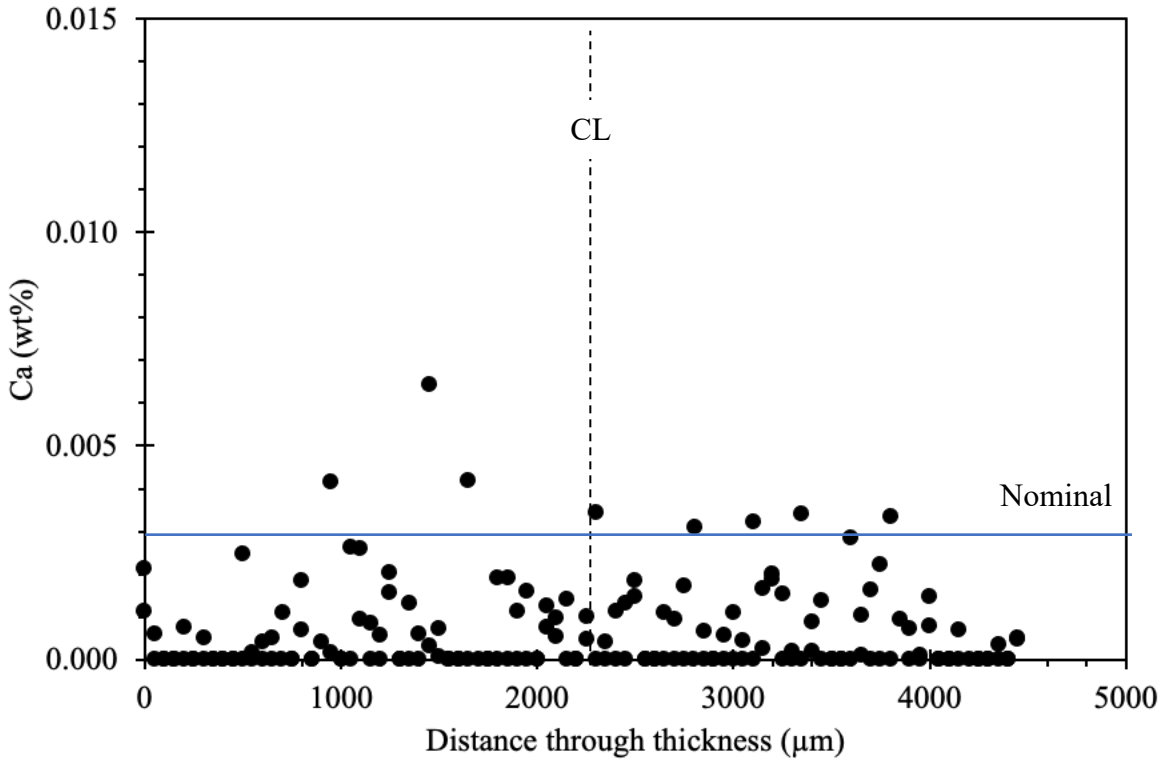


**Figure B12** Weight percent of Ca obtained from EMPA line scan in sample 4052

## B.4 4081

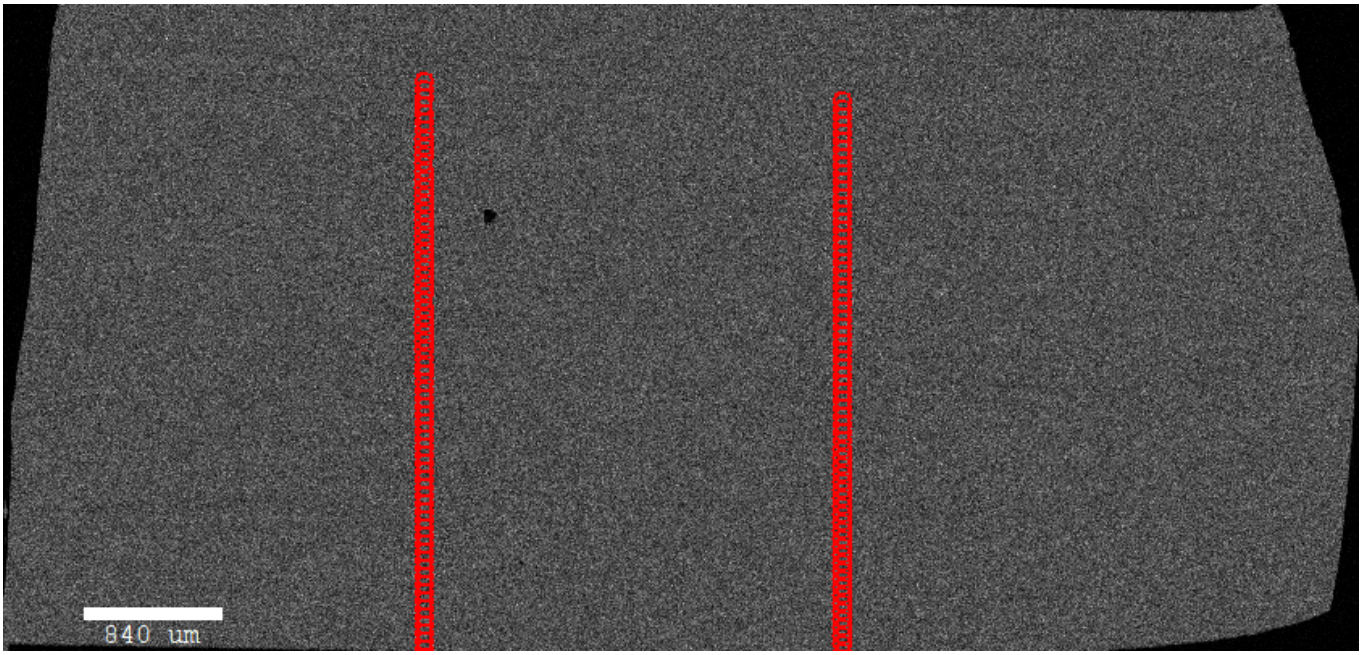


**Figure B13** Line scan location of points for sample 4081

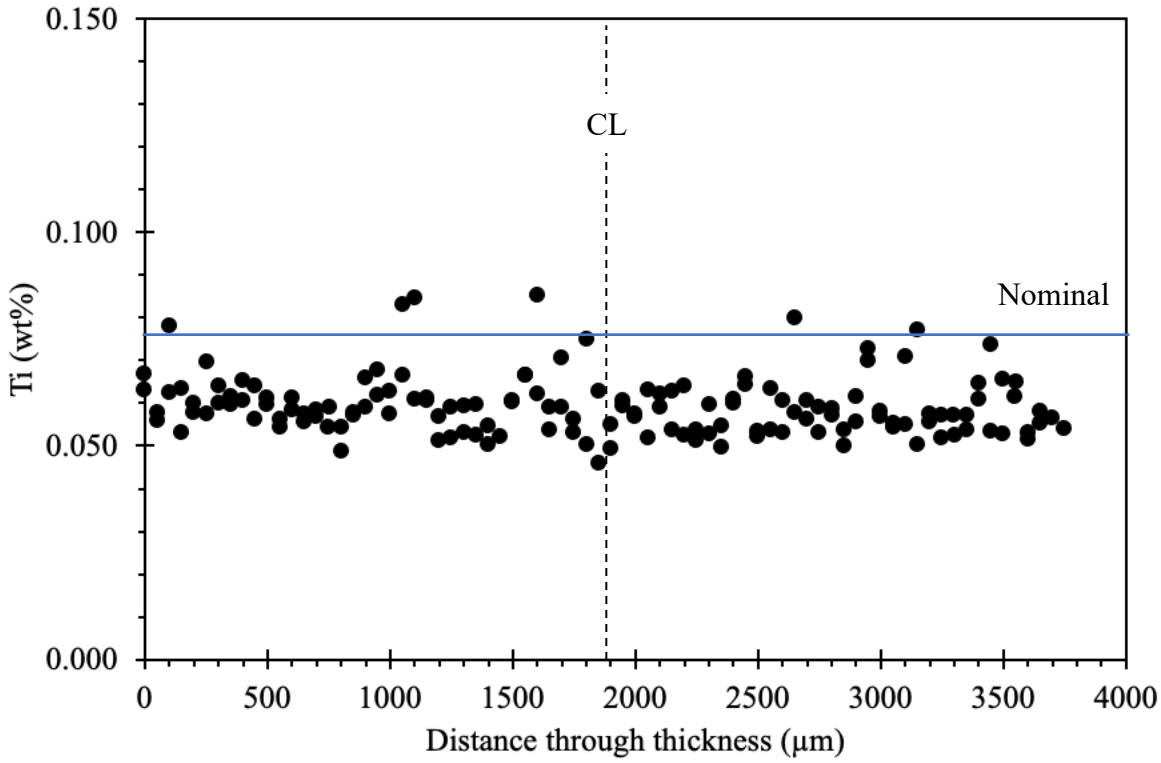


**Figure B14** Weight percent of Ti obtained from EMPA line scan in sample 4081

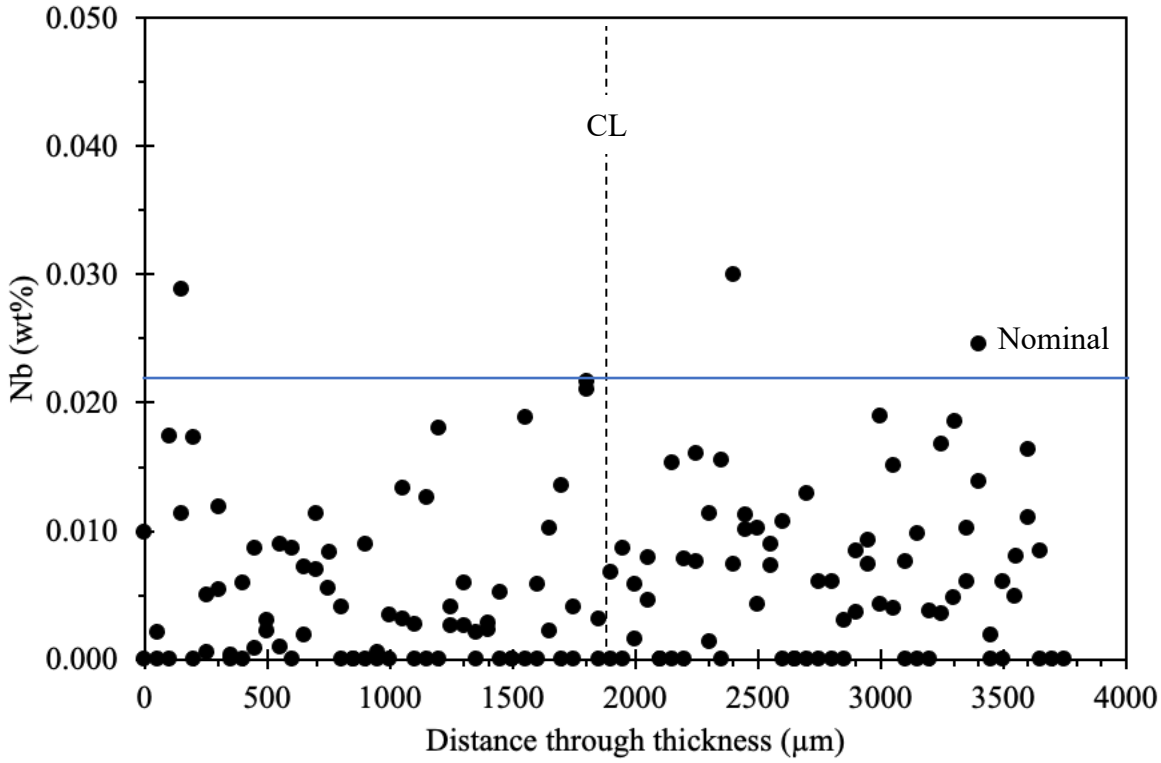


**Figure B15** Weight percent of Nb obtained from EMPA line scan in sample 4081

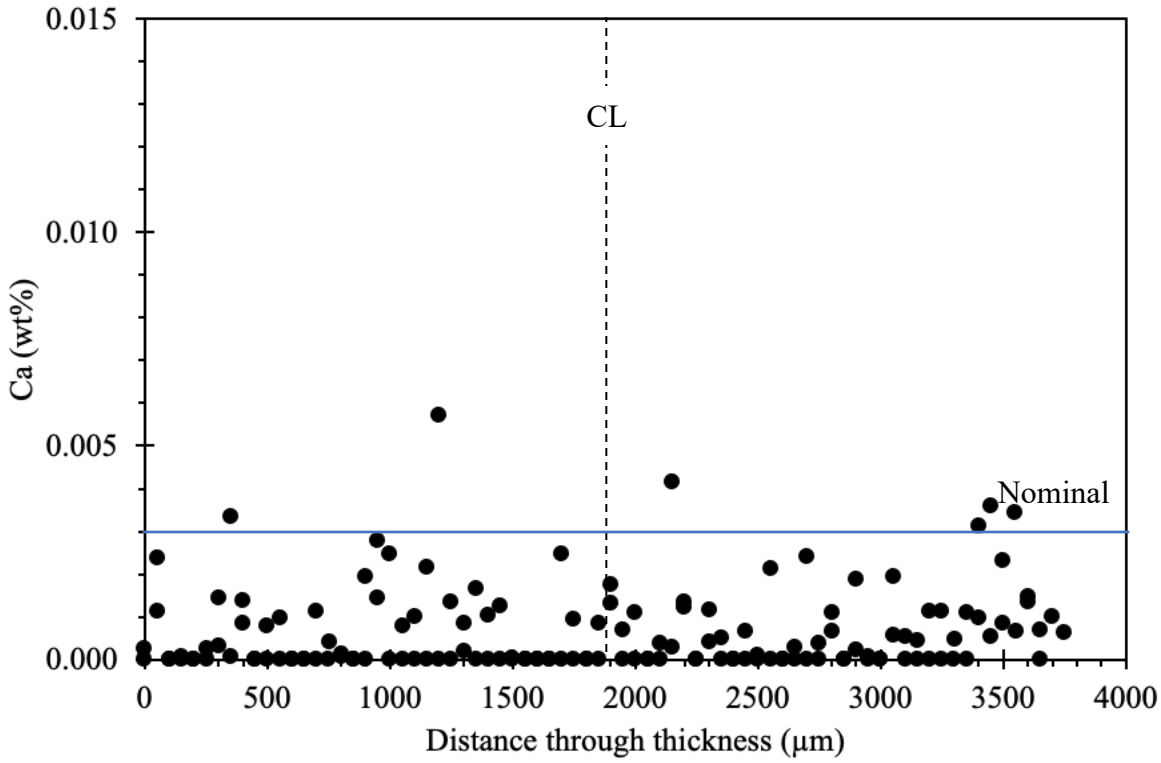


**Figure B16** Weight percent of Ca obtained from EMPA line scan in sample 4081

## B.5 4068

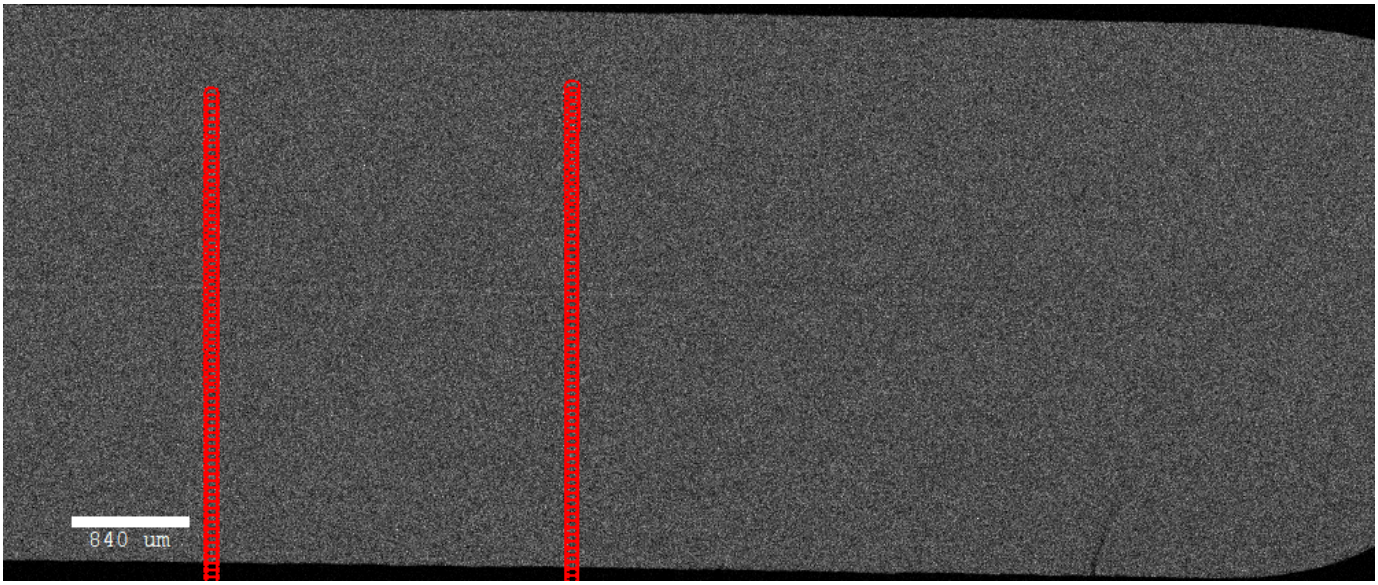


**Figure B17** Line scan location of points for sample 4068

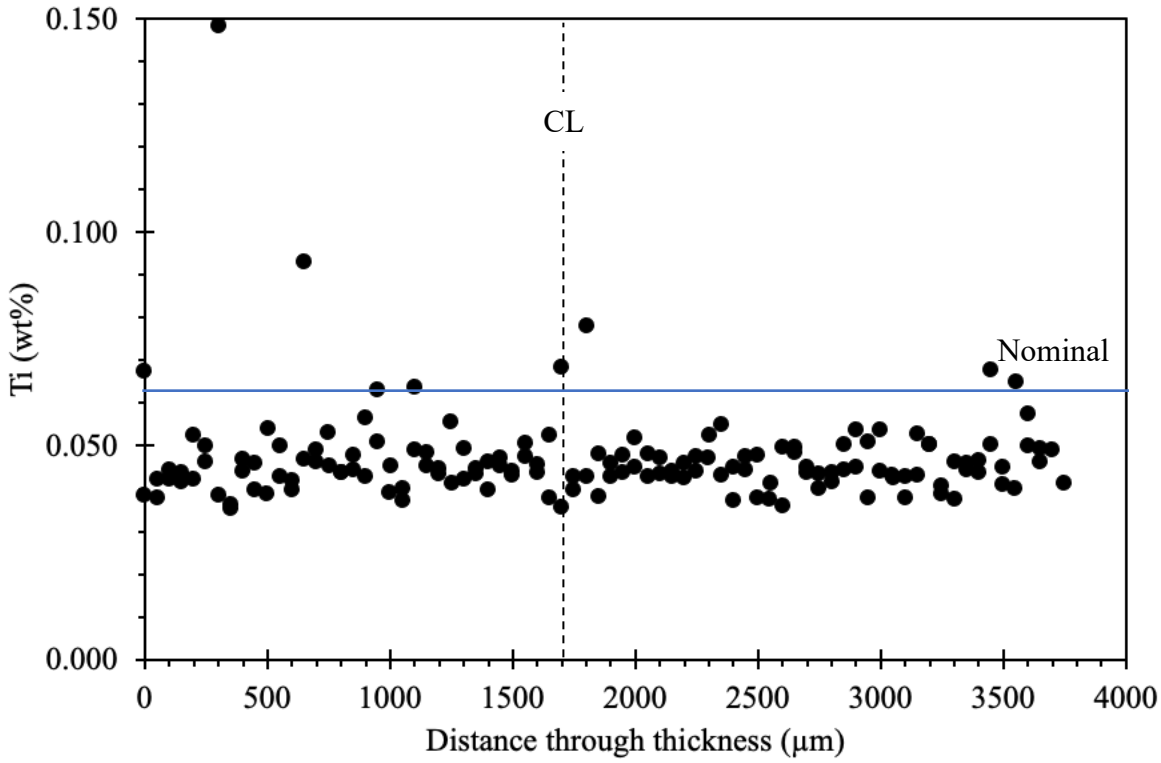


**Figure B18** Weight percent of Ti obtained from EMPA line scan in sample 4068

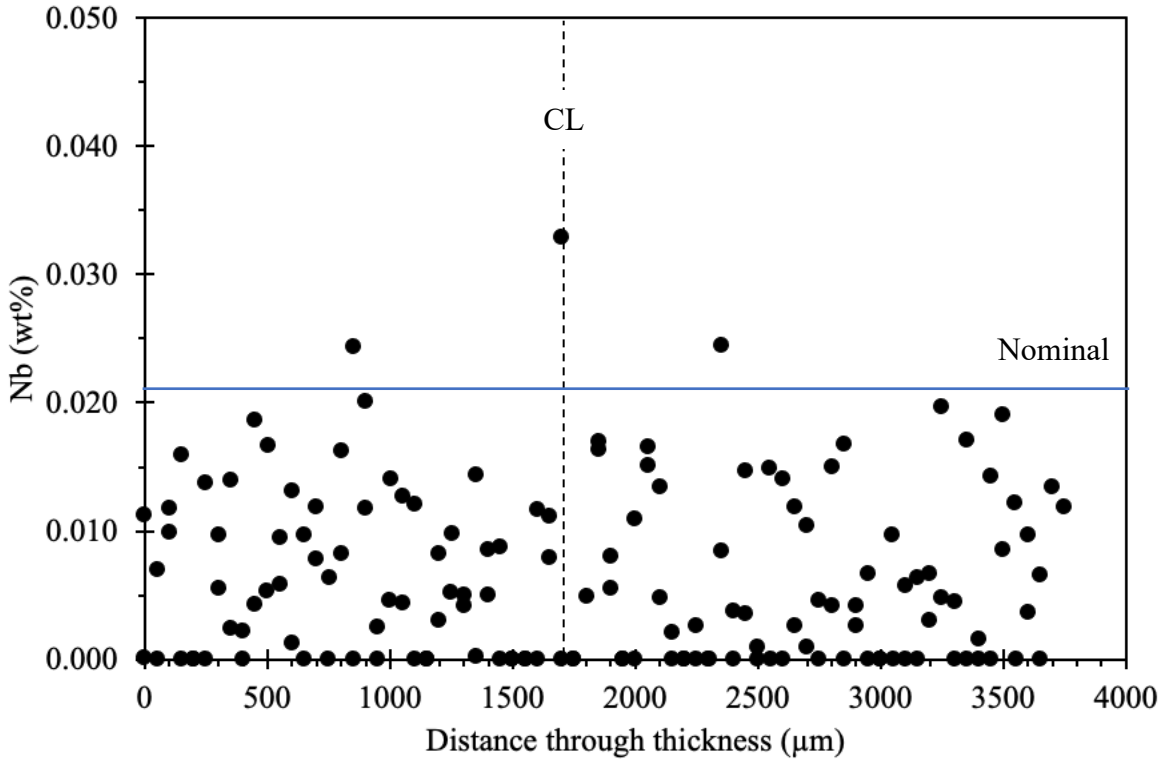


**Figure B19** Weight percent of Nb obtained from EMPA line scan in sample 4068

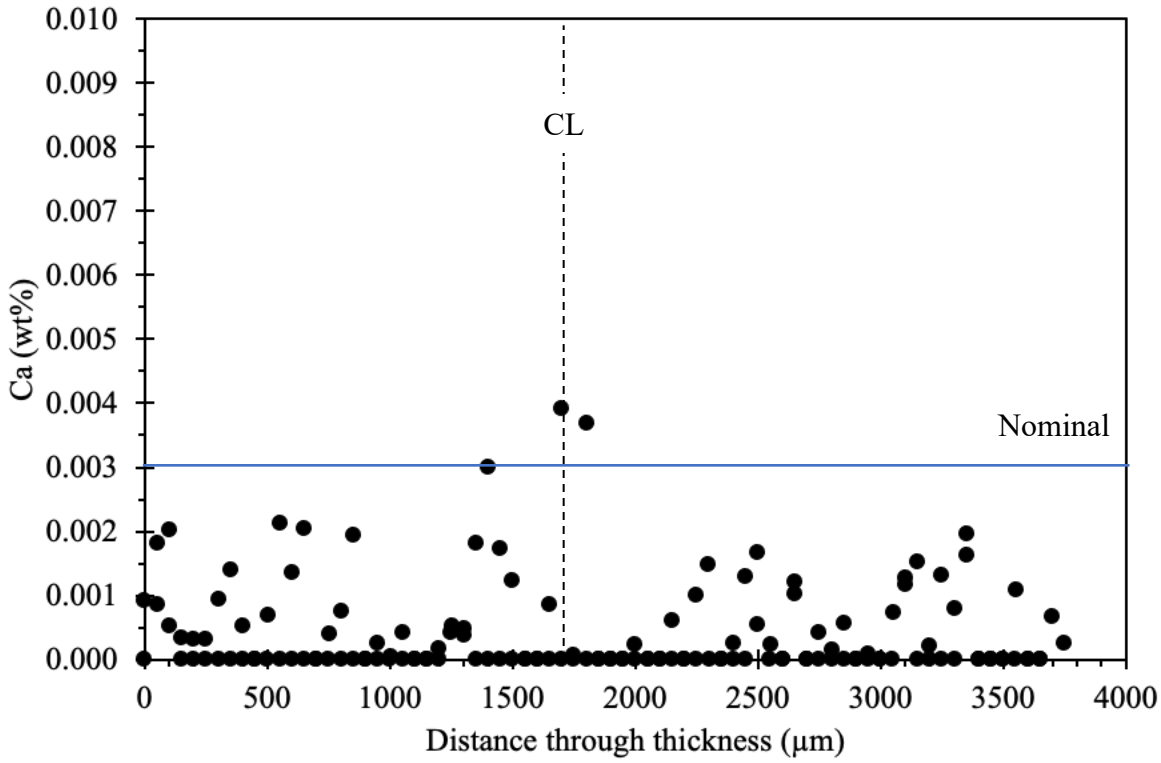


**Figure B20** Weight percent of Ca obtained from EMPA line scan in sample 4068

## B.6 4093

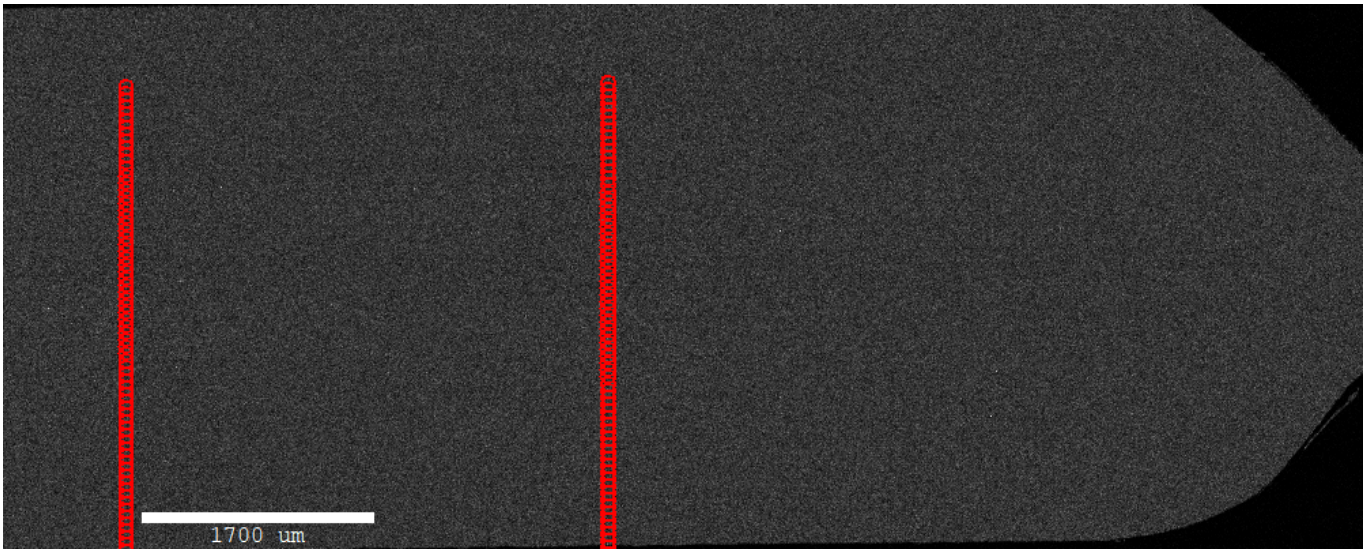


**Figure B21** Line scan location of points for sample 4093

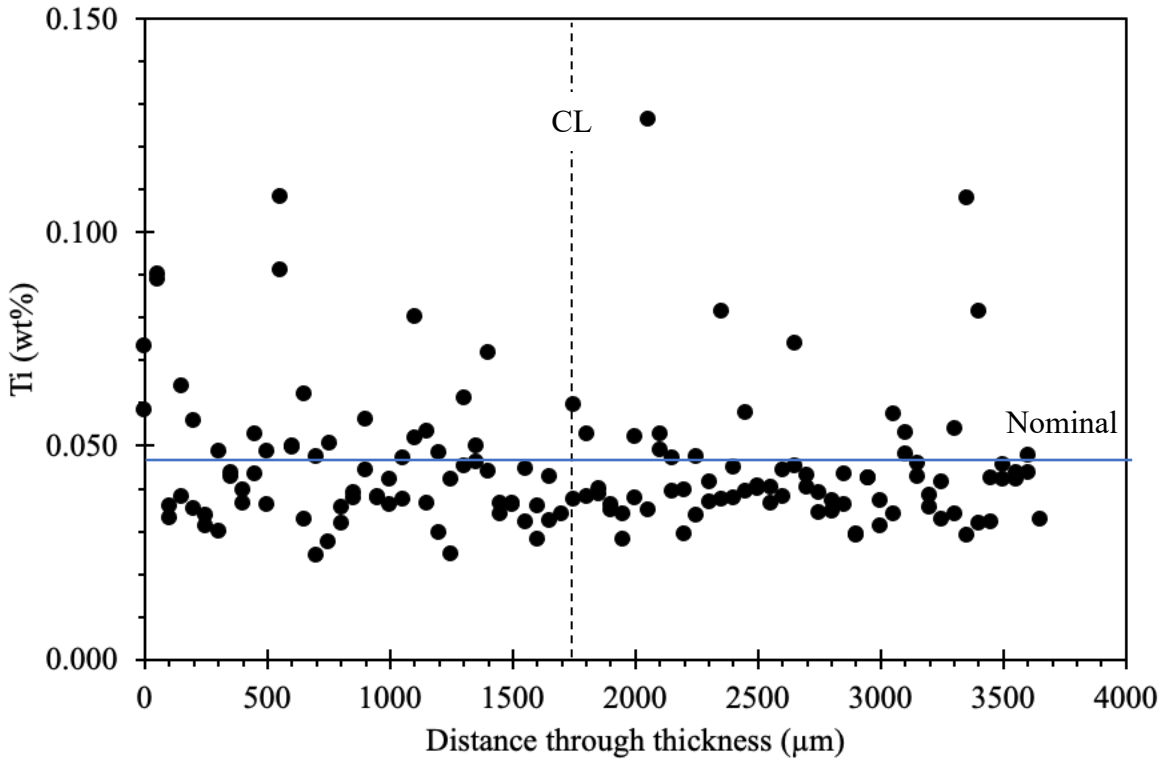


**Figure B22** Weight percent of Ti obtained from EMPA line scan in sample 4093

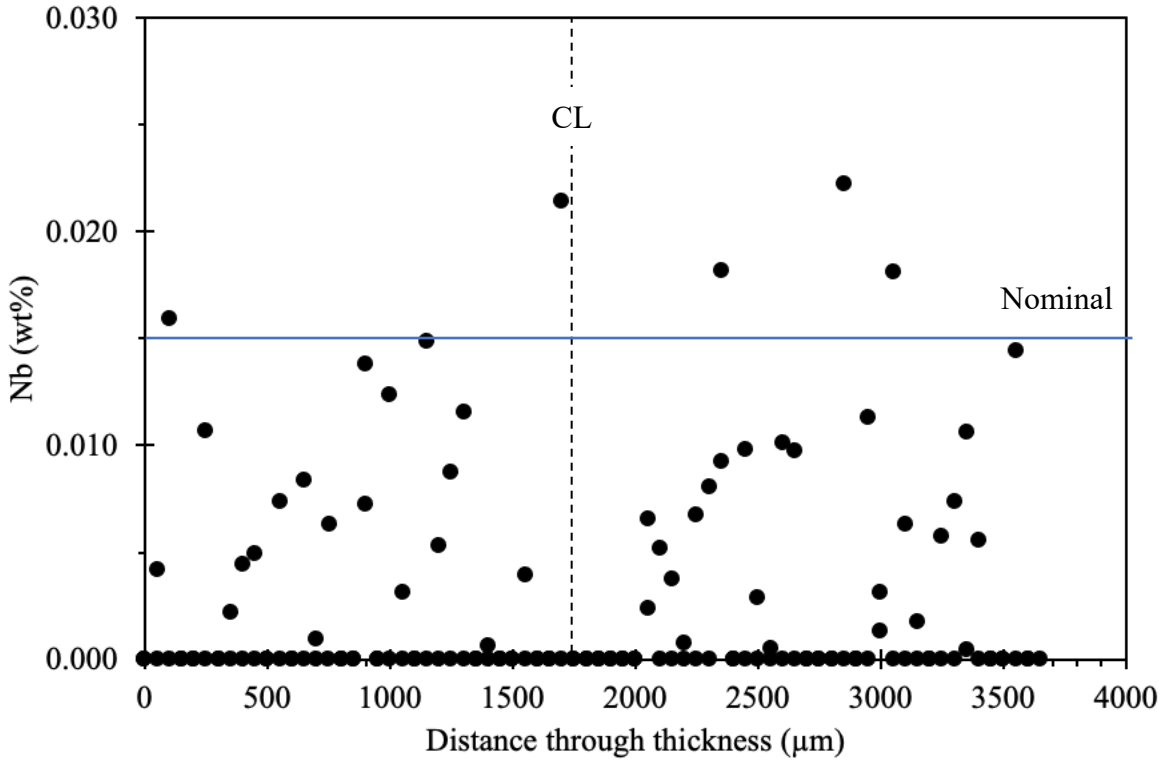


**Figure B23** Weight percent of Nb obtained from EMPA line scan in sample 4093

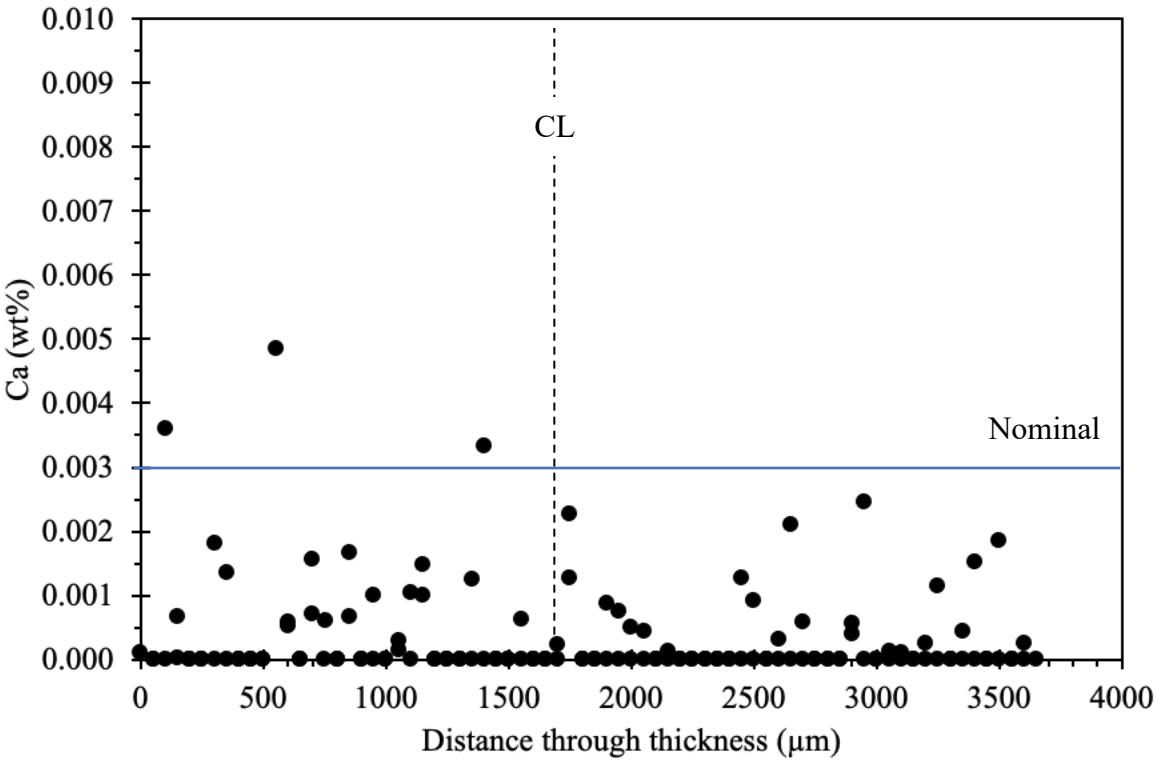


**Figure B24** Weight percent of Ca obtained from EMPA line scan in sample 4093

# Appendix C – EMPA Codes

Appendix C presents the scripts of the two codes used for EMPA analysis: Greyscale Image Converting Program and EMPA Precipitate Analysis Program.

## C.1 Greyscale Image Converting Program

```
import numpy as np
from PIL import Image as im
import sys
import os
from pathlib import Path

def GS_Convert(image_path):
    map = im.open(image_path)
    # Convert Image to a numpy array
    maparray = np.array(map)
    # Take first R color channel of image and ignore B and G channels
    maparray = maparray[:,:,0]
    text_path = image_path.parent / (image_path.stem + '.txt')
    np.savetxt (text_path,maparray ,delimiter=',',newline='\n',fmt="%.3f")


image_path = Path(input("Enter Folder path or Image Path:
").replace('"',''))
valid_ext = {'.tif'}

if image_path.is_dir():
    print("Is Folder")
    for image in os.listdir(image_path):
        if Path(image).suffix in valid_ext:
            GS_Convert(Path(image))
elif image_path.is_file():
    print("Is File")
    GS_Convert(image_path)
else:
    print("Invalid Path")

print("Conversion complete! Press any key to exit script.")
os.system('pause')
```

## C.2 EMPA Precipitate Analysis Program

```
import numpy as np
from numpy import asarray
from PIL import Image as im

# Manganese Module
def MnModule(MnGSVal):
    mapMn = im.open('4280_00012_WDS1_Mn_LTAP_.tif')
    # Convert Image to a numpy array`
    maparrayMn = asarray(mapMn)
```

```
    maparrayMn = maparrayMn[:,:,0]
    # Value Threshold
    Coords = np.where (maparrayMn >= MnGSVal)

    CoordList = list(zip(Coords[0],Coords[1]))
    CoordListSave = np.array(CoordList)
    np.savetxt ( 'List of Coordinates for
Mn.txt',CoordListSave,delimiter=',',newline='\n',fmt="%d")
    # End of Module
    return CoordList

# Titanium Module
def TiModule(TiGSVal):
    mapTi = im.open('4280_00012_WDS3_Ti_LLIF_.tif')
    # Convert Image to an array
    maparrayTi = asarray(mapTi)
    maparrayTi = maparrayTi[:,:,0]
    # Value Threshold
    Coords1 = np.where (maparrayTi >= TiGSVal)

    CoordList1 = list(zip(Coords1[0],Coords1[1]))
    CoordListSave1 = np.array(CoordList1)
    np.savetxt ( 'List of Coordinates for
Ti.txt',CoordListSave1,delimiter=',',newline='\n',fmt="%d")
    #End of Module
    return CoordList1

# Niobium Module
def NbModule(NbGSVal):
    mapNb = im.open('4280_00012_WDS4_Nb_PET_.tif')
    # Convert Image to a numpy array`
    maparrayNb = asarray(mapNb)
    maparrayNb = maparrayNb[:,:,0]
    # Value Threshold
    Coords2 = np.where (maparrayNb >= NbGSVal)

    CoordList2 = list(zip(Coords2[0],Coords2[1]))
    CoordListSave2 = np.array(CoordList2)
    np.savetxt ( 'List of Coordinates for
Nb.txt',CoordListSave2,delimiter=',',newline='\n',fmt="%d")
    #End of Module
    return CoordList2

# Calcium Module
def CaModule(CaGSVal):
    mapCa = im.open('4280_00012_WDS5_Ca_LPET_.tif')
    # Convert Image to an array
    maparrayCa = asarray(mapCa)
    maparrayCa = maparrayCa[:,:,0]
    # Value Threshold
    Coords3 = np.where (maparrayCa >= CaGSVal)

    CoordList3 = list(zip(Coords3[0],Coords3[1]))
    CoordListSave3 = np.array(CoordList3)
```

```
    np.savetxt ( 'List of Coordinates for
Ca.txt',CoordListSave3,delimiter=',',newline='\n',fmt="%d")
    #End of Module
    return CoordList3

def SModule(SGSVal):
    # Sulfur Module
    mapS = im.open('4280_00012_WDS2_S_PET_.tif')
    # Convert Image to an array
    maparrayS = asarray(mapS)
    maparrayS = maparrayS[:,:,0]
    # Value Threshold
    Coords4 = np.where (maparrayS >= SGSVal)

    CoordList4 = list(zip(Coords4[0],Coords4[1]))
    CoordListSave4 = np.array(CoordList4)
    np.savetxt ( 'List of Coordinates for
S.txt',CoordListSave4,delimiter=',',newline='\n',fmt="%d")
    #End of Module
    return CoordList4

def Elementrun(temp0):
    temp1 = []
    for i in temp0:
        if i == 1:
            MnGSVal = int(input("Assign a GS value for Mn: "))
            temp1.append(MnModule(MnGSVal))
        elif i == 2:
            TiGSVal = int(input("Assign a GS value for Ti: "))
            temp1.append(TiModule(TiGSVal))
        elif i == 3:
            NbGSVal = int(input("Assign a GS value for Nb: "))
            temp1.append(NbModule(NbGSVal))
        elif i == 4:
            CaGSVal = int(input("Assign a GS Value for Ca: "))
            temp1.append(CaModule(CaGSVal))
        elif i == 5:
            SGSVal = int(input("Assign a GS value for S: "))
            temp1.append(SModule(SGSVal))
        else:
            print("No Module Selected")
    return temp1

def CompModule(*argv):
    sets = []
    for list in argv:
        #print(list)
        #break
        sets.append(set(list))
    common_coords = set.intersection(*sets)
    return common_coords


def main():
```

```
    print("List of Elements: Mn, Ti, Nb, Ca, S")
    userinput = int(input("Enter the number of elements to be run (1-5):
"))
    print("Module Numbers\n Mn = 1\n Ti = 2\n Nb = 3\n Ca = 4\n  S = 5")
    temp0 = []
    for i in range(userinput):
        moduleinput = int(input("Enter module numbers that are to be run:
"))
        temp0.append(moduleinput)

    temp1 = Elementrun(temp0)
    coords_in_common = CompModule(*temp1)
    common_list = list(coords_in_common)
    common_list.sort()
    Listsave = np.array(common_list)
    np.savetxt ( 'List of Common
Coordinates.txt',Listsave,delimiter=',',newline='\n',fmt="%d")
    # Coordinate Filter
    filtered_list = []
    filtered_list1 = []
    filtered_list2 = []
    filtered_list3 = []
    for x in common_list:
        if 0 <= x[0] <= 82:
            filtered_list.append(x)
        elif 82 < x[0] <= 164:
            filtered_list1.append(x)
        elif 164 < x[0] <= 246:
            filtered_list2.append(x)
        elif 246 < x[0] <= 328:
            filtered_list3.append(x)

    with open("Coordinates from Top Edge to Top Quarter Line.txt", 'w') as
file:
        for line in filtered_list:
            file.write(str(line).strip('()') + '\n')

    with open("Coordinates from Quarter to Center Line.txt", 'w') as file:
        for line in filtered_list1:
            file.write(str(line).strip('()') + '\n')

    with open("Coordinates from Center to Bottom Quarter.txt", 'w') as
file:
        for line in filtered_list2:
            file.write(str(line).strip('()') + '\n')

    with open("Coordinates from Bottom Quarter to Bottom Edge.txt", 'w')
as file:
        for line in filtered_list3:
            file.write(str(line).strip('()') + '\n')

main()
```

# Appendix D – Lognormal Distributions

Appendix D presents the greyscale and line scan distributions for Ti and Nb.

## D.1 Ti Distributions

### D.1.1 4175

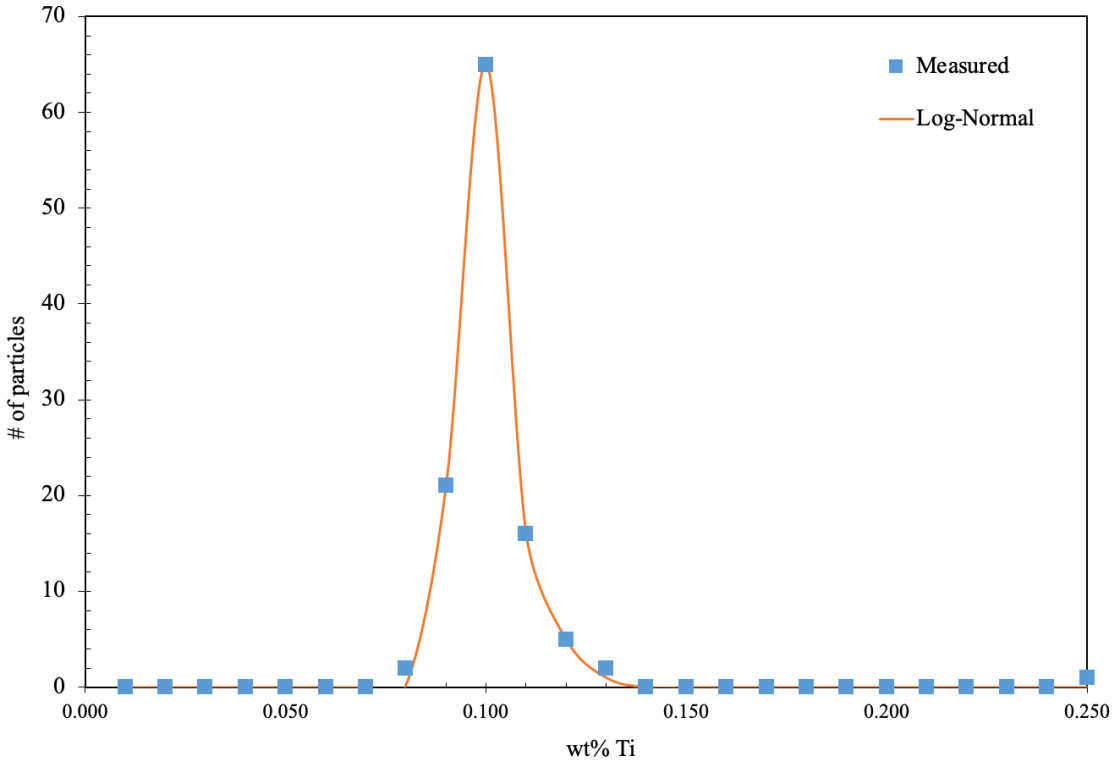


**Figure D1** Ti line scan data plotted against its lognormal distribution for sample 4175

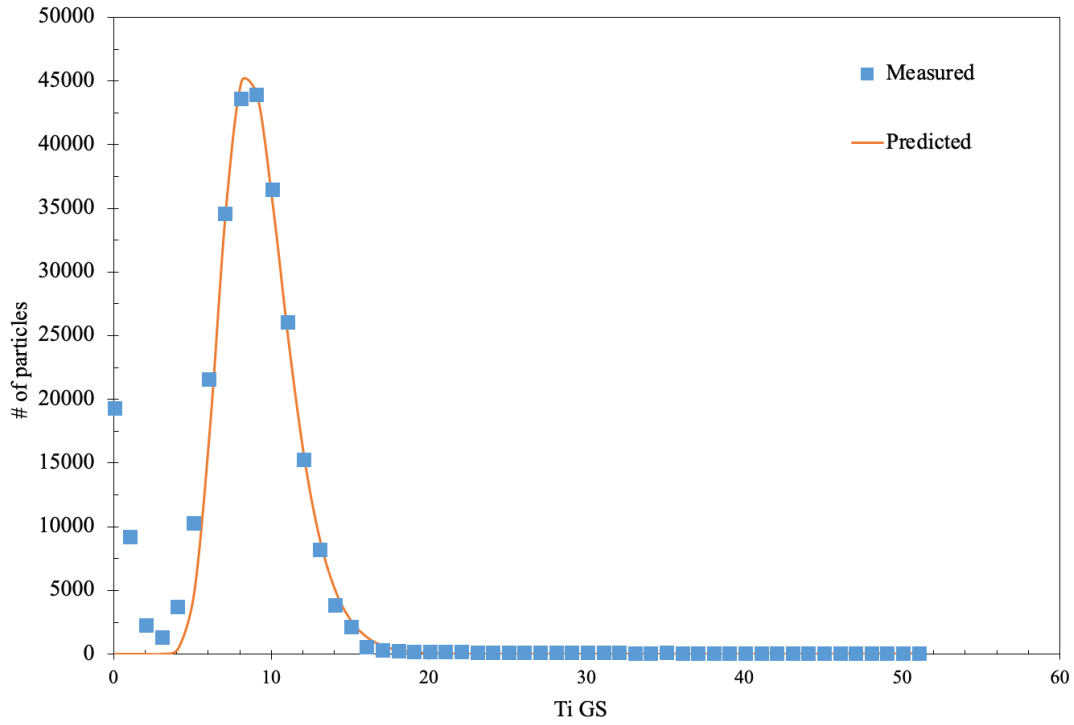


**Figure D2** Ti greyscale data plotted against its lognormal distribution for sample 4175

D.1.2 4372

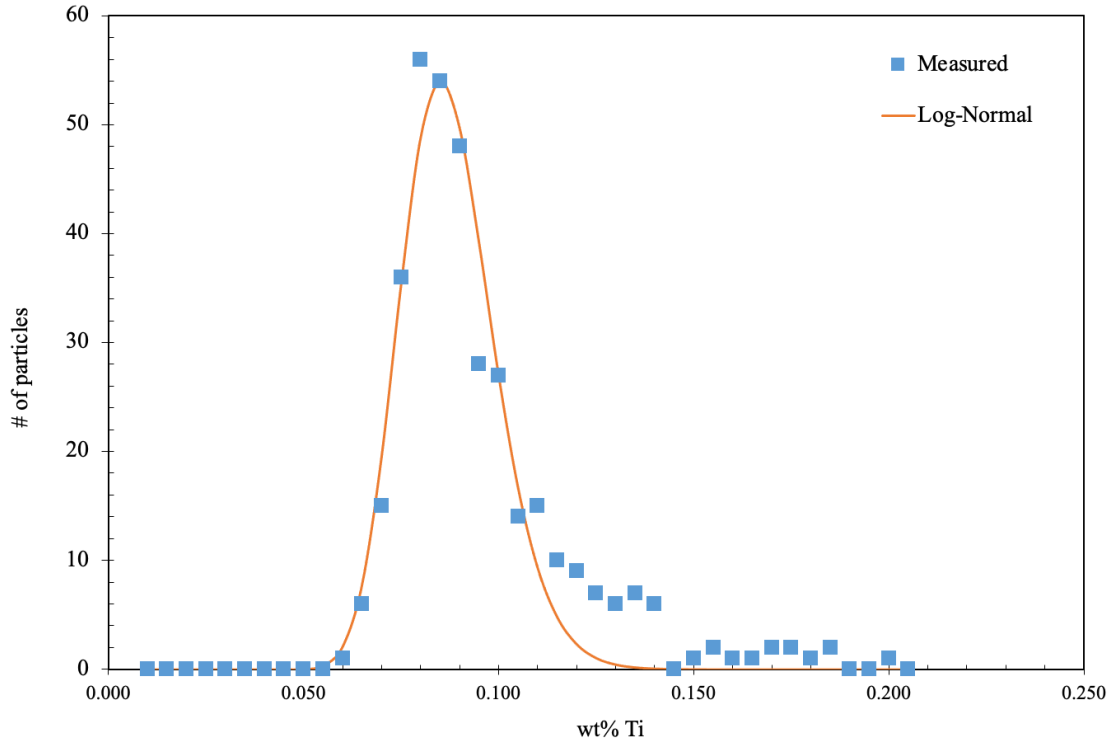


**Figure D3** Ti line scan data plotted against its lognormal distribution for sample 4372

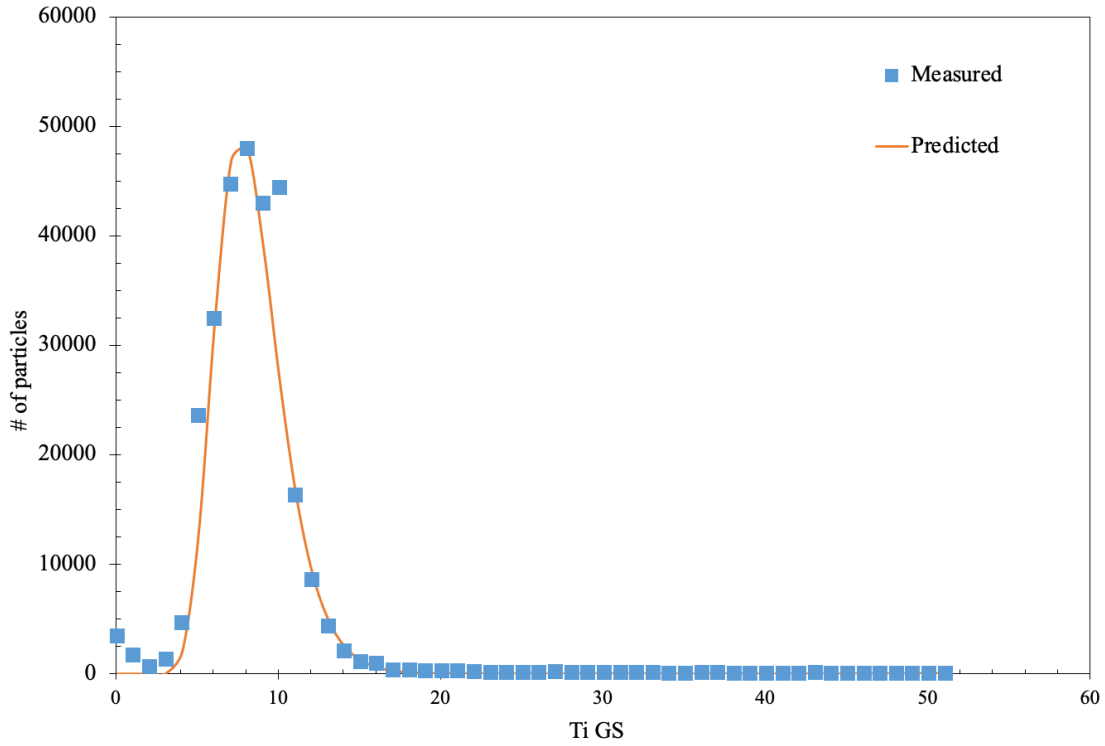


**Figure D4** Ti greyscale data plotted against its lognormal distribution for sample 4372

D.1.3 4052

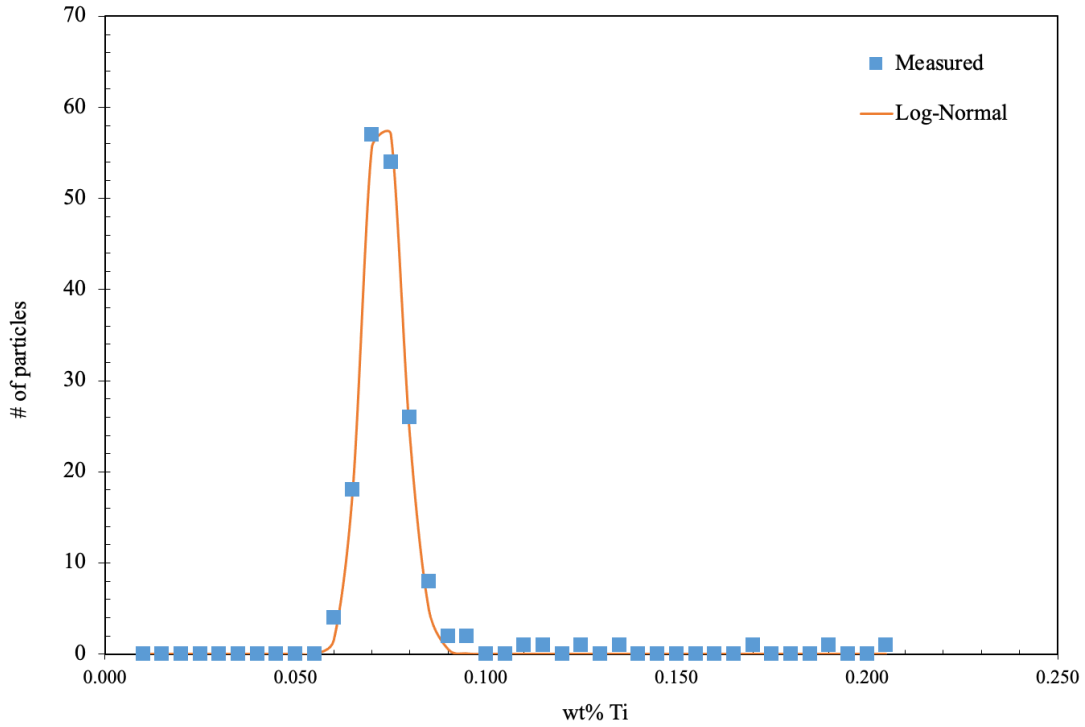


**Figure D5** Ti line scan data plotted against its lognormal distribution for sample 4052

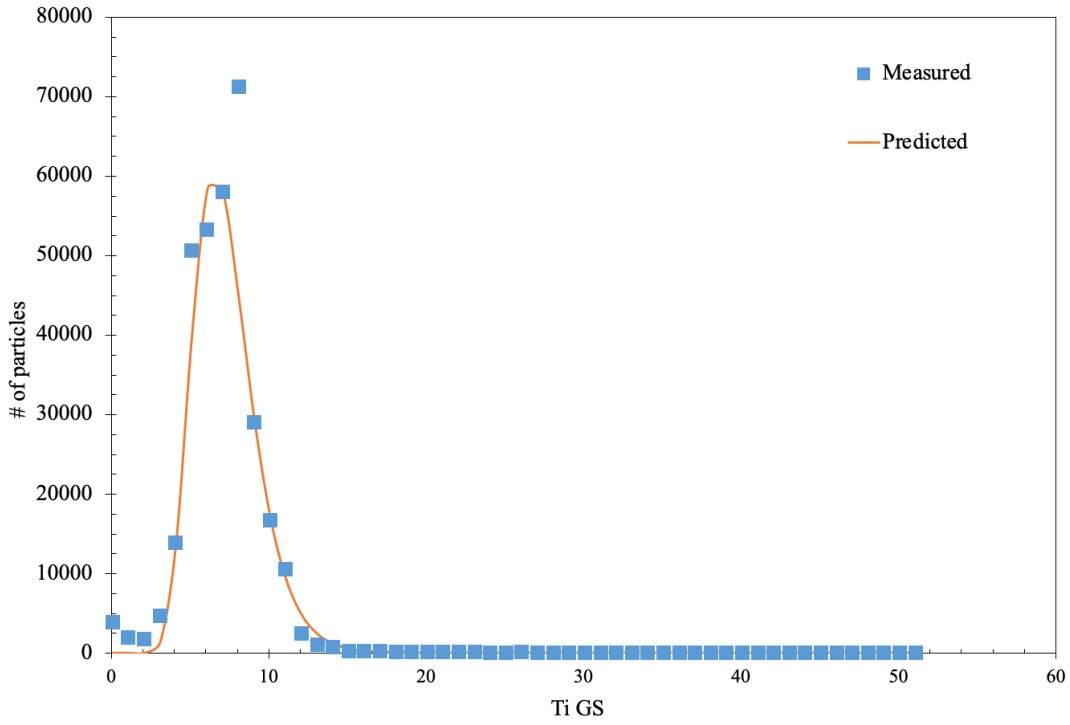


**Figure D6** Ti greyscale data plotted against its lognormal distribution for sample 4052

D.1.4 4081

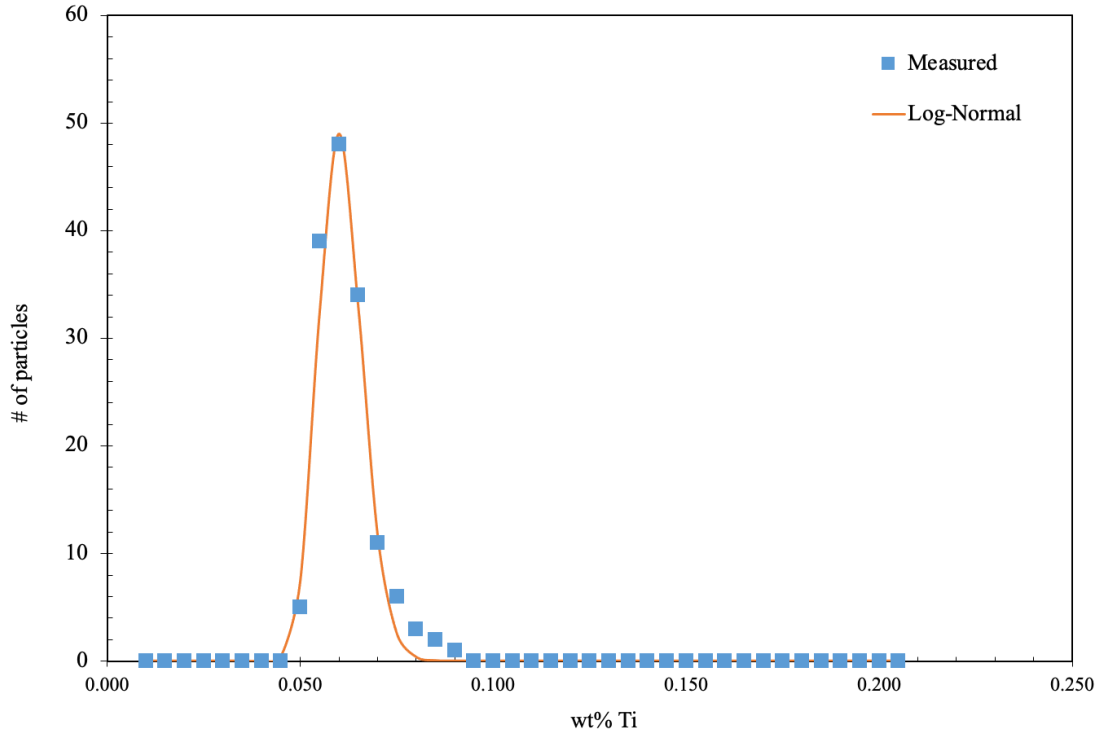


**Figure D7** Ti line scan data plotted against its lognormal distribution for sample 4081

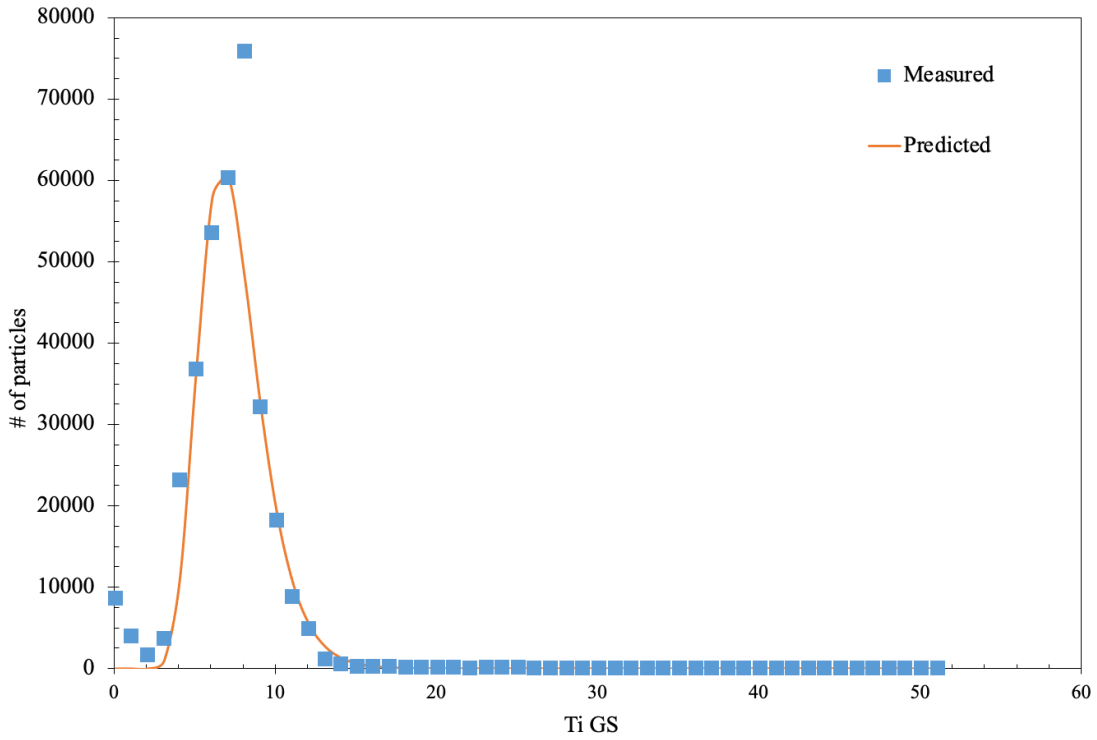


**Figure D8** Ti greyscale data plotted against its lognormal distribution for sample 4081

D.1.5 4068

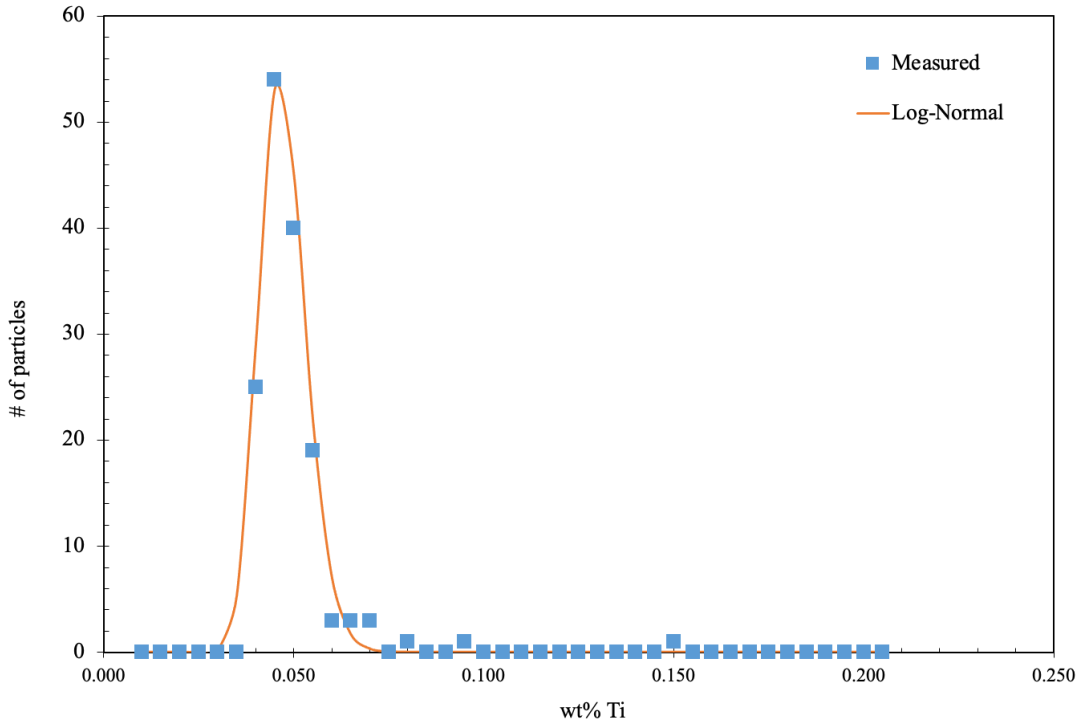


**Figure D9** Ti line scan data plotted against its lognormal distribution for sample 4068

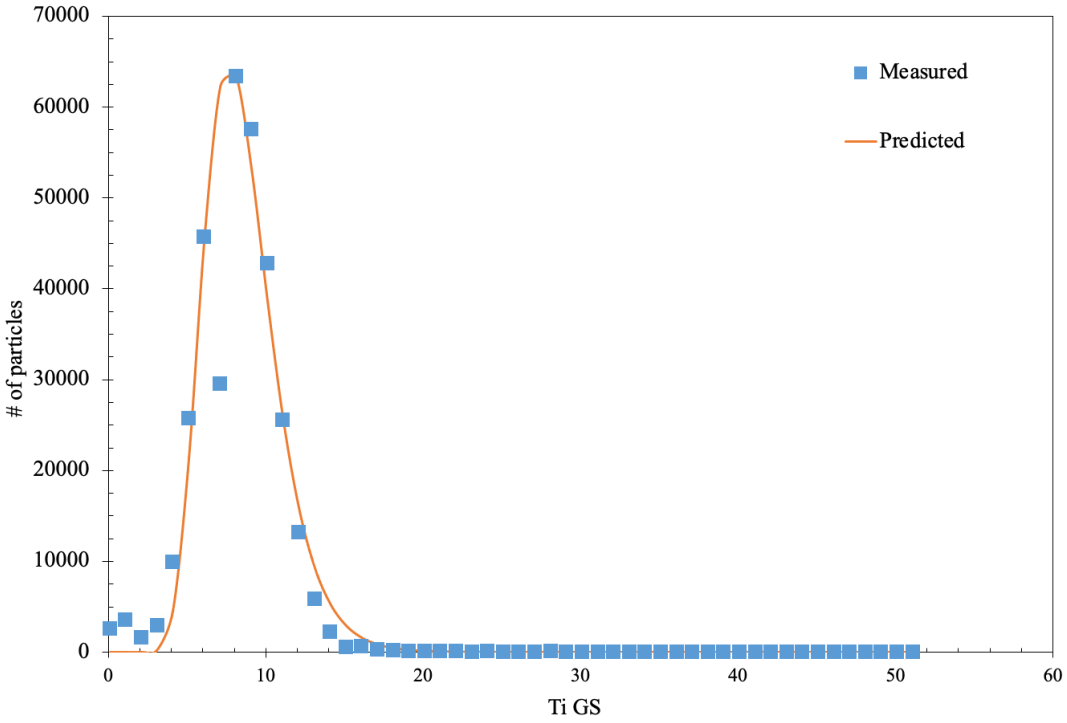


**Figure D10** Ti greyscale data plotted against its lognormal distribution for sample 4068

D.1.6 4093

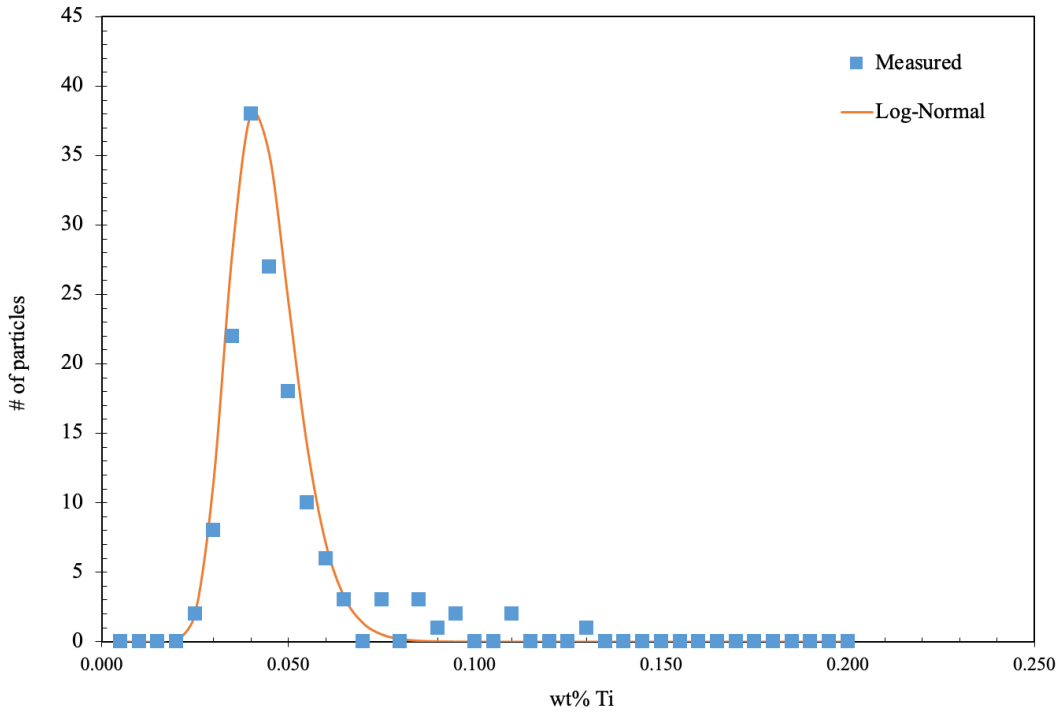


**Figure D11** Ti line scan data plotted against its lognormal distribution for sample 4093

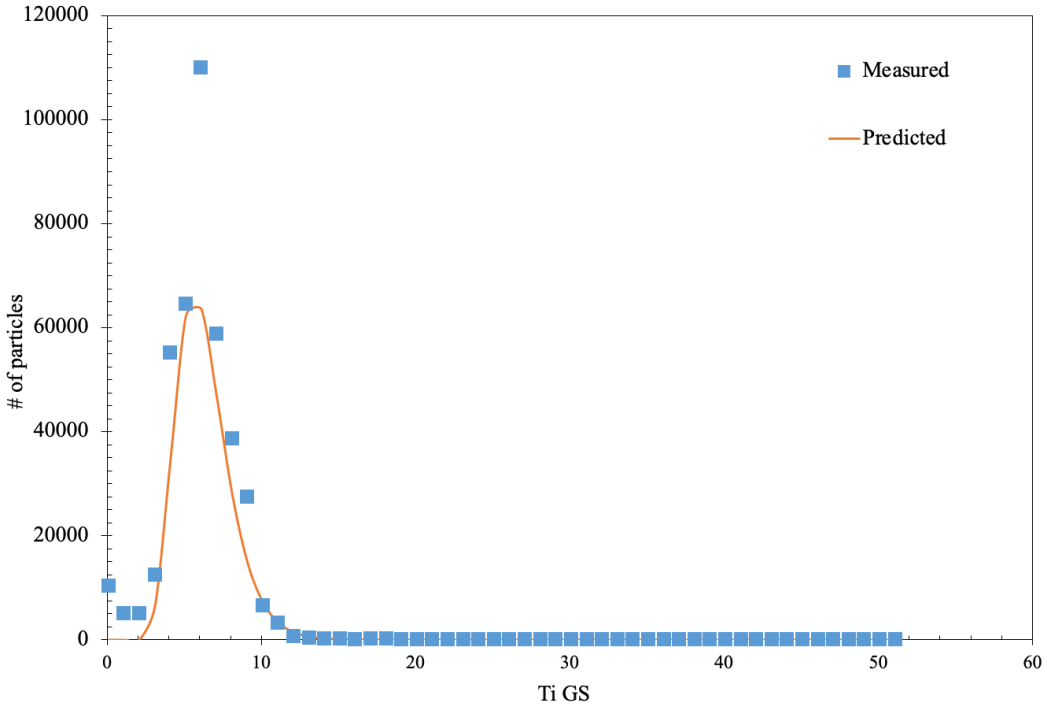


**Figure D12** Ti greyscale data plotted against its lognormal distribution for sample 4093

D.1.7 Ti z-score vs. ln(GS) example

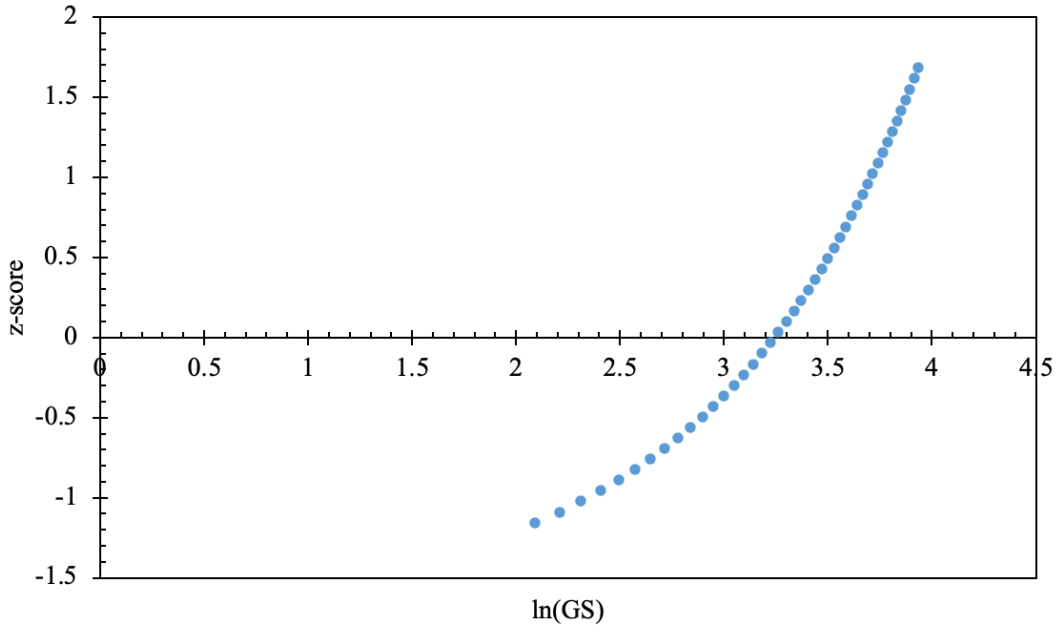


**Figure D13** z-score vs. ln(GS) plot for Ti lognormal curve in sample 4052

## D.2 Nb Distributions

### D.2.1 4280

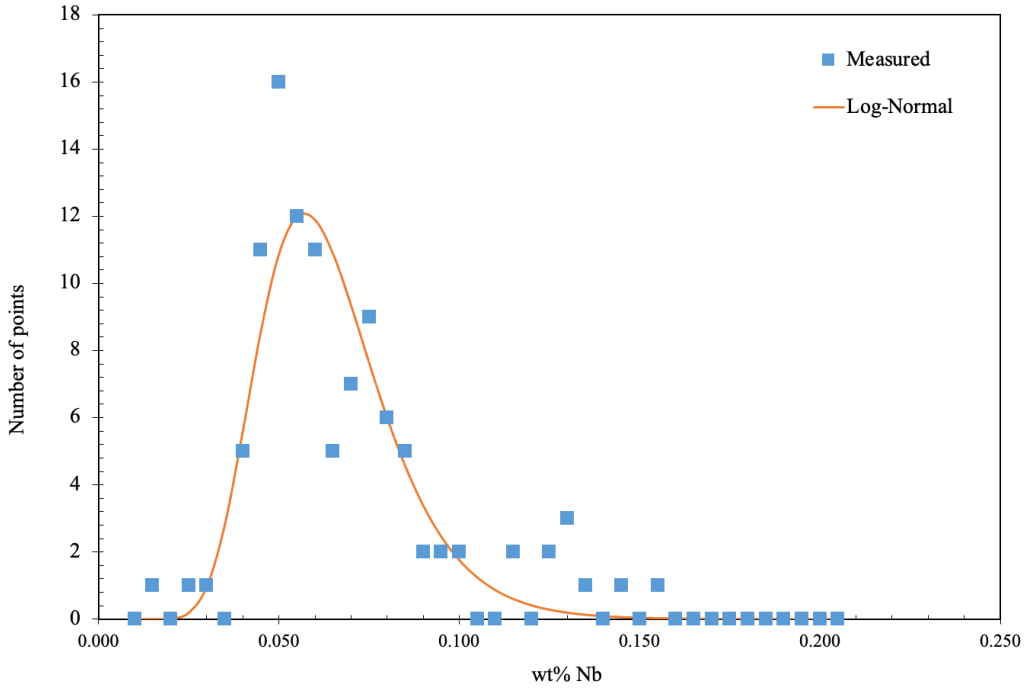


**Figure D14** Nb line scan data plotted against its lognormal distribution for sample 4280

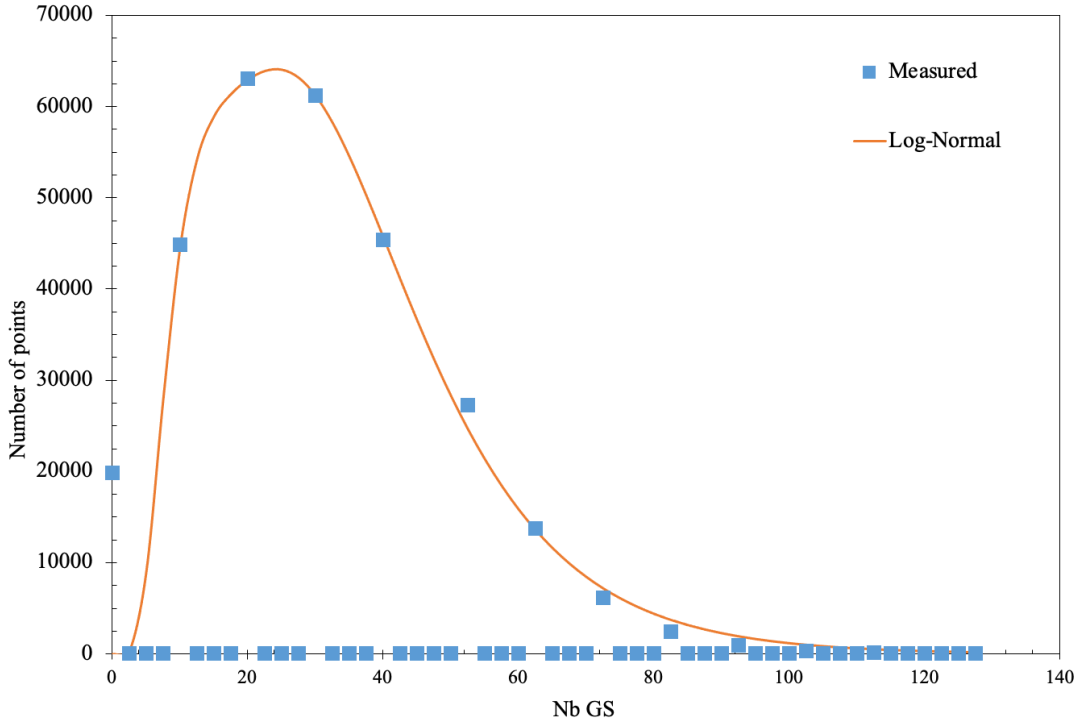


**Figure D15** Nb greyscale data plotted against its lognormal distribution for sample 4280

D.2.2 4175

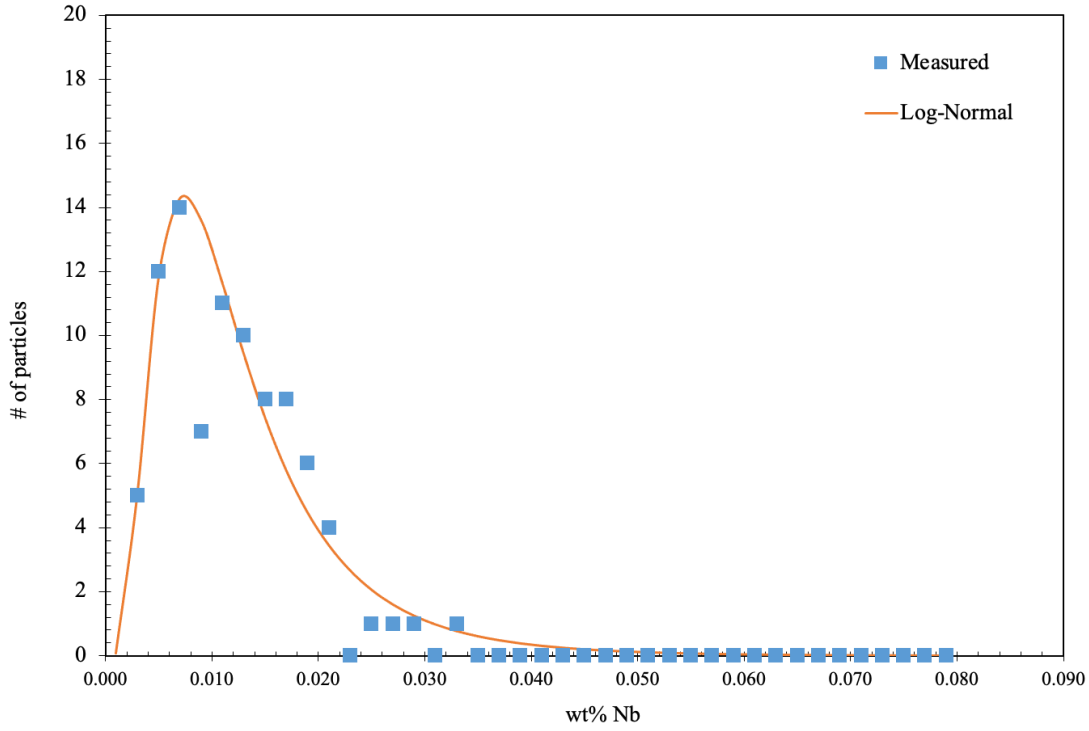


**Figure D16** Nb line scan data plotted against its lognormal distribution for sample 4175

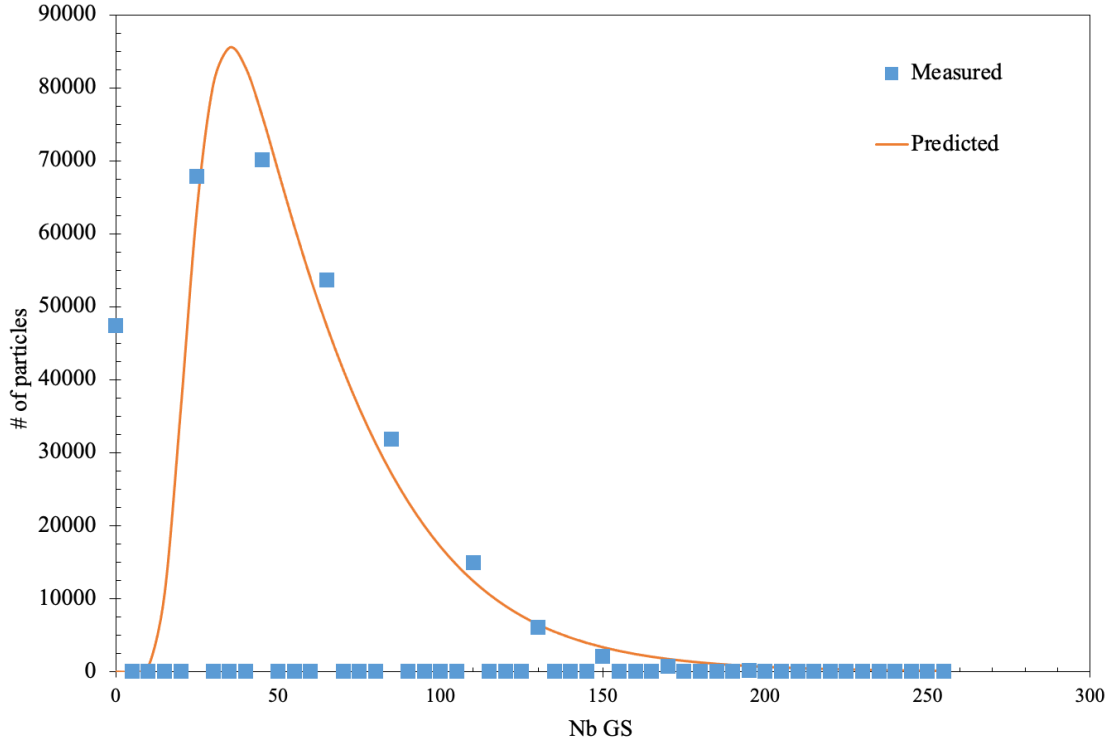


**Figure D17** Nb greyscale data plotted against its lognormal distribution for sample 4175

D.2.3 4372

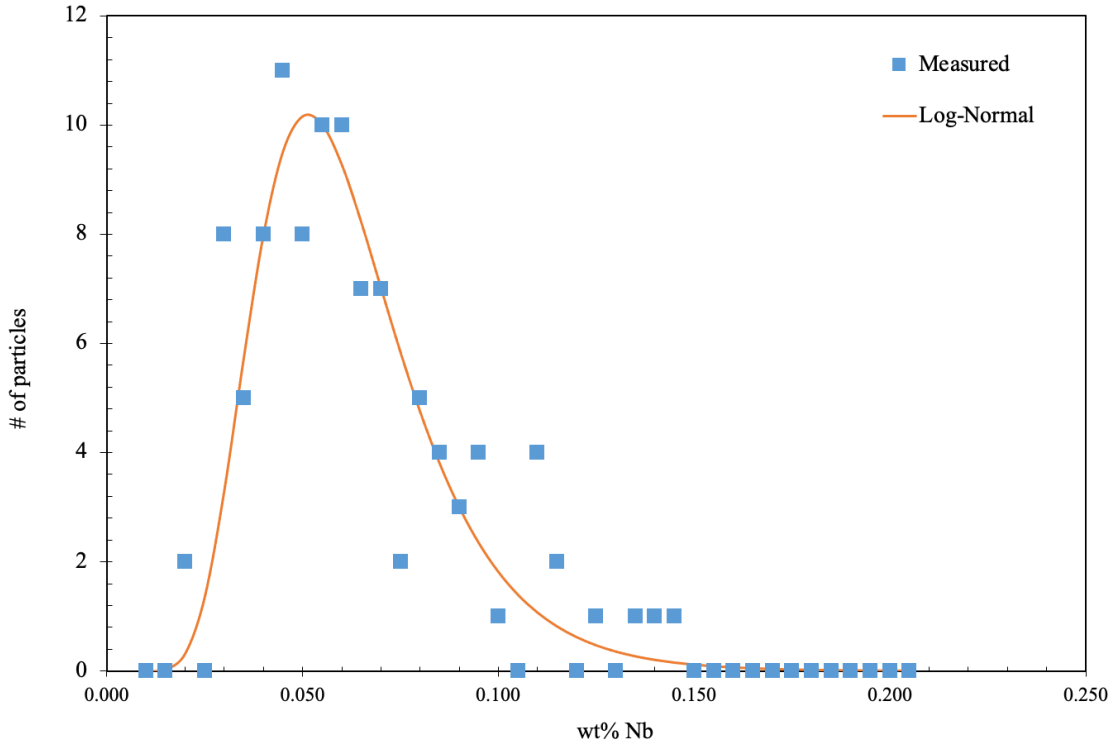


**Figure D18** Nb line scan data plotted against its lognormal distribution for sample 4372

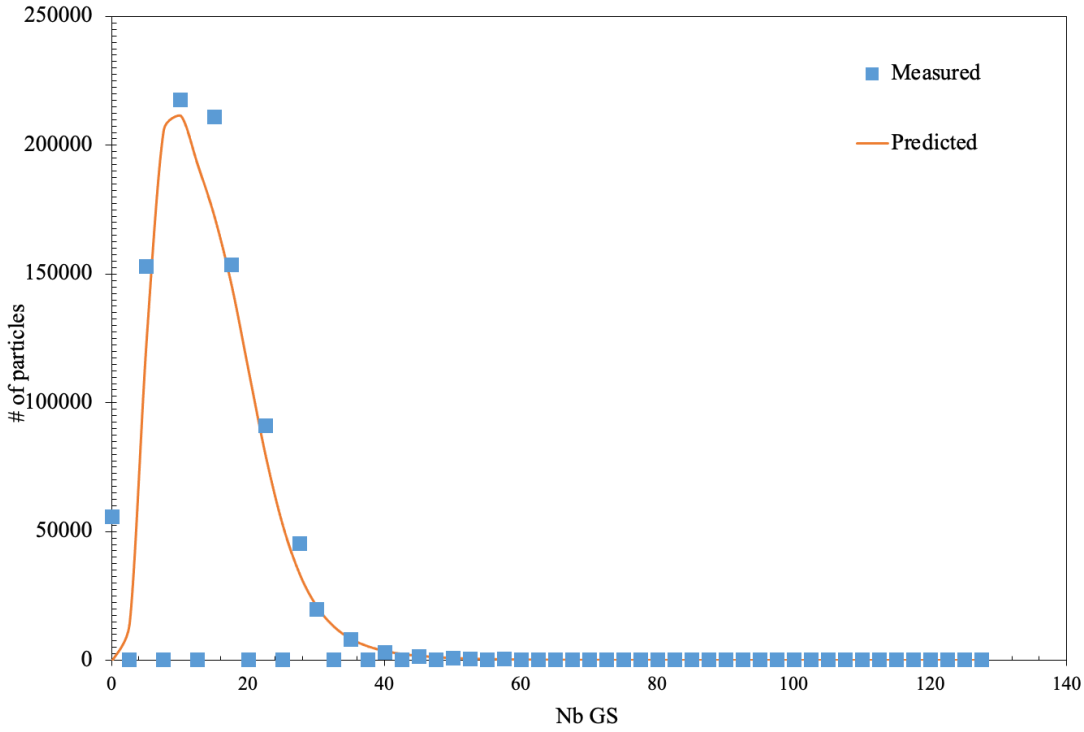


**Figure D19** Nb greyscale data plotted against its lognormal distribution for sample 4372

D.2.4 4052

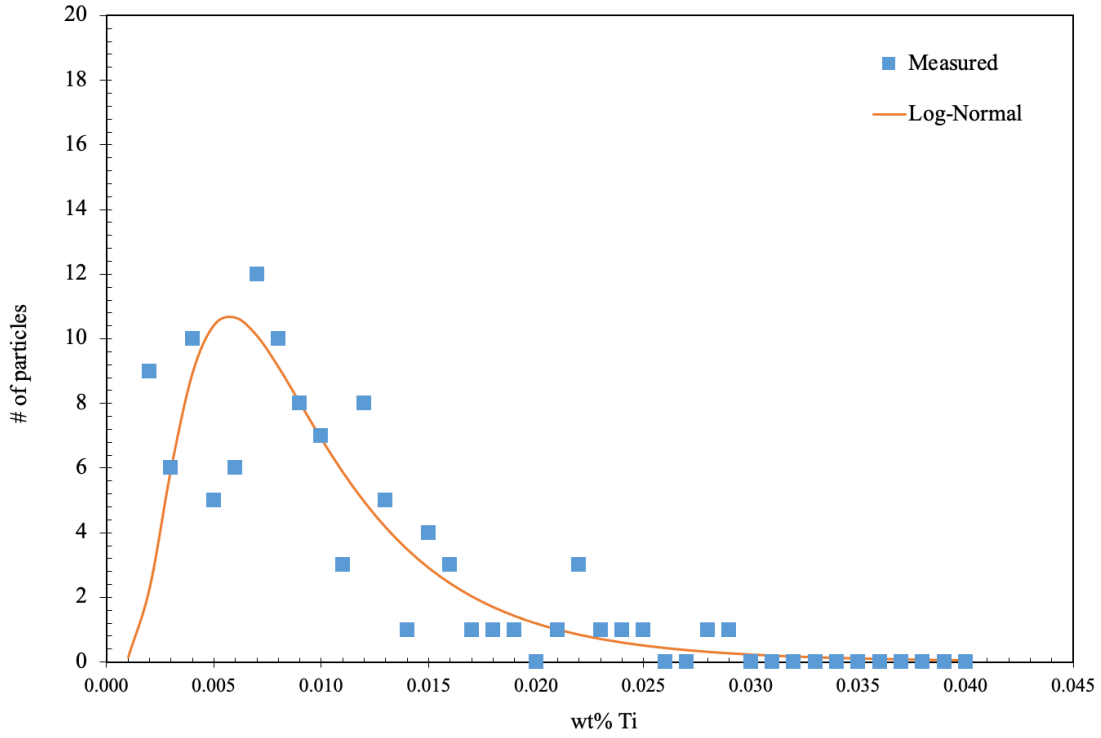


**Figure D20** Nb line scan data plotted against its lognormal distribution for sample 4052

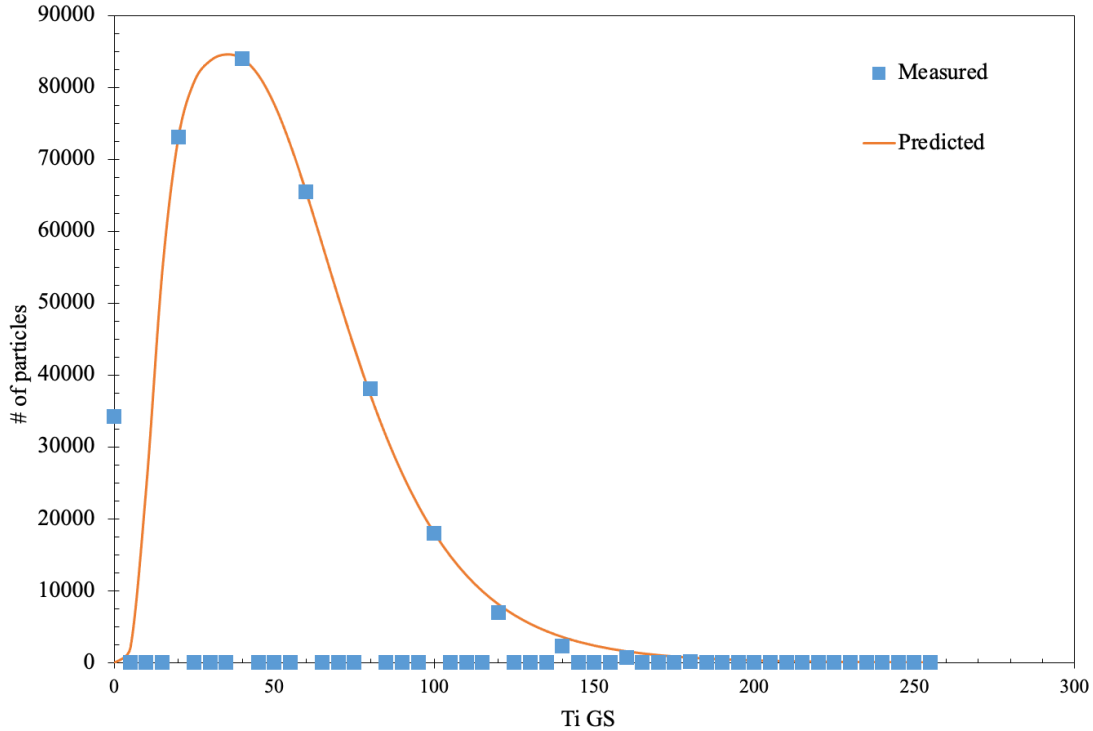


**Figure D21** Nb greyscale data plotted against its lognormal distribution for sample 4052

D.2.5 4081

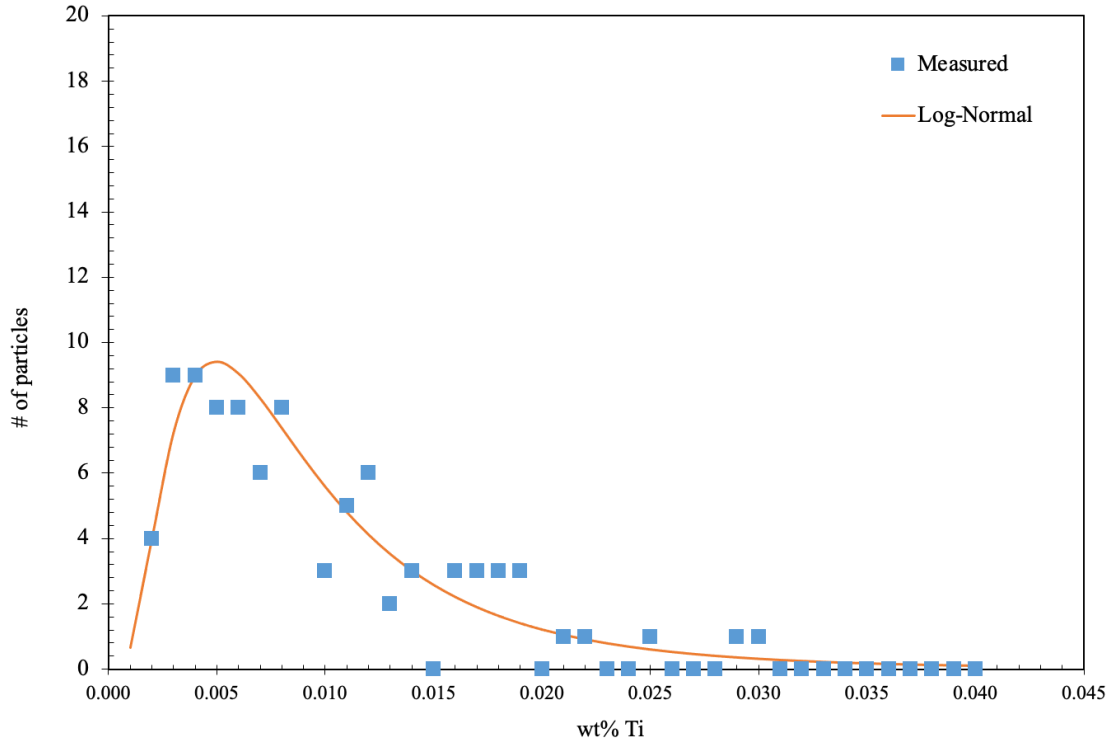


**Figure D22** Nb line scan data plotted against its lognormal distribution for sample 4081

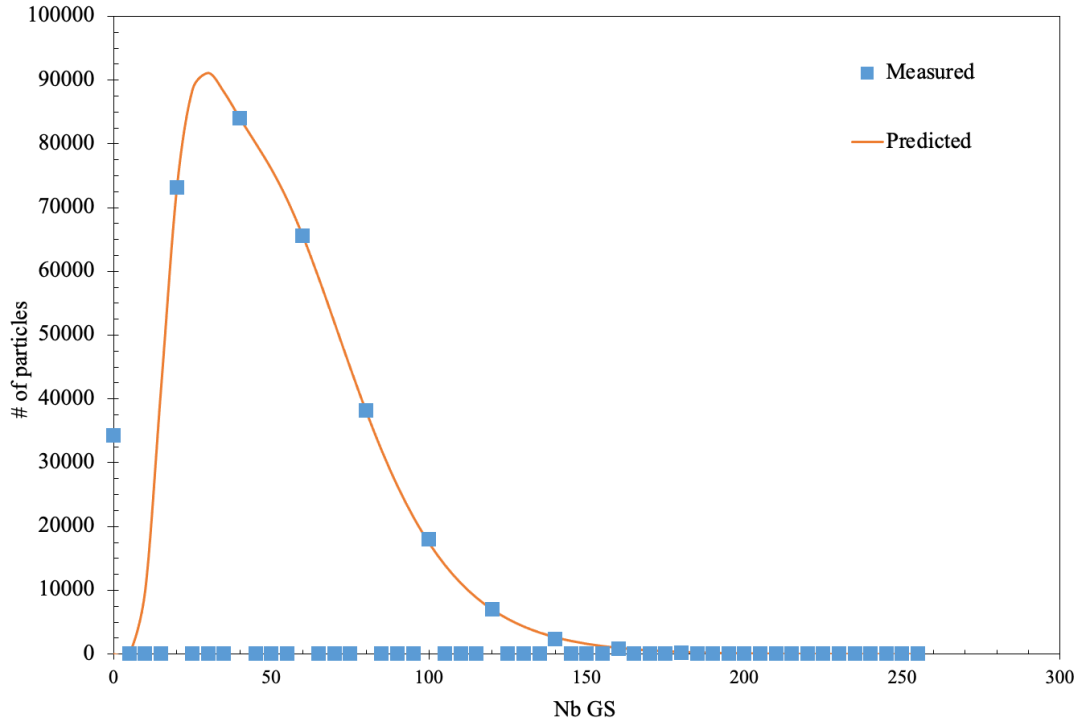


**Figure D23** Nb greyscale data plotted against its lognormal distribution for sample 4081

D.2.6 4068

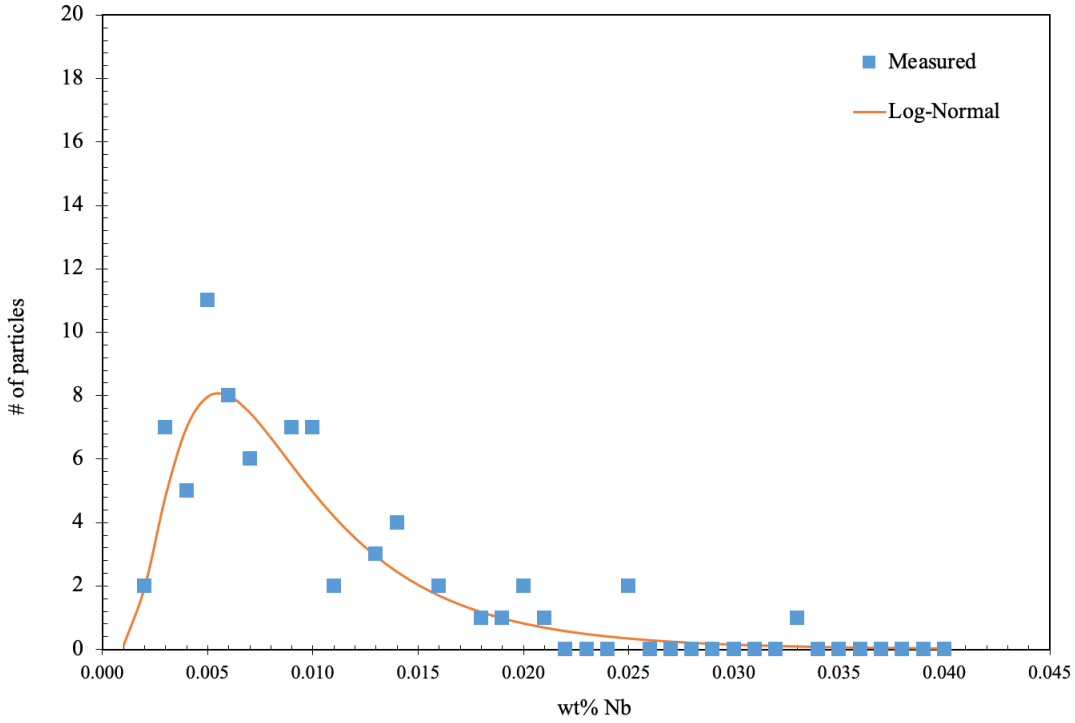


**Figure D24** Nb line scan data plotted against its lognormal distribution for sample 4068

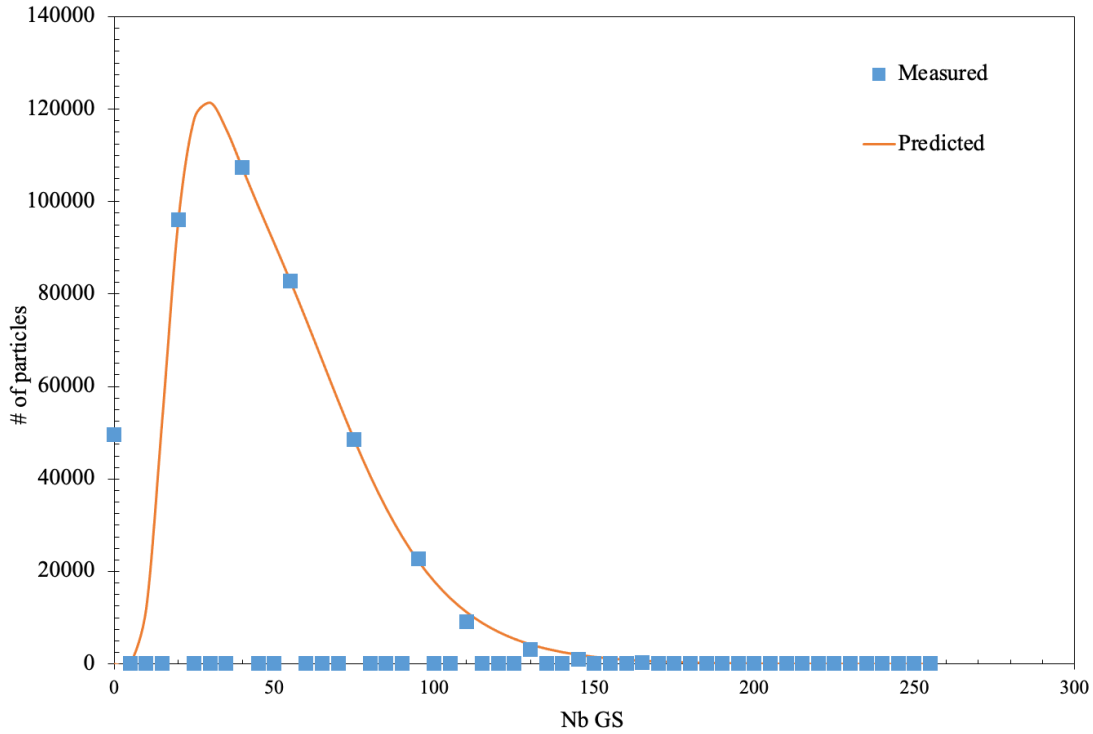


**Figure D25** Nb greyscale data plotted against its lognormal distribution for sample 4068

D.2.7 Nb z-score vs. ln(GS) example

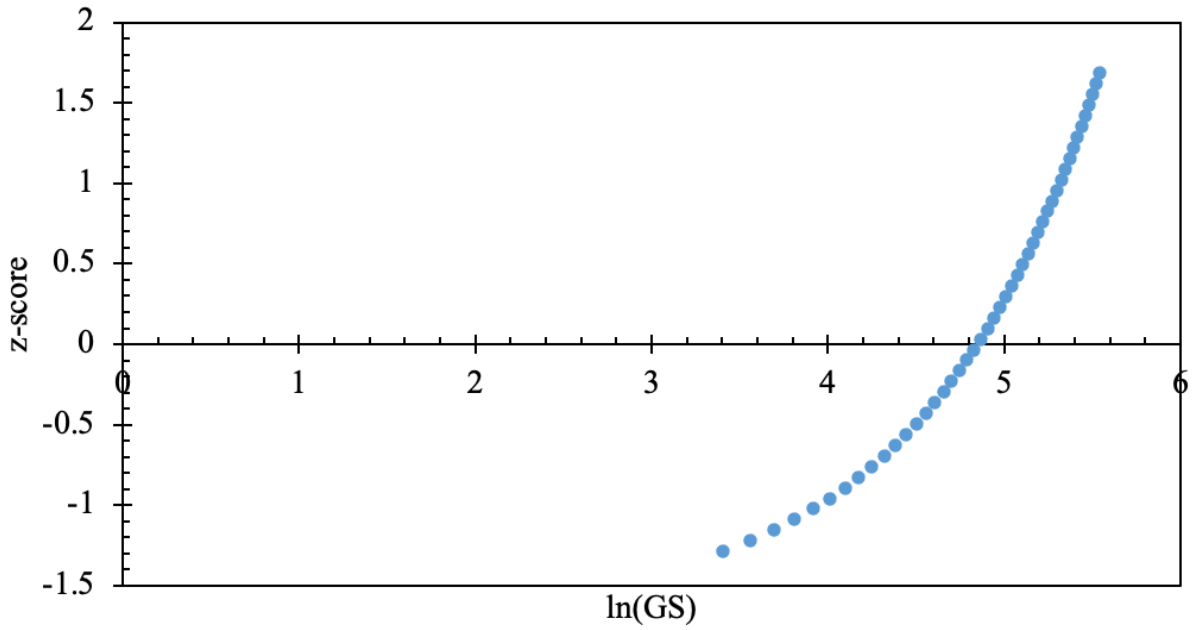


**Figure D26** z-score vs. ln(GS) plot for Nb lognormal curve in sample 4052

# Appendix E – Thermocalc Plots

Appendix E presents plots of the volume fractions obtained on Thermocalc for CaS compared to Ti, N, Ca, and S contents in the steels.

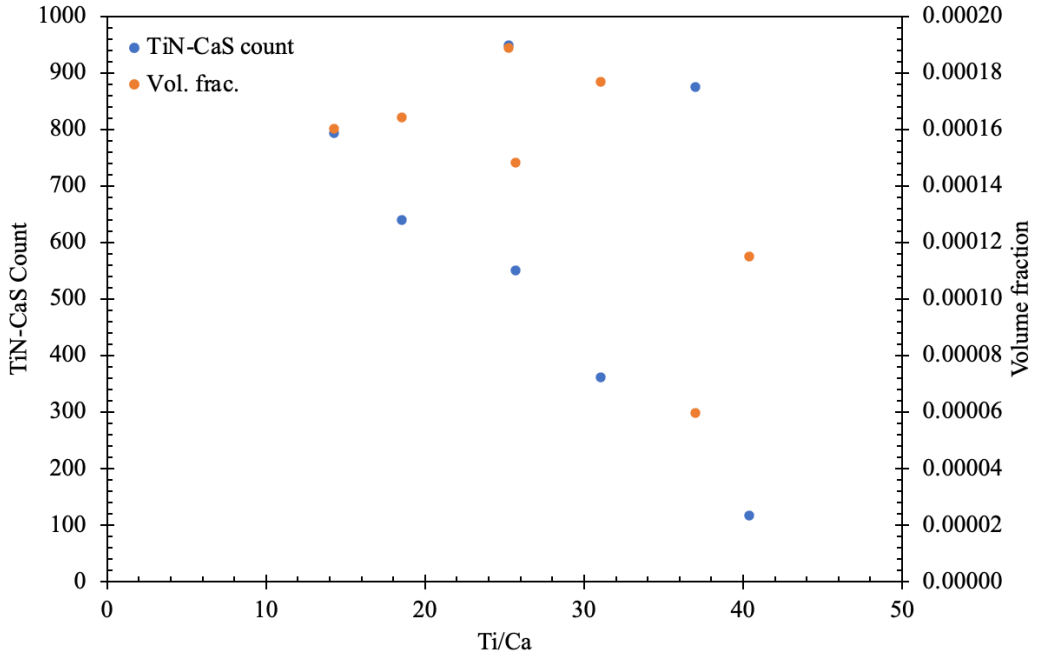


**Figure E1** Ti/Ca ratio vs. EMPA TiN-CaS count and CaS volume fraction from Thermocalc

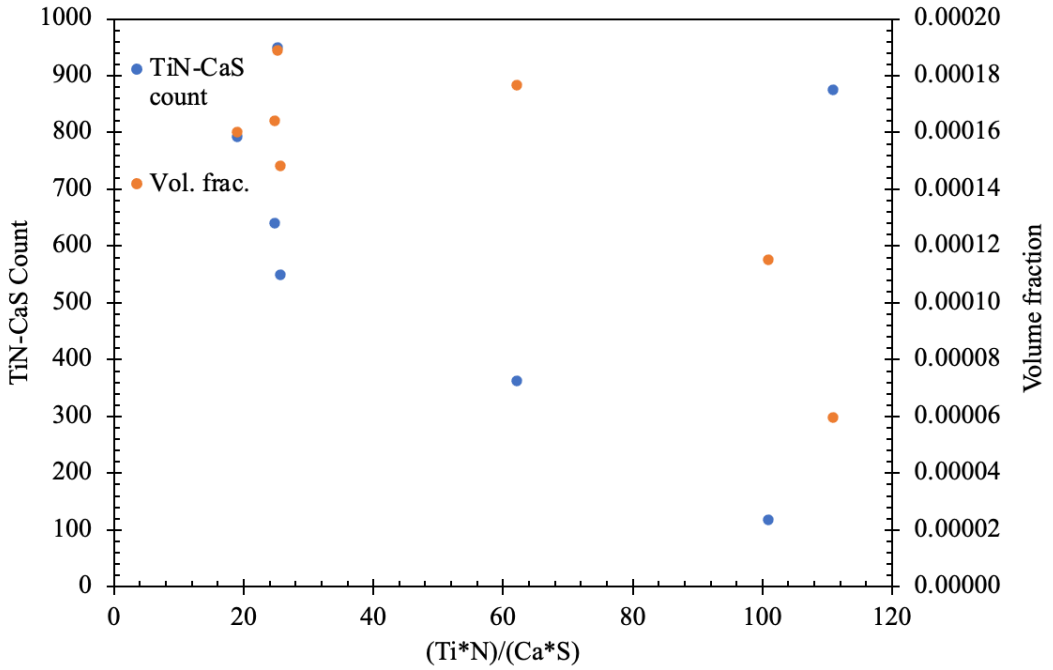


**Figure E2** Ti*N/Ca*S ratio vs. EMPA TiN-CaS count and CaS volume fraction from Thermocalc

# Appendix F – Normal Size Distributions

Appendix F presents the normal size distributions for samples 4175, 4052, and 4093.

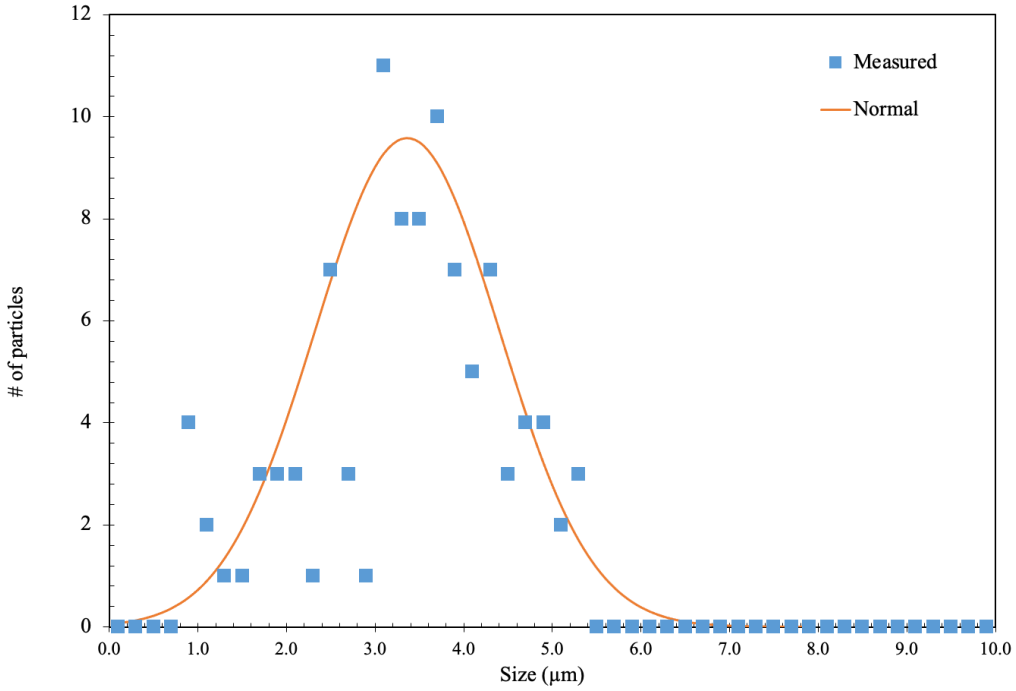


**Figure F1** Normal size distribution for sample 4175

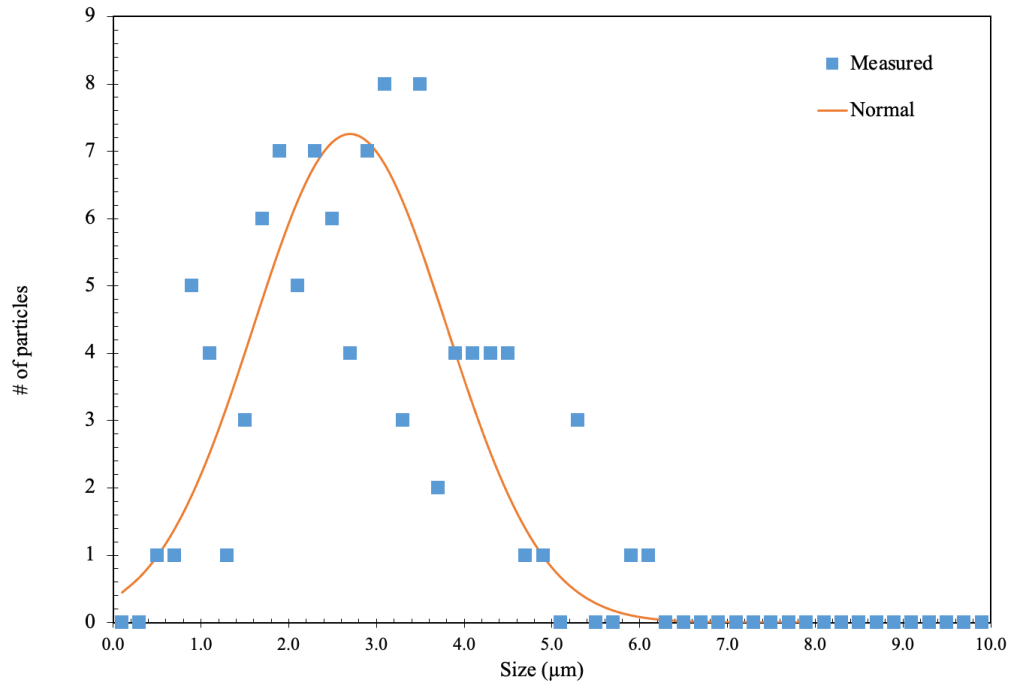


**Figure F2** Normal size distribution for sample 4052

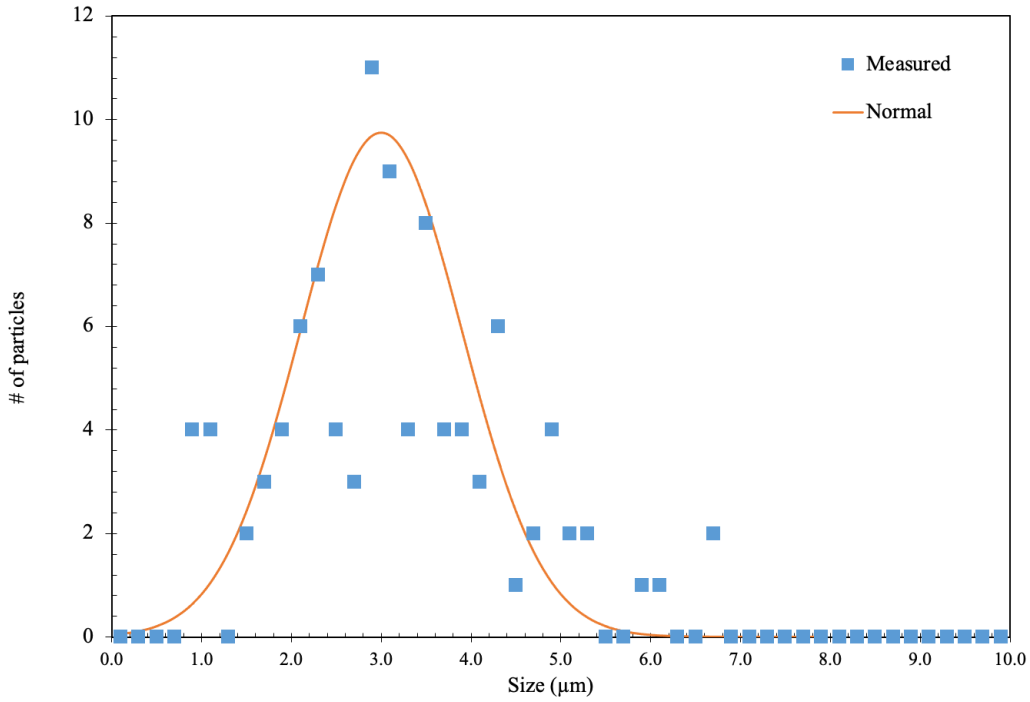


**Figure F3** Normal size distribution for sample 4093

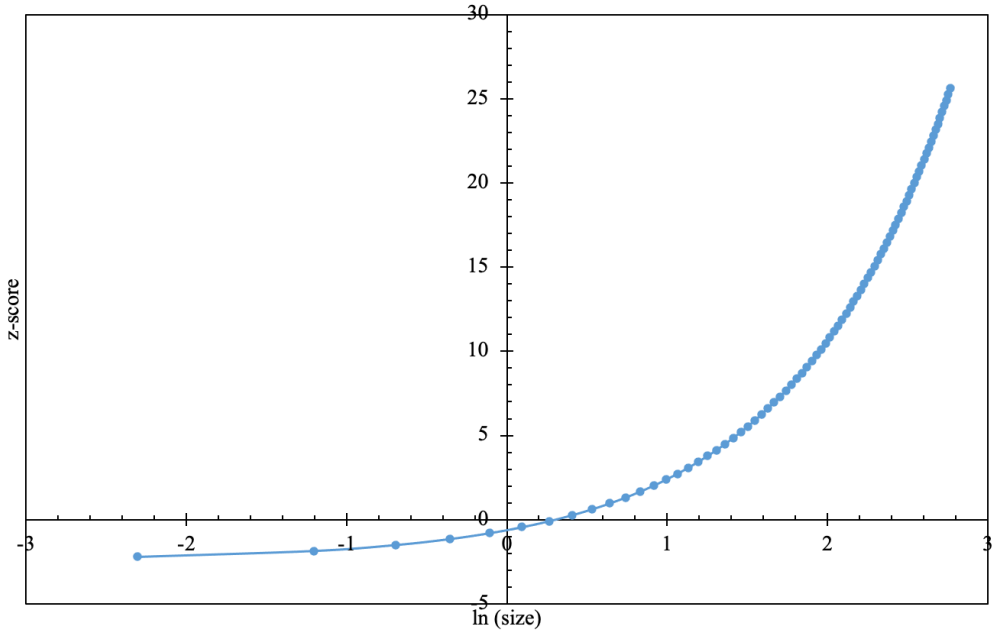


**Figure F4** z-score vs. ln(size) for size lognormal distribution in sample 4280